University of Padova

Doctoral Thesis
Cycle XXXIII

Lumped-Parameter Models for Congenital Diseased and Sex-Specific Cardiovascular Circulations

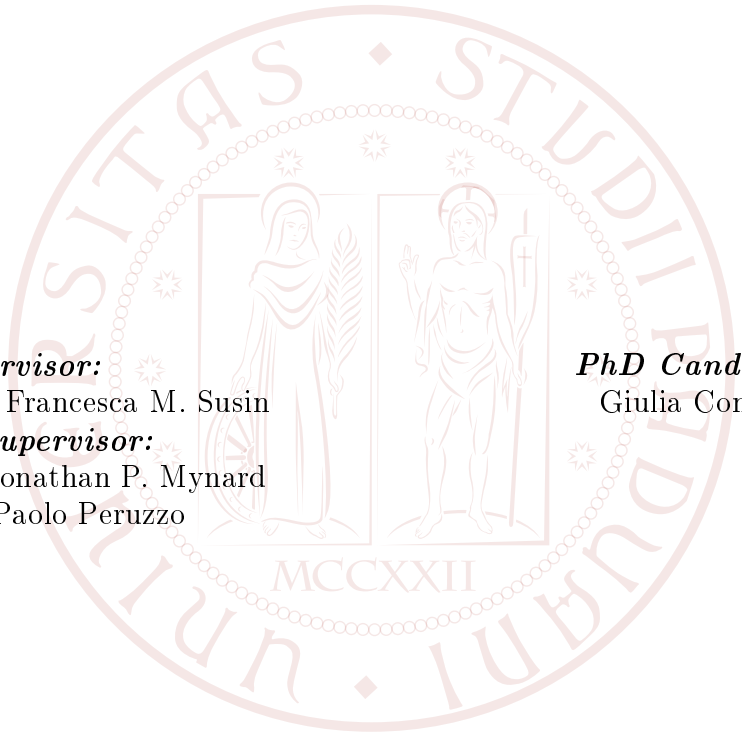

Supervisor:
Prof. Francesca M. Susin
Co-supervisor:
Dr. Jonathan P. Mynard
Ing. Paolo Peruzzo

PhD Candidate:
Giulia Comunale

Laboratory of Cardiovascular Fluid Dynamics
Department of Civil, Environmental and Architectural Engineering

Padova, 30/09/2020

The natural history of science is the study of the unknown. If you fear it you're not going to study it and you're not going to make any progress.

Michael E. DeBakey

Abstract

In this thesis, numerical modeling, and in particular lumped parameter models, are harnessed to investigate and highlight complex cardiovascular interactions in settings of normal physiology and pathology. The following topics are addressed:

i) Fontan circulation. The Fontan circulation results from a surgical palliation performed in children who were born with only one working ventricle. This allows life to be sustained solely by the systemic heart, and caval veins are directly connected to the pulmonary arteries due to the absence of the pulmonary heart. This circulatory arrangement has been widely studied, however, a deep understanding of the typical drawbacks, i.e., reduced cardiac output (CO) and increased central venous pressure (CVP) as well as the effects of high pulmonary vascular resistance (PVR), is still missing. Moreover, prior numerical modeling studies have focused mainly on the comparison between the biventricular and the Fontan circulation without distinguishing, and deriving, age-specific parameters. For the above reasons, first, it is highlighted by a numerical approach the reason behind the drawbacks, i.e., the diastolic ventricular pressure intrinsically affects the suboptimal hemodynamics, and the possibility to lower it may improve the overall Fontan hemodynamics. This, in parallel, suggests a potential target for designing surgical or technical solutions to mitigate the complications of the Fontan circulation. Second, age-specific and circulation-specific models are derived and compared, and the effects of high PVR are analyzed. The adult and pediatric cases for both the uni- and bi-ventricular circulation are considered. The comparison highlights the ability to capture the intrinsic features of each circulation thanks to age-specific parameters, but also, the Fontan circulation is more sensitive than the biventricular one to PVR changes, and this sensitivity (in Fontan cases) decreases with age when considering CVP, whereas it is almost constant in terms of CO.

ii) Right ventricular dysfunction. From the Fontan circulation naturally arises the study of the pulmonary ventricle, i.e., the right ventricle (RV). Historically, the importance of the RV has been underestimated, and a deep gap still exists on the clinical management which leads to mis- and underdiagnosis. To overcome the gap and improve knowledge about the RV and its dysfunction, a numerical model able to compute the key features of RV dysfunction is developed for the first time. Interestingly, the model captures the passive conduit behavior of RV for severe degrees of dysfunction, shed-

ding new light on debated clinical findings. Indeed, it is shown that the appearance of a late peak in pulmonary flow, in association with the RV conduit behavior, is intrinsically related to an increased ventricular stiffness.

iii) Ventricular outflow tract obstruction. Ventricular outflow tract (VOT) obstruction refers to any pathology that causes a reduction in CO and an increase in the pressure gradient across the semilunar (aortic or pulmonary) valve. Numerical literature has mainly focused on adult aortic stenosis; however, also primary cardiac tumors may cause VOT obstruction, and, importantly, these pathologies are more dangerous in pediatric patients than in adults due to the fast rate of growth, compared to the small heart dimensions. Thus, a pediatric numerical model able to reproduce the hemodynamic changes that arise when the right or left VOT is obstructed is developed. The model reliably predicts changes in shape, pressure gradient and CO. Thus, the potential of the model in identifying the obstruction size that produces a given pressure gradient and/or a given CO could make the model a useful tool for both the prediction of critical conditions and the planning of surgery aimed at restoring normal/acceptable hemodynamics.

iv) Sex-specific cardiovascular modeling. Sex analysis is a field that has been developing in recent years due to the gap that exists between sexes in terms of knowledge, diagnosis, and treatment. In the past, medical research mainly focused on male subjects for deriving physiological understanding, but this may not always applicable to the female population, especially in the cardiovascular field. The gap extends also to numerical modeling which is based on clinical data and, thus, has been developed considering as a standard case a subject of 70 kg and 175 cm. However, these values resemble the male population rather than the female one. Fortunately, in clinical research attention on sex is increasingly being recognized, and recently, sex-specific research has highlighted the hemodynamic differences that exist between men and women. However, the same does not hold for the numerical research in which models are still calibrated with typical male parameters. To overcome this gap and improve the awareness of sex-research, for the first time, a woman-specific model is developed and validated with only female-specific clinical data. The model is also compared with a male-specific model, highlighting the need to consider sex also in the numerical research.

v) Pregnancy. Pregnancy is a unique dynamic process in which significant hemodynamic and structural changes arise in the maternal circulation. However, prior modeling studies have focused almost exclusively on the fe-

tal side and/or on the interaction between the mother and the fetus. Only two previous works considered the whole maternal circulation, however, they did not study the structural remodeling that occurs during gestation. Thus, for the first time, a model able to capture the hemodynamic and structural changes during gestation is developed. It is hypothesized that cardiac remodeling is governed by homeostatic values of myofiber and wall shear stresses, and results are promising. Thus, the prediction of cardiac remodeling could have a significant impact not only in the modeling field, but also in the physiological field.

A wide range of significant topics in the cardiovascular field have been analyzed in this thesis, tied them together into a cohesive theme: even if all the topics have a significant scientific, social, and ethical relevance, they have not been widely studied in previous works. The purpose of this thesis is hence to improve the knowledge of complex cardiovascular pathophysiological conditions, which in future may lead to new tools to improve the diagnosis and the treatment of these complex conditions. The work presented in this thesis has been developed in collaboration with Pediatric Cardiologists and Heart Surgeons of the University Hospital of Padova (Italy).

Sommario

In questa tesi, la modellazione numerica, e in particolare modelli a parametri concentrati, sono utilizzati per indagare ed evidenziare complesse interazioni cardiovascolari in condizioni fisiologiche e patologiche. Di seguito, si presentano i diversi argomenti trattati:

i) Circolazione di Fontan. La circolazione di Fontan (univentricolare) è il risultato di una palliazione chirurgica eseguita su bambini nati con un solo ventricolo funzionante. Questa circolazione, in cui le vene cave vengono direttamente collegate alle arterie polmonari a causa dell'assenza del cuore polmonare, permette di sostenere la vita grazie al solo cuore sistemico. La circolazione di Fontan è stata ampiamente studiata in letteratura, tuttavia, manca ancora una profonda comprensione delle tipiche complicanze legate a tale circolazione, vale a dire la riduzione della gittata cardiaca (*cardiac output*, CO) e l'aumento della pressione venosa centrale (*central venous pressure*, CVP), nonché degli effetti di un'elevata resistenza vascolare polmonare (*pulmonary vascular resistance*, PVR). Inoltre, precedenti studi di modellazione numerica si sono concentrati principalmente sul confronto tra la circolazione biventricolare e la circolazione di Fontan senza distinguere, e derivarne, parametri specifici per l'età. Per le ragioni di cui sopra, in primo luogo, si evidenzia con un approccio numerico la causa alla base delle complicanze: la pressione diastolica ventricolare influisce intrinsecamente sull'emodinamica non ottimale di Fontan, e la possibilità di ridurre tale pressione può migliorare l'emodinamica complessiva. Questo, in parallelo, suggerisce un potenziale obiettivo per la progettazione di soluzioni chirurgiche o tecniche per mitigare le complicanze della circolazione di Fontan. In secondo luogo, vengono derivati e confrontati modelli specifici per l'età e per la circolazione, e vengono analizzati gli effetti di un'elevata PVR. Vengono considerati casi adulti e pediatrici sia per la circolazione uni- e bi-ventricolare. Il confronto mostra la capacità di riprodurre le caratteristiche intrinseche di ogni circolazione grazie a parametri specifici per l'età, e mette in evidenza che la circolazione di Fontan è più sensibile di quella biventricolare ai cambiamenti di PVR. Tale sensibilità (nei casi di Fontan) diminuisce con l'età se si considera la CVP, mentre è quasi costante in termini di CO.

ii) Disfunzione ventricolare destra. Dalla circolazione di Fontan nasce naturalmente lo studio del ventricolo polmonare, cioè del ventricolo destro (*right ventricle*, RV). Storicamente, l'importanza del ventricolo destro è stata sottovalutata, ed esiste ancora una profonda lacuna nella gestione clinica

che porta ad inaccuratezze e diagnosi errate. Per superare questa lacuna e migliorare la conoscenza del ventricolo destro e delle sue disfunzioni, viene sviluppato per la prima volta un modello numerico in grado di calcolare le caratteristiche emodinamiche intrinseche delle disfunzioni del ventricolo destro. È interessante notare che il modello è in grado di riprodurre il "comportamento a condotto passivo" del ventricolo destro per gradi severi di disfunzione, supportando scoperte cliniche che sono state oggetto di dibattito. Infatti, con il modello, è dimostrato che la comparsa di un picco tardivo nel flusso polmonare, in associazione al comportamento a condotto passivo del RV, è intrinsecamente legata ad una maggiore rigidità ventricolare.

iii) Ostruzione del tratto di efflusso ventricolare. L'ostruzione del tratto di efflusso ventricolare (*ventricular outflow tract*, VOT) si riferisce a qualsiasi patologia che causa una riduzione del CO e un aumento del gradiente di pressione attraverso la valvola semilunare (aortica o polmonare). La letteratura numerica si è concentrata principalmente sulla stenosi aortica degli adulti; tuttavia, anche i tumori cardiaci primari possono causare l'ostruzione del VOT e, cosa importante, queste patologie sono più pericolose nei pazienti pediatrici che negli adulti a causa del rapido tasso di crescita rispetto alle piccole dimensioni del cuore. Si è sviluppato così un modello numerico pediatrico in grado di riprodurre i cambiamenti emodinamici che si verificano quando il VOT destro o sinistro è ostruito. Il modello prevede in modo affidabile i cambiamenti di forma delle onde di flusso e pressione, il gradiente di pressione e il CO. Quindi, le potenzialità del modello nell'identificare la dimensione dell'ostruzione che produce un determinato gradiente di pressione e/o un determinato CO potrebbe rendere il modello uno strumento utile sia per la previsione delle condizioni critiche che per la pianificazione di interventi chirurgici volti a ripristinare un'emodinamica normale/accettabile.

iv) Modellazione cardiovascolare sesso-specifica. Il ruolo del sesso è un ambito di ricerca che si è sviluppato negli ultimi anni a causa del divario esistente tra i sessi in termini di conoscenza, diagnosi e trattamento. In passato la ricerca medica, da cui sono derivate conoscenze fisiologiche, si è concentrata principalmente su soggetti maschili, tuttavia, tali conoscenze potrebbero non essere applicabili alla popolazione femminile, soprattutto in campo cardiovascolare. Il divario si estende anche alla modellazione numerica, che, basandosi su dati clinici, è stata sviluppata considerando come caso standard un soggetto di 70 kg e 175 cm. Tuttavia, questi valori rappresentano più facilmente la popolazione maschile che non quella femminile. Fortunatamente, nella ricerca clinica l'attenzione sul sesso è sempre più ri-

conosciuta e, recentemente, la ricerca sesso-specifica ha messo in evidenza le differenze emodinamiche che esistono tra uomini e donne. Lo stesso non vale per la ricerca numerica in cui i modelli sono ancora calibrati con i tipici parametri maschili. Per superare questa lacuna e migliorare la consapevolezza della ricerca sul sesso, per la prima volta viene sviluppato un modello donna-specifico, validandolo con soli dati clinici femminili. Il modello viene anche confrontato con un modello uomo-specifico, evidenziando la necessità di considerare il sesso anche nella modellazione numerica.

v) Gravidanza. La gravidanza è un processo dinamico unico nel suo genere, in cui nella circolazione materna si verificano significativi cambiamenti emodinamici e strutturali. Tuttavia, in letteratura, gli studi di modellazione si sono concentrati quasi esclusivamente sul lato fetale e/o sull'interazione tra la madre e il feto. Solo due lavori precedenti hanno considerato l'intera circolazione materna, ma non hanno studiato il rimodellamento strutturale che si verifica durante la gestazione. Così, per la prima volta, è stato sviluppato un modello in grado di riprodurre i cambiamenti emodinamici e strutturali materni durante la gestazione. Si ipotizza che il rimodellamento cardiaco sia governato da valori omeostatici di stress della miofibra e sforzi di taglio a parete, e i risultati sono promettenti. Pertanto, la possibilità di previsione del rimodellamento cardiaco potrebbe avere un impatto significativo non solo nel campo della modellazione numerica, ma anche in quello fisiologico.

In questa tesi è stata analizzata un'ampia gamma di argomenti significativi in ambito cardiovascolare, legati tra loro da un tema comune: anche se tutti gli argomenti hanno una significativa rilevanza scientifica, sociale ed etica, non sono stati ampiamente studiati in letteratura. Lo scopo di questa tesi è quindi quello di migliorare la conoscenza delle complesse condizioni fisiopatologiche cardiovascolari, che in futuro potranno portare a nuovi strumenti per migliorare la diagnosi e il trattamento di queste complesse condizioni. Il lavoro presentato in questa tesi è stato sviluppato in collaborazione con Cardiologi e Cardiochirurghi Pediatrici dell'Ospedale Universitario di Padova.

Contents

List of Figures

List of Tables

1 Introduction

Contents

Numerical modeling of physio-pathological cardiovascular flows is emerging as a powerful tool in bioengineering research and, consequently, in clinical practice. However, even a brief review of the clinical and biomedical literature highlights that models usually focus on specific fields, typically regarding acquired cardiovascular conditions and simulating the average subject with a height of about 75 cm and weight of 70 kg, i.e., more resembling the male population rather than the female one.

The research illustrated in this thesis will cover issues that specifically relate to arguments historically neglected in the numerical fields, i.e., congenital heart disease, right ventricle, women, and children. These topics

have a significance on a scientific, social, and ethical level, and their analysis may improve the understanding and clinical management of complex physio-pathological conditions. Thus, in this thesis, mathematical modeling is utilized to investigate several relatively complex cardiovascular interactions that occur in physiological and pathological conditions. Specifically, 1) congenital heart disease, 2) right ventricular dysfunction, 3) ventricular obstructions, 4) the relevance of the sex-specific medicine, and finally 5) a particular "altered" physiological condition i.e., pregnancy, are considered. This chapter provides an overview of the physiological cardiovascular system and the mentioned physio-pathological conditions, and then establishes the motivation for using mathematical modeling. Finally, the overall objectives and thesis organization are outlined. Note that all the work presented in this thesis is based on clinical needs, and it has been developed in collaboration with Pediatric Cardiologists and Heart Surgeons of the University Hospital of Padova (Italy).

1.1 The cardiovascular system

The cardiovascular system, also called circulatory system, circulates blood in order to transport nutrients, oxygen, hormones, carbon dioxide, waste products, and blood cells to and from the different parts of the body. It provides nourishment and maintains homeostasis, i.e., the body balance [1].

1.1.1 Structure

The cardiovascular system is composed of two systems connected in series: the pulmonary and systemic circulations. The two systems together form a closed loop as shown in Fig. 1.1. The former creates a loop through the lungs where the blood is circulated at low pressure and becomes oxygenated. The latter pumps blood at high pressure into a network of parallel branches formed by the different organs. The amount of blood to each branch is determined by vascular bed resistance. These resistances, all together, form the total vascular resistance (TVR), also called systemic vascular resistance (SVR), i.e, the vascular resistance offered by the systemic circulation. On the other hand, the resistance offered by the pulmonary circulation is called pulmonary vascular resistance (PVR).

Arteries

The arteries are low-resistance vessels characterized by elastic walls. The largest artery is the aorta (Ao), the first part of the systemic circulation,

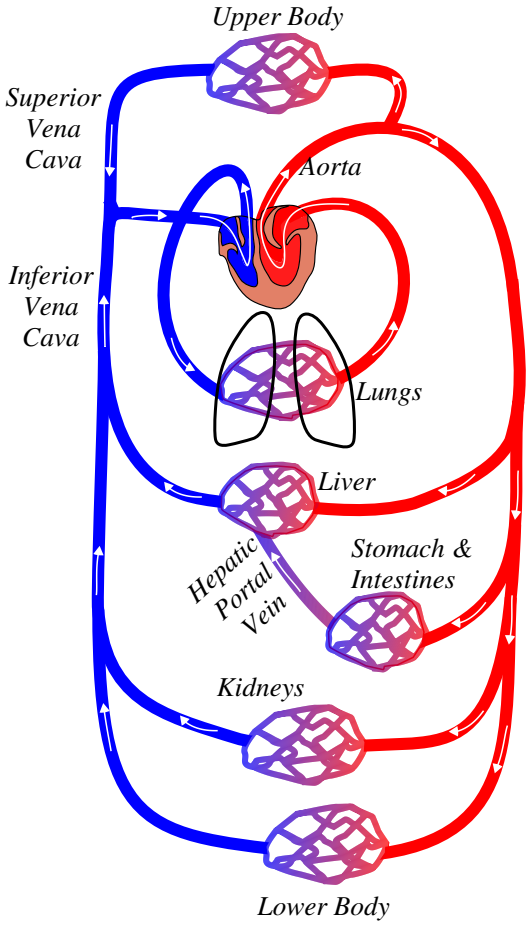

Figure 1.1: *The cardiovascular system comprises the pulmonary and systemic circulations. In red and in blue the oxygenated and deoxygenated blood, respectively.*

that together with the other arteries, converts the pulsatile blood from the left ventricle into a quasi continuous flow [1]. From the aorta depart several branches to supply the upper and lower bodies (above and under the heart). Moving further from the left ventricle, the arteries decrease in size until reaching the capillaries, i.e., the vascular beds within organs and tissues.

Vascular bed

Vascular beds are composed of very small vessels characterized by a high resistance which main components are arterioles. It is here that the pressure drastically drops. Into the vascular bed, the capillaries from the arteries merge with the venules, i.e., small veins, that bring the blood into the venous system.

Veins

The venules merge into veins that form the venous system. The two largest veins are: the superior vena cava (SVC) that drains the blood from the upper body and the inferior vena cava (IVC) that drains the blood from the lower body. These veins empty into the right atrium. Veins are characterized by a low resistance and high compliance, indeed, they are considered the blood reservoir of the body.

Portal system

The portal system is a unique system in which a capillary bed drains directly into another capillary bed through veins. The only example in the human body is the network of hepatic portal veins. This network originates from the gastrointestinal tract and drains into the liver.

Blood flow distribution

The systemic vascular beds are exposed to similar mean arterial pressure (also called perfusion pressure). This ensures that the distribution of blood to the single organ is determined by the local organ vascular resistance, which varies from tissue to tissue.

Heart

The heart is a pump composed of four chambers: two atria and two ventricles. The left atrium and ventricle (LA, LV) belong to the systemic circulation whereas the right atrium and ventricle (RA, RV) to the pulmonary circulation. The heart circulates oxygenated blood to the body and deoxygenated blood to the lungs.

The right atrium receives deoxygenated blood from SVC and IVC and drains it into the right ventricle. From here, the blood is pumped through the pulmonary system. The latter is composed by the pulmonary arteries (PuA), the lungs, where the blood oxygenates, and the pulmonary veins (PuVe). PuVe drain the oxygenated blood into the left atrium from where it is pumped into the left ventricle. Once in LV, the blood is pumped into the aorta, where the systemic system starts (Fig. 1.1).

Heart Valves

The heart comprises four valves: the mitral (Mv) and the aortic (Aov) valves in the left heart, and the tricuspid (Tv) and the pulmonary (Pv) valves in

the right heart. The mitral and the triscupid valves are located between the respective atrium and ventricle, and for that, they are called atrioventricular (AV) valves. The aortic and the pulmonary valves, instead, are called semilunar valves and they are located between the ventricle and the respective artery.

Heart valves open and close passively depending on the pressure gradient across them and, for the closing phase, a hydrodynamic force due to flowing blood. When open, the presence of heart valves assures unidirectional flow of blood. When closed, they allow to isolate each chamber preventing retrograde flow.

1.1.2 Heart mechanical events

The heart is a muscular pump whose walls are made of cardiac muscle, called myocardium, characterized by an involuntary activation [1]. The heart activity is defined by a cardiac cycle that results in periodical mechanical events.

Cardiac phases

The cardiac cycle consists of two phases defined by the ventricular activity: systole, i.e., the ventricular contraction, and diastole, i.e., the ventricular relaxation. Normally, diastole accounts for approximately two-thirds of the cardiac cycle, with the remaining one-third occupied by the systole.

During the isovolumic contraction phase of systole, the ventricles contract, atrioventricular valves close and intraventricular pressure rises until overcoming the pressures in the aorta and in the pulmonary arteries. This allows Aov and Pv to open, thus allowing ventricular ejection. Once systole ends, diastole starts and ventricles relax. During this phase, the semilunar valves close, intraventricular pressure actively falls below atrial pressure allowing the atrioventricular valves to open (active ventricular relaxation). First, atria passively drain blood into ventricles thanks to the positive pressure difference between atrium and ventricle providing about 80% of ventricular filling. Then, diastasis, i.e., slow filling before atrial contraction, adds about 5%. Finally, atrial contraction completes the ventricular filling providing the remaining 15% of ventricular volume [2]. Once the ventricles are filled again, the cardiac cycle ends and a new one starts with another systole. Note that, during diastole, when AV open, blood flows continuously from the veins into the atria and into the ventricles. At this time, the so called "conduit phase" specific of atria happen because they behave as a conduit allowing the blood to flow directly from veins to ventricles.

To define the amount of blood that is ejected from the ventricle, it is possible to use different terms: stroke volume (SV) defines the amount of blood ejected at each systole; and cardiac output (CO) refers to the volume of blood ejected every minute. $CO = SV \cdot HR$, with HR the heart rate, i.e., the number of heartbeats (cardiac phases) per minute. As for the volumes, also for the pressures there are some definitions: *i)* the maximum pressure exerted against the arterial walls when ventricles contract is the systolic blood pressure (SBP), *ii)* the minimum pressure exerted against the arterial walls when ventricles relax is the diastolic blood pressure (DBP), and *iii)* the mean arterial pressure (MAP) is the mean pressure exerted against the arterial walls. MAP is the time average of instantaneous pressure, and it is often approximated as $MAP = 2/3 \cdot DBP + 1/3 \cdot SBP$.

Determinants of the heart filling and ejection

Cardiac output is influenced by three main factors, namely *1)* preload, *2)* afterload, and *3)* myocardial contractility.

Preload is actually the pre-stretch of the myofibers (before systole starts), but on a chamber-level is generally defined as the end-diastolic volume (EDV). The influence of EDV on cardiac output is known as Frank-Starling's law. This law states that the force of contraction is determined by the diastolic (maximal) length of the ventricular myofibers.

Afterload is technically the stress that the myofibers contract against. On a chamber level this is approximated as the pressure that the ventricles have to overcome to eject the blood once the semilunar valves are open.

Myocardial contractility, i.e. the intrinsic ability of the myofibers to generate force under a given set of loading conditions, is a mechanical property of the myofibers.

On the other hand, ventricular filling is also fundamentally important and depends on several factors. *i)* The filling pressure of blood returning to the atria, *ii)* the ability of AV valves to fully open (without diseases that prevent a complete opening), and *iii)* high ventricular compliance, i.e., the ability of the ventricle to fully expand with little resistance (it depends on the ventricular wall properties).

1.1.3 Ventricular pressure-Volume relationships

The analysis of ventricular pressure-volume relationships allows the evaluation of the efficiency of ventricular contractions and their workload. It is possible to evaluate the stroke work (SW), with a rough estimate given by

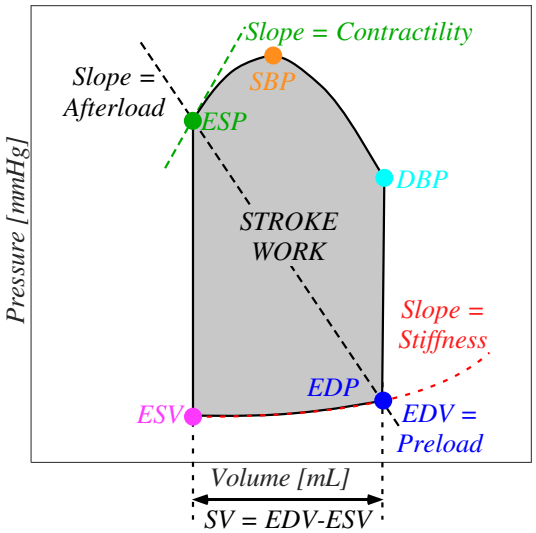

Figure 1.2: *Ventricular pressure-volume relationships. DBP, diastolic pressure, EDP and EDV, end-diastolic pressure and volume, ESP and ESV, end-systolic pressure and volume, SBP, systolic pressure, SV, stroke volume, stroke work is given by the grey area, stiffness is the slope of the red dotted curve approximated to a line, contractility is the slope of the green dotted line, afterload is the slope of the black dotted line.*

$SW = SV \cdot MAP$, by computing the area of the ventricular pressure-volume (PV) loop. Moreover, at the end of systole it is possible to determine the cardiac contractility that reflects the active contractile properties of cardiac muscle; whereas, at end-diastole, PV shows the ventricular stiffness, i.e, the passive properties. In fact, the slope of the end-systolic pressure volume relation is used as an index of contractility, and the slope of the end-diastolic pressure volume relation after approximation to a line is used as an index of stiffness (Fig. 1.2).

1.2 Cardiovascular diseases

The term cardiovascular diseases (CVDs) indicates all the pathologies that affect the cardiovascular system.

The European Cardiovascular Society reports that in 2017 there were 19.9 million new cases of CVD. Moreover, CVD is the leading cause of mortality in Europe with 1.9 million (39% of all deaths) and 2.2 million (47% of all deaths) deaths in male and female population, respectively [3]. Thus, a deep understanding of these pathologies may have an important social, ethical, and economic impact.

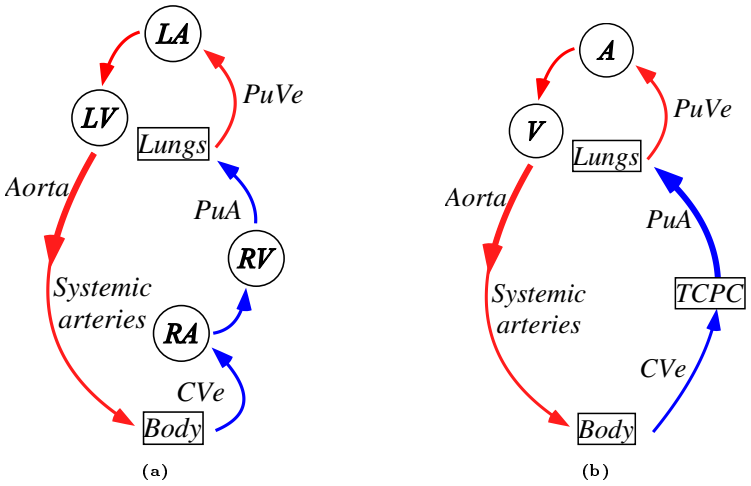

Figure 1.3: *Schematic representation of (a) the physiological biventricular circulation and (b) the Fontan (univentricular) circulation. In red and in blue, oxygenated and deoxygenated blood, respectively. LA and LV, left atrium and ventricle, RA and RV, right atrium and ventricle, A and V, single atrium and ventricle in the Fontan circulation, PuA and PuVe, pulmonary arteries and veins, CVe, caval veins and TCPC, total-cavopulmonary connection.*

In the following the focus will be posed on three particular CVDs which are usually neglected in numerical modeling literature and which deserve a deep attention due to their impact on patients' daily life and relevance in the clinical management: *i)* congenital heart disease, *ii)* ventricular dysfunction, and *iii)* ventricular obstructions.

1.2.1 Congenital heart disease

Congenital heart disease (CHD) refers to defect in the heart or in the great vessels that arises during the fetal development. These pathologies are often life-threatening and require surgical intervention within the first year of life. The incidence of CHD is generally estimated at $\sim 1\%$ of live births worldwide [4]. Even if it seems a small percentage, CHDs are the most common diagnosed birth defects [5].

Among the several CHDs, in this thesis, the focus will be posed on the hypoplastic heart syndrome.

Fontan circulation

The hypoplastic heart syndrome (HHS) is a type of single ventricle defects, and, as the name suggests, it is a pathology in which one ventricle is hy-

poplastic, or undeveloped. After birth, there is only one working ventricle that has to sustain both the systemic and pulmonary circulations, that, in this particular case, are connected in parallel (and not in series as in the physiological circulation). This circuit is characterized by a ventricular volume overload and low blood oxygenation. For these reasons, this circuit is not sustainable for a long time and surgical interventions are required from early life [6].

In 1971 Francis Fontan suggested a surgery capable of reconstructing separated systemic and pulmonary circulations, reducing the volume overload and increasing blood oxygenation. This is a staged approach divided in three surgical interventions. The last stage is the so called Fontan procedure. At the end of the procedure, the systemic veins are directly connected to the pulmonary arteries by the total-cavopulmonary connection (TCPC)[1], without the intervention of a ventricle (see Fig. 1.3). If this intervention fixes the drawbacks of the single ventricle circulation, on the other hand, it causes a chronic caval veins hypertension and it is associated to a reduced cardiac output, which may ultimately lead to ventricular and/or multi-organs failure [7].

Thanks to the improved techniques, survival to the third decade of life of Fontan patients is common nowadays. However, some morbidity and complications arise in the long-term postoperative, whose hemodynamic cascade is not fully understood [7]. Indeed, the key features for long-term Fontan morbidities seem still unclear, as well as the role of PVR not only on CO, but also on CVP. Thus, numerical modeling may improve the understanding of the complex Fontan circulation.

1.2.2 Ventricular dysfunction

Ventricular dysfunction (VD) refers to cardiac disorders in which the ventricle does not work properly. Such ventricular impairment is often classified into *i)* systolic and *ii)* diastolic dysfunction. When VD is advanced, it can lead to heart failure (HF), i.e., the inability of the heart to supply the required amount of blood to the body. Consequently, there exist two types of

[1]Since the first surgery, there has been several types of connection between CVe and PuA. At the beginning, surgeons used to connect the atrium of the not working side with PuA (artriopulmonary connection). This technique is not used anymore and the more recent TCPC is preferred due to the better outcomes. There are two types of TCPC: *i)* the intracardiac TCPC (lateral tunnel), in which the connection is throughout the atrium and *ii)* the extracardiac TCPC, in which the hypoplastic side of the heart is completely bypassed [6].

HF:

- *Systolic failure*: the ventricle is not able to contract properly, so it pumps a lower amount of blood. It is also called heart failure with reduced ejection fraction (HFrEF);
- *Diastolic failure*: the ventricle does not relax properly because the muscle is stiffer than normal and the ventricle cannot fill with the adequate quantity of blood. It is also called heart failure with preserved ejection fraction (HFpEF).

However, the two dysfunctions can also occur together thus producing a combined systolic and diastolic dysfunction (failure).

If the ventricular function and its pathology have been widely studied when considering the left ventricle [8, 9, 10, 11], the same does not hold for RV. In fact, the right ventricle has long been underestimated, and, in the past, it was wrongly believed it could not affect the overall wellness of the circulation due also to the absence of the pulmonary heart (i.e., RV in biventricular circulation) in Fontan patients. The neglect of RV led to limited knowledge about this ventricle and its pathologies, resulting in difficulties in recognizing RV dysfunctions, mis- and under-diagnoses, and lower clinical management [12, 13]. For all the above reasons, in this thesis, the focus is posed on RV and its dysfunction. Numerical modeling is harnessed with the purpose to improve the knowledge on the key features of RV and its pathologies.

1.2.3 Ventricular outflow tract obstruction

Ventricular outflow tract (VOT) obstruction is a defect in which either the right or left ventricular outflow tract is completely or partially obstructed. There are several disorders that lead to VOT obstruction. On the right side, right VOT (RVOT) is mainly caused by defect in the pulmonary valve, the supravalvular region, or the pulmonary artery, e.g., pulmonary atresia, pulmonary valve stenosis, hypoplastic right heart syndrome, and the Tetralogy of Fallot [14]. Analogously, left VOT (LVOT) is mainly due to defect in the aortic valve, or located at the subvalvular or supravalvular level, e.g., aortic valve stenosis, supravalvular aortic stenosis, coarctation of the aorta, and hypoplastic left heart syndrome [15]. Beyond these pathologies, RVOT or LVOT obstruction may also be caused by primary cardiac tumors in the proximity of the pulmonary or aortic valve. Primary cardiac tumors arise in the heart, and, usually, they are characterized by round or oval shape with

smooth or lobulated surface [16].
In pediatric patients, these obstruction are still a significant challenge [17] and they can be hemodynamically relevant due to the fast rate of growth and small dimension of infants' heart [18]. Moreover, numerical literature posed almost exclusively the attention on the adult aortic stenosis. Thus, in this thesis, a tool able to study both the left and right ventricular outflow tract obstruction is developed with particular attention on the pediatric population.

1.3 Sex differences in cardiovascular physiology

In the past four decades, attention to sex has been developed, transforming many aspects of biomedical and public health research [19]. It may appear strange that the inclusion of sex, i.e., an intrinsic characteristic of every person determined by our biology, started only 40 years ago, however, historically, physiology and medicine were developed considering mainly the male population, neglecting the sex as a variable of influence on outcomes [20]. Scientists and physiologists were influenced by cultural trends that considered science as a male-dominated profession, resulting in most of human and animal studies conducted and focused on the male population [20]. Thus, the traditional physiological principles were based on the 70 kg healthy man or on male animals [20]. Women were treated as smaller men assuming that no differences existed between the two sexes, except for the reproductive organs, i.e., women were studied according to the "Bikini Medicine" [21]. This term was coined by Nanette K. Wenger and indicates that women were treated focusing on the bikini-defined areas, thus on the breasts and the reproductive organs [22].

Cardiology is one of the best examples of innovation derived by the inclusion of sex [19]. For years cardiovascular diseases (CVDs) were considered as primarily a male pathology, however, sex and gender analyses have shown that CVD is the major killer of adult women in developed countries [19]. The clinical standards obtained from male patho-physiology caused a sex-gap that determined mis- and under-diagnoses for women. Indeed, the female symptomatology often differs from the male one, e.g., stroke in women is not usually associated with chest and left arm pain [23]. Another example of sex innovation considers the sex-gap in which men were neglected compared to women. Indeed, osteoporosis was long considered as a post-menopausal female pathology, resulting in women-specific screening, diagnosis, and treatment. Nowadays, it is known that women suffer from os-

teoporosis at an earlier age than men, but men over 75 years old constitute one-third of hip fractures and when men break the hips they die more often than women. Thus, osteoporosis research needs to pertain also to men. [24].

The development of sex- and gender-specific medicine allows to improve diagnoses and treatments. It is helping to increase the awareness of sex differences, and clinical research has started taking into account both sexes when defining trials. Several worldwide organizations are emphasizing the need for sex-specific research with the US National Institutes of Health, the European Union, the World Health Organization, and the Canadian Institutes of Health that require medical research to include both sexes and minorities (different genders). Similarly, the Italian Ministry of Health published on the official journal a paper title "Gender as a determinant of health" [25]. This focuses on the need to ensure equity of care and treatment between men and women, starting from the awareness that, in the past, medicine, and consequently medical research, was based almost exclusively on the male population.

Despite the recent recognition of the importance of sex on clinical researches, numerical modeling still does not consider sex as an influential variable, and models are calibrated only with the standard parameters of 70 kg and 175 cm. Thus, in the numerical research there still a sex-gap to be overcome. To give a contribution in the development of the awareness of sex importance, in this thesis, also sex-specific models are constructed and analyzed. In particular, a woman-specific model is derived and compared with a sex-independent model, i.e., without specific reproductive organs.

1.4 Pregnancy

Pregnancy is a unique dynamic process characterized by significant physiological changes in the maternal body that arise soon after conception. Particularly, the maternal cardiovascular system undergoes adaptation to satisfy the increased maternal and fetal metabolic demands. The main purpose is to guarantee an adequate uteroplacental blood circulation to ensure healthy fetal development.

When the maternal changes are inadequate, maternal and fetal morbidities can arise. For example, an insufficient peripheral resistance reduction can cause maternal hypertension, and placental insufficiency or preeclampsia are often related to elevated uteroplacental vascular resistance which can cause intrauterine growth retardation [26, 27]. Notice that a failure to

meet gestational adaptation may highlight previously silent maternal cardiac pathologies.

In the following, the most relevant pregnancy-related physiological changes in *healthy* pregnancy are discussed.

1.4.1 Hemodynamic changes

Physiological cardiovascular alterations start soon after conception to increase uterine perfusion. In particular, in healthy pregnancy, cardiac output and arterial compliance increase, blood pressure remains stable, whereas total vascular resistance decreases.

Blood volume

Blood volume significantly increases during pregnancy, starting in the first few weeks of gestation and progressively augmenting until reaching an increase of about 50% towards the end of pregnancy [28, 29].

In addition to that, during pregnancy, the blood volume redistributes among organs, e.g., there is an increase of blood to the uterus and to the kidneys [28].

Heart rate

Heart rate starts increasing from the first trimester (T1) and reaches a peak that is 15-25% higher than the baseline value in the third trimester (T3) [27, 30].

Stroke volume

Stroke volume is reported to increase by about 20-30% starting in the first few weeks of gestation. Some investigators have reported that SV reaches a peak in the second trimester (T2) [26, 28], while others found that SV increases until term [29, 30].

Cardiac output

Cardiac output increases throughout pregnancy starting from T1 and reaching a peak by T2 to T3 with values 50% higher than pre-pregnancy values [26, 28, 29]. In early pregnancy, CO increases mainly due to the increase of SV whereas, as pregnancy advances, HR affects more CO.

Blood pressure

Systolic blood pressure is almost stable during pregnancy, whereas diastolic blood pressure and mean arterial pressure decrease until reaching a nadir at T2 [26, 27, 28, 29, 30]. This behavior reflects the total vascular resistance decrease together with the increase in the total vascular compliance and CO.

Systemic vascular resistance

The total vascular resistance decreases rapidly during T1, but there is debate around whether it then remains low or increases. Fu [26] suggests that TVR remains low from T1 and throughout pregnancy. On the other hand, Sanghavi and Rutheford report that TVR decreases from the early beginning of pregnancy, but it shows a nadir at the middle of T2 and then the systemic resistance reaches a plateau or slightly increases [27].

Pulmonary vascular resistance

Analogously to TVR, also pulmonary vascular resistance decreases by approximately 30% during pregnancy, determining a further afterload decrease [29]. The ability to decrease PVR may be compromised in patients with shunt due to a congenital cardiac lesion with important implications since the balance between TVR and PVR may be disrupted during pregnancy [29].

Total arterial compliance

The pulsatile component of the afterload can be defined considering the total arterial compliance. This is mainly determined by the elastic properties of the arterial systemic circulation due to the presence of elastic vessels (arteries). Total arterial compliance is reported to increase by about 30% during T1, stabilizing until term [26, 30].

1.4.2 Geometrical changes

In healthy pregnancies, it is reported that the heart undergoes structural and functional remodeling. This adaptation is physiological and regresses at the end of the pregnancy.

Atria

In literature, atrial dilation is reported to start in T1 reaching a peak in T3 with a maximal increase in left atrial (LA) dimension of 14% [26, 30].

Moreover, changes in the right atrium are reported to be greater compared to the left one [27].

Ventricles

Left ventricular end-diastolic volume increases by 5–10% during pregnancy determining an analogous increase of the LV end-diastolic dimension (LVEDD). The LV end-systolic dimension (LVESD) also increases by about 20% [30, 31].

Pregnancy can be seen as a prolonged stress condition that determines a rise also of the LV wall thickness. This is reported to progressively increase by about 15-30% since T1. Moreover, also LV mass rises by 30–50%, which is clear evidence of cardiac remodeling. Interestingly, the ratio of LV wall thickness to chamber dimension is not significantly changing, showing an eccentric hypertrophy that differs from the concentric hypertrophy typical of pathologies [26, 27, 30].

Also the right ventricle shows a remodeling during pregnancy. Recent studies highlight a 40% increase in the RV mass (RVM) with variations in the right ventricle greater than in the LV [27].

Ventricular function

Conflicting results are reported in the literature regarding systolic and diastolic function during pregnancy. Some referred to an improved systolic function due to an afterload reduction (SVR reduction) [28]. Others found a worsened diastolic function in T3 or they reported no variation or improved function [26].

Wall stress

Wall stress (WS) is the force generated in the myocardial fibers due to the intraventricular pressure. It is approximately proportional to the ventricular pressure (P) and radius (r), and inversely linked to the ventricular wall thickness (h), according to the LaPlace law: $WS = P \cdot r/h$ [32].

It is clear that in the maternal body, several modifications arise during pregnancy, affecting both the hemodynamics and the cardiac structures. Despite these significant hemodynamic and structural changes in the maternal circulation, prior modeling studies have focused almost exclusively on the fetal side or on the interaction between the mother and the fetus [33, 34, 35, 36, 37]. Only two previous works focused on the whole maternal circulation [38, 39], however, they did not consider the structural remod-

eling that occur during gestation. Thus, an extension of previous works is necessary to obtain a complete overview on the maternal changes, especially knowing that in the clinical practice, both hemodynamic and structural adaptations are monitored to assure healthy pregnancies. For these reasons, in this thesis, the aim is to develop a model able to capture both the hemodynamic and structural variations that occur in the maternal circulation during gestation.

1.5 Mathematical modeling of the cardiovascular system

The cardiovascular system is a complex structure that can be described in terms of pressures and flow rates at different sites of interest, at least for the purposes of research and clinical practice. Nowadays, technological development allows us to non-invasively measure and visualize blood flow. Even if the latter is a non-invasive technique, sometimes the acquisition requires long times that are not always feasible, e.g., when studying the pediatric cohort. Moreover, non-invasive pressure and flow measurements in all vessels/cardiac chambers is not possible. This means that the present technology does not allow simultaneous clinical measurements of all physiological signals that are required to fully describe a particular pathophysiological condition and the interactions among different vascular sections.

Animal experiments can be an alternative to clinical measurements but still have ethical limits in addition to the costs and the intrinsic differences that do exist between animals and humans.

A further possibility is represented by *in vitro* experiments, but they can also be very expensive, and usually are time-consuming; moreover, they require to properly reproduce reliable phantoms of both solid contours and circulating fluid able to reproduce all the intrinsic interactions.

For all the above reasons, mathematical models can be very useful tools with the advantages to be flexible, ethical, and with limited costs. Particularly, numerical modeling of the cardiovascular system is a developing tool increasingly used also in clinical practice. It allows to describe the pressures and flows obtaining non-invasive information, with the advantage of highlighting the relationships between the different functional elements. Moreover, they may be a potential tool to gain information on complex physiopathological conditions, especially on those pathologies still not known in detail.

The use of mathematical models is well recognized in medical and engineering literature [40, 41, 42, 43, 44, 45, 46, 47, 48, 49]. Several models were used to describe functions and properties [50, 51, 52], to understand interactions [53, 54, 55], and to study possible surgical outcomes [56, 57, 58]. Moreover, there exist different types of models from zero (0D) to three dimensions (3D). If the latter can represent in all the dimensions the problem of interest giving also spatial information, the time and computational costs force to use 3D models only to investigate the blood flow of a localized vascular region. On the other hand, theoretically, 0D models do not account for the spatial propagation of pressure/flow waves because they are derived by the spatial average of the variables of interest. However, the development of multi-compartment 0D models, i.e., the combination of series and parallel compartments, e.g., the thoracic aorta in series with the abdominal aorta to describe the aorta, enables the inclusion of wave propagation (i.e., pressure/flow wave distribution within for example the aorta) still maintaining a reduced computational cost while representing the entire blood circulation. Thus, 0D models allow to assess the effects of several functional elements of the circulation and to highlight cause-effect relationships between each cardiovascular contribution. For these reasons, 0D models are a potential tool to gain information on complex physio-pathological conditions, allowing to study both the single organs and the effects of a localized alteration on the whole circulation.

The issues I deal with in this thesis currently find insufficient or no attention in prior cardiovascular modeling studies. The objective of this thesis is, therefore, to contribute to the development of the knowledge of the pathophysiology of the problems investigated here that in the future, may result in tools capable of assisting the cardiologists and heart surgeons in the diagnosis and treatment of these conditions. The decision to use 0D modeling arises from the desire to understand in detail how a pathological/altered condition (localized or not) can affect the entire blood circulation. In fact, 0D models enable to highlight, from a physiological point of view, the intrinsic relationships that exist in a complex system such as the cardiovascular system. It is well known that a localized pathology, for example, the total cavo-pulmonary connection of Fontan patients, can have effects on the entire cardiovascular system, however, the hemodynamic cascade that these conditions cause is not yet fully understood. It is therefore clear how the choice of 0D models makes possible to achieve these objectives.

1.6 Thesis objectives and organization

The main goal of this thesis is to harness mathematical modeling, particularly 0D models, to investigate and highlight complex cardiovascular interactions in the physiological and pathological blood circulations. Particularly, the physiological and pathological conditions, described in this chapter from an anatomical and physiological point of view, are specifically analyzed as follows:

1. *Description of the mathematical tools.* Before building the models of the overall circulations, the basic elements and computational blocks, together with the mathematical derivations, are described in Chapter 2. In this chapter it is also specified how to assign the values of the parameters and the sensitivity analysis conducted to evaluate the models.

2. *Develop models of cardiovascular disease.* Models of cardiovascular diseases introduced in this chapter are developed and analyzed in Chapter 3-5. First, the adult and pediatric Fontan circulations are considered comparing them with the biventricular ones and analyzing the intrinsic limits of the univentricular circulation as well as the effects of high pulmonary vascular resistance. Second, the Fontan circulation is considered as an extreme case of the pulmonary ventricular dysfunction, and, from this question, the awareness of the lack of understanding regarding RV has been highlighted. Thus, RV dysfunction is considered and studied (Chapter 4). Finally, ventricular outflow obstruction in pediatric patients is considered (Chapter 5).

3. *Sex-specific models.* Chapter 6 presents a lumped-parameter model capable of reproducing female-specific hemodynamics. The effect of the uterus on the overall circulation is analyzed and the hemodynamic differences between the standard case of a 70 Kg male (usually considered in mathematical models) and a 58 Kg female case are highlighted. Moreover, in Chapter 7, a model able to reproduce pregnant hemodynamics is constructed. For the first time, both the hemodynamic and geometrical changes typical of pregnancy are considered, and a cardiac remodeling algorithm that reproduces the key homeostatic principles that seem to drive the cardiac remodeling is developed.

Finally in Chapter 8, a general discussion and conclusion are reported.

Bibliography

[1] P. Kam and I. Power, *Principles of Physiology for the Anaesthetist*. CRC Press, 2015.

[2] R. D. Miller, L. Eriksson, L. A. Fleisher, J. P. Wiener-Kronish, and W. L. Young, "Miller's anesthesia," in *Miller's anesthesia*, pp. 2827–2827, 2010.

[3] A. Timmis, N. Townsend, C. P. Gale, A. Torbica, M. Lettino, S. E. Petersen, E. A. Mossialos, A. P. Maggioni, D. Kazakiewicz, H. T. May, *et al.*, "European society of cardiology: cardiovascular disease statistics 2019," *European Heart Journal*, vol. 41, no. 1, pp. 12–85, 2020.

[4] B. W. Yoo, "Epidemiology of congenital heart disease with emphasis on sex-related aspects," in *Sex-Specific Analysis of Cardiovascular Function*, pp. 49–59, Springer, 2018.

[5] W. Wu, J. He, and X. Shao, "Incidence and mortality trend of congenital heart disease at the global, regional, and national level, 1990–2017," *Medicine*, vol. 99, no. 23, p. e20593, 2020.

[6] M. Gewillig, "The fontan circulation," *Heart*, vol. 91, no. 6, pp. 839–846, 2005.

[7] G. R. Veldtman, A. R. Opotowsky, S. G. Wittekind, J. Rychik, D. J. Penny, M. Fogel, B. S. Marino, and M. Gewillig, "Cardiovascular adaptation to the f ontan circulation," *Congenital heart disease*, vol. 12, no. 6, pp. 699–710, 2017.

[8] C. Luo, D. Ramachandran, D. L. Ware, T. S. Ma, and J. W. Clark, "Modeling left ventricular diastolic dysfunction: classification and key indicators," *Theoretical Biology and Medical Modelling*, vol. 8, no. 1, p. 14, 2011.

[9] R. Leischik, H. Littwitz, B. Dworrak, P. Garg, M. Zhu, D. J. Sahn, and M. Horlitz, "Echocardiographic evaluation of left atrial mechanics: function, history, novel techniques, advantages, and pitfalls," *BioMed research international*, vol. 2015, 2015.

[10] M. R. Zile, C. F. Baicu, and W. H. Gaasch, "Diastolic heart failure—abnormalities in active relaxation and passive stiffness of the left ventricle," *New England Journal of Medicine*, vol. 350, no. 19, pp. 1953–1959, 2004.

[11] S. A. Luis, J. Chan, and P. A. Pellikka, "Echocardiographic assessment of left ventricular systolic function: an overview of contemporary techniques, including speckle-tracking echocardiography," in *Mayo Clinic Proceedings*, vol. 94, pp. 125–138, Elsevier, 2019.

[12] N. M. Pradhan, C. Mullin, and H. D. Poor, "Biomarkers and right ventricular dysfunction," *Critical care clinics*, vol. 36, no. 1, pp. 141–153, 2020.

[13] C. Selton-Suty and Y. Juillière, "Non-invasive investigations of the right heart: how and why?," *Archives of Cardiovascular Diseases*, vol. 102, no. 3, pp. 219–232, 2009.

[14] T. M. Bashore, "Adult congenital heart disease: right ventricular outflow tract lesions," *Circulation*, vol. 115, no. 14, pp. 1933–1947, 2007.

[15] E. Franchi, M. Cantinotti, N. Assanta, C. Viacava, L. Arcieri, and G. Santoro, "State of the art and prospective for percutaneous treatment for left ventricular outflow tract obstruction," *Progress in Pediatric Cardiology*, vol. 51, pp. 55–61, 2018.

[16] B. Ramlawi and M. J. Reardon, "Cardiac tumors: Treatment," in *Clinical Cardio-Oncology*, pp. 91–119, Elsevier, 2016.

[17] B. Alsoufi, T. Karamlou, B. W. McCrindle, and C. A. Caldarone, "Management options in neonates and infants with critical left ventricular outflow tract obstruction," *European journal of cardio-thoracic surgery*, vol. 31, no. 6, pp. 1013–1021, 2007.

[18] M. A. Padalino, V. L. Vida, G. Boccuzzo, M. Tonello, G. E. Sarris, H. Berggren, J. V. Comas, D. Di Carlo, R. M. Di Donato, T. Ebels, *et al.*, "Surgery for primary cardiac tumors in children: early and late results in a multicenter european congenital heart surgeons association study," *Circulation*, vol. 126, no. 1, pp. 22–30, 2012.

[19] L. Schiebinger, "Gendered innovations in biomedicine and public health research," in *Sex and Gender Aspects in Clinical Medicine*, pp. 5–8, Springer, 2012.

[20] V. M. Miller, "Why are sex and gender important to basic physiology and translational and individualized medicine?," *American Journal of Physiology-Heart and Circulatory Physiology*, 2014.

[21] P. L. Kerkhof and V. M. Miller, *Sex-specific analysis of cardiovascular function*, vol. 1065. Springer, 2018.

[22] M. Gulati, "Women and cv disease: Beyond the bikini," 2017.

[23] A. Berglund, K. Schenck-Gustafsson, and M. von Euler, "Sex differences in the presentation of stroke," *Maturitas*, vol. 99, pp. 47–50, 2017.

[24] L. Schiebinger and I. Klinge, "Gendered innovation in health and medicine," *GENDER–Zeitschrift für Geschlecht, Kultur und Gesellschaft*, vol. 7, no. 2, 2015.

[25] M. della Salute, "Il genere come determinante della salute. lo sviluppo della medicina di genere per garantire equità e appropriatezza della cura," *Quaderni del Ministero della Salute*, vol. 26, 2016.

[26] Q. Fu, "Hemodynamic and electrocardiographic aspects of uncomplicated singleton pregnancy," in *Sex-Specific Analysis of Cardiovascular Function*, pp. 413–431, Springer, 2018.

[27] M. Sanghavi and J. D. Rutherford, "Cardiovascular physiology of pregnancy," *Circulation*, vol. 130, no. 12, pp. 1003–1008, 2014.

[28] J. G. Ouzounian and U. Elkayam, "Physiologic changes during normal pregnancy and delivery," *Cardiology clinics*, vol. 30, no. 3, pp. 317–329, 2012.

[29] M. Suresh, R. L. Preston, R. Fernando, and M. C LaToya Mason, *Shnider and Levinson's anesthesia for obstetrics*. Lippincott Williams & Wilkins, 2012.

[30] K. Melchiorre, R. Sharma, and B. Thilaganathan, "Cardiac structure and function in normal pregnancy," *Current Opinion in Obstetrics and Gynecology*, vol. 24, no. 6, pp. 413–421, 2012.

[31] N. Kametas, F. McAuliffe, J. Hancock, J. Chambers, and K. Nicolaides, "Maternal left ventricular mass and diastolic function during pregnancy," *Ultrasound in Obstetrics and Gynecology: The Official Journal of the International Society of Ultrasound in Obstetrics and Gynecology*, vol. 18, no. 5, pp. 460–466, 2001.

[32] N. Westerhof, N. Stergiopulos, M. I. Noble, and B. E. Westerhof, *Snapshots of hemodynamics: an aid for clinical research and graduate education*. Springer, 2018.

[33] I. L. Chernyavsky, O. E. Jensen, and L. Leach, "A mathematical model of intervillous blood flow in the human placentone," *Placenta*, vol. 31, no. 1, pp. 44–52, 2010.

[34] P. Garcia-Canadilla, P. A. Rudenick, F. Crispi, M. Cruz-Lemini, G. Palau, O. Camara, E. Gratacos, and B. H. Bijens, "A computational model of the fetal circulation to quantify blood redistribution in intrauterine growth restriction," *PLoS computational biology*, vol. 10, no. 6, 2014.

[35] G. Pennati, M. Bellotti, and R. Fumero, "Mathematical modelling of the human foetal cardiovascular system based on doppler ultrasound data," *Medical engineering & physics*, vol. 19, no. 4, pp. 327–335, 1997.

[36] A. B. Queyam, S. K. Pahuja, and D. Singh, "Simulation and analysis of umbilical blood flow using markov-based mathematical model," *International Journal of Intelligent Systems and Applications*, vol. 9, no. 3, p. 41, 2017.

[37] R. G. Shah, T. Girardi, G. Merz, P. Necaise, and C. M. Salafia, "Hemodynamic analysis of blood flow in umbilical artery using computational modeling," *Placenta*, vol. 57, pp. 9–12, 2017.

[38] J. Carson, M. Lewis, D. Rassi, and R. Van Loon, "A data-driven model to study utero-ovarian blood flow physiology during pregnancy," *Biomechanics and modeling in mechanobiology*, vol. 18, no. 4, pp. 1155–1176, 2019.

[39] C. Corsini, E. Cervi, F. Migliavacca, S. Schievano, T.-Y. Hsia, and G. Pennati, "Mathematical modelling of the maternal cardiovascular system in the three stages of pregnancy," *Medical Engineering & Physics*, vol. 47, pp. 55–63, 2017.

[40] D. A. de Zélicourt, A. Marsden, M. A. Fogel, and A. P. Yoganathan, "Imaging and patient-specific simulations for the fontan surgery: current methodologies and clinical applications," *Progress in pediatric cardiology*, vol. 30, no. 1-2, pp. 31–44, 2010.

[41] D. E. Schiavazzi, A. Baretta, G. Pennati, T.-Y. Hsia, and A. L. Marsden, "Patient-specific parameter estimation in single-ventricle lumped circulation models under uncertainty," *International journal for numerical methods in biomedical engineering*, vol. 33, no. 3, p. e02799, 2017.

[42] L. Asner, M. Hadjicharalambous, R. Chabiniok, D. Peresutti, E. Sammut, J. Wong, G. Carr-White, P. Chowienczyk, J. Lee, A. King, *et al.*, "Estimation of passive and active properties in the human heart using 3d tagged mri," *Biomechanics and modeling in mechanobiology*, vol. 15, no. 5, pp. 1121–1139, 2016.

[43] L. Asner, M. Hadjicharalambous, R. Chabiniok, D. Peressutti, E. Sammut, J. Wong, G. Carr-White, R. Razavi, A. King, N. Smith, *et al.*, "Patient-specific modeling for left ventricular mechanics using data-driven boundary energies," *Computer Methods in Applied Mechanics and Engineering*, vol. 314, pp. 269–295, 2017.

[44] S. Pant, C. Corsini, C. Baker, T.-Y. Hsia, G. Pennati, I. E. Vignon-Clementel, M. of Congenital Hearts Alliance (MOCHA) Investigators, *et al.*, "Data assimilation and modelling of patient-specific single-ventricle physiology with and without valve regurgitation," *Journal of biomechanics*, vol. 49, no. 11, pp. 2162–2173, 2016.

[45] T. Hang, "In vitro multi-scale patient-specific modeling of hemodynamics in stage 1 norwood palliation for the treatment of single ventricle heart disease," 2015.

[46] A. Baretta, C. Corsini, A. L. Marsden, I. E. Vignon-Clementel, T.-Y. Hsia, G. Dubini, F. Migliavacca, G. Pennati, and T. M. O. C. H. Alliance, "Respiratory effects on hemodynamics in patient-specific cfd models of the fontan circulation under exercise conditions," *European Journal of Mechanics-B/Fluids*, vol. 35, pp. 61–69, 2012.

[47] S. Safaei, C. P. Bradley, V. Suresh, K. Mithraratne, A. Muller, H. Ho, D. Ladd, L. R. Hellevik, S. W. Omholt, J. G. Chase, *et al.*, "Roadmap for cardiovascular circulation model," *The Journal of physiology*, vol. 594, no. 23, pp. 6909–6928, 2016.

[48] M. C. Fitzpatrick, C. T. Bauch, J. P. Townsend, and A. P. Galvani, "Modelling microbial infection to address global health challenges," *Nature microbiology*, vol. 4, no. 10, pp. 1612–1619, 2019.

[49] A. Albanese, L. Cheng, M. Ursino, and N. W. Chbat, "An integrated mathematical model of the human cardiopulmonary system: model development," *American Journal of Physiology-Heart and Circulatory Physiology*, vol. 310, no. 7, pp. H899–H921, 2016.

[50] R. Burattini and P. O. Di Salvia, "Development of systemic arterial mechanical properties from infancy to adulthood interpreted by four-element windkessel models," *Journal of Applied Physiology*, vol. 103, no. 1, pp. 66–79, 2007.

[51] G. Pennati and M. Bellotti, "Doppler waveforms of the human fetal cardiovascular system: a mathematical model," *WIT Transactions on Biomedicine and Health*, vol. 2, 1970.

[52] F. Migliavacca, G. Pennati, G. Dubini, R. Fumero, R. Pietrabissa, G. Urcelay, E. L. Bove, T.-Y. Hsia, and M. R. de Leval, "Modeling of the norwood circulation: effects of shunt size, vascular resistances, and heart rate," *American Journal of Physiology-Heart and Circulatory Physiology*, vol. 280, no. 5, pp. H2076–H2086, 2001.

[53] W. P. Santamore and D. Burkhoff, "Hemodynamic consequences of ventricular interaction as assessed by model analysis," *American Journal of Physiology-Heart and Circulatory Physiology*, vol. 260, no. 1, pp. H146–H157, 1991.

[54] M. Vollkron, H. Schima, L. Huber, and G. Wieselthaler, "Interaction of the cardiovascular system with an implanted rotary assist device: simulation study with a refined computer model," *Artificial organs*, vol. 26, no. 4, pp. 349–359, 2002.

[55] T. Arts, J. Lumens, W. Kroon, and T. Delhaas, "Control of whole heart geometry by intramyocardial mechano-feedback: a model study," *PLoS Comput Biol*, vol. 8, no. 2, p. e1002369, 2012.

[56] K. Pekkan, I. B. Aka, E. Tutsak, E. Ermek, H. Balim, I. Lazoglu, and R. Turkoz, "In vitro validation of a self-driving aortic-turbine venous-assist device for fontan patients," *The Journal of thoracic and cardiovascular surgery*, vol. 156, no. 1, pp. 292–301, 2018.

[57] Z. Keshavarz-Motamed, "A diagnostic, monitoring, and predictive tool for patients with complex valvular, vascular and ventricular diseases," *Scientific Reports*, vol. 10, no. 1, pp. 1–19, 2020.

[58] C. Corsini, C. Baker, E. Kung, S. Schievano, G. Arbia, A. Baretta, G. Biglino, F. Migliavacca, G. Dubini, G. Pennati, *et al.*, "An integrated approach to patient-specific predictive modeling for single ventricle heart palliation," *Computer methods in biomechanics and biomedical engineering*, vol. 17, no. 14, pp. 1572–1589, 2014.

2 Lumped-parameter modeling of the cardiovascular system

Contents

In this chapter, the mathematical description of the circulation model is formulated. First, the basic equations are derived, second, specific components of the circulation are described, including the vascular beds, the heart model, the heart valves, the total cavo-pulmonary connection (TCPC), and the coupling of different order models. Third, the determination of parameters is analyzed, and, finally, a sensitivity analysis is reported. The methodologies shown here are used in later chapters to study specific clinical applications (Chapters 3-7).

2.1 Introduction

The lumped-parameter (also known as 0D) methodology is a helpful tool to represent a complex system as the whole cardiovascular system. 0D models allow both to describe normal circulation and to study specific cardiovascular conditions, e.g., ventricular dysfunction, pulmonary hypertension etc., providing reliable results on pressure and flow waveform, i.e., on the bulk properties of blood flow. They also have two main advantages: *i)* 0D models enable to immediately discriminate the contribution of the various functional elements, highlighting the cause-effect relation, and *ii)* they allow to simulate the hemodynamics of the *whole* circulation, while maintaining low computational cost. Moreover, they can be easily combined with higher-dimensional models, for example to create a $0D-3D$ or $0D-1D$ model.

As with many biological systems, the cardiovascular system may be considered to consist of elementary components that interact with each other. A smart and effective way to describe these systems is founded on the identification of the basic elements and their exchanges [1]. In modeling, the basic elements (such as organs or apparatuses) that can be considered as a whole are assembled together and described as a single functional element, also called compartment. Thus, with focus on the cardiovascular system, depending on the level of accuracy requested, a model can, for example, represent all the systemic organs in an individual compartment, or each organ of interest, e.g., kidneys, liver, uterus, can be described by separate compartments [1]. The cardiovascular system is represented by mathematically describing the different compartments and the interactions among them, i.e., multi-compartment model. Particularly, considering 0D models, the behavior of blood within each compartment is obtained by considering the pressure and the flow rate averaged over the three space dimensions.

Note that, historically, the first attempt to represent a district of the cardiovascular system was made by replicating the flow in the systemic arteries with one compartment, i.e., single-compartment model. The difficulty to reproduce the fundamental features of the circulation with only one compartment led researchers to more complex multi-compartment models. The following section provides a brief history of 0D models.

2.1.1 Brief history

Based on the available literature, the first use of lumped-parameters model dated back to 1733, when Rev Stephen Hales proposed a model composed of

only one compartment [2]. The model was subsequently named Windkessel, suggesting that the pressure changes within the big arteries were due to the arterial elasticity properties [3]. It was only in 1899 that the German physiologist Otto Frank quantitatively expressed this theory further developing the Windkessel model by providing the rigorous mathematical treatment of the two-parameter model. He was able to approximate the hemodynamics of the systemic circulation through a resistance (R) and a capacitance (C) using the electro-hydraulic analogy [4]. Despite the two-parameter model represents well the afterload on the heart explaining the diastolic pressure decay, it does not capture the high frequency components associated with the pressure reflections and it fails in reproducing the systolic pressure [5]. To overcome the limitation of the two-parameter model, Westerhof et al. [6] developed the 3-element Windkessel model, also called Westkessel model. In the 3-element model the aortic characteristics impedance of the arterial tree is reproduced, allowing the description of flow and pressure throughout the entire cardiac cycle [5]. Finally, Stergiopulos et al. [7] added an inductive element (L) to improve the behavior of the input impedance in low frequencies, creating the 4-element Windkessel model [5]. Over the years, Windkessel models have been expanded by creating multi-element models (one compartment) with connections in series and in parallel of R, C, and L, which, despite the complexity, have not improved the resulting simulated global hemodynamics [5].

To represent flow and pressure in different segments of the system, the single compartment model has been changed to a multi-compartment model [5, 8]. This methodology divides the cardiovascular system in different segments using a combination of RLC elements. Each segment is representative of an organ/apparatus of interest and represents the local characteristics. The combination of the compartments gives the possibility to create a model of the whole circulation.

Nowadays, 0D models are widely used for studying the whole circulation while maintaining low the computational cost. To give some examples, when studying congenital heart diseases [9], exercise physiology [10], patient-specific palliative devices [11], nervous system regulation [12] and many others.

2.2 Lumped model for a compliant vessel

The purpose of this section is to derive the 0D equations for blood flow within a cylindrical vessel, assuming an incompressible viscous Newtonian flow and following the approach proposed in [1, 13, 14] (Fig. 2.1). We denote v, the

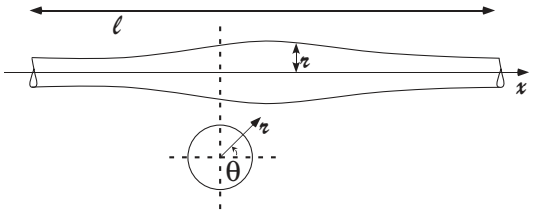

Figure 2.1: *Compliant vessel of length l and radius R.*

local velocity, P, the local pressure, A, the local cross-sectional area, r, the local radius, l, the length of the vessel, Q, the flow rate and x, is the axial dimension. We also assume:

- axial symmetry;
- radial displacement;
- fixed cylindrical axis;
- uniform pressure over each cross-section;
- narrow long compliant vessel (the ratio of the radius over the length is small, $r/l = e \ll 1$);
- negligible gravitational effects;
- dominance of axial velocity, i.e., null circumferential velocity ($v_\theta = 0$).

To obtain the mathematical description of blood flow, we consider the Navier-Stokes and mass conservation equations:

$$\nabla P = -\rho \frac{d\vec{v}}{dt} + \mu \nabla^2 \vec{v}$$
$$\nabla \cdot \vec{v} = 0$$

where ρ is the blood density and μ is the dynamic viscosity.

Considering the previous assumptions and by integrating the equations over the section of the pipe, the set of 1D equations is obtained [1, 13, 14]:

$$\begin{cases} \frac{\partial Q}{\partial x} + \frac{\partial A}{\partial t} = 0 \\ \frac{\partial Q}{\partial t} + \frac{\partial}{\partial x}\left(\alpha \frac{Q^2}{A}\right) + \frac{A}{\rho}\frac{\partial P}{\partial x} = -8\pi\nu\frac{Q}{A}. \end{cases} \tag{2.1}$$

In Eq. (2.1), α is the momentum-flux correction coefficient and ν is the kinematic blood viscosity. Moreover, a parabolic Poiseuille profile is assumed to define the viscous term ($-8\pi\nu\frac{Q}{A}$). The unknowns are A, P, and Q, and in

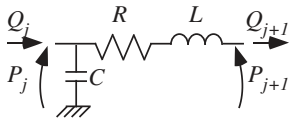

Figure 2.2: *Example of lumped-parameter compartment. j and $j+1$, upstream and downstrem sections, respectively. P, pressure, Q, flow rate, R, resistance, C, compliance and L, inductance.*

order to solve the system, it needs to add another equation: the constitutive law for the vessel tissues. An example, that allows to keep the model simple, is a linear algebraic relation between the pressure and the wall displacement which results in the function: $P(A) = \frac{\beta_0}{A_0}\left(\sqrt{A} - \sqrt{A_0}\right)$, with A_0 the constant reference area and β_0 a constant parameter related to the physical properties of the vascular tissue [1]. Linearizing around the reference stationary state and integrating over the axial coordinate lead to the lumped description (see previous works for details [1, 13, 14]):

$$\begin{cases} C\frac{d\hat{P}}{dt} + Q_d - Q_u = 0 \\ L\frac{d\hat{Q}}{dt} + P_d - P_u = -R\hat{Q}. \end{cases} \tag{2.2}$$

In Eq. (2.2), $\hat{P}$ is the mean pressure over the whole pipe compartment, $\hat{Q}$ is the mean flow rate over the whole compartment, and the subscript u and d indicate the upstream and downstream variables, respectively. Moreover, Eq. (2.2) has been written considering the electro-hydraulic analogy where the lumped-parameters, resistance R, compliance C, and inductance L, represent the viscous resistance to flow, the wall deformability and the blood inertia, respectively. These lumped-parameters are obtained as:

$$R = \frac{8\mu l}{\pi R_0^4}, \qquad C = \frac{3\pi R_0^3 l}{2Eh}, \qquad L = \frac{\rho l}{\pi R_0^2}, \tag{2.3}$$

with E the material Young's (or incremental) modulus and h the vessel thickness.

Now, denote with j and $j+1$ the upstream and downstream sections, respectively (Fig. 2.2). Assuming, for example, that Q_j and P_{j+1} are known and that the unknowns are the state variables of the system (i.e., the following equalities hold: $\hat{P} = P_j$ and $\hat{Q} = Q_{j+1}$), the previous equation reduces to Eq. (2.4), represented by Fig. 2.2.

$$\begin{cases} C\frac{dP_j}{dt} = Q_j - Q_{j+1} \\ L\frac{dQ_{j+1}}{dt} = P_j - P_{j+1} - RQ_{j+1}. \end{cases} \tag{2.4}$$

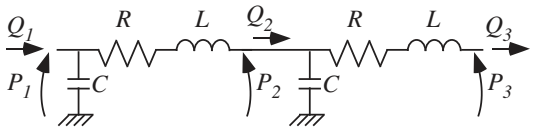

Figure 2.3: *Example of a series of two compartments. P, pressure, Q, flow rate, R, resistance, C, compliance and L, inductance.*

The number of pipe compartments varies depending on the level of accuracy required and the connection is simply obtained by considering the cascade of compartments. For example, for a series of two pipe compartments (Fig. 2.3) the system of equations reads:

$$\begin{cases} C\frac{dP_1}{dt} = Q_1 - Q_2 \\ L\frac{dQ_2}{dt} = P_1 - P_2 - RQ_2 \\ C\frac{dP_2}{dt} = Q_2 - Q_3 \\ L\frac{dQ_3}{dt} = P_2 - P_3 - RQ_3. \end{cases} \tag{2.5}$$

It is clear that the choice of the parameters actually adopted to describe the single compartment hemodynamics depends on the relevance that each functional contributions have on the considered pipe compartment. For example, in analogy to cylindrical tubes, the bulk properties of vascular beds can also be represented by similar lumped-parameters and since the key feature of the micro-vascular beds is the dissipative effect, they can be replicated by only a resistance (R). On the other hand, the great vessels have important elastic properties, represented by C, and minimal dissipative effects (R), whereas the inertial terms (L) may or may not be included depending on the level of accuracy required. For this reason, depending on the specific organ and specific requirements, any combination of lumped-parameters is allowed.

Moreover, this methodology is suitable for the description of both the systemic and pulmonary circulations.

Note that, 0D models neglect, for example, the pressure dependence of compliances. However, it has been demonstrated the efficiency of this simple methodology in effectively reproducing the hemodynamics also in case of non-linearities [15]. Thus, 0D models are here used to obtain an overview of the global hemodynamics.

2.3 Lumped model for the heart

To create a closed-loop system and opportunely represent the whole blood circulation, it is necessary to include the heart.

2.3.1 Elastance model

The four heart chambers can be modeled according to their anatomical structure and the contracting/relaxing action is simulated by a time-varying elastance[1] function derived from the recognized myocardial elastance theory described by Suga et al. [16]. The model is applied as in [17]. Thus, the pressure within each heart chamber ($P(t)$) reads

$$P(t) = E(t)(V(t) - V_{p=0}) \tag{2.6}$$

where $E(t)$ is the time-varying elastance, $V(t)$ is the chamber volume and $V_{p=0}$ is the unstressed volume at zero pressure. Eq. (2.6) implies that if $E(t)$ increases, then during the isovolumic phase the pressure also increases whereas during ejection the pressure decreases because of the volume reduction. This highlights how an increased elastance is associated with the myocardial contraction. On the other hand, the relaxation is related to a decreasing $E(t)$, resulting in a decreasing pressure in the isovolumic phase and in an increasing volume during the chamber's filling [18].

The use of the elastance model allows to easily represent the functional heart properties by means of few parameters. Myocardial contractility is defined by the maximum contraction force, i.e., the maximal elastance E_{max}, and the passive compliance (elastic) properties, i.e., the stiffness defined by the minimal elastance E_{min}. The $E(t)$ time-variation is simulated via a 'two-Hill' function which accounts for contractile (g_1) and relaxation (g_2) phases of the cardiac cycle as

$$E(t) = k\left(\frac{g_1}{1+g_1}\right)\left(\frac{1}{1+g_2}\right) + E_{min}. \tag{2.7}$$

k is a scaling factor used to guarantee that $\max E(t) = E_{max}$ as

$$k = \frac{E_{max} - E_{min}}{\max\left[\left(\frac{g_1}{1+g_1}\right)\left(\frac{1}{1+g_2}\right)\right]} \tag{2.8}$$

[1] The elastance (=1/compliance) is a measure of the stiffness of the heart chamber.

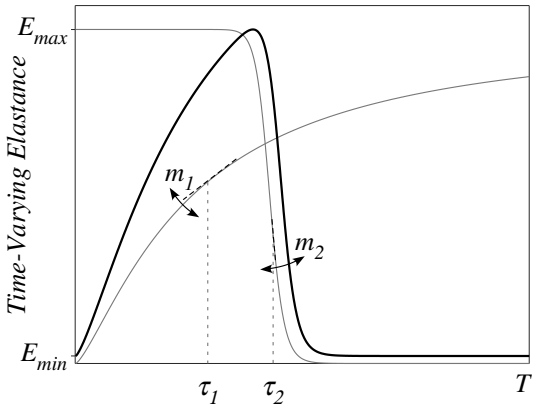

Figure 2.4: *Double Hill Function and example of the resulting time-varying elastance. τ determines the relative appearance in time and m the steepness.*

and

$$g_1 = \left(\frac{t - t_{onset}}{\tau_1}\right)^{m_1}, \qquad g_2 = \left(\frac{t - t_{onset}}{\tau_2}\right)^{m_2}. \tag{2.9}$$

The chamber's contraction and relaxation are determined by the first and the second Hill functions (Eq. 2.9), respectively; τ controls the relative appearance in time within the heartbeat, t_{onset} is the time-shift for the atrial contraction, and m governs the steepness. Note that, the relation between τ and m and the duration of the different phases of the heartbeat and the resulting contraction/relaxation are clear, however, the quantitative links between these parameters and the cardiac mechanics are still not fully defined. An example of time-varying elastance is reported in Fig. 2.4.

To note, the explicit representation of the interactions between chambers as previously reproduced in other works [17, 18, 19] is here neglected.

2.4 Lumped model for the heart valves

In the heart there are four valves: mitral (Mv) and aortic valve (Ao) in the left heart, and tricuspid (Tv) and pulmonary valve (Pv) in the right heart. The presence of the valves is fundamental to completely separate the heart chambers and prevent backflow during systole, aiding with cardiac efficiency. For this reason, it is fundamental to represent the heart valves to properly simulate the heart hemodynamics.

Following, two models used in the following chapters to represent the heart valves are presented.

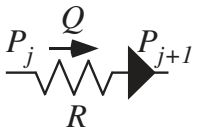

Figure 2.5: *Hydraulic equivalent of the diode-resistance pairs representing the pressure-dependent behavior of heart valves. P_j and P_{j+1} are the pressures either side of the valve, R the valve resistance and Q the flow across it.*

2.4.1 Valve as an ideal diode

The simplest way to simulate the heart valves is to consider them as an ideal diode in series with a resistance (lumped representation in Fig. 2.5): they open and close instantaneously and they allow the blood to flow through only when there is a positive pressure gradient across them, forcing a unidirectional flow. The corresponding equation hence is

$$Q = \begin{cases} \frac{P_j - P_{j+1}}{R}, & \text{if } P_j - P_{j+1} \geqslant 0 \\ 0, & \text{otherwise.} \end{cases} \tag{2.10}$$

with P_j and P_{j+1} the pressure upstream and downstream, respectively, R the valve resistance and Q the flow rate.

Notice that Eq. (2.10) assume a linear relation between Q and ΔP (i.e., laminar flow). Alternatively, a square relationship of the kind $\Delta P = K \cdot Q^2$ (i.e., turbulent flow) can be adopted [20].

2.4.2 Valve dynamics model

Another way to simulate heart valves is to consider a more complex model of their dynamics. The model here reported was proposed in [21].

In this model, the dynamics are simulated by considering the total head conservation equation and neglecting friction losses. In particular, the valve dynamics are determined by only *i*) the static pressure drop across the valve, and *ii*) the current valve state. The Bernoulli equation can be applied as

$$P_j - P_{j+1} = BQ|Q| + L\frac{dQ}{dt} \tag{2.11}$$

with P_j and P_{j+1} the pressure upstream and downstream the valve, Q the flow rate, B the Bernoulli resistance, and L the blood inertance. B takes into account the pressure drops due to convective acceleration and dynamics pressure losses related to the diverging flow field downstream the vena contracta, whereas, L accounts for pressure drop due to the rapid accel-

eration/deceleration of the blood across the valve. These parameters are obtained as

$$B = \frac{\rho}{2A_{eff}^2}, \qquad L = \frac{\rho l_{eff}}{A_{eff}}, \tag{2.12}$$

where l_{eff} and A_{eff} are the effective valve length and area, respectively. The former is proportional to the valve inertance and it is determined such that the pressure gradient across the valve is properly estimated [22]. Specific values are taken from literature [21, 22]. The latter, i.e., A_{eff}, is computed by

$$A_{eff}(t) = \left[A_{eff_{max}}(t) - A_{eff_{min}}(t)\right]\zeta(t) + A_{eff_{min}}(t) \tag{2.13}$$

where ζ is the valve state index (that varies between 0 and 1), and $A_{eff_{max}}$ and $A_{eff_{min}}$ are the maximum and minimum effective orifice areas that characterize the valve. The valve state varies according to

$$\frac{d\zeta}{dt} = \begin{cases} (1-\zeta)K_{vo}(P_j - P_{j+1}), & \text{if } P_j - P_{j+1} \geqslant 0 \\ \zeta K_{vc}(P_j - P_{j+1}), & \text{if } P_j - P_{j+1} < 0 \end{cases} \tag{2.14}$$

in which the equation depends on the opening (K_{vo} is the opening rate coefficient) and closing of the valve (K_{vc} is the closing rate coefficient). See [21] for more details.

2.5 Lumped model for the TCPC

The total cavopulmonary connection (TCPC) is a particular connection that is surgically constructed in Fontan patients, i.e., when there is a "single ventricle" pathology (Fig. 2.6a). It is created to directly link the blood flow from the inferior vena cava to the pulmonary arteries, with the superior vena cava connected to the right pulmonary artery. The purpose is to direct the systemic venous blood to the lungs. The resulting system is typically characterized by elevated systemic venous and caval pressure associated to an altered pulmonary arterial hemodynamics [23]. Due to these features, the inclusion of the TCPC is fundamental to properly represent the specific hemodynamics that characterizes these particular patients.

In literature, the total cavopulmonary connection has been deeply studied, particularly focusing on the blood flow inside the TCPC, that is characterized by a non-physiological geometry that causes turbulent flow. The interest in the specific TCPC hemodynamics led the researchers to developed 3D models that can replicate the turbulent vortices inside the connection

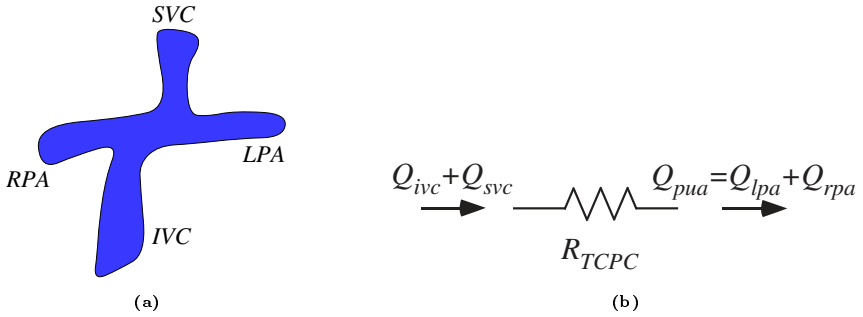

Figure 2.6: *(a) Illustration and (b) lumped model of the total cavopulmonary connection (TCPC) which links the inferior and superior vena cavae (IVC and SVC, respectively) with the left and right pulmonary arteries (LPA and RPA, respectively). Q_{ivc} and Q_{svc}, flows from IVC and SVC, respectively, Q_{pua}, Q_{lpa}, and Q_{rpa}, total arterial flow and LPA and RPA flows, respectively.*

[11, 24, 25, 26, 27].

In this thesis, the focus is on understanding how the TCPC (non- physiological connection) alters the global pulmonary hemodynamics and the overall circulation, rather than on the analysis on the local kinematic and dynamic flow field inside this particular compartment. For this reason, the TCPC is represented as a simple resistance to account for pressure losses due to the complex TCPC geometry (Fig. 2.6b). In particular, we assumed that $P_j - P_{j+1} = R_{TCPC} \cdot Q$ with $R_{TCPC} = 0.036$ mmHg·s/mL. The value assigned to R_{TCPC} was taken from Pekkan et al. [23]. They developed a lumped-parameters model to study the use of a ventricular assist device (VAD) in pediatric patients with congenital heart disease. Note that, in this thesis, due to the lack of clinical data, the same value of R_{TCPC} is applied in both adult and pediatric Fontan model.

2.6 The coupling of different order models

One advantage of lumped-parameter models is that coupling them with higher-order models to study localized conditions while obtaining an overview of the global hemodynamics is relatively straightforward. This allows simulating the overall circulation while studying the effect of the particular condition both locally and on the overall hemodynamics. For example, it is possible to couple the 0D model of the whole circulation with the 1D model of the outflow ventricular tract as described in [28] (notice that this latter coupling can also be seen as a further possibility of simulating heart valves and their dynamics in 0D heart models).

In this section the coupling of lumped models with the solution of 1D

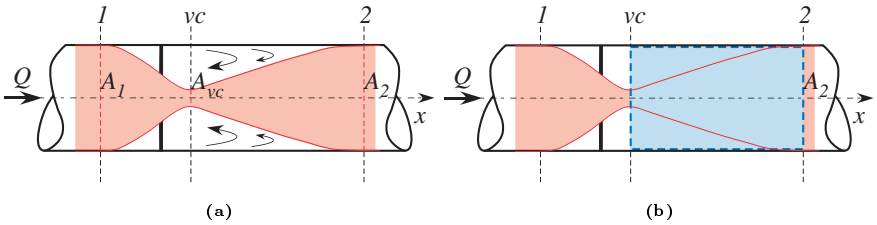

Figure 2.7: *Schematic representation of (a) the flow (red) throughout the narrowing and (b) the control volume (blue) used to compute the momentum conservation. Q is the flow rate, x the longitudinal axis, at location 1 (upstream the narrowing) and 2 (downstream the narrowing) the jet has area equal to $A_1 = A_2 = A$; whereas, at location vc (minimum area) the jet has area A_{vc}. The lateral area of the control volume is equal to the flow area at location 1 and 2: A_2.*

model to study the hemodynamics in presence of a local narrowing is described. The resulting model will be used in Chapter 5.

2.6.1 Flow model through a local narrowing

The present model can be used every time a local dissipation takes place in a cardiovascular district that can be assimilated to a cylindrical pipe; for example, in the presence of valve stenosis or primary cardiac tumors in the outflow ventricular tract (the latter will be further discussed in Chapter 5).

The model assumes a circular tube with a circular orifice (Fig. 2.7). Due to the presence of the narrowing, the flow starts contracting exhibiting a jet as in Fig. 2.7a. Blood flow accelerates from location *1* up to the vena contracta, where it reaches the minimum area A_{vc} (location *vc*). It then decelerates expanding its area (downstream *vc*) and fully reattaching to the tube wall at location *2*. Between location *1* and *vc*, it is reasonable to neglect energy dissipation because the static pressure is converted in kinetic energy. On the other side, in the expansion region, the presence of eddies causes energy loss, i.e., an irreversible pressure loss between location *vc* and *2* occurs. In the following, only the energy dissipation is considered, neglecting the convective[2] and temporal acceleration[3]. Moreover, it is here considered an orifice (or narrowing) of constant area.

The dissipated energy can be computed assuming the model of Fig. 2.7, considering a Newtonian incompressible flow with undeformable walls: the area A of the pipe is constant in time t and along the axis x.

[2]The convective acceleration is linked to the possible difference in the pipe area between location *1* and *2*.

[3]The temporal acceleration is linked to the flow unsteadiness.

Considering mass conservation, the flow rate Q is

$$Q(t) = V_1 \cdot A_1 = V_2 \cdot A_2 \tag{2.15}$$

with V_1 and V_2 and A_1 and A_2 the mean velocity and area at location *1* and *2*, respectively. Note that the assumption of constant area implies $V_1 = V_2$.

Given the previous assumptions and neglecting the gravitational force, the conservation of energy between location *1* and *2* reads

$$E_1 - E_2 = \frac{P_1 - P_2}{\gamma} = \Delta E_{1\to 2} \tag{2.16}$$

where E is the total head, P/γ is the flow energy, and ΔE is the local energy loss.

The purpose now is to obtain a description for $\Delta E_{1\to 2}$. As previously explained, in the model of Fig. 2.7, dissipation occurs only between vc and *2*, so $\Delta E_{1\to 2} = \Delta E_{vc\to 2}$. Using again the energy conservation equation we hence have:

$$\Delta E_{1\to 2} = \Delta E_{vc\to 2} = \frac{P_{vc} - P_2}{\gamma} + \frac{V_{vc}^2 - V_2^2}{2g}. \tag{2.17}$$

Applying the conservation of momentum along axis x to the blue control volume of Fig. 2.7b, we obtain:

$$(P_{vc} - P_2)\, A_2 + \rho Q\, (V_{vc} - V_2) = 0 \tag{2.18}$$

and suitably rearranging

$$\frac{P_{vc} - P_2}{\gamma} = \frac{V_2\, (V_2 - V_{vc})}{g}. \tag{2.19}$$

The application of Eq. (2.19) into Eq. (2.17) results in

$$\Delta E_{1\to 2} = \Delta E_{vc\to 2} = \frac{(V_{vc} - V_2)^2}{2g} \tag{2.20}$$

and finally, the pressure drop is given as

$$\frac{P_1 - P_2}{\gamma} = \frac{(V_{vc} - V_2)^2}{2g} = \frac{Q^2}{2g} \frac{1}{A_{vc}^2} \left(1 - \frac{A_{vc}}{A_2}\right)^2 \tag{2.21}$$

where A_{vc} and A_2 are the flow area at location vc and *2*, respectively.

Note that the model here presented is similar to Garcia et al.'s work [29] and it is a simple version of other works [18, 28, 30, 31, 32]. Indeed,

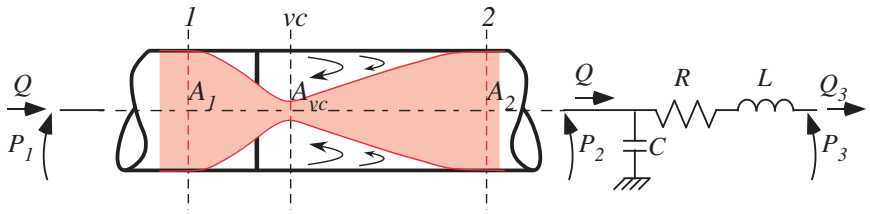

Figure 2.8: *Schematic representation of 0D model with a local narrowing's model.*

A_{vc} physiologically varies over time but it is here assumed to be constant over the heartbeat and Q is assumed to be instantaneously constant. Thus, despite the model here presented neglects the dynamics of the flow and the valve, it allows to describe the pressure drop that occurs in a cylindrical tube when there is a local dissipation, maintaining a low computational cost. This representation is hence enough for the purpose of this thesis.

2.6.2 Coupling 0D models with other models

The model expressed by Eq. (2.21) can be easily coupled to a 0D model. The schematic representation of an example is reported in Fig. 2.8.

In this particular case, assuming for example that the areas A_{vc} and A_2 and the pressures P_1 and P_2 are known, one can compute the flow rate Q as

$$Q = \sqrt{2g \cdot \frac{P_1 - P_2}{\gamma} \cdot \left(\frac{A_{vc} \cdot A_2}{A_2 - A_{vc}} \right)^2}. \tag{2.22}$$

The knowledge of Q can then be applied in Eq. (2.4) to solve the 0D model of Fig. 2.8.

2.7 Parameter estimation

Once the lumped-parameter model is constructed and the equations are defined, the estimation of parameter' values is a fundamental step to guarantee the model's physiological relevance. Obviously, the adoption of parameters able to reproduce physio/pathological conditions will assure significant results.

To that aim, the use of clinical measurements would be the ideal approach. Unfortunately, in many settings this is only possible with very few parameters, such as heart rate, systolic and diastolic blood pressures, that are easily measurable from non-invasive clinical exams. Indeed, if the measurements require invasive techniques, often they are not feasible to perform

especially when considering healthy conditions. Beyond that, even if tests are non-invasive, if they take long to perform, or they may not provide adequate accuracy, they are not adequate. Moreover, some parameters are a mathematical construction to represent the physiology. For example, $V_{p=0}$ in Eq. (2.6) is a parameter that cannot be directly measured in the clinic.

When the parameters can not be directly derived, e.g., as in the cases previously described, or other practical reasons (e.g. cost, ethical constraints etc), the best option is to identify the value of the parameters in the clinical and numerical literature, searching for reasonable values that can be applied in the context of the research. This step is not that easy as it can seem. Indeed, often in the clinical and numerical literature, different research groups set clinical trials without considering sex, gender, age, and weight differences, or if they do consider these features, often the authors do not report the parameters divided into these categories. Moreover, sometimes the same parameter can be measured with different methodologies, e.g., blood pressure can be derived non-invasively by oscillometric, or invasively by catherisation, with techniques characterized by different accuracy. Thus, the possibility to choose among several options has the drawback to include some possible errors. For these reasons, the use of literature data requires the analysis of a big amount of literature with strong skills and deep attention necessary to identify the right parameter's value that best suits the model. However, even if difficult and time-consuming, the use of literature data is usually a good option since these values are often derived from clinical trials or from models validated with clinical data.

When neither direct clinical measurements nor data from literature are available, e.g., the constructed model has more parameters than the existing models, the only reasonable option is to derive parameter' values by considering some reasonable assumptions and rules based on knowledge of the basic physiology. In the following subsection, this latter approach is explained in more detail.

2.7.1 Practical estimation of parameters

When the value of a particular parameter is not directly measurable and is not available in the literature, general knowledge from physiological literature can be employed to aid with parameter estimation.

Let's consider the scheme of Fig. 2.9 to simulate a specific organ, e.g., the uterus, the kidneys, and so on. The model is divided in three sections: one dedicated to the arterial side, one to describe the micro-vascular bed and another one for the venous side. It is reasonable to assume that the parame-

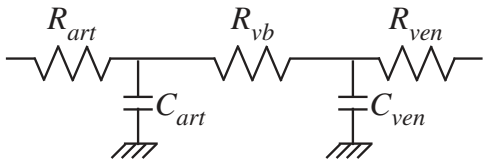

Figure 2.9: *Example of lumped model to describe an organ. The model is composed by the arterial side, the resistance R_{art} and the compliance C_{art}, the vascular bed, the resistance R_{vb}, and the venous side, the resistance R_{ven} and the compliance C_{ven}.*

ters required to describe the arterial and venous sides are a resistance and a capacitance. This because, in this specific case, the main characteristics to be reproduced are the elastic properties and the pressure dissipation effect. On the other side, the vascular bed is characterized by a network of small blood vessels whose main characteristic is the dissipative effect. For this reason, it is feasible to represent it with a resistance.

By knowing the amount of blood that arrives to the organ (usually, this information is available on literature) and the perfusion pressure, it is possible to compute the total resistance of the organ. The latter is the simple sum of the three R in series. For example, considering the kidneys: the renal blood flow is about 20% of the cardiac output, CO is around $4-5$ L/min and the perfusion pressure is around 76 mmHg [33]. This allows to compute $R_{tot} = R_{art} + R_{vb} + R_{ven} = 76/(20\%\cdot\text{CO})$. Now, it is reasonable to assume that $R_{vb} = 92\%R_{tot}$, $R_{art} = 5\%R_{tot}$ and $R_{ven} = 3\%R_{tot}$ [34]. The partition comes from the knowledge of the physiology. Indeed, the vascular bed is a network of small vessels that includes all most of the resistance vessels, i.e. arterioles, as well as capillaries and thus it is the compartment with the largest dissipation effect. On the other hand, the key feature of arteries and veins is the elastic property and they have only a small dissipative effect. Moreover, veins tend to be bigger than arteries, and thus veins have smaller resistances than arterial vessels. To calibrate the compliances, other knowledge from the physiology can be exploted. Indeed, it is known that there exists a time constant when considering resistance and compliance: $\tau = R \cdot C$, and its value for the systemic circulation is approximately 0.81 s. This allows to compute $C_{art} = \tau/R_{vb}$ [18]. Finally, the venous compliance is known to be 25-30 times greater than C_{art} [33].

This is a simple example of how to derive parameters when they are neither directly measurable nor available in the literature.

It is clear that, if the outputs of the model do not replicate the desired

hemodynamics, an iterative approach can be applied, adjusting the parameters by tuning in order to achieve a desired target value of some haemodynamic quantity. For example, the total vascular volume may be iteratively adjusted to achieve reasonable cardiac output and global pressures.

2.8 Sensitivity analysis

Model outputs clearly depend on the values chosen for input parameters. To understand the role of each parameter and the effect on the output, a sensitivity analysis can be performed to learn to what extent uncertainties in the model inputs will lead to uncertainty in the model outputs.

Ideally, one would compute a global sensitivity analysis that allows to analyze the whole parameter space. Pianosi et al. [35] developed a tool for the global sensitivity analysis applicable to several models. However, in this thesis, a relatively simple approach has been taken to sensitivity analysis, which assumes that the model does not have strong non-linearities and there are not strong interactions between parameters, i.e., the choice of relevant parameters relies on physical and physiological model relations [36]. For these reasons, a local sensitivity analysis is here performed.

2.8.1 Local sensitivity Analysis

The local sensitivity analysis is here conducted by changing one parameter at a time and analyzing the variations of the outputs as in [18]. Ideally, the sensitivity should be analyzed for every parameter. In reality, when the model has many inputs, this is not feasible or particularly useful. For this reason, it is important to select the most relevant parameters considering physiological relations and taking into accounts the global effect on the generation of pressure and blood flow. For example, it is more relevant to analyze the changing of the systemic vascular resistance (SVR), i.e., the effect of the entire systemic resistances, rather than changing every single R, e.g., the renal arterial resistance, at least when the research question is not focused on renal hemodynamics.

Denoting by X an input parameter and by Y an output parameter, the local sensitivity analysis shows how a change in X to a new value X^* determines a change in Y, i.e., a new value Y^*. For every output of interest it is therefore possible to determine the sensitivity, and in particular the

sensitivity of its mean value as

$$S_{mean} = \frac{\Delta Y}{\Delta X} = \frac{mean(Y^*) - mean(Y)}{mean(Y)} \left(\frac{X}{X^* - X} \right). \tag{2.23}$$

If S_{mean} results in a negative value, it indicates that a variation of X causes an opposite variation in Y, e.g., X increases and Y decreases.

All the models presented in this thesis are run harnessing the built-in MATLAB® function *ode15s* with an absolute and a relative tolerances of $1e-6$, solving a closed-loop system. An example of MATLAB® code is shown in Appendix A. The results are obtained after reaching the periodic steady state and they are validated considering literature data. A sensitivity analysis is also conducted.

Bibliography

[1] L. Formaggia and A. Veneziani, "Reduced and multiscale models for the human cardiovascular system," *Lecture notes VKI lecture series*, vol. 7, 2003.

[2] S. Hales, "Statistical essays: Concerning haemastaticks; or, an account of some hydraulick and hydrostatical experiments made on the blood and blood-vessels of animals," *London: W. Innys and R. Manby*, vol. 1733, p. 1733, 1733.

[3] N. Westerhof, J.-W. Lankhaar, and B. E. Westerhof, "The arterial windkessel," *Medical & biological engineering & computing*, vol. 47, no. 2, pp. 131–141, 2009.

[4] O. Frank, "Die grundform des arteriellen pulses [basic shape of the arterial pulse]," *Zeitschriftfür Biologie*, vol. 37, pp. 483–526, 1899.

[5] I. Kokalari, T. Karaja, and M. Guerrisi, "Review on lumped parameter method for modeling the blood flow in systemic arteries," 2013.

[6] N. Westerhof, "Bosman f, de vries cj, noordergraaf a," *Analog studies of the human systemic arterial tree. J Biomech*, vol. 2, pp. 121–143, 1969.

[7] N. Stergiopulos, B. E. Westerhof, and N. Westerhof, "Total arterial inertance as the fourth element of the windkessel model," *American Journal of Physiology-Heart and Circulatory Physiology*, vol. 276, no. 1, pp. H81–H88, 1999.

[8] Y. Shi, P. Lawford, and R. Hose, "Review of zero-d and 1-d models of blood flow in the cardiovascular system," *Biomedical engineering online*, vol. 10, no. 1, p. 33, 2011.

[9] S. Shimizu, D. Une, T. Kawada, Y. Hayama, A. Kamiya, T. Shishido, and M. Sugimachi, "Lumped parameter model for hemodynamic simulation of congenital heart diseases," *The Journal of Physiological Sciences*, vol. 68, no. 2, pp. 103–111, 2018.

[10] E. Kung, G. Pennati, F. Migliavacca, T.-Y. Hsia, R. Figliola, A. Marsden, and A. Giardini, "A simulation protocol for exercise physiology in fontan patients using a closed loop lumped-parameter model," *Journal of biomechanical engineering*, vol. 136, no. 8, 2014.

[11] C. Corsini, C. Baker, E. Kung, S. Schievano, G. Arbia, A. Baretta, G. Biglino, F. Migliavacca, G. Dubini, G. Pennati, *et al.*, "An integrated approach to patient-specific predictive modeling for single ventricle heart palliation," *Computer methods in biomechanics and biomedical engineering*, vol. 17, no. 14, pp. 1572–1589, 2014.

[12] M. Ursino, "Interaction between carotid baroregulation and the pulsating heart: a mathematical model," *American Journal of Physiology-Heart and Circulatory Physiology*, vol. 275, no. 5, pp. H1733–H1747, 1998.

[13] S. Čanić and E. H. Kim, "Mathematical analysis of the quasilinear effects in a hyperbolic model blood flow through compliant axi-symmetric vessels," *Mathematical Methods in the Applied Sciences*, vol. 26, no. 14, pp. 1161–1186, 2003.

[14] V. Milišić and A. Quarteroni, "Analysis of lumped parameter models for blood flow simulations and their relation with 1d models," *ESAIM: Mathematical modelling and numerical analysis*, vol. 38, no. 4, pp. 613–632, 2004.

[15] A. Cappello, G. Gnudi, and C. Lamberti, "Identification of the three-element windkessel model incorporating a pressure-dependent compliance," *Annals of biomedical engineering*, vol. 23, no. 2, pp. 164–177, 1995.

[16] H. Suga, K. Sagawa, and A. A. Shoukas, "Load independence of the instantaneous pressure-volume ratio of the canine left ventricle and effects of epinephrine and heart rate on the ratio," *Circulation research*, vol. 32, no. 3, pp. 314–322, 1973.

[17] J. P. Mynard and J. J. Smolich, "One-dimensional haemodynamic modeling and wave dynamics in the entire adult circulation," *Annals of biomedical engineering*, vol. 43, no. 6, pp. 1443–1460, 2015.

[18] J. P. Mynard, *Computer modelling and wave intensity analysis of perinatal cardiovascular function and dysfunction.* PhD thesis, Department of Paediatrics, The University of Melbourne, Heart Research Group, Murdoch Childrens Research Institute, 2011.

[19] X. Zhang, H. Haneishi, and H. Liu, "Multiscale modeling of the cardiovascular system for infants, children, and adolescents: Age-related alterations in cardiovascular parameters and hemodynamics," *Computers in biology and medicine*, vol. 108, pp. 200–212, 2019.

[20] D. Garcia, P. Pibarot, and L.-G. Durand, "Analytical modeling of the instantaneous pressure gradient across the aortic valve," *Journal of biomechanics*, vol. 38, no. 6, pp. 1303–1311, 2005.

[21] J. Mynard, M. Davidson, D. Penny, and J. Smolich, "A simple, versatile valve model for use in lumped parameter and one-dimensional cardiovascular models," *International Journal for Numerical Methods in Biomedical Engineering*, vol. 28, no. 6-7, pp. 626–641, 2012.

[22] Y. Sun, B. Sjoberg, P. Ask, D. Loyd, and B. Wranne, "Mathematical model that characterizes transmitral and pulmonary venous flow velocity patterns," *American Journal of Physiology-Heart and Circulatory Physiology*, vol. 268, no. 1, pp. H476–H489, 1995.

[23] K. Pekkan, D. Frakes, D. De Zelicourt, C. W. Lucas, W. J. Parks, and A. P. Yoganathan, "Coupling pediatric ventricle assist devices to the fontan circulation: simulations with a lumped-parameter model," *ASAIO journal*, vol. 51, no. 5, pp. 618–628, 2005.

[24] D. A. de Zélicourt, A. Marsden, M. A. Fogel, and A. P. Yoganathan, "Imaging and patient-specific simulations for the fontan surgery: current methodologies and clinical applications," *Progress in pediatric cardiology*, vol. 30, no. 1-2, pp. 31–44, 2010.

[25] A. Baretta, C. Corsini, W. Yang, I. E. Vignon-Clementel, A. L. Marsden, J. A. Feinstein, T.-Y. Hsia, G. Dubini, F. Migliavacca, G. Pennati, *et al.*, "Virtual surgeries in patients with congenital heart disease: a multi-scale modelling test case," *Philosophical Transactions of the Royal Society A: Mathematical, Physical and Engineering Sciences*, vol. 369, no. 1954, pp. 4316–4330, 2011.

[26] M. A. Fogel, R. H. Khiabani, and A. Yoganathan, "Imaging for preintervention planning: pre-and post-fontan procedures," *Circulation: Cardiovascular Imaging*, vol. 6, no. 6, pp. 1092–1101, 2013.

[27] K. S. Sundareswaran, K. Pekkan, L. P. Dasi, K. Whitehead, S. Sharma, K. R. Kanter, M. A. Fogel, and A. P. Yoganathan, "The total cavopulmonary connection resistance: a significant impact on single ventricle hemodynamics at rest and exercise," *American Journal of Physiology-Heart and Circulatory Physiology*, vol. 295, no. 6, pp. H2427–H2435, 2008.

[28] F. M. Susin, "Complete unsteady one-dimensional model of the net aortic pressure drop," *The Open Biomedical Engineering Journal*, vol. 13, no. 1, 2019.

[29] D. Garcia, P. Pibarot, J. G. Dumesnil, F. Sakr, and L.-G. Durand, "Assessment of aortic valve stenosis severity: a new index based on the energy loss concept," *Circulation*, vol. 101, no. 7, pp. 765–771, 2000.

[30] D. F. Young and F. Y. Tsai, "Flow characteristics in models of arterial stenoses—ii. unsteady flow," *Journal of biomechanics*, vol. 6, no. 5, pp. 547–559, 1973.

[31] N. Stergiopulos, D. Young, and T. Rogge, "Computer simulation of arterial flow with applications to arterial and aortic stenoses," *Journal of biomechanics*, vol. 25, no. 12, pp. 1477–1488, 1992.

[32] D. Garcia, L. Kadem, D. Savéry, P. Pibarot, and L.-G. Durand, "Analytical modeling of the instantaneous maximal transvalvular pressure gradient in aortic stenosis," *Journal of biomechanics*, vol. 39, no. 16, pp. 3036–3044, 2006.

[33] P. Kam and I. Power, *Principles of Physiology for the Anaesthetist*. CRC Press, 2015.

[34] G. Comunale, F. M. Susin, and J. P. Mynard, "A female-specific cardiovascular lumped-parameter model," in *2020 42nd Annual International Conference of the IEEE Engineering in Medicine Biology Society (EMBC)*, pp. 2654–2657, 42nd Annual International Conferences of the IEEE Engineering in Medicine and Biology Society in conjunction with the 43rd Annual Conference of the Canadian Medical and Biological Engineering Society, 2020.

[35] F. Pianosi, F. Sarrazin, and T. Wagener, "A matlab toolbox for global sensitivity analysis," *Environmental Modelling & Software*, vol. 70, pp. 80–85, 2015.

[36] M. Broomé, E. Maksuti, A. Bjällmark, B. Frenckner, and B. Janerot-Sjöberg, "Closed-loop real-time simulation model of hemodynamics and oxygen transport in the cardiovascular system," *Biomedical engineering online*, vol. 12, no. 1, pp. 1–20, 2013.

3 | I Application: Fontan Circulation

Contents

In this chapter, the single ventricle (Fontan) circulation is considered and compared to the biventricular circulation. First, the intrinsic limits of the Fontan circulation are analyzed. Particularly, the drawbacks of the univentricular circulation, i.e., low cardiac output and venous hypertension, are investigated. Second, age-specific and circulation-specific models are derived and compared, and the sensitivity to the pulmonary vascular resistance is analyzed.

The first part has been presented at the 7th International Conference on Computational Bioengineering [1], whereas, the second part has been presented at the XXXVI National Conference on Hydraulics and Hydraulic Constructions [2]. Here, an improved version of these works is presented.

3.1 Introduction

Congenital heart disease refers to defects of the heart and/or major blood vessels that arise during fetal development. They are the most common congenital malformations, with an overall incidence of about 1 out of 100 live births [3]. In particular, functionally univentricular CHD, i.e., single ventricle, has an incidence from 0.08 to 0.4 per 1000 live birth, with the most common pathology being the left hypoplastic heart syndrome (left HHS) [4]. Single ventricle circulation is characterized by a poorly developed ventricle in size and morphology with reduced functionality (Fig. 3.1). In single ventricle newborns, the only functioning ventricle must support both systemic and pulmonary circulation, resulting in reduced oxygenation of the blood due to the communication[1] between the two circulations, and an overload of the ventricle itself [5]. If left untreated, these complications usually lead to patient death [6]. For this reason, from the first weeks of life, infants affected by single ventricle heart defect undergo a series of consecutive surgical operations aimed at the complete separation between oxygenated and non-oxygenated blood within the circulatory system [7]. The last stage of this series of interventions is called Fontan circulation; in it the only functioning ventricle pumps blood through the systemic and pulmonary circulation which are connected in series through the total cavo-pulmonary connection. However, this type of intervention is palliative, because although on one hand it allows the child to survive, restoring proper oxygenation of the blood, on the other it determines a cardiovascular circulation substantially different from the physiological one, in terms of both flows and pressures.

Although most patients with a Fontan circulation have a good quality of life and reach adulthood, a large number of complications may arise, leading to late Fontan failure. Indeed, the persistence of hemodynamic abnormalities may lead to complications in the medium-long term, including venous hypertension, reduced systemic flow, and protein-losing enteropathy, which can ultimately cause ventricular and/or multi-organ failure [5, 7]. In presence of ventricular failure, heart transplantation is often the only available option for survival [5].

The above complications have been widely investigated from the medical point of view, and still are [5, 8, 9]. However, a lack of knowledge still persists about the development of the hemodynamic cascade that, starting from surgeries, leads to Fontan failure. For example, it is known that ab-

[1] The communication between the systemic and pulmonary circulation is the ductus arteriosus that is present during fetal development and normally closes at birth. However, this communication has to remain open after birth in children with single ventricle.

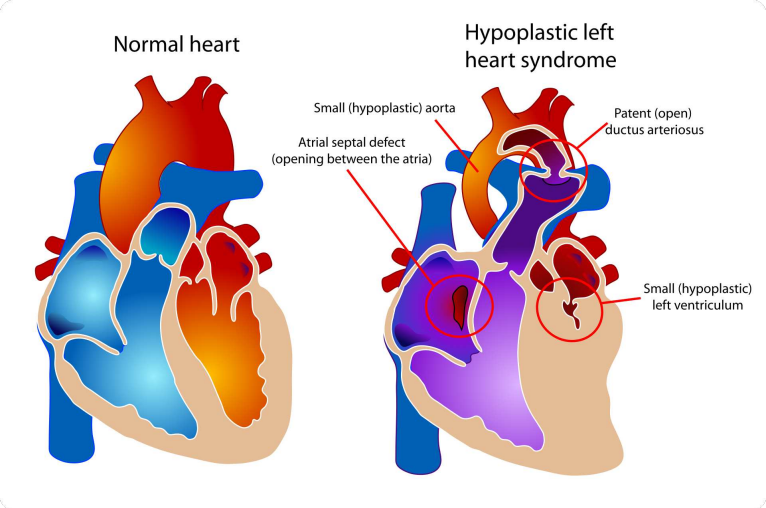

Figure 3.1: *Healthy and hypoplastic left heart, taken from Wikipedia.*

normally high venous blood pressure and increased pulmonary resistance are connected, but the basic hemodynamic factors driving that occurrence are not clear [10]. It has been clinically hypothesized but never mathematically demonstrated before that high venous pressure may be due to the limited diastolic function of the single ventricle [10]. Moreover, it is known that pulmonary vascular resistance (PVR) affects Fontan outcomes [10], and PVR is a known complication of Fontan patients [11]. However, it is still unclear if PVR is intrinsically related to the Fontan structure or it is caused by Fontan complications. Thus, the ability of 0D modeling in highlighting the role and the effect of each functional element of the circulation can be of great help in clarifying the scenario.

This chapter presents 0D models comparing the healthy and Fontan circulations. First, the focus is posed on understanding the fundamental physiological factors that lead to venous hypertension[2], by comparing the behavior of pressure levels in biventricular and univentricular circulations. In particular, the hypothesis of Gewillig and Brown [10] that high venous pressure is linked to the diastolic function of the single ventricle is tested (Section 3.2). Second, the purpose is to construct age-specific (adult and pediatric) and circulation specific (i.e., biventricular and Fontan) models, and to evaluate the effects of PVR changes on each circulation (Section 3.3). For all the conditions analyzed, the purpose is to reproduce *real* physiological and pathological cases in both adult and pediatric ages. Thus, case-specific pa-

[2]Venous hypertension is defined as caval vein pressure higher than 15 mmHg [12])

rameters will be considered in the following. A different operational choice is to model the univentricular circulation with parameters adopted for the biventricular circulation. However, the results of such simulation would not reproduce real cases because the presence of TCPC alters itself the parameters of the circulation. At most, it would supply indications on a circulation structurally equal to Fontan but in an individual with physiological circulation.

3.2 Intrinsic characteristics of the Fontan circulation

3.2.1 Methods

The lumped-parameters methodology described in Chapter 2 is used to build models of the biventricular and univentricular circulations. The models are shown in Fig. 3.2a and Fig. 3.2b, respectively.

The biventricular circulation includes the four heart chambers and valves, and the systemic and pulmonary circulations. Systemic and pulmonary circulations are represented by the model in Fig. 3.2c (Eq. (2.3)). This model reproduces the elastic properties of the arteries and veins as well as of the small vessels and the viscous friction effects. Finally, the heart valves are represented as diodes (Subsection 2.4.1).

The Fontan circulation is derived from the biventricular circulation by substituting the right heart with the total cavo-pulmonary connection. TCPC is represented as described in Section 2.5.

The purpose of this section is to understand the factors that lead to venous hypertension in Fontan patients. The hypothesis is that the intrinsic limit of the Fontan circulation is the minimum pressure that the single ventricle can reach in diastole, as suggested by Gewillig and Brown [10]. For this purpose, several pressure conditions are prescribed (i.e., boundary condition, BC) on the systemic ventricle (LV and the Fontan ventricle, FV, respectively), and the resulting hemodynamics is analyzed in terms of pressure levels in different districts of the circulation. In particular, for both the biventricular and Fontan circulation, two fluid-dynamic conditions are simulated: *i)* steady-state, and *ii)* pulsatile physiological condition. In the former a constant physiologic systolic pressure is applied to both the systemic and pulmonary heart (whatever present). In this condition, pressures are computed by considering realistic fixed pressure drops, i.e., in systole, the pressure goes from about 120 mmHg in LV to 3 mmHg in the systemic veins ($\Delta p \approx 117$ mmHg), and from 25 mmHg in RV to 9 mmHg in LA

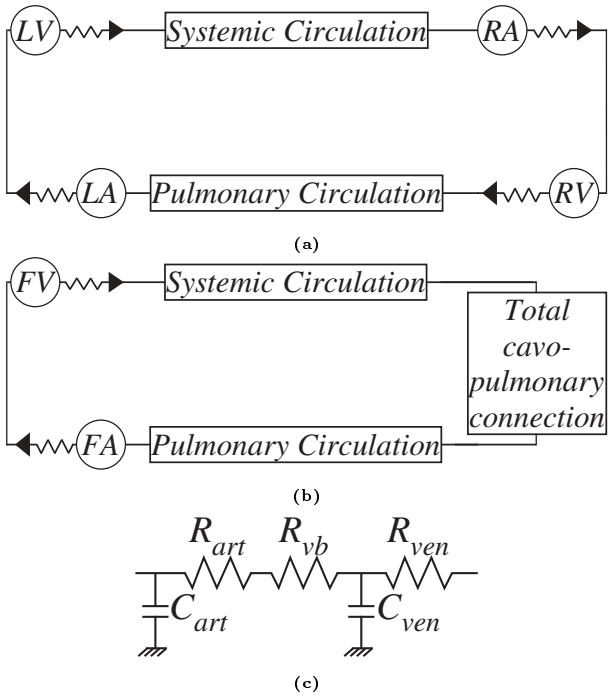

Figure 3.2: *Schematic representation of (a) the biventricular circulation, (b) the Fontan (univentricular) circulation, and (c) the lumped model of the systemic and pulmonary circulations. The two models comprise the systemic arteries, vascular bed, and veins, and the pulmonary arteries, vascular bed, and veins. The biventricular circulation includes the four heart chambers (LA, LV, RA, and RV) and heart valves, whereas the Fontan circulation is characterized by the single ventricle and atrium (FV, FA) and only two heart valves, together with the total cavo-pulmonary connection. The systemic and pulmonary circulations are characterized by the arterial side (R_{art}, C_{art}), the vascular bed (R_{vb}), and the venous side (R_{ven}, C_{ven}).*

($\Delta p \approx 16$ mmHg) [13]. The same pressure drops are then applied to the Fontan circulation starting from the single ventricle. In the physiological condition, the right ventricle and the atria are reproduced as in Section 2.3 by the time-elastance model. The systemic ventricle, instead, is represented by prescribing physiological pressure waves. In particular, in the pulsatile physiological condition, different pressure boundary conditions are considered for the Fontan circulation, and the prescribed pressure on FV is opportunely modified to highlight the effect of the pumping and suction properties of FV on the circulation. Starting from the physiological pressure condition (in the following called baseline), the further specific conditions that are implemented are: *i)* reduced pressure condition, both in systole and diastole, *ii)* increased pumping action, i.e., increased FV pressure in systole, and *iii)* increased suction action, i.e., reduced FV pressure in diastole. All

these conditions are tested to understand which pressure configuration helps in avoiding high venous pressure in the Fontan circulation.

For both the models, parameters' calibration is conducted as described in Section 2.7, with the lumped-parameters derived by applying the rules reported in the Subsection 2.7.1. Particularly, to reproduce real cases, the models are calibrated taking into account the clinical data reported in [14]. Hence, the biventricular model represents an average 26 y.o. person with body surface area (BSA) of 1.79 m^2, HR of 70 bpm, SVR = 0.93 mmHg·s/mL, MAP of 86 mmHg, and CO of 5.7 L/min. On the other hand, the Fontan model reproduces an average Fontan 26 y.o. patient, BSA of 1.75 m^2, HR of 74 bpm, SVR = 0.912 mmHg·s/mL, MAP of 81 mmHg, and CO of 5.9 L/min. Finally, PVR is set equal to 0.06 and 0.073 mmHg·s/mL for the biventricular and Fontan circulations, respectively. These values are taken from [15] and [9], respectively. Note that, due to the lack of clinical data specific for adult Fontan patients, the pediatric value derived by Pekkan et al. [16] is applied to R_{TCPC} (see Section 2.5). Moreover, these input values are used only in the pulsatile physiological condition whereas to make easier the computation, realistic fixed pressure drops are assumed in the steady-state condition.

Table 3.1: *Heart parameters values.*

	Systemic ventricle	**Pulmonary ventricle**	**Systemic atrium**	**Pulmonary atrium**
$E_{max}[mmHg/mL]$				
Biventricular	2.80	0.450	0.156	0.09
Fontan	3.08	-	0.1716	-
$E_{min}[mmHg/mL]$				
Biventricular	0.070	0.035	0.09	0.045
Fontan	0.063	-	0.081	-
$V_{p=0}[mL]$				
Biventricular	10	40	3	7
Fontan	50	-	3	-
$\tau_1[s]$	$0.269T$	$0.269T$	$0.110T$	$0.110T$
$\tau_2[s]$	$0.452T$	$0.452T$	$0.180T$	$0.180T$
$m_1[-]$	1.32	1.32	1.99	1.99
$m_2[-]$	21.9	21.9	11.2	11.2
$t_{onset}[s]$	0	0	$0.85T$	$0.85T$
$R[mmHg \cdot s/mL]$	0.02	0.001	0.01	0.01

T is the heartbeat period. If not specified, the same value is used in the biventricular and Fontan circulations.

For the heart, values from [15] are applied to the biventricular circulation. In the Fontan circulation, these values are modified to meet the desired hemodynamics and to represent the vigorous systolic and diastolic function that is a common adaptation in Fontan patients [12]. Finally, the values of the valves' resistances are set to simulate a healthy valve condition in both the models. Values of the heart parameters are reported in Table 3.1. Note that the values of the systemic ventricle are not used in this section (a boundary condition is applied), but they are however reported since they will be used in the next Section.

3.2.2 Results

Steady-state simulations

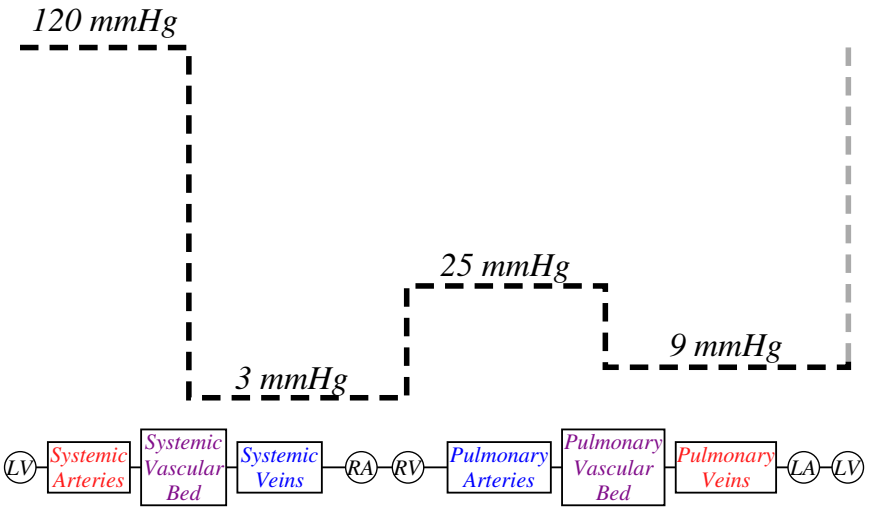

Figure 3.3: *Adult biventricular pressure levels of the steady-state simulation. In red and blue, oxygenated and deoxygenated blood, respectively, and in purple, mixed oxygenated and deoxygenated blood.*

The results of the steady-state simulations are reported in Fig. 3.3-3.5 in terms of pressure behavior along the compartments of the whole circuit. The biventricular circulation shows the typical physiological values in both the left and right districts (Fig. 3.3). The pressure levels of the Fig. 3.4 (Fontan circulation) are derived considering the pressure in FV as the leading force, i.e., the FV pressure is imposed. Notice that the adopted value of 120 mmHg can be considered as normal in adult Fontan patients. As it is highlighted in the plot, the imposed pressure on FV leads to an unfeasible condition in which the single atrium (Fontan atrium, FA) reaches a negative pressure

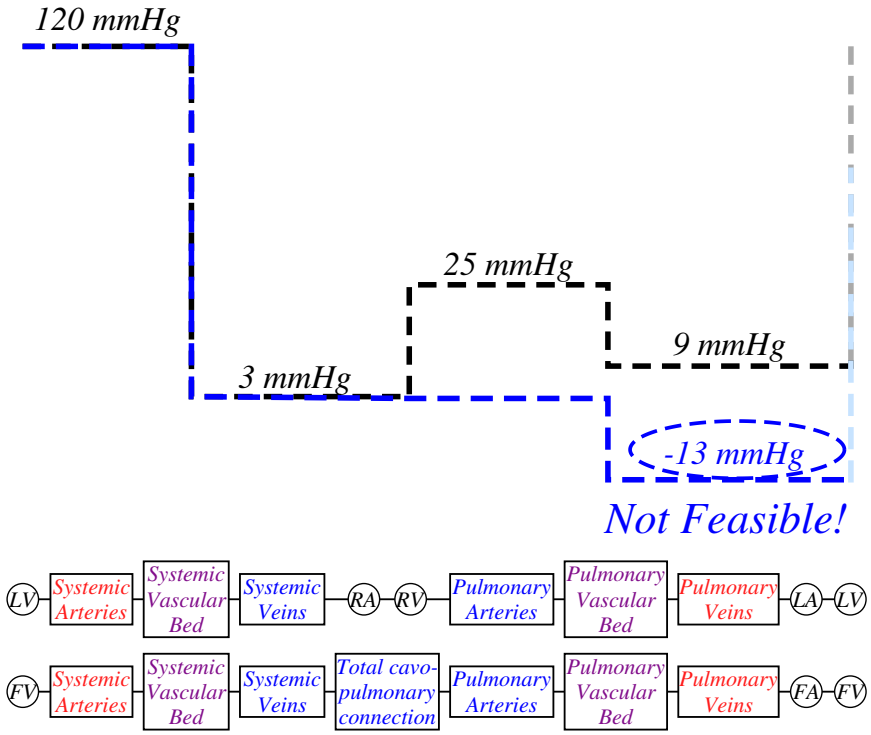

Figure 3.4: *Adult pressure levels of the steady-state simulation for the Fontan (univentricular) circulation when the FV pressure is considered the forcing threshold (imposed BC pressure). The pressure levels are reported in black and blue for the biventricular circulation (from Fig. 3.3) and the Fontan circulation with FV limit, respectively. In red and blue, oxygenated and deoxygenated blood, respectively, and in purple, mixed oxygenated and deoxygenated blood.*

of -13 mmHg. The computed unrealistic FA pressure value suggests that in the Fontan circulation the physical limit is determined by the pressure condition in FA. For this reason, the pressure levels of Fig. 3.5 are derived imposing the physiological pressure on FA as the intrinsic threshold (i.e., FA is prescribed). As it can be seen from the plot, the pressure levels represents realistic pressures measured in Fontan patients with venous hypertension [12, 14, 17], except for the systemic arterial hypertension that is due to the fixed pressure drop considered in the systemic circulation. The hypothesis that the FA working condition, i.e., the pressure prescribed to FA, is the intrinsic limit of the circulation, i.e., FA pressure determines realistic Fontan pressure and venous hypertension is hence confirmed. From the steady-state simulation, the computed results hence suggest that the downstream pressure, i.e., FA pressure, forces high venous pressure because FA is not able to lower its pressure below certain values.

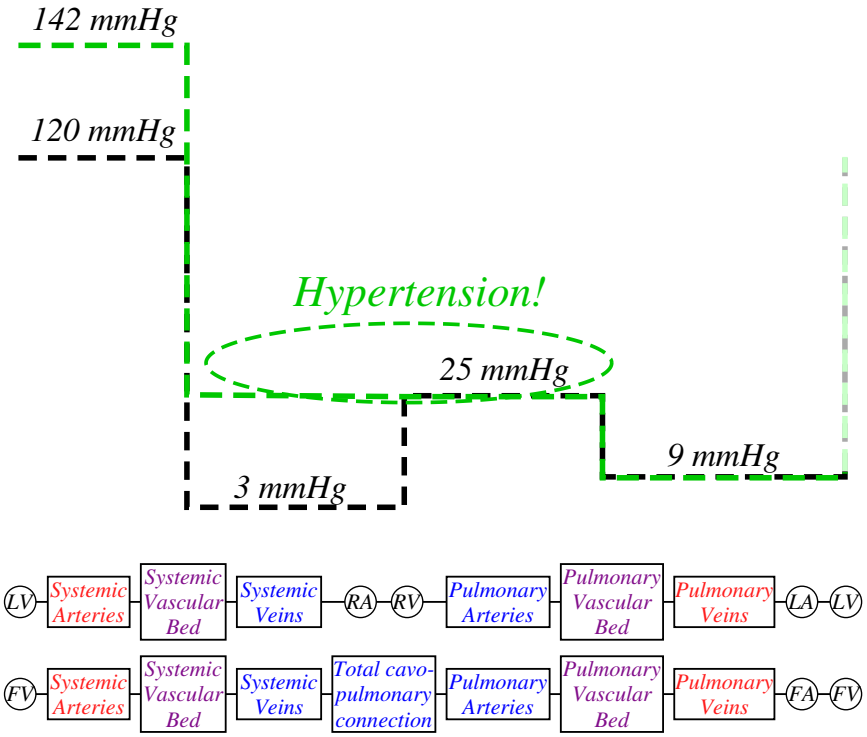

Figure 3.5: *Adult pressure levels of the steady-state simulation for the Fontan (univentricular) circulation when the FA pressure is considered as the intrinsic threshold (imposed BC pressure). It is shown that the downstream pressure, i.e., the atrial pressure, is the physical limit that causes hypertension in the TCPC. The pressure levels are reported in black and green for the biventricular circulation (from Fig. 3.3) and the Fontan circulation with FA limit, respectively. In red and blue, oxygenated and deoxygenated blood, respectively, and in purple, mixed oxygenated and deoxygenated blood.*

Pulsatile physiological simulations

For the pulsatile physiological simulations, first, the ability of the models to behave as expected is verified. Table 3.2 and 3.3 report the outputs of the biventricular and Fontan circulations compared with *in vivo* reference data, respectively. The two models agree very well with the specific literature. Particularly, these models are capable of representing the global hemodynamic variables in terms of volumes, pressures, and also flows specific for healthy and Fontan adults.

Expected hemodynamic behavior is found also in terms of waveforms, as it is shown in Fig. 3.6. In Fig. 3.6a and 3.6c the pressures and flows of the biventricular circulation are reported, whereas, in Fig. 3.6b and 3.6d the Fontan condition is considered. Interestingly, the Fontan model is able to

Table 3.2: *Comparison of the biventricular model hemodynamics with in vivo reference data.*

Parameter	Units	Model	Reference
Total resistance			
SVR	mmHg·s/mL	0.93	0.93 (±0.21)[14]
PVR	mmHg·s/mL	0.06	0.06 (0.02-0.09)[18]
Volume			
LV_{max}	mL	126	131 (±29)[14]
RV_{max}	mL	161	171 (121-221)[19]
LA_{max}	mL	113	103 (±30)[20]
RA_{max}	mL	120	101 (37-177)[21]
LV_{min}	mL	43	50 (±33)[14]
RV_{min}	mL	78	64 (34-94)[19]
LA_{min}	mL	61	44 (±13)[20]
RA_{min}	mL	78	50 (15-92)[21]
Cardiac flows			
SV	mL	83	81 (±16)[14]
CO	L/min	5.8	5.66 (±1.14)[14]
Pressure			
SBP	mmHg	117	115 (±14)[14]
DBP	mmHg	65	71 (±17)[14]
PuA (systolic)	mmHg	18.1	22.5 (±1.0)[22]
PuA (mean)	mmHg	13.2	15.5 (±2.6)[22]
LAP (mean)	mmHg	8.7	7.9 (±1.2)[22]

Reference data given as a mean, with range or standard deviation in parentheses. See text for abbreviation.

reproduce the characteristic reduction in cardiac output (as seen by reduced Q_{ao}). In the figures, the almost constant pressure and flow of the TCPC are also reported, with values of about 18 mmHg and 90 mL/s, respectively, in agreement with the data of Pekkan et al. [23].

Pressure levels of the pulsatile condition refer to the mean values in systole. Fig. 3.7 shows the pressure levels for the biventricular and Fontan circulations for the different ventricular pressure conditions analyzed. Fig. 3.7a shows the pressure levels for the biventricular and Fontan circulations with baseline pressure. As for the steady-state, the imposition of a physiological downstream pressure leads to venous hypertension, with a value of about 18 mmHg. The pressure levels obtained assuming a reduced systolic and diastolic ventricular pressure are shown in Fig. 3.7b. When the pressure

Table 3.3: *Comparison of the Fontan model hemodynamics with in vivo reference data.*

Parameter	Units	Model	Reference
Total resistance			
SVR	mmHg·s/mL	0.91	0.91 ($\pm$0.36)[14]
PVR	mmHg·s/mL	0.073	0.073 ($\pm$0.031)[9]
Volume			
FV_{max}	mL	106	168 ($\pm$63)[14]
FV_{min}	mL	35	86 ($\pm$69)[14]
Cardiac flows			
SV	mL	71	82 ($\pm$28)[14]
CO	L/min	5.2	5.86 ($\pm$1.90)[14]
Pressure			
SBP	mmHg	117	110 ($\pm$15)[14]
DBP	mmHg	73	67 ($\pm$19)[14]
$PCWP$	mmHg	14.3	10.3 ($\pm$3.5)[17]
$Ptcpc$	mmHg	17.8	15.0 ($\pm$4.0)[9]

Reference data given as a mean, with range or standard deviation in parentheses. See text for abbreviation.

is reduced in the whole heartbeat, it favors a reduction in the TCPC close to the physiological value, but, at the same time, it causes a SBP of about 100 mmHg. This value is lower than would normally be observed in a 26 year old person. Fig. 3.7c reports the mean systolic pressure when an increased ventricular pumping action (contractility) is considered. This condition simulates the effect of the introduction of pumps that are often considered in the clinical practice for the failing Fontan patients [24, 25]. The rationality behind is to help the single ventricle to pump. However, as it is shown here, an increased pumping action helps by increasing the ventricular and systolic arterial pressure but it does not help in terms of reducing TCPC/venous pressure. Finally, an increased ventricular suction action is considered in Fig. 3.7d. This simulation shows that if the single atrium would be able to reduce its pressure to about 0 mmHg, the hypertension that characterizes the Fontan patients would be solved. Indeed, the ventricular and SBP pressures are equal to the biventricular case and, at the same time, the TCPC pressure is reduced.

Fig. 3.8 shows the cardiac output for the different conditions considered. CO decreases in the Fontan circulation to about 5.2 L/min in both physiological and reduced pressures conditions. On the other hand, the Fontan circulation with increased pumping action or increased suction action restores

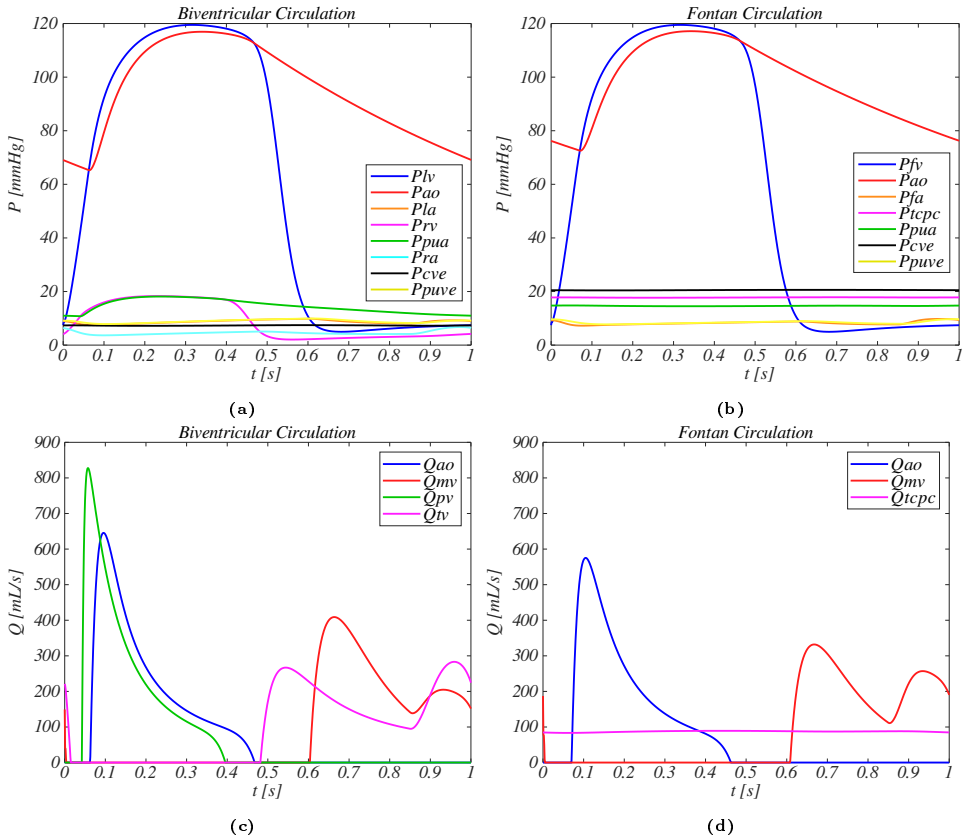

Figure 3.6: *Hemodynamic waveforms of the biventricular and Fontan models. (a) and (c) pressures and valves flows of the biventricular model, respectively, and (b) and (d) pressures and valves flows of the Fontan model, respectively.*

the CO to a value that is almost the same as the biventricular circulation of about 5.7 L/min.

3.3 Adult *vs* pediatric healthy and Fontan patients and the effect of PVR

In this section, age-specific (adult and pediatric) models for both the biventricular and Fontan circulation are derived, and the effects of PVR changes on each configuration are analyzed.

3.3.1 Methods

The biventricular and Fontan models presented previously (Section 3.2) are here utilized. Differently from before, boundary conditions on the systemic

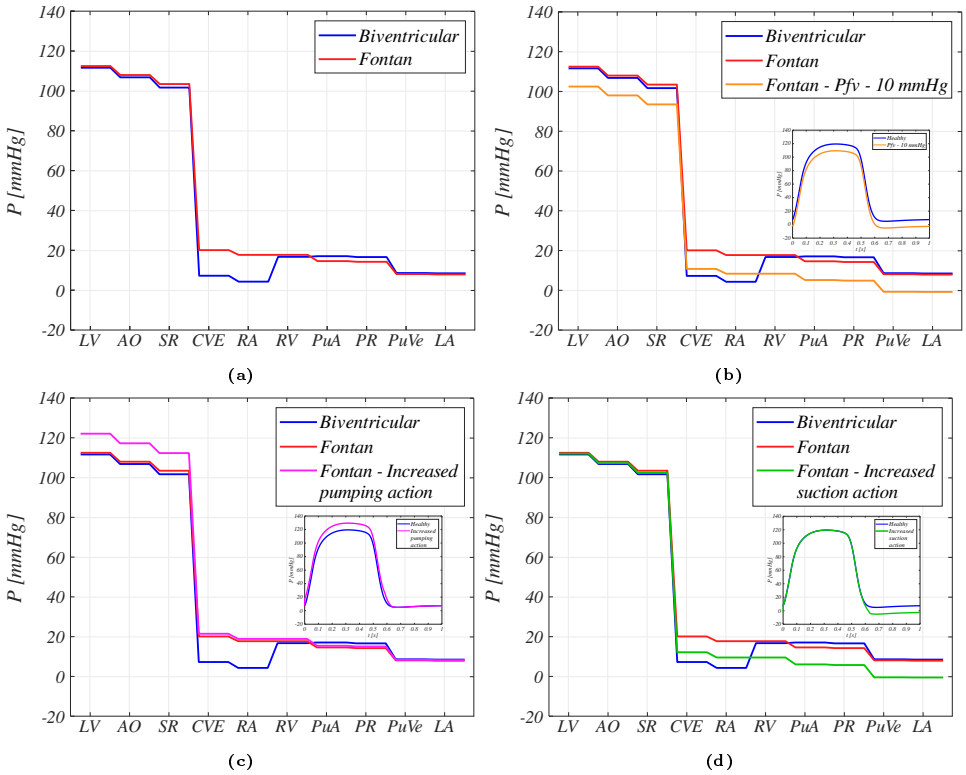

Figure 3.7: *Pressure levels of the pulsatile physiological simulation. (a) Biventricular vs Fontan circulation, (b) biventricular vs Fontan circulation with physiological and reduced FV pressure, (c) biventricular vs Fontan circulation with physiological pressure and increased pumping action, and (d) biventricular vs Fontan circulation with physiological pressure and increased suction action. In blue, the biventricular circulation, in red, the Fontan circulation with physiological pressure, in orange, Fontan circulation with reduced pressure, in magenta, the Fontan circulation with increased pumping action, and, in green, the Fontan circulation with increased suction action. In the insets, the applied systemic ventricular pressure (LV and FV). LV, left ventricle, AO, aorta and systemic arterial vessels, SR, systemic vascular bed, CVE, caval veins, RA, right atrium, RV, right ventricle, PuA, pulmonary arterial vessels, PR, pulmonary vascular bed, PuVe, pulmonary venous vessels, and LA, left atrium. Note that in this figure, LV refers to the systolic ventricle, i.e., both the left and the single ventricle in the bi- and uni-ventricular circulation, respectively. Analogously, LA is the systemic atrium, and thus, it refers to both the left and single atrium, and the right heart (RA, RV) refers to TCPC when considering the Fontan circulation.*

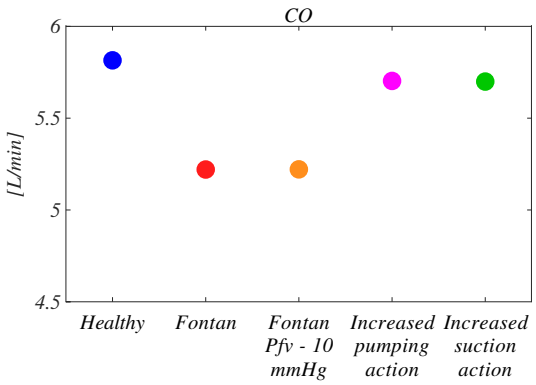

Figure 3.8: *Cardiac output for the different conditions considered. In blue and in red, the biventricular and Fontan circulations with physiological ventricular pressure, respectively. In orange, magenta, and green, the Fontan circulation with reduced pressure, increased pumping action, and increased suction action, respectively.*

ventricle are not prescribed, but the time-varying elastance model is applied to every heart chamber (Section 2.3). For the adult circulation, the same parameters as before are utilized. For the pediatric case, the parameters' derivation methodology is used (Section 2.7). Particularly, the case of a 10 y.o. child is considered for both the biventricular and Fontan models. This is chosen because the final surgery resulting in the Fontan circulation is usually performed between 18 months and 5 years of age [4, 26] and the purpose here is to simulate a "stabilized" Fontan circulation. Moreover, in literature, the clinical data available on the pediatric cohort usually refer to this age.

The biventricular model is calibrated to simulate a BSA of 1.18 m^2, HR of 79 bpm, SVR and PVR equal to 1.2 and 0.22 mmHg·s/mL, respectively, MAP of 76 mmHg, and CO of 3.8 L/min [13, 27, 28]. The Fontan model reproduces a child with BSA of 1.07 m^2, HR of 89 bpm, SVR and PVR of 1.4 and 0.09 mmHg·s/mL, MAP of 73 mmHg, and CO of 3.3 L/min [26, 29, 30]. The choice to consider specific parameters for each configuration allows to derive age-specific parameters in agreement with the methodology described in Section 2.7 and it is done to reproduce real cases. For both the models, values of the heart are taken from the adult model adjusting by fine-tuning the $V_{p=0}$ value of Eq. (2.6) to meet the desired hemodynamics. This is done assuming that the maximum and minimum heart forces are generated depending on the initial fiber length, determined by $V_{p=0}$, in agreement with the Frank-Starling law. This is a strong assumption but the choice to maintain the same heart parameters for the adult and pediatric models and varying only $V_{p=0}$ is due to the lack of data from which derive more specific

Table 3.4: *Heart parameters values for the pediatric case.*

	Systemic ventricle	**Pulmonary ventricle**	**Systemic atrium**	**Pulmonary atrium**
$E_{max}[mmHg/mL]$				
Biventricular	2.80	0.450	0.156	0.09
Fontan	3.08	-	0.1716	-
$E_{min}[mmHg/mL]$				
Biventricular	0.070	0.035	0.09	0.045
Fontan	0.063	-	0.081	-
$V_{p=0}[mL]$				
Biventricular	-10	-20	-30	-40
Fontan	7	-	-10	-
$\tau_1[s]$	$0.269T$	$0.269T$	$0.110T$	$0.110T$
$\tau_2[s]$	$0.452T$	$0.452T$	$0.180T$	$0.180T$
$m_1[-]$	1.32	1.32	1.99	1.99
$m_2[-]$	21.9	21.9	11.2	11.2
$t_{onset}[s]$	0	0	$0.85T$	$0.85T$
$R[mmHg \cdot s/mL]$	0.02	0.001	0.01	0.01

T is the heartbeat period. If not specified, the same value is used in the biventricular and Fontan circulations.

parameters. Indeed, the variation of one parameter ($V_{p=0}$) instead of all the heart parameters for each heart chamber makes the adjustment more controllable. Table 3.4 shows the heart parameters values for the pediatric case.

The effect of high pulmonary vascular resistance is also studied because high PVR represents a known complication of Fontan patients [11]. The understanding of how PVR increments can affect the global hemodynamics may give useful information for understanding the role of PVR in the Fontan circulation. PVR is altered between 5% and 50% from the baseline value, based on the range of values reported in [9]. The PVR analysis is conducted for all the four configurations considered: *i)* the adult biventricular case, *ii)* the pediatric biventricular case, *iii)* the adult Fontan case, and *iv)* the pediatric Fontan case. In particular, the analysis of PVR changes in each configuration enables the understanding of the age-specific and circulation-specific PVR sensitivity.

3.3.2 Results

In Table 3.5 the outputs of the biventricular models for the adult and pediatric case are reported and compared with *in vivo* data obtained from

literature. Fig. 3.9a-3.9d show the waveforms of the adult and pediatric biventricular circulations. The biventricular model, both with adult and pediatric parameters, is able to represent the *in vivo* hemodynamics. There is a very good agreement both in terms of pressures and flows, and also in terms of mean values and waveforms. Particularly, thanks to the appropriate calibration, the model correctly represents the lower pressures and flows typical of children.

In Table 3.6 the outputs of the Fontan models for the adult and pediatric case are reported and compared with *in vivo* data obtained from the literature. In Fig. 3.9e-3.9h the waveforms are shown. As for the biventricular case, the adult case is characterized by higher values of pressures and flows compared to the pediatric one, as expected. Comparing the biventricular model with the Fontan circulation equivalent for age, the simulations reproduce the complications of the Fontan patients, i.e., decreased CO and increased central venous pressure (CVP) (Fig. 3.10).

Focusing on the effect of the PVR, Fig. 3.11 shows *i)* the absolute cardiac output and central venous pressure and *ii)* the percentage variations of CO and CVP, as PVR changes. In terms of CO, the Fontan model ($\sim 11\%$) is more sensitive to PVR than the biventricular ($\sim 4\%$) circulation when considering the adult case. This difference almost disappears in the pediatric configuration, with about ($\sim 11\%$) and ($\sim 10\%$) in the Fontan and biventricular model, respectively. Moreover, in the biventricular circulation, the pediatric case results in bigger CO changes compared to the adult one, whereas this difference diminishes in the Fontan circulation (Fig. 3.11b). Interestingly, the CVP of the biventricular circulation is not affected by the increment of PVR ($< 2\%$). On the other hand, as PVR increases, the central venous pressure increases for the Fontan patients (Fig. 3.11c). Moreover, the influence on CVP is greater in pediatric ($\sim 9\%$) than in adult ($\sim 6\%$) Fontan case (Fig. 3.11d).

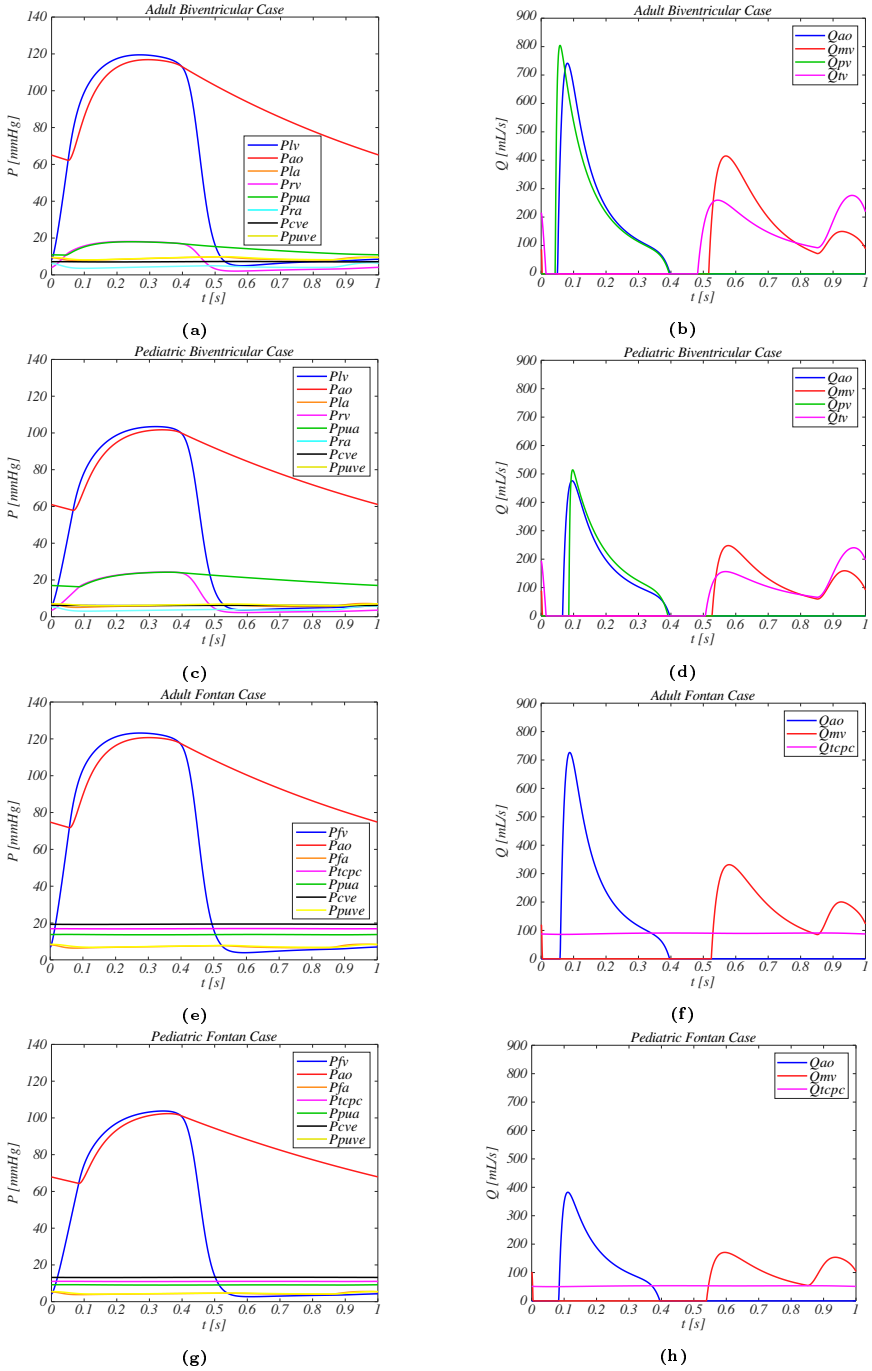

Figure 3.9: *Hemodynamic waveforms of the biventricular and Fontan configurations. (a) The pressures and (b) the flows of the adult biventricular circulation, (c) the pressures and (d) the flows of the pediatric biventricular circulation, (e) the pressures and (f) the flows of the adult Fontan circulation, and (g) the pressures and (h) the flows of the pediatric Fontan circulation.*

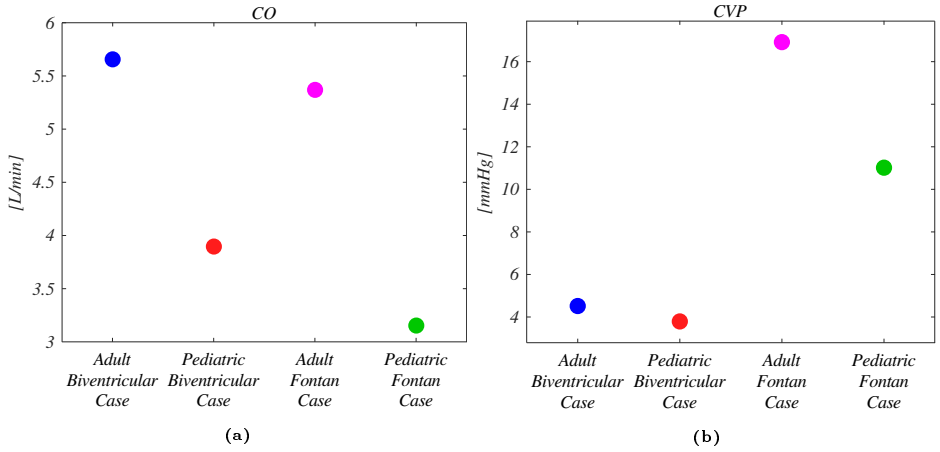

Figure 3.10: *(a) Cardiac outputs and (b) central venous pressure of the four conditions considered. In blue, the adult biventricular case, in red, the pediatric biventricular case, in magenta, the adult Fontan case, and in green, the pediatric Fontan case.*

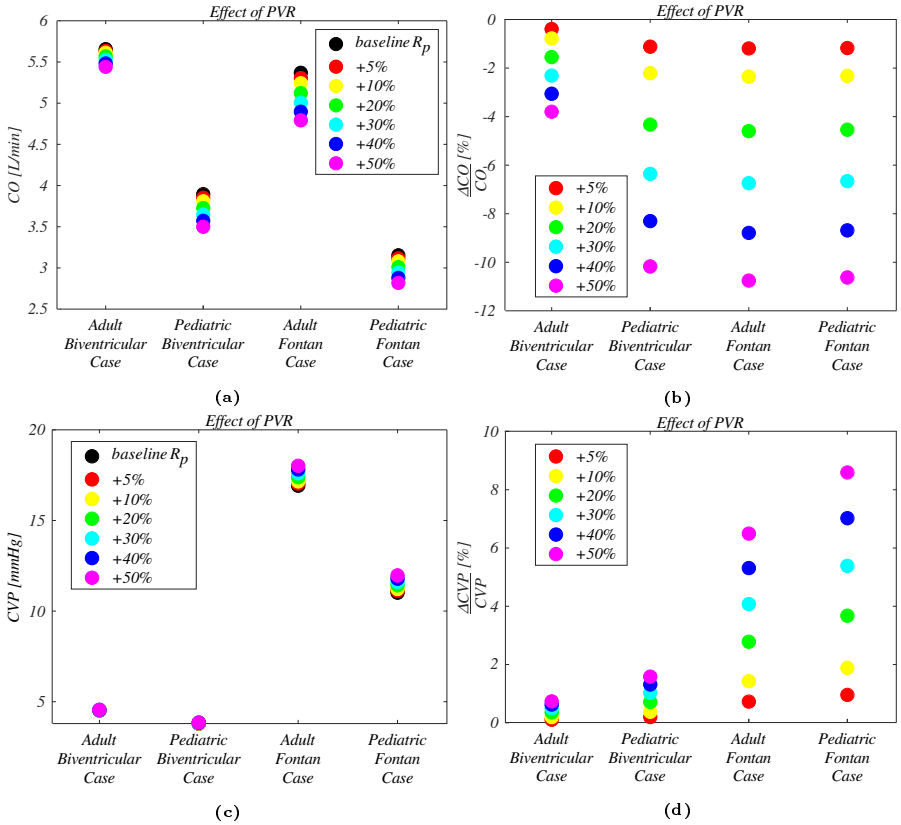

Figure 3.11: *(a) Cardiac outputs, (b) percentage change in CO, (c) central venous pressure, and (d) percentage change in CVP of the four conditions considered as PVR changes.*

Table 3.5: *Comparison of the biventricular model hemodynamics with in vivo reference data for the adult and pediatric case.*

Parameter	**Units**	**Adult**		**Pediatric**	
		Model	**Reference**	**Model**	**Reference**
Total resistance					
SVR	mmHg·s/mL	0.93	0.93 ($\pm$0.21)[14]	1.2	(0.9-1.5)[13]
PVR	mmHg·s/mL	0.06	0.06 (0.02-0.09)[18]	0.22	(0.03-0.24)[13]
Volume					
LV_{max}	mL	132	131 ($\pm$29)[14]	75.48	79.06 ($\pm$10.62)[31]
RV_{max}	mL	159	171 (121-221)[19]	82.90	82.60 ($\pm$12.98)[31]
LA_{max}	mL	112	103 ($\pm$30)[20]	43.5	33.8(28.2-45.0)[32]
RA_{max}	mL	117	101 (37-177)[21]	47.9	80 ($\pm$24.9)[33]
LV_{min}	mL	51	50 ($\pm$33)[14]	26.1	27.1 ($\pm$13.5)[31]
RV_{min}	mL	78	64 (34-94)[19]	33.6	31.9 ($\pm$15.4)[31]
LA_{min}	mL	64	44 ($\pm$13)[20]	14.3	12.6 (9.6-16.6)[32]
RA_{min}	mL	76	50 (15-92)[21]	20.7	36.5 ($\pm$12.4)[33]
Cardiac flows					
SV	mL	81	81 ($\pm$16)[14]	49.4	51.9 ($\pm$8.3)[31]
CO	L/min	5.66	5.66 ($\pm$1.14)[14]	3.90	3.78 ($\pm$0.59)[31]
Pressure					
SBP	mmHg	117	115 ($\pm$14)[14]	102	103 ($\pm$6)[34]
DBP	mmHg	62	71 ($\pm$17)[14]	58	62 ($\pm$8)[34]
PuA (mean)	mmHg	13.1	15.5 ($\pm$2.6)[22]	18.9	16.6 ($\pm$7.5)[35]

Reference data given as a mean, with range or standard deviation in parentheses. See text for abbreviation.

Table 3.6: *Comparison of the Fontan model hemodynamics with in vivo reference data for the adult and pediatric case.*

Parameter	**Units**	**Adult**		**Pediatric**	
		Model	**Reference**	**Model**	**Reference**
Total resistance					
SVR	mmHg·s/mL	0.91	0.91 ($\pm$0.36)[14]	1.40	1.40 ($\pm$0.39)[30]
PVR	mmHg·s/mL	0.073	0.073 ($\pm$0.031)[9]	0.090	0.095 ($\pm$0.056)[30]
Volume					
FV_{max}	mL	161	168 ($\pm$63)[14]	76	82 ($\pm$30)[30]
FV_{min}	mL	89	86 ($\pm$69)[14]	40	35 ($\pm$36)[30]
Cardiac flows					
SV	mL	73	82 ($\pm$28)[14]	36	47 ($\pm$19)[30]
CO	L/min	5.37	5.86 ($\pm$1.90)[14]	3.16	3.21 ($\pm$0.86)[30]
Pressure					
$Ptcpc$	mmHg	17	15 ($\pm$4)[9]	11	
CVP	mmHg	19	17 ($\pm$2)[30]	13	12 ($\pm$3)[29]
PuA (mean)	mmHg	14	13 ($\pm$2)[29]	9	11 ($\pm$3)[29]
AOP (mean)	mmHg	99	88($\pm$11)[29]	85	87 ($\pm$9)[29]

Reference data given as a mean, with range or standard deviation in parentheses. See text for abbreviation.

3.4 Model Sensitivity Analysis

The sensitivity of the models is investigated as explained in Section 2.8. 16 and 11 inputs[3] are varied, and 21 and 16 outputs are evaluated for the biventricular and Fontan circulation, respectively.

Tables 3.7 and 3.8 show the results of the sensitivity analysis for the biventricular and Fontan circulation, respectively. Inputs are ordered following the global influence, computed as the sum of $|S|$ for all the outputs analyzed, showing the most influential on the left. Outputs are ordered based on the overall sensitivity, computed as the median value of $|S|$ for all the inputs, with the most sensitive at the top. Figures 3.12 and 3.13 report the graphical representation of the sensitivity analysis for the biventricular and Fontan circulation, respectively. This time, outputs are listed on the horizontal axis and inputs listed on the vertical axis. Note that, in the figure, outputs are ordered with the most sensitive on the left, and inputs are ordered with the most influential at the bottom.

For the biventricular circulation, the most influential parameters are those related to the heart chamber contractility (e.g., $E_{max_{RA}}$, $E_{max_{LA}}$, and $E_{max_{RV}}$), which is somehow expected. These parameters are known from the physiology to affect pressures and flows, however, interestingly, the contractility of LV is less influential than that of the other heart chambers. This may be due to the extended research attention posed on LV compared to the other heart chambers, suggesting that the left ventricular parameter is better estimated. Thus, the high sensitivity of the other heart chambers' parameters suggests that research needs to focus also on them to derive pertinent values and be able to simulate real cases. The most sensitive outputs are those related to the systemic arterial side and the volumes, that are directly linked to the heart chamber contractility. Moreover, only few output variables are sensitive to the variation of inputs, and this is clearly visible from the figure that shows a cluster of larger data points in the left side. The least sensitive outputs signals are the right ventricular and pulmonary venous pressures, and this could be related to the reservoir functionality of the high-compliance pulmonary circulation.

[3] C_{global} refers to all the systemic compliances, both arterial and venous ones.

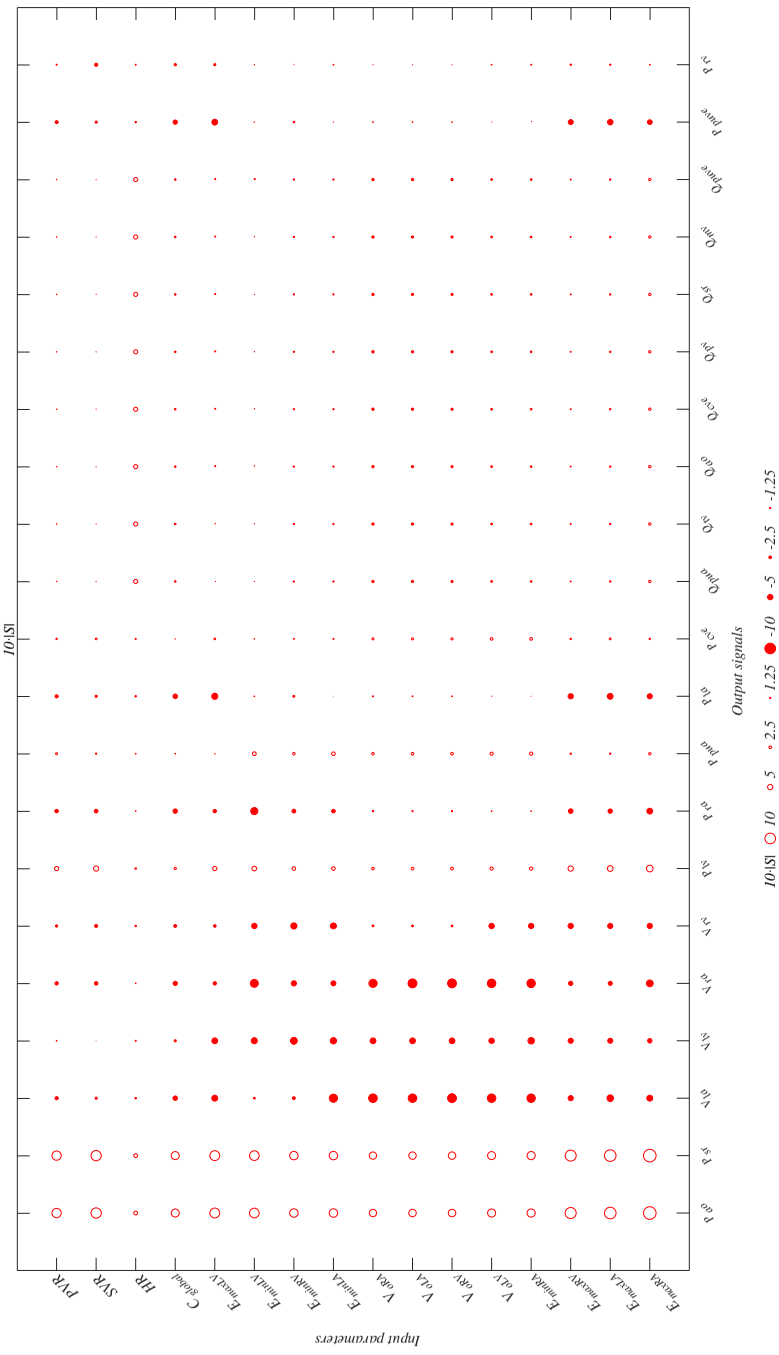

Figure 3.12: *Graphical representation of the sensitivity of the outputs to the 25% variation of the inputs for the biventricular model. A larger symbol corresponds with higher sensitivity and filled/empty circles correspond to negative/positive S. Outputs are ordered according to the overall sensitivity (the most sensitive on the left) and inputs are ordered based on the global influence (the most influential at the bottom).*

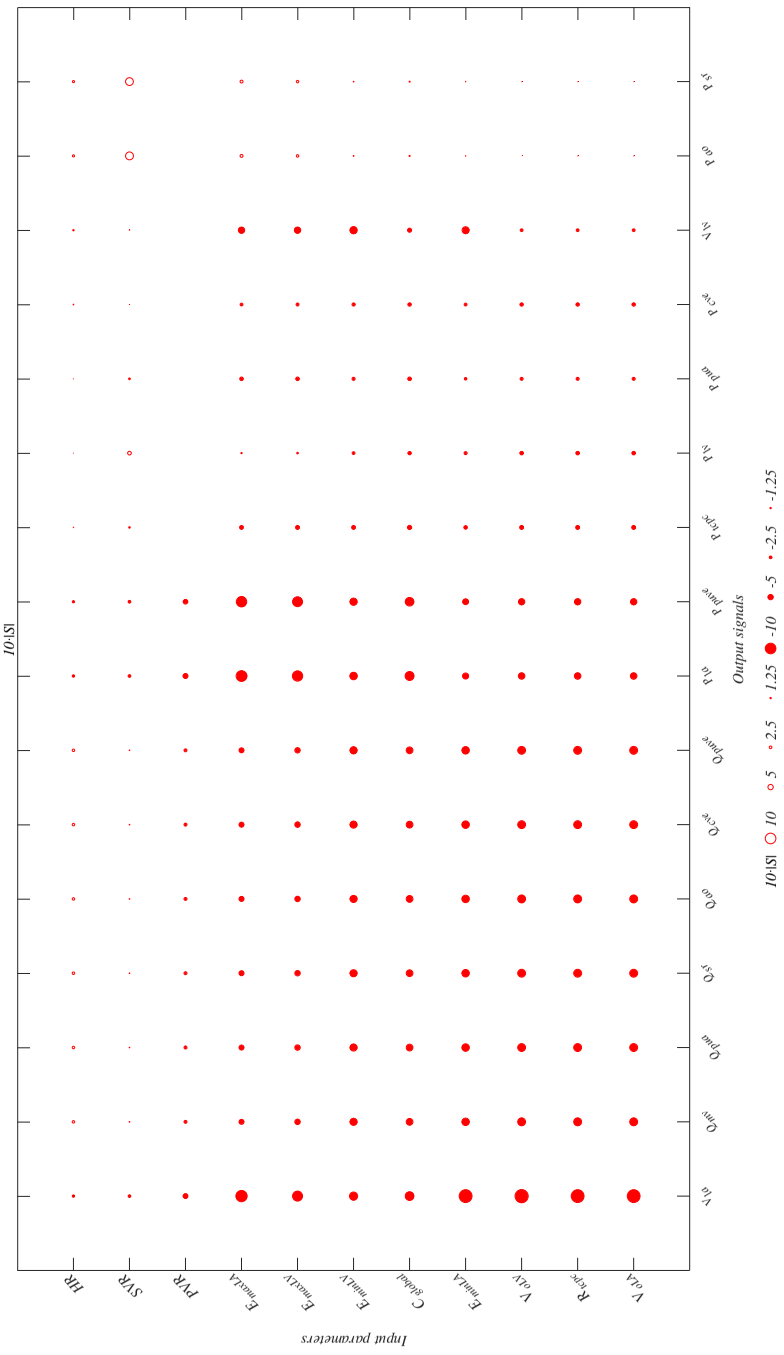

Figure 3.13: *Graphical representation of the sensitivity of the outputs to the 25% variation of the inputs for the Fontan model. A larger symbol corresponds with higher sensitivity and filled/empty circles correspond to negative/positive S. Outputs are ordered according to the overall sensitivity (the most sensitive on the left) and inputs are ordered based on the global influence (the most influential at the bottom).*

Table 3.7: *Mean sensitivities (S) of output signals to the input parameters for the biventricular model. The inputs are ordered based on the global influence (the most influential on the left), the outputs are ordered based on the overall sensitivity (the most sensitive at the top).*

	$\mathbf{E}_{max_{RA}}$	$\mathbf{E}_{max_{LA}}$	$\mathbf{E}_{max_{RV}}$	$\mathbf{E}_{min_{RA}}$	$\mathbf{V}_{p=0_{LV}}$	$\mathbf{V}_{p=0_{RV}}$	$\mathbf{V}_{p=0_{LA}}$	$\mathbf{V}_{p=0_{RA}}$	$\mathbf{E}_{min_{LA}}$	$\mathbf{E}_{min_{RV}}$	$\mathbf{E}_{min_{LV}}$	$\mathbf{E}_{max_{LV}}$	$\mathbf{C}_{global}$	**HR**	**SVR**	**PVR**
Pao	1.191	1.096	1.039	0.770	0.757	0.704	0.700	0.690	0.796	0.794	0.913	0.933	0.757	0.368	0.970	0.877
Psr	1.187	1.092	1.035	0.768	0.755	0.702	0.698	0.688	0.793	0.791	0.909	0.930	0.754	0.367	0.967	0.874
Vla	-0.551	-0.616	-0.479	-0.790	-0.798	-0.832	-0.803	-0.809	-0.766	-0.266	-0.167	-0.558	-0.419	-0.140	-0.203	-0.293
Vlv	-0.413	-0.473	-0.475	-0.608	-0.503	-0.535	-0.538	-0.544	-0.588	-0.643	-0.566	-0.543	-0.201	-0.100	0.015	-0.063
Vra	-0.638	-0.379	-0.407	-0.789	-0.797	-0.830	-0.832	-0.767	-0.464	-0.484	-0.747	-0.306	-0.395	-0.058	-0.325	-0.307
Vrv	-0.492	-0.482	-0.492	-0.496	-0.502	-0.162	-0.164	-0.168	-0.550	-0.576	-0.506	-0.239	-0.270	-0.135	-0.284	-0.204
Plv	0.628	0.541	0.494	0.317	0.305	0.257	0.253	0.245	0.343	0.333	0.444	0.398	0.208	0.149	0.487	0.401
Pra	-0.543	-0.403	-0.433	-0.060	-0.071	-0.115	-0.118	-0.126	-0.335	-0.358	-0.665	-0.322	-0.416	-0.056	-0.342	-0.322
Ppua	0.213	0.129	0.138	0.308	0.296	0.248	0.245	0.236	0.343	0.233	0.353	0.043	0.060	0.067	-0.113	0.187
Pla	-0.475	-0.544	-0.491	-0.017	-0.028	-0.072	-0.076	-0.084	0.013	-0.167	-0.061	-0.573	-0.428	-0.141	-0.206	-0.297
Pcve	0.129	0.177	0.136	0.261	0.250	0.202	0.199	0.190	0.103	0.088	-0.054	0.164	0.038	0.108	0.166	0.142
Qpua	0.224	0.139	0.091	-0.150	-0.161	-0.203	-0.207	-0.214	-0.117	-0.117	-0.004	-0.002	-0.147	0.389	0.031	-0.050
Qtv	0.223	0.139	0.091	-0.149	-0.160	-0.203	-0.206	-0.214	-0.119	-0.119	-0.006	-0.003	-0.147	0.389	0.030	-0.050
Qao	0.225	0.139	0.092	-0.149	-0.160	-0.203	-0.206	-0.213	-0.116	-0.117	-0.004	-0.002	-0.146	0.390	0.031	-0.049
Qcve	0.225	0.139	0.092	-0.149	-0.160	-0.203	-0.206	-0.214	-0.115	-0.116	-0.004	-0.002	-0.146	0.390	0.030	-0.049
Qpv	0.224	0.139	0.092	-0.150	-0.160	-0.203	-0.207	-0.214	-0.117	-0.117	-0.004	-0.002	-0.146	0.390	0.031	-0.049
Qsr	0.224	0.139	0.092	-0.150	-0.160	-0.203	-0.206	-0.214	-0.117	-0.117	-0.004	-0.002	-0.146	0.390	0.030	-0.049
Qmv	0.224	0.138	0.091	-0.149	-0.160	-0.202	-0.206	-0.213	-0.116	-0.117	-0.004	-0.002	-0.146	0.389	0.030	-0.050
Qpuve	0.224	0.139	0.093	-0.149	-0.159	-0.202	-0.206	-0.213	-0.116	-0.117	-0.004	-0.001	-0.145	0.390	0.031	-0.048
Ppuve	-0.442	-0.512	-0.460	-0.001	-0.012	-0.057	-0.060	-0.068	0.029	-0.148	-0.041	-0.543	-0.404	-0.131	-0.202	-0.274
Prv	-0.071	-0.127	-0.134	0.087	0.075	0.030	0.026	0.018	0.080	0.009	-0.023	-0.193	-0.214	-0.083	-0.295	-0.101

Pao, aortic pressure, Psr, systemic vascular bed pressure, Vla, LA volume, Vlv, LV volume, Vra, RA volume, Vrv, RV volume, Plv, LV pressure, Pra, RA pressure, Ppua, pulmonary arterial pressure, Pla, LA pressure, Pcve, caval vein pressure, Qpua, pulmonary arterial flow, Qtv, tricuspid valve flow, Qao, aortic valve pressure, Qcve, caval vein flow, Qpv, pulmonary valve flow, Qsr, systemic vascular bed flow, Qmv, mitral valve flow, Qpuve, pulmonary venous flow, Ppuve, pulmonary venous pressure, Prv, RV pressure.

Table 3.8: *Mean sensitivities (S) of output signals to the input parameters for the Fontan model. The inputs are ordered based on the global influence (the most influential on the left), the outputs are ordered based on the overall sensitivity (the most sensitive at the top).*

	$\mathbf{V}_{p=0_{LA}}$	**Rtcpc**	$\mathbf{V}_{p=0_{LV}}$	$\mathbf{E}_{min_{LA}}$	$\mathbf{C}_{global}$	$\mathbf{E}_{min_{LV}}$	$\mathbf{E}_{max_{LV}}$	$\mathbf{E}_{max_{LA}}$	**PVR**	**SVR**	**HR**
Vla	-1.206	-1.206	-1.240	-1.208	-0.814	-0.772	-0.937	-1.057	-0.457	-0.253	-0.217
Qmv	-0.743	-0.743	-0.741	-0.702	-0.637	-0.671	-0.511	-0.472	-0.280	-0.060	0.234
Qpua	-0.744	-0.744	-0.741	-0.702	-0.637	-0.671	-0.511	-0.471	-0.279	-0.059	0.235
Qsr	-0.744	-0.744	-0.742	-0.702	-0.637	-0.671	-0.511	-0.471	-0.279	-0.059	0.234
Qao	-0.744	-0.744	-0.741	-0.702	-0.636	-0.671	-0.511	-0.471	-0.279	-0.059	0.234
Qcve	-0.744	-0.744	-0.741	-0.702	-0.636	-0.671	-0.511	-0.471	-0.279	-0.059	0.235
Qpuve	-0.743	-0.743	-0.740	-0.701	-0.635	-0.670	-0.510	-0.471	-0.278	-0.058	0.235
Pla	-0.611	-0.611	-0.609	-0.568	-0.839	-0.704	-0.969	-1.014	-0.469	-0.258	-0.222
Ppuve	-0.593	-0.593	-0.590	-0.549	-0.811	-0.681	-0.933	-0.976	-0.439	-0.253	-0.210
Ptcpc	-0.373	-0.373	-0.370	-0.327	-0.398	-0.363	-0.368	-0.360	0.000	-0.143	0.041
Plv	-0.334	-0.334	-0.332	-0.288	-0.313	-0.268	-0.153	-0.115	0.151	0.349	0.017
Ppua	-0.286	-0.286	-0.283	-0.238	-0.341	-0.291	-0.334	-0.334	0.066	-0.163	-0.004
Pcve	-0.317	-0.317	-0.314	-0.270	-0.321	-0.297	-0.276	-0.263	0.083	-0.008	0.066
Vlv	-0.267	-0.267	-0.265	-0.663	-0.387	-0.681	-0.598	-0.596	-0.149	-0.035	-0.125
Pao	-0.006	-0.006	-0.003	0.045	0.101	0.071	0.236	0.278	0.539	0.742	0.201
Psr	-0.009	-0.009	-0.006	0.042	0.096	0.067	0.230	0.273	0.534	0.735	0.200

Vla, LA volume, Qmv, mitral valve flow, Qpua, pulmonary arterial flow, Qsr, systemic vascular bed flow, Qao, aortic valve pressure, Qcve, caval vein flow, Qpuve, pulmonary venous flow, Pla, LA pressure, Ppuve, pulmonary venous pressure, Ptcpc, TCPC pressure, Plv, LV volume, Ppua, pulmonary arterial pressure, Pcve, caval vein pressure, Vlv, LV volume, Pao, aortic pressure, Psr, systemic vascular bed pressure.

For the Fontan circulation, the resistance of the TCPC is found to be one of the most influential parameter. This is a known drawback of the univentricular circulation that depends on the reconstructed total cavo-pulmonary connection. Indeed, it is known that even mild increment in PVR increases the risk of Fontan failure [9]. Moreover, the results show that higher PVR causes lower flows, and thus lower body perfusion. Also the ventricular volume-related parameters ($V_{p=0}$) are influential parameters, however, these are mathematical parameters that relate to the size of the heart chambers. Thus, it is reasonable that changes in heart dimensions affect the overall hemodynamics. Moreover, once identified the value that matches simulated and real hemodynamics, $V_{p=0}$ is kept constant during the simulations and thus does not affect the outcomes. The most sensitive outputs are those related to LA that may be affected by the TCPC; whereas the least sensitive outputs are those of the systemic arterial side. This is likely to be related to the separation from TCPC by the presence of the systemic heart. Again, a cluster on the left is visible in the figure.

3.5 Discussion

In the first section (Section 3.2), 0D numerical models of the biventricular and Fontan circulations are developed, analyzing several ventricular pressure conditions and highlighting the fundamental physiological elements at the basis of venous hypertension. Particularly, *i)* a reduced pressure condition (both in systole and diastole), *ii)* an increased pumping action, i.e., increased systolic FV pressure, and *iii)* an increased suction action, i.e., reduced diastolic FV pressure, are simulated starting from the baseline simulation. The analysis of several pressure conditions allows to highlight and understand the intrinsic limitations of the Fontan circulation. Indeed, low cardiac output and TCPC hypertension are shown to be related to the physical working condition of the single ventricle, e.g., the amount of PVR that the ventricle has to face [9]. The outputs of the simulations confirm the hypothesis that it is the downstream pressure, i.e., the diastolic ventricular pressure, the intrinsic limit of the Fontan circulation that causes the typical hypertension measured in these patients. Moreover, it is shown that the possibility lowering the pressure in the single atrium helps to reduce the TCPC pressure and, at the same time, increases cardiac output. The diastolic function (ventricular suction) as the limitation of the Fontan circulation has already been hypothesized by clinicians [10] but never demonstrated before by numerical models, thus, with the results reported in this Chapter, a mathematical confirmation of the clinical hypothesis is provided. Table 3.9 summarizes the

outputs of the simulations.

Table 3.9: *Summary of the outputs of the simulation.*

	P_{tcpc}	CO
Biventricular with physiological ventricular pressure	physio	physio
Fontan with physiological ventricular pressure	hyper	hypo
Fontan with reduced ventricular pressure	physio	hypo
Fontan with increased pumping action	hyper	physio
Fontan with increased suction action	physio	physio

'physio', 'hyper', and 'hypo' stand for physiological, higher than normal, and lowen than normal, respectively.

Some other published works analyze the Fontan circulation by means of 0D models. However, the focus of these works has been posed on the Fontan exercise capacity [36] and the analysis of the dependence of fluid dynamic variables on the respiration [37], on the effects of modifications of the Fontan circuit by fenestration or hepatic vein exclusion [38], and on the impact of assist devices [24, 25]. Only Liang et al. in [39] tried to understand the effects of the cardiovascular properties on clinically relevant hemodynamic variables, showing a greater variability in Fontan than in healthy patients of venous pressure due to the absence of the pulmonary heart. They also identified the ventricular diastolic function but as a CO determinant rather than the leading cause of TCPC hypertension. This result hence represents a novel element that not only helps in clarifying the hemodynamic cascade at the basis of the Fontan circulation failure but also suggests that there is the need to think on new possibilities in designing surgical or technical solutions able to mitigate the early and long term complications of Fontan circulation. Indeed, up to now, the focus has been put on the pumping action of possible assist devices. However, the results show that the Fontan limitation is the diastolic and not the systolic function. Moreover pumps have been shown to have several drawbacks, and, as Shimizu et al. pointed out in [24], a partial cavopulmonary assist device could help in increasing the cardiac output but at the same time it increases SVC pressure limiting its applicability.

Moreover, despite the large number of studies in the literature that consider the Fontan circulation, there are no studies that derived and compared age-specific circulations in both the healthy and Fontan conditions. Only recently (in 2019) Zhang et al. [40] published a work aimed at simulating the hemodynamics in children and in adults. However, their work compared the adult and the pediatric case for the biventricular circulation only. Also, and maybe even more importantly, in their work the Fontan pediatric case

is derived by the healthy biventricular model without changing the parameters: to us, using the same parameters for both the biventricular and Fontan circulation is an important limitation because it is well known, for example, that PVR is higher in Fontan patients and that the cardiac mechanics differ in healthy and univentricular population. So, to the best of our knowledge, the work presented in Section 3.3, has the novelty of deriving and comparing adult and pediatric circulations both in the healthy and Fontan circulation. Moreover, the Fontan models (both adult and pediatric) are derived considering both the particular cardiovascular structure of the reconstructed circulation and *age-specific* Fontan parameters. The calibration methodology described in the Subsection 2.7.1 together with the use of age-, BSA-, and circulation-specific parameters, such as SVR and PVR, guarantees the ability to represent the specific hemodynamics. Indeed, the good agreement between the models' outputs and *in vivo* data for both the overall hemodynamic variables, e.g., EF, CO, SBP, and the waveforms confirms the robustness of the models. And this holds for both the pressures and the flows. Of course, the use of clinical data able to reproduce in detail every considered hemodynamics requires the development of a critical analysis of a very large amount of published literature but, in our opinion, such a step is unavoidable to obtain useful and reliable results.

The effect of PVR on the circulation is also analyzed. The simulations show that the increase of PVR causes a reduction in CO in both the healthy and Fontan circulations, however, the change is bigger for the Fontan model that shows an increased sensitivity to PVR. Indeed, in the clinical literature, it is well known that the outcomes of the Fontan circulation are PVR-dependent [10, 12]. On the other hand, the high sensitivity of the pediatric biventricular model suggests that also in a healthy child of 10 y.o. the PVR value is fundamental to reproduce physiological hemodynamics. Indeed, it is known that in pediatric ages, PVR has a high variability, PVR $\gtrsim$ 2.4 mmHg·s/mL for newborns until PVR $\sim$ 0.09 mmHg·s/mL for adolescents [13], with value that further reduces until reaching PVR $\sim$ 0.06 mmHg·s/mL for adults [15]. On the other hand, the model captures this high sensitivity for the pediatric age. Thus, it is fundamental a fine-tuning for the PVR value to assure the correspondence between the model's outputs and the real case simulated. This sensitivity is almost canceled for the adult biventricular case, as expected. Instead, in Fontan patients, also in the adult case CO is primarily controlled by PVR, i.e., the resistance of the neoportal system[4] surgically constructed [10]. These results show once again the ability

[4]In the Fontan circulation a portal system is surgically constructed. Indeed, as defined

of the model to capture the control mechanisms of hemodynamics in the different cases considered, both pediatric and adult, and both biventricular and univentricular. The Fontan model is more sensitive to PVR than the biventricular one also in terms of CVP. Indeed, the caval vein pressure of the biventricular model (both adult and pediatric) is not affected by a change of PVR and this is because, in the physiological circulation, the caval veins are completely separated from the pulmonary circulation. On the other hand, an increase of PVR in the Fontan circulation causes an increase in CVP, and this is a well-known morbidity that may affect Fontan patients in the mid-long term follow-up [41]. Moreover, the pediatric Fontan case is more influenced than the adult one by PVR changes. Results suggest that in Fontan patients, the sensitivity to PVR changes decreases with age when considering CVP, whereas remains almost constant in terms of CO. These results seem to deserve further attention. Thus, with these models, the hemodynamic cascade that causes the morbidities typical of Fontan failure has been numerically confirmed. This cause-effect link is very important because several studies reported the Fontan morbidities (e.g., high CVP) as the hemodynamic alterations that cause Fontan failure [9]. However, the outputs showed that high PVR causes low CO and high CVP, i.e., the intrinsic characteristic (high PVR) of the reconstructed circulation may lead to morbidities. The dependency on PVR has been already hypothesized by Egbe et al. [9] by analyzing *in vivo* data, and, with the Fontan model, a further mathematical confirmation that even a mild PVR increment leads to low CO and high CVP has been provided.

3.6 Conclusion

In this Chapter the physiological limitations of the Fontan circulation are analyzed. The use of pressure levels enables a clear and immediate perspective on the effect of any specific functional compartment on the pressure behavior. Steady flow simulations revealed that, in *the absence of the pulmonary heart* pumping action, a physiological pressure can be maintained in TCPC only for unattainable low pressure in the systemic heart. Pulsatile flow simulation confirmed that result. It shows that the leading factor of abnormally high pressures in TCPC is the limited capability of the single ventricle to express a sufficiently strong suction effect. This finding might open new pos-

in Chapter 1, the portal system is a unique system in which a capillary bed drains directly into another capillary bed through veins. This happens in the Fontan circulation in which the sytemic bed pools blood into the pulmonary bed without receiving energy from a pump.

sibilities in designing surgical or technical solutions able to mitigate the early and long term complications of the Fontan circulation. Moreover, specific age-dependent models are developed, for both the biventricular and Fontan circulations. The adult and pediatric hemodynamics are compared, and the specific hemodynamics is represented for each configuration. The derivation of Fontan age-specific model is a novelty in the engineering background, where, usually, biventricular model parameters are employed. Thus, usually, the differences between the Fontan and biventricular models lie in the TCPC district in place of the pulmonary heart. Also, the typical lower CO of the pediatric and Fontan cases is simulated, and the more sensitivity of the Fontan circulation to PVR is shown. Thus, on one hand, the consideration of parameters specific for each condition allows to represent the characteristic features of all cases. On the other hand, the analysis of the influence of PVR on the circulations highlights the hemodynamic cascade at the basis of the Fontan circulation morbidities.

Bibliography

[1] G. Comunale, M. Padalino, G. Stellin, G. Burriesci, P. Peruzzo, and F. M. Susin, "Physiology of single ventricle circulation: basic hydraulics explains basic complications," in *Proceedings of the 7th International Conference on Computational Bioengineering*, 7th International Conference on Computational Bioengineering, 2017.

[2] G. Comunale, M. Padalino, G. Stellin, P. Peruzzo, and F. M. Susin, "Modellazione della circolazione di fontan: confronto tra il caso adulto e il paziente pediatrico," in *Atti del XXXVI Convegno Nazionale di Idraulica e Costruzioni Idrauliche*, 2018.

[3] J. Butterworth, D. Mackey, and J. Wasnick, "Anesthesia for patients with cardiovascular disease," *Dalam: Morgan & Mikhail's Clinical Anesthesia, penyunting. Edisi ke-4. New York: Mc GrawHill*, pp. 463–478, 2006.

[4] J. P. van der Ven, E. van den Bosch, A. J. Bogers, and W. A. Helbing, "State of the art of the fontan strategy for treatment of univentricular heart disease," *F1000Research*, vol. 7, 2018.

[5] M. Gewillig and D. J. Goldberg, "Failure of the fontan circulation," *Heart failure clinics*, vol. 10, no. 1, pp. 105–116, 2014.

[6] A. Jalali, G. F. Jones, D. J. Licht, and C. Nataraj, "Application of mathematical modeling for simulation and analysis of hypoplastic left heart syndrome (hlhs) in pre-and postsurgery conditions," *BioMed research international*, vol. 2015, 2015.

[7] D. A. de Zélicourt, A. Marsden, M. A. Fogel, and A. P. Yoganathan, "Imaging and patient-specific simulations for the fontan surgery: current methodologies and clinical applications," *Progress in pediatric cardiology*, vol. 30, no. 1-2, pp. 31–44, 2010.

[8] C. L. Hebson, N. M. McCabe, R. W. Elder, W. T. Mahle, M. McConnell, B. E. Kogon, E. Veledar, M. Jokhadar, R. N. Vincent, A. Sahu, *et al.*, "Hemodynamic phenotype of the failing fontan in an adult population," *The American journal of cardiology*, vol. 112, no. 12, pp. 1943–1947, 2013.

[9] A. C. Egbe, H. M. Connolly, W. R. Miranda, N. M. Ammash, D. J. Hagler, G. R. Veldtman, and B. A. Borlaug, "Hemodynamics of fontan failure: the role of pulmonary vascular disease," *Circulation: Heart Failure*, vol. 10, no. 12, p. e004515, 2017.

[10] M. Gewillig and S. C. Brown, "The fontan circulation after 45 years: update in physiology," *Heart*, vol. 102, no. 14, pp. 1081–1086, 2016.

[11] C. de Lange, "Imaging of complications following fontan circulation in children—diagnosis and surveillance," *Pediatric Radiology*, 2020.

[12] G. R. Veldtman, A. R. Opotowsky, S. G. Wittekind, J. Rychik, D. J. Penny, M. Fogel, B. S. Marino, and M. Gewillig, "Cardiovascular adaptation to the f ontan circulation," *Congenital heart disease*, vol. 12, no. 6, pp. 699–710, 2017.

[13] B. Boville and L. C. Young, "Quick guide to pediatric cardiopulmonary care," 2015.

[14] H. Saiki, B. W. Eidem, T. Ohtani, M. A. Grogan, and M. M. Redfield, "Ventricular-arterial function and coupling in the adult fontan circulation," *Journal of the American Heart Association*, vol. 5, no. 9, p. e003887, 2016.

[15] J. P. Mynard and J. J. Smolich, "One-dimensional haemodynamic modeling and wave dynamics in the entire adult circulation," *Annals of biomedical engineering*, vol. 43, no. 6, pp. 1443–1460, 2015.

[16] K. Pekkan, D. Frakes, D. De Zelicourt, C. W. Lucas, W. J. Parks, and A. P. Yoganathan, "Coupling pediatric ventricle assist devices to the fontan circulation: simulations with a lumped-parameter model," *ASAIO journal*, vol. 51, no. 5, pp. 618–628, 2005.

[17] A. Agarwal, C. Cunnington, A. Sabanayagam, L. Zier, C. E. McCulloch, I. S. Harris, E. Foster, D. Atkinson, A. Bryan, P. Jenkins, *et al.*, "Cardiopulmonary exercise testing in the evaluation of liver disease in adults who have had the fontan operation," *Archives of cardiovascular diseases*, vol. 111, no. 4, pp. 276–284, 2018.

[18] W. Milnor, "Hemodynamic 2nd edn (baltimore, md: William and wilkins)," 1989.

[19] A. M. Maceira, S. K. Prasad, M. Khan, and D. J. Pennell, "Reference right ventricular systolic and diastolic function normalized to age, gender and body surface area from steady-state free precession cardiovascular magnetic resonance," *European heart journal*, vol. 27, no. 23, pp. 2879–2888, 2006.

[20] L. E. Hudsmith, S. E. Petersen, J. M. Francis, M. D. Robson, and S. Neubauer, "Normal human left and right ventricular and left atrial dimensions using steady state free precession magnetic resonance imaging," *Journal of cardiovascular magnetic resonance*, vol. 7, no. 5, pp. 775–782, 2005.

[21] B. Sievers, M. Addo, F. Breuckmann, J. Barkhausen, and R. Erbel, "Reference right atrial function determined by steady-state free precession cardiovascular magnetic resonance," *Journal of Cardiovascular Magnetic Resonance*, vol. 9, no. 5, pp. 807–814, 2007.

[22] P. Argiento, R. R. Vanderpool, M. Mulè, M. G. Russo, M. D'Alto, E. Bossone, N. C. Chesler, and R. Naeije, "Exercise stress echocardiography of the pulmonary circulation: limits of normal and sex differences," *Chest*, vol. 142, no. 5, pp. 1158–1165, 2012.

[23] K. Pekkan, I. B. Aka, E. Tutsak, E. Ermek, H. Balim, I. Lazoglu, and R. Turkoz, "In vitro validation of a self-driving aortic-turbine venous-assist device for fontan patients," *The Journal of thoracic and cardiovascular surgery*, vol. 156, no. 1, pp. 292–301, 2018.

[24] S. Shimizu, T. Kawada, D. Une, M. Fukumitsu, M. J. Turner, A. Kamiya, T. Shishido, and M. Sugimachi, "Partial cavopulmonary

assist from the inferior vena cava to the pulmonary artery improves hemodynamics in failing fontan circulation: a theoretical analysis," *The Journal of Physiological Sciences*, vol. 66, no. 3, pp. 249–255, 2016.

[25] G. A. Giridharan, M. Ising, M. A. Sobieski, S. C. Koenig, J. Chen, S. Frankel, and M. D. Rodefeld, "Cavopulmonary assist for the failing fontan circulation: impact of ventricular function on mechanical support strategy," *ASAIO journal (American Society for Artificial Internal Organs: 1992)*, vol. 60, no. 6, p. 707, 2014.

[26] H. Ohuchi, K. Yasuda, A. Miyazaki, T. Iwasa, H. Sakaguchi, O. Shin, M. Mizuno, J. Negishi, K. Noritake, and O. Yamada, "Comparison of prognostic variables in children and adults with fontan circulation," *International journal of cardiology*, vol. 173, no. 2, pp. 277–283, 2014.

[27] G. N. Cattermole, P. M. Leung, P. S. Mak, S. S. Chan, C. A. Graham, and T. H. Rainer, "The normal ranges of cardiovascular parameters in children measured using the ultrasonic cardiac output monitor," *Critical care medicine*, vol. 38, no. 9, pp. 1875–1881, 2010.

[28] L. Krovetz, T. McLoughlin, M. Mitchell, and G. Schiebler, "Hemodynamic findings in normal children," *Pediatric research*, vol. 1, no. 2, pp. 122–130, 1967.

[29] H. Ohuchi, A. Miyazaki, Y. Wakisaka, K.-i. Watanabe, K. Kishiki, O. Yamada, T. Yagihara, and S. Echigo, "Systemic ventricular morphology-associated increased qrs duration compromises the ventricular mechano-electrical and energetic properties long-term after the fontan operation," *International journal of cardiology*, vol. 133, no. 3, pp. 371–380, 2009.

[30] H. Ohuchi, A. Miyazaki, J. Negishi, Y. Hayama, M. Nakai, K. Nishimura, H. Ichikawa, I. Shiraishi, and O. Yamada, "Hemodynamic determinants of mortality after fontan operation," *American heart journal*, vol. 189, pp. 9–18, 2017.

[31] C. Lorenz, "The range of normal values of cardiovascular structures in infants, children, and adolescents measured by magnetic resonance imaging," *Pediatric cardiology*, vol. 21, no. 1, pp. 37–46, 2000.

[32] K. Linden, F. Goldschmidt, K. T. Laser, C. Winkler, H. Körperich, R. Dalla-Pozza, J. Breuer, and U. Herberg, "Left atrial volumes and phasic function in healthy children: Reference values using real-time

three-dimensional echocardiography," *Journal of the American Society of Echocardiography*, vol. 32, no. 8, pp. 1036–1045, 2019.

[33] N. Kawel-Boehm, A. Maceira, E. R. Valsangiacomo-Buechel, J. Vogel-Claussen, E. B. Turkbey, R. Williams, S. Plein, M. Tee, J. Eng, and D. A. Bluemke, "Normal values for cardiovascular magnetic resonance in adults and children," *Journal of Cardiovascular Magnetic Resonance*, vol. 17, no. 1, p. 29, 2015.

[34] T. Poutanen, E. Jokinen, H. Sairanen, and T. Tikanoja, "Left atrial and left ventricular function in healthy children and young adults assessed by three dimensional echocardiography," *Heart*, vol. 89, no. 5, pp. 544–549, 2003.

[35] H.-Y. Qi, R.-Y. Ma, L.-X. Jiang, S.-P. Li, S. Mai, H. Chen, M. Ge, M.-Y. Wang, H.-N. Liu, Y.-H. Cai, *et al.*, "Anatomical and hemodynamic evaluations of the heart and pulmonary arterial pressure in healthy children residing at high altitude in china," *IJC Heart & Vasculature*, vol. 7, pp. 158–164, 2015.

[36] E. Kung, G. Pennati, F. Migliavacca, T.-Y. Hsia, R. Figliola, A. Marsden, and A. Giardini, "A simulation protocol for exercise physiology in fontan patients using a closed loop lumped-parameter model," *Journal of biomechanical engineering*, vol. 136, no. 8, 2014.

[37] A. Baretta, C. Corsini, A. L. Marsden, I. E. Vignon-Clementel, T.-Y. Hsia, G. Dubini, F. Migliavacca, G. Pennati, and T. M. O. C. H. Alliance, "Respiratory effects on hemodynamics in patient-specific cfd models of the fontan circulation under exercise conditions," *European Journal of Mechanics-B/Fluids*, vol. 35, pp. 61–69, 2012.

[38] C. Puelz, S. Acosta, B. Rivière, D. J. Penny, K. M. Brady, and C. G. Rusin, "A computational study of the fontan circulation with fenestration or hepatic vein exclusion," *Computers in biology and medicine*, vol. 89, pp. 405–418, 2017.

[39] F. Liang, H. Senzaki, C. Kurishima, K. Sughimoto, R. Inuzuka, and H. Liu, "Hemodynamic performance of the fontan circulation compared with a normal biventricular circulation: a computational model study," *American Journal of Physiology-Heart and Circulatory Physiology*, vol. 307, no. 7, pp. H1056–H1072, 2014.

[40] X. Zhang, H. Haneishi, and H. Liu, "Multiscale modeling of the cardiovascular system for infants, children, and adolescents: Age-related

alterations in cardiovascular parameters and hemodynamics," *Computers in biology and medicine*, vol. 108, pp. 200–212, 2019.

[41] M. Gewillig, "The fontan circulation," *Heart*, vol. 91, no. 6, pp. 839–846, 2005.

4 | II Application: Right Ventricular Dysfunction

Contents

Right ventricular (RV) dysfunction has long been neglected compared to the left ventricular dysfunction and specific studies are still lacking. There is an increasing need to focus on RV to get an insight into its hemodynamic features. A deep knowledge of RV dysfunction will improve its recognition and treatment, simplifying the clinical management. For this reason, in this chapter, the work aims at evaluating for the first time the effect of isolated RV dysfunction by numerical modeling.
Lumped-parameter modeling is applied to represent the physio-pathological hemodynamics. Different grades of impairment are simulated considering three forms of dysfunction: systolic, diastolic, and combined systolic and diastolic. In each scenario, the ventricular function is set up to simulate the mechanical myocardial pathological variations.

Hemodynamic alterations arising from the three forms of RV dysfunction are calculated and compared. It is shown that results accord with clinical observations, and RV dysfunction affects both the systemic and pulmonary hemodynamics. Validation with *in vivo* data is carried out, showing the clinical potentiality of the model, such as the capability of identifying the degree of RV impairment.
This study is an important step towards improving the understanding, recognition, and management of RV dysfunction.

This work may be considered a corollary of the study of the Fontan circulation (Chapter 3) in that total cavopulmonary connection in the Fontan is functionally equivalent to a right ventricle that is completely impaired. Thus, the Fontan circulation can be considered as an extreme case of RV dysfunction. From this consideration, also the complete (or almost complete) dysfunction is compared with the Fontan circulation.

Preliminary results of this work have been presented at the Fifth IAHR Europe Congress [1], and a further extension is here reported.

4.1 Introduction

Left ventricular systolic and diastolic dysfunctions have been studied extensively and are described as main causes of heart failure (HF) [2, 3, 4], whereas less attention has been paid to systolic and diastolic dysfunction of the right ventricle (RV). In the literature, RV has been largely underestimated compared to the left ventricle (LV) and, in the past, it was wrongly believed that RV could not affect cardiac output (CO) and systemic pressures [5, 6, 7]. The importance of RV has been recognized, and its role in cardiac hemodynamics has been highlighted [8, 9]. The circulatory system is a closed-loop where the function of both ventricles is crucial. Therefore, not infrequently, impairment of one of the two ventricles precipitates impairment of the other [10]. Although LV impairment is most common, a recent study reported that RV myocardial infarction is not an infrequent problem, estimated to occur in around 20-50% of patients with inferior myocardial infarction [11]. Unfortunately, there is limited information that allow us to easily distinguish RV from LV dysfunctions, despite it is evident that early diagnosis of RV myocardial infarction reduces the risks of death, cardiogenic shock, ventricular tachycardia and fibrillation, and atrioventricular block [11].

In the present study, a lumped-parameter model of the complete cir-

culation is implemented to analyze for the first time the consequences of isolated RV dysfunction on global cardiovascular circulation. The study of the functional properties of RV by highlighting the effects of its dysfunction can improve the understanding of this forgotten ventricle [8] allowing in the future an easier clinical management of ventricular dysfunction. To do so, this Chapter is structured as follows. In Section 2 the numerical model is introduced and simulation are performed to analyze the different types of right ventricular dysfunctions. In Section 3 the results of the numerical simulations are reported. First, the analysis focuses on flow and pressure waveforms in particular districts of the cardiovascular system, as well as on some global indexes related to the performance of the ventricles. Second, the model is setup in order to compare the outputs with the clinical results of patients affected by right ventricular dysfunctions. Finally, the comparison between the RV dysfunction and the Fontan circulation is also performed. In Section 4 the model sensitivity analysis is reported, and in Section 5 some comments to the results are drawn, and the limitations of the model are considered. Finally, conclusions on the present problem are reported in Section 6.

4.2 Methods

In order to carry out an extensive analysis of different degrees of right ventricular dysfunction, a lumped-parameter (0D) model able to represent the entire cardiovascular system is developed. This choice represents the best cost/benefit option because 0D models provide reliable results in terms of pressure and flow waves with low computational cost [12, 13, 14, 15].

4.2.1 Hemodynamic model

The circulation is simulated considering the scheme of Fig. 4.1 (used also in Ch. 3 to simulate the biventricular circulation). It comprises the systemic and pulmonary circulations, the four heart chambers, and valves. To simulate the conduit vascular networks, the small resistance to flow due to blood viscosity (R) and the compliance due to vessel elasticity (C) are reproduced; whereas the vascular beds are represented considering only the dissipation effects (represented by R). The heart is represented by the elastance model as described in Section 2.3, and the heart valves are represented as diodes (Subsection 2.4.1). Note that, the present model does not account for chamber interaction via septa [16, 17, 18, 19, 20].

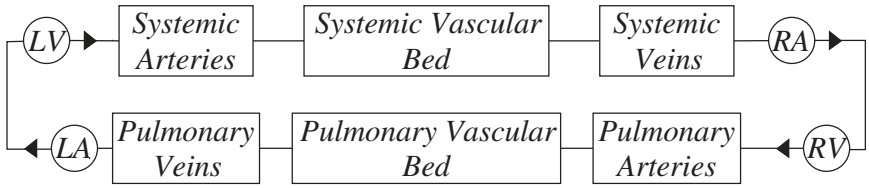

Figure 4.1: *Circulation model composed of: left ventricle (LV), systemic arteries, vascular bed, and veins, right ventricle (RV), right atrium (RA), pulmonary arteries, vascular bed, and veins, left atrium (LA) and heart valves (►).*

4.2.2 Ventricular dysfunction

The dysfunction of the ventricle is due to pathologies that can affect both the contractility of the myocardial fibers and then their capability to eject blood, i.e., systolic dysfunction, and /or the ventricular passive mechanism of filling, i.e., diastolic dysfunction. According to these two types of dysfunction, the global hemodynamics is analyzed considering the following three scenarios: *i)* isolated right ventricular systolic dysfunction, *ii)* isolated right ventricular diastolic dysfunction, and *iii)* combined systolic and diastolic dysfunction.
As mentioned in Section 4.1, to date, few data are available for modeling the impairment of the right ventricle. Accordingly, in this work, the following assumptions are made:

- That RV dysfunction is caused by the same types of impairments that affect the LV, i.e., systolic dysfunction is mainly determined by a reduction in RV contractile force whereas diastolic dysfunction is mostly due to increased ventricular stiffness. Thus, the parameters of the dysfunctional right heart are determined in analogy with the LV impairment;
- secondary mechanisms due to the primary RV dysfunction, e.g., adaptation mechanism such as the variations of the systemic vascular resistance, which may alter the hemodynamics, are excluded.

For each scenario, the following steps are carried out. First, parameters reproducing the hemodynamics of a representative healthy person are determined, and second, the altered parameters in the presence of a complete (systolic and/or diastolic) dysfunctional ventricle are defined. In order to analyze the different severities of the dysfunction, all the parameters involved are then varied linearly, from the healthy to the dysfunctional condition, by introducing the percentage of impairment (p) that ranges from 0% (healthy condition) to 100% (complete dysfunctional condition).
Specific descriptions of the mechanisms of ventricle impairment and the consequences on the parameters of the model are briefly described in the next

three subsections.

Isolated systolic dysfunction

Systolic dysfunction (SD) refers to the ventricle's inability to pump the adequate amount of blood due to impaired myocardial function, increased afterload, structural abnormalities, or the combination of the previous diseases [21]. SD is reproduced through a reduction of the maximal contraction force, $E_{max_{RV}}$, together with an increase in systolic times. Indeed, it has been shown that the myocardial performance index (MPI), i.e., the ratio between the atrioventricular closure opening time (TCO) and the ejection fraction (ET), increases with systolic impairment [22, 23]. For these reasons, $E_{max_{RV}}$ is reduced to zero when ventricular contractility is fully compromised, whereas $\tau_{1_{RV}}$ and $\tau_{2_{RV}}$ are increased from 0.2152 s and 0.3616 s to 0.4304 s and 0.7232 s, respectively (see Eq. (2.7) - (2.9)).

Isolated diastolic dysfunction

Diastolic dysfunction (DD) refers to the ventricular inability to fill its cavity due to decreased distensibility, delayed relaxation, and abnormal filling. For DD, there are three patterns of impaired filling, which represent progressively worse diastolic dysfunction [21, 24]. The most life-threatening condition (grade III of diastolic dysfunction), i.e., the restrictive filling, is represented. In this stage of DD, the ventricular wall stiffness largely increases whereas the tricuspid filling deceleration time decreases [25]. These changes are obtained by increasing $E_{min_{RV}}$ from 0.035 mmHg/mL to 0.140 mmHg/mL and $m_{2_{RV}}$ from 21.9 to 87.6, similarly to other works focused on the LV dysfunction [26].

Combined diastolic and systolic dysfunction

Combined diastolic and systolic dysfunction (CD) results from the combination of SD and DD, and it is reproduced by superimposing both the previous dysfunctions. For this reason, in the model, $E_{max_{RV}}$ is reduced, $\tau_{1_{RV}}$ and $\tau_{2_{RV}}$ are increased, and $E_{min_{RV}}$ and $m_{2_{RV}}$ are increased. Note that, the main CD results are obtained by imposing the same degree of systolic and diastolic impairment. However, in clinical practice, the pathology may manifest with a predominance of systolic or diastolic dysfunction. An example is reported in Section 4.3 where the model is used to identify the rate of impairment of patients.

Complete RV dysfunction and Fontan circulation

To further understand the role of the right ventricle, the almost complete/-complete dysfunction, i.e., $p = \{90\%, 99\%, 100\%\}$, is compared with the adult Fontan circulation model of Chapter 3, Fig. 3.2b.

Time-varying elastance

The aforementioned changes relate to alterations of the right time-varying elastances. Fig. 4.2 shows the time-varying elastance for the systolic, diastolic, and combined dysfunctions, resulted from the change of the parameters of Eq. (2.7) - (2.9), as described previously. In the systolic dysfunction (Fig. 4.2a), $E_{max_{RV}}$, the maximum contraction force, decreases linearly with p increasing, from 0.45 mmHg/mL in the healthy condition to the minimum value of $E_{min_{RV}}$ for the complete impairment ($E_{min_{RV}}$= 0.035 mmHg/mL). At the same time, the ejection time increases as well as the acceleration time, resulting in a delayed of the peak as the pathology worsens. On the contrary, in the diastolic dysfunction (Fig. 4.2b), $E_{max_{RV}}$ is rather constant and the systolic phase slightly varies with p, ranging between the 37% and the 40% of the heartbeat. However, an increase of ventricular stiffness and the decrease of the deceleration times are due to larger value of $E_{min_{RV}}$ and $m_{2_{RV}}$, respectively. Finally, in the combined dysfunction (Fig. 4.2c) the combination of the previous effects is visible.

4.2.3 Parameters' Values

To properly calibrate the model, the methodology proposed in [27] is used to represent the physiological hemodynamics (described in Section 2.7). For the systemic circulation, systemic vascular resistance (SVR) is computed as $SVR = P_{perf}/CO$, where P_{perf} is perfusion pressure, i.e., the mean pressure that perfuses the systemic organs. The systemic vascular resistance has three components: arterial, venous, and vascular bed resistances. The arterial (R_{art}) and venous (R_{ven}) resistances represent the flow resistance in the large vessels, and they are $5\%SVR$ and $3\%SVR$, respectively. The larger dissipation effect is considered in the small vessels simulated by the vascular bed resistance (R_{vb}) which is $92\%SVR$. The arterial compliance is then computed as $C_{art} = \tau/R_{vb}$, with τ the time constant of the circulation (τ=0.81 s [28]), and the venous compliance as $C_{ven} = 30 \cdot C_{art}$ [29]. For the pulmonary circulation, the value of the pulmonary vascular resistance (PVR) is taken from literature [30] (PVR=0.06 mmHg· s/mL), and the same distribution of the systemic circulation is assumed among pulmonary arte-

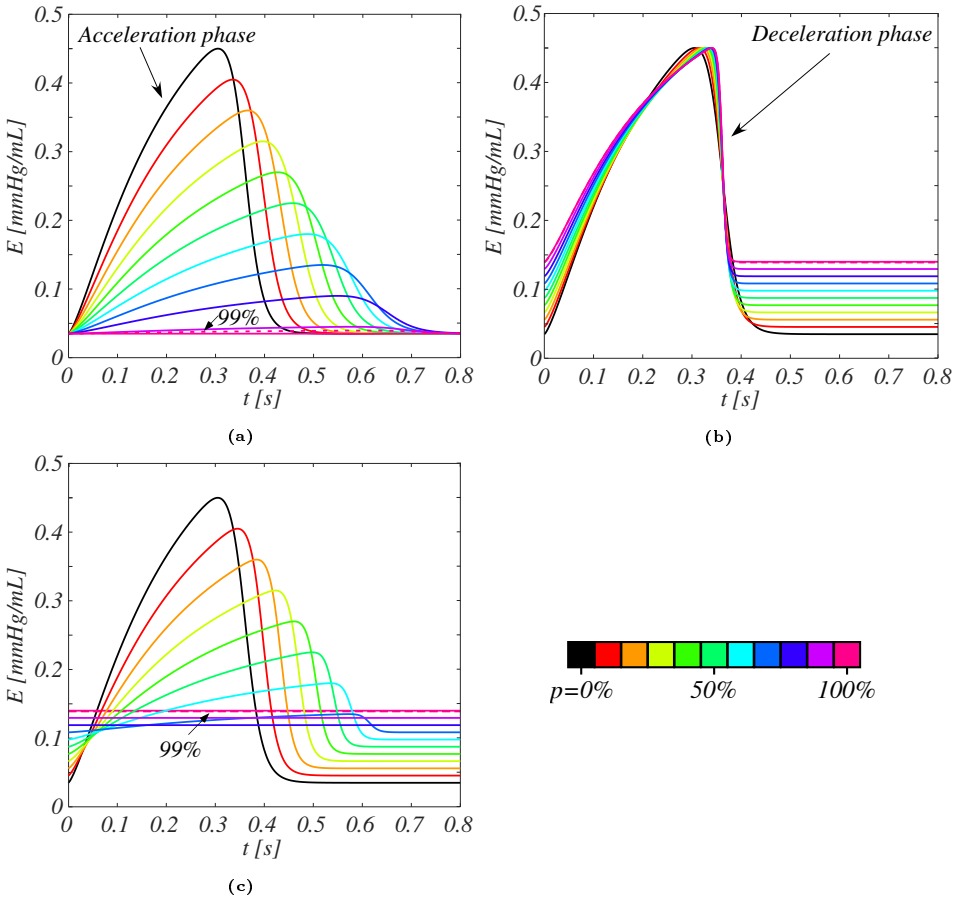

Figure 4.2: *Right ventricular activation function. (a) systolic dysfunction, (b) diastolic dysfunction, and (c) combined dysfunction. Black line: healthy RV; colored lines: RV systolic impairment from 10% to 100% degree, including 99% (dotted magenta line).*

rial, venous and vascular bed resistances, i.e., R_{art}=5%PVR, R_{ven}=3%PVR, and R_{vb}=92%PVR. Finally, the arterial and venous pulmonary compliances are taken from Tanaka et al. [31] (C_{pua}=6.7 mL/mmHg and C_{puve}=15.8 mL/mmHg). For the heart, values from Mynard et al. [32, 33] are used. Note that, for the healthy simulation, adjustment of the unstressed volume ($V_{p=0}$) of Eq. (2.6) is necessary to meet the desired hemodynamics. These values are then kept constant when considering the right ventricular dysfunction. Finally, valve parameters are set to simulate the resistance observed in the healthy condition. All the heart parameters are reported in Table 4.1. For the Fontan circulation, the same parameters as the adult case of the previous chapter (Chapter 3) are considered.

Table 4.1: *Heart parameters values.*

	LV	**RV**	**LA**	**RA**
$E_{max}[mmHg/mL]$	2.80	0.450	0.13	0.09
$E_{min}[mmHg/mL]$	0.070	0.035	0.09	0.045
$V_{p=0}[mL]$	20	30	3	7
$\tau_1[s]$	$0.269T$	$0.269T$	$0.110T$	$0.110T$
$\tau_2[s]$	$0.452T$	$0.452T$	$0.180T$	$0.180T$
$m_1[-]$	1.32	1.32	1.99	1.99
$m_2[-]$	21.9	21.9	11.2	11.2
$t_{onset}[s]$	0	0	$0.85T$	$0.85T$
$R_{valve}[mmHg \cdot s/mL]$	0.01	0.01	0.005	0.005

T is the heart period.

4.2.4 Simulations

To properly analyze the effect of RV dysfunction, the healthy condition is first considered. Particularly, the model is calibrated to meet the hemodynamics of an average person of 75 Kg and body surface area (BSA) of 1.9 m^2, having an HR of 75 bpm, a cardiac output of 6.5 L/min and a perfusion pressure of 97 mmHg [33]. Different grades of the three types of dysfunction are then considered by varying the percentage of pathology (p) from 10% to 100%, included the 99% case used in the comparison with the Fontan circulation. It is worth noting that with the percentage of 100% the ventricle loses any contractility and/or compliance property, making the right ventricle a totally passive chamber without pumping or suction function. This condition is rarely meet in clinical practice because of its extreme severity, and it is here considered to obtain a full description of the pathophysiology. Finally, the sensitivity analysis to verify the influence of parameters on the model is carried out and reported in Section 4.4.

4.2.5 Clinical validation

To validate the model with respect to a real scenario, the *in vivo* investigation of Browning et al. [34] is considered. In this study, patients are affected by pulmonary arterial hypertension (PAH) and DD i.e., they suffer from a condition that matches our definition of combined RV dysfunction since PAH is known to be associated with severe systolic dysfunction [35]. To setup the model, the degree of impairment is identified as follows. First, knowing that the systolic functionality alters ventricular performances i.e., EF [36], the systolic dysfunction required to obtain the EF_{RV} reduction reported by the authors [34] is found. Second, the degree of diastolic dysfunction is tuned

to minimize the difference between the predicted results and measured data reported in Browning et al. [34].

4.3 Results

Table 4.2 reports the comparison between the outputs of the healthy simulation and *in vivo* reference data. The model well represents the global hemodynamic variables, with values within the physiological ranges for both volumes and pressures. As shown in Fig. 4.3, the computed pressures, flows, and volumes waveforms are representative of familiar waveforms seen in these territories. The left heart is characterized by higher flow peaks than the right side, and the LV exhibits a pressure almost 6 times greater than that in the RV, both having a stroke volume of about 80 mL.

Table 4.2: *Comparison of the healthy condition hemodynamics with in vivo reference data given as a mean, with range or standard deviation in parentheses.*

Parameters	**Model**	**Reference**
CO [L/min]	6.2	6.5 (3.6-9.4)[30]
Total vascular resistance		
SVR [mmHg·s/mL]	0.89	0.8 (0.5-1.1)[30]
PVR [mmHg·s/mL]	0.06	0.06 (0.02-0.09)[30]
Volume		
LV (max) [mL]	144	150± 31[37]
RV (max) [mL]	153	173± 39[37]
LA (max) [mL]	111	97± 27[37]
RA (max) [mL]	107	101 (37-177)[38]
LV (min) [mL]	62	47± 15[37]
RV (min) [mL]	71	69± 22[37]
LA (min) [mL]	72	44± 13[37]
RA (min) [mL]	66	50 (15-92)[38]
Pressure		
SBP [mmHg]	120	125± 7[39]
DBP [mmHg]	66	73± 5[39]
PuA (systolic) [mmHg]	18.3	22.5± 1.0[40]
PuA (mean) [mmHg]	13.5	15.5± 2.6[40]
E/A ratio		
Mitral [-]	4.6	0.6-2.6[41]
Tricuspid [-]	1.1	0.8-2.3[41]

Fig. 4.4 shows the pressures and flows estimated for the three RV dysfunctions considered in various districts of the vascular circuit. In the first column, SD outputs are presented. As p increases, the right atrial (RA) pressure increases. The exacerbation of the impairment also flattens the late-systolic peak (v-wave) and emphasizes the end-diastolic peak (a-wave), despite the unaltered right atrial functionality. On the other hand, RV pressure exhibits a marked reduction of the systolic peak and an increase of the diastolic pressures. On the contrary, the pulmonary arterial (PuA) pressure substantially reduces over the whole heartbeat. Both the two pressures curves have flattened profiles as the pathology worsens and the systolic phase increases according to $E(t)$ displayed in Fig. 4.2a. The increase in Pra is offset by the increase in the diastolic Prv, resulting in a reduction of the E wave. Such a reduction is compensated, in part, by an increase of the A wave on the tricuspid valve flow (Qtv) (Fig. 4.4a$_4$). From an impairment of 70%,

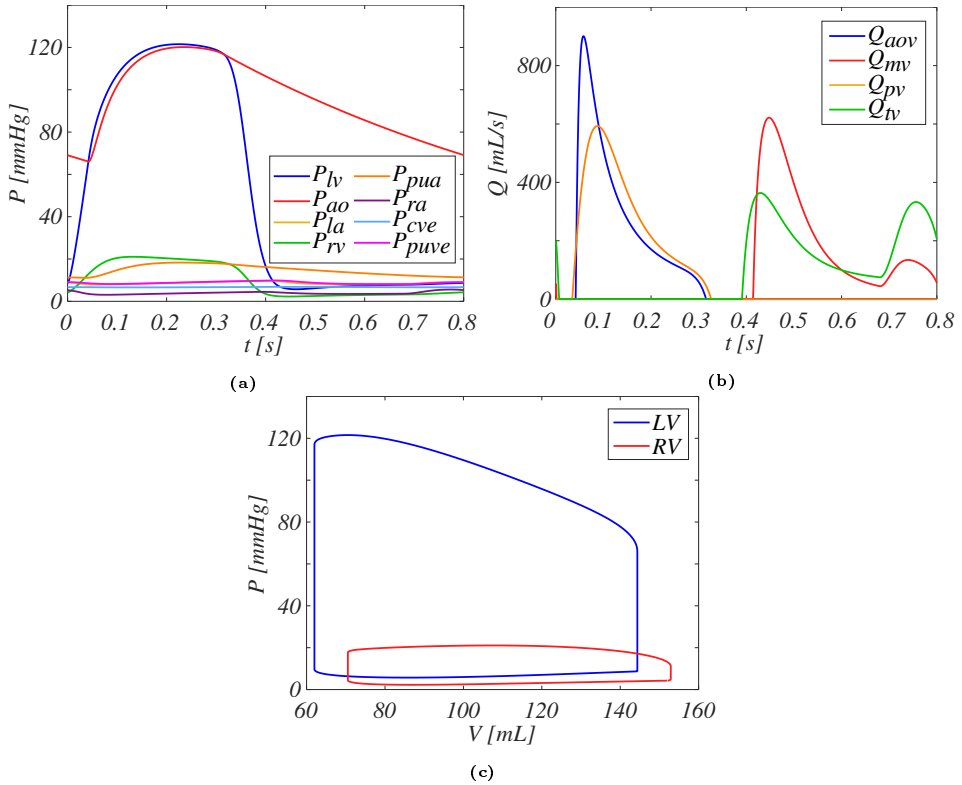

Figure 4.3: *Hemodynamic waveforms of the healthy condition. (a) Pressures, (b) flows, and (c) pressure-volume (pV) loops. Subscripts: lv, left ventricle; Ao, aortic and arterial vessels; sr, systemic vascular bed; rv, right ventricle; PuA, pulmonary arteries; pr, pulmonary vascular bed; Aov, aortic valve; Mv, mitral valve; Pv, pulmonary valve, and Tv, tricuspid valve.*

E wave completely disappears, and the A wave reaches a peak of about 600 mL/s, double compared to the healthy case (300 mL/s), whose maximum is observed for p=80%. The loss of contractility affects also the flow across the pulmonary valve (Qpv) (Fig. 4.4a$_5$). Qpv abruptly lessens at systolic peak and, for a complete SD, Qpv shows an almost constant waveform.

The outputs due to the diastolic dysfunction are reported in the second column of Fig. 4.4. According to $E(t)$ function, the shape of all the variables during the cardiac cycle remains unaltered for the different grades of dysfunction. The simulated pressures in the right atrium and in the pulmonary artery exhibit a positive and negative shift with p increasing, respectively. Consistently, Prv decreases during systole and increases during diastole as DD increases. The flow due to these pressure variations between RA and RV (Qtv) shows higher peaks for both the E and A waves, characterized, the former, by an increasing flow deceleration and, the latter, by an increasing flow acceleration (Fig. 4.4b$_4$). On the other hand, the peak of Qpv reduces, but the ejection time of the ventricle slightly increases. Interestingly, for severe DD (p>60%), the pulmonary valve opening is anticipated at the end of diastole, i.e., atrial contraction is causing pressure to rise above pulmonary arterial pressure, such that the pulmonary valve opens before the onset of ventricular systole (Fig. 4.4b$_5$).
Finally, the results provided by the CD case are reported in the third column of Fig. 4.4. The diastolic dysfunction mostly affects the output variables during the diastole, whereas the systolic dysfunction influences the results during the whole cardiac cycle, since the increment of the ejection time has an effect also in the early-diastole.

Fig. 4.5 reports the pressure-volume (pV) loops for RV (subscript 1) and LV (subscript 2) for the three dysfunctions considered. When SD is imposed on the right ventricle, RV end-systolic volume (ESV) increases and so does the RV end-diastolic volume (EDV). However, ESV increases more than EDV, resulting in a reduction of the stroke volume (SV = EDV-ESV). The impaired pumping activity causes a reduction in RV systolic pressures that, considering the volume increase, shifts the RV pV loops in downward/rightward direction. For the worst pathological condition, RV completely loses the ability to eject blood and the pV loop collapses in a line, as expected when the ventricle becomes a passive chamber (Fig. 4.5a$_1$). The impairment of RV affects also LV that reduces both the volumes and pressures (Fig. 4.5a$_2$). The diastolic dysfunction has an opposite effect on RV pV loops than SD (Fig. 4.5b$_1$). Both RV ESV and RV EDV reduce of about 30% and 20%, respectively. The inability to fill the cavity significantly increments the end-diastolic pressures (EDPs) and at the same time reduces the

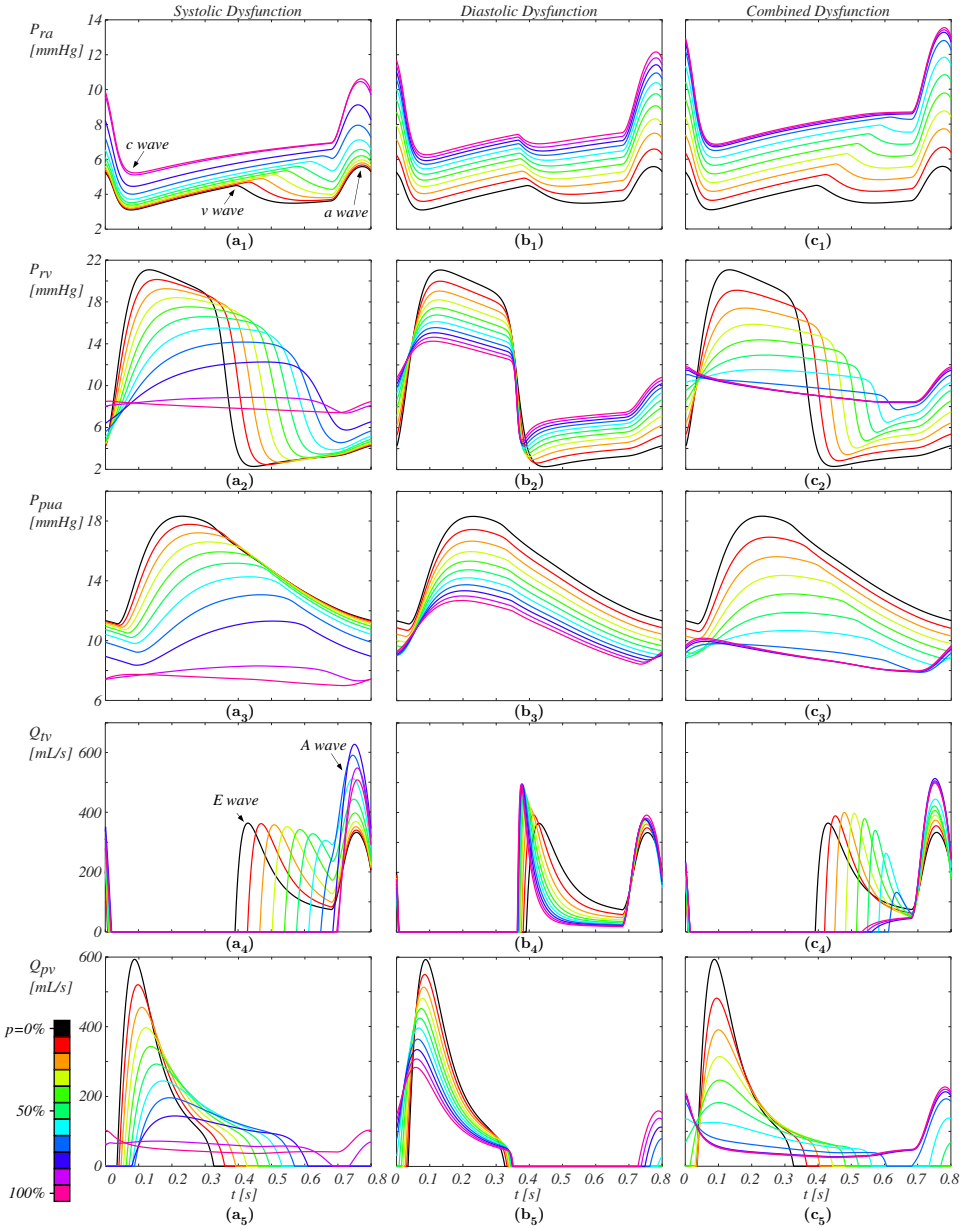

Figure 4.4: *Pressures and flows for a heartbeat in the three dysfunctions. (a) systolic dysfunction, (b) diastolic dysfunction and (c) combined dysfunction. Pra, pressure in the right atrium (subscript 1); Prv, pressure in the right ventricle (subscript 2); Ppua, pressure in the pulmonary arteries (subscript 3); QTv, flow across the tricuspid valve (subscript 4); QPv, flow across the pulmonary valve (subscript 5). Black solid line, healthy biventricular configuration; colored lines; the corresponded degree of RV impairment from 10% to 100%.*

systolic pressures, causing the shrinking of the loops with leftward/downward shifts. The effects on the LV are similar to the SD case, although the leftward/downward shift of the loops is lower for p>60% (Fig. 4.5b$_2$). In the presence of the combined dysfunction, the pressure-volumes of RV have downward shifts in which the systolic dysfunction shift is counterbalanced by the diastolic one (Fig. 4.5c$_1$). Also LV pV loops are affected by both systolic and diastolic dysfunction with pV loops displayed in intermediate positions with respect to the SD and DD cases (Fig. 4.5c$_2$).

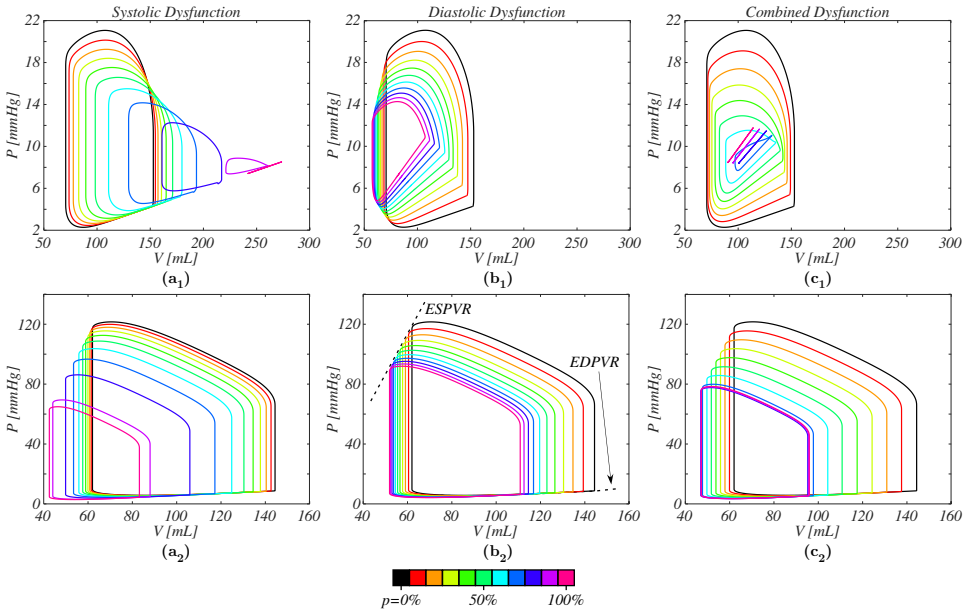

Figure 4.5: *Pressure-volume loops for RV (subscript 1) and LV (subscript 2). a) systolic dysfunction, b) diastolic dysfunction, and c) combined systolic and diastolic dysfunction. Black solid line, healthy configuration; coloured lines; the corresponded degree of RV impairment from 10% to 100%.*

Fig. 4.6 presents mean central venous pressure (CVP), cardiac index, defined as CI = CO/BSA, and ejection fraction (EF) of both the ventricles. The quantities are compared with *in vivo* reference values, whose normal physiological ranges are indicated by grey areas. All the types of dysfunction determine an increase in CVP (Fig. 4.6a). SD is outside the physiological ranges for severe impairments (p>80%), DD oversteps for moderate dysfunction (p>40%), and CD goes beyond the ranges for p>30%. All the dysfunctions depress the ventricular functionality resulting in hypoperfusion (Fig. 4.6b). In the early stage of impairment, SD determines a lower CI reduction than DD. For p>70% CI is outside the physiological ranges for both SD and DD, however, for SD, CI plummets. On the other hand, the

combination of dysfunctions speeds the overstepping of the ranges (p>40%). The response in terms of EF[1] highlights the role of RV contractility (Fig. 4.6c). EF_{RV} is estimated about 55% in the whole range of DD impairment. Conversely, SD causes a significant EF reduction (from 55% to 15% for p=0% and p=100%, respectively), and in the CD case, the loss of contractility determines an EF decrement up to p=70%. For more severe CD impairment EF is almost constant. As already pointed out for the pV loops, RV dysfunction causes a diminution of LV performance for all types of dysfunction (Fig. 4.6d). LV is generally less compromised by the RV impairment and EF is lower than the *in vivo* threshold only for severe impairments in the SD and CD cases, reaching values of about 50%. On the other hand, in the DD case, EF_{LV} worsens of about 8%, remaining within physiological ranges.

Finally, in Table 4.3 are reported the comparison between the numerical results and the *in vivo* data of Browning et al. [34] for RV EDV, RV ESV, EFRV, and CI. The tuning procedure indicated that CD with a systolic and diastolic impairment of 67% and 20%, respectively, i.e., CD with different degree of systolic and diastolic dysfunctions, correctly match the *in vivo* data [34]. In particular, the model outputs consistently estimated the indexes reported in this specific study, with differences within the measurement error.

Table 4.3: *Comparison of the CD condition outputs with in vivo reference data from Browning et al. [34]*

Parameters	**Reference**	**CD** p_{sys}=**67%** - p_{dias}=**20%**
RV (max) [mL]	181± 17	172
RV (min) [mL]	123± 17	112
EF_{RV} [-]	35± 3	35
CI [L/min/m^2]	2.5± 0.2	2.4

Firstly, the systolic rate of impairment is chosen by matching the observed and the computed EF_{RV}. Browing et al. [34] estimated EF_{RV} in the range between 32% and 38%, which is found in the SD case when p is set equal to 67%. Once the systolic grade of impairment is identified, the diastolic dysfunction is identified by a sensitivity analysis. The computed diastolic dysfunction is equal to p=20%. Thus, the numerical outputs are computed considering CD with a systolic and diastolic impairment of 67% and 20%, respectively.

[1]Ejection fraction (EF) is a common clinical marker that is used as a surrogate for contractility.

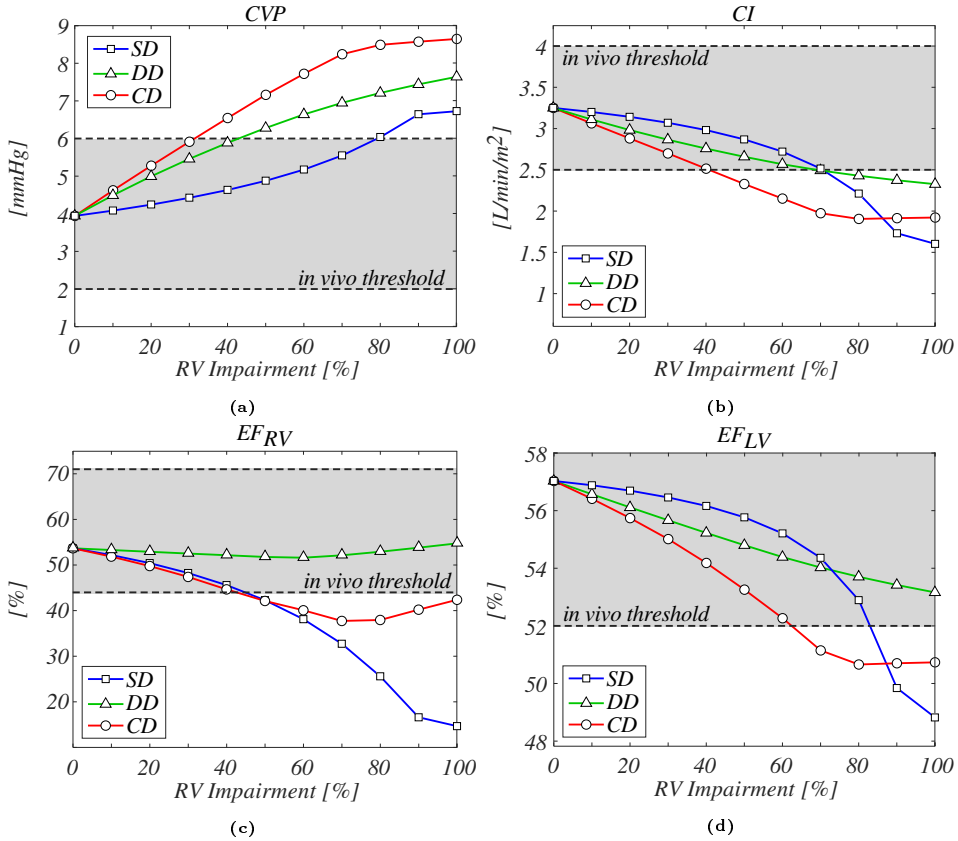

Figure 4.6: *Comparison at various rates of impairment between the different types of dysfunctions and in vivo reference data. □, systolic dysfunction, △, diastolic dysfunction, and ○, combined systolic and diastolic dysfunction. a) CVP, mean pressure in the central veins and in vivo data [42], b) CI, cardiac index and in vivo data [42], and EF, ejection fraction for c) RV (EF_{RV}) and in vivo data [43], and d) LV (EF_{LV}) and in vivo data [44].*

4.3.1 Comparison between the RV dysfunction and the Fontan circulation

In Fig. 4.7 only SD and CD are compared to the univentricular circulation because with DD, RV keeps its contractile functionality, thus maintaining a double-ventricular circulation. In the systolic dysfunctions, the impairment of the contractile activity leads to waveforms similar to the Fontan circulation. Indeed, from 90% dysfunction, both Prv and Ppua are almost constant over the heartbeat with a Fontan-like trend. However, the value computed in the univentricular circulation is higher than the resulting complete RV dysfunction. Differences in absolute values are visible also on the systemic pV loops, i.e., LV and the single ventricle for RV impairment and the Fontan

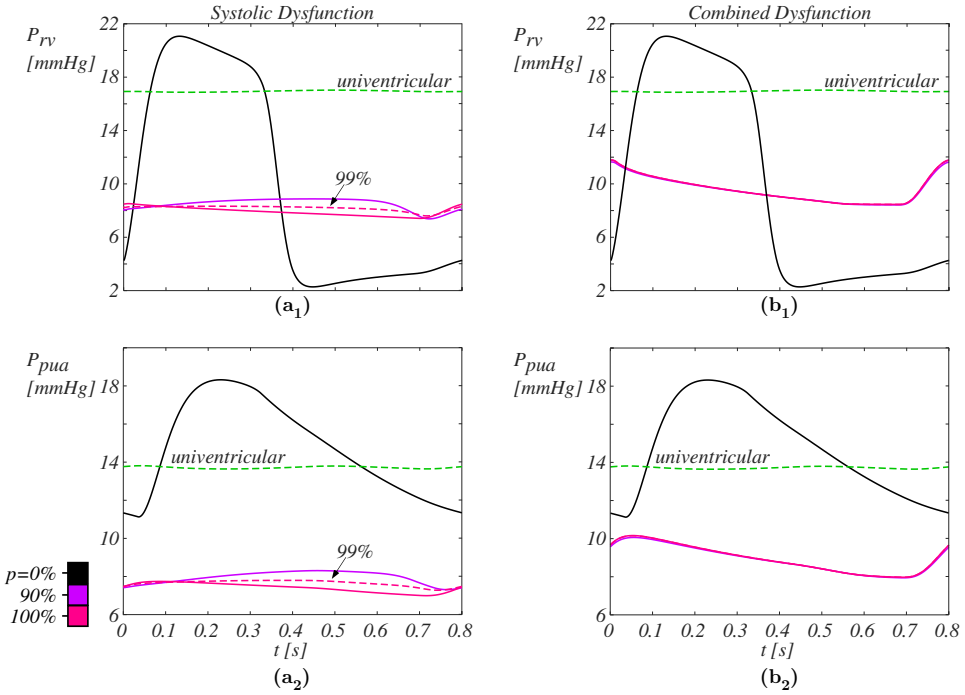

Figure 4.7: *Pressures and flows for a heartbeat for the almost complete RV dysfunction and the Fontan circulation. (a) systolic dysfunction, and (b) combined dysfunction. Prv, pressure in the right ventricle (single ventricle in the Fontan circulation) (subscript 1); and, Ppua, pressure in the pulmonary arteries (subscript 2). Black solid line, healthy biventricular configuration; green dotted line, Fontan (univentricular) circulation; colored lines; 90% to 100% RV dysfunction, including the 99% impairment (magenta dotted line).*

circulation, respectively (Fig. 4.8). The univentricular circulation maintains a physiological stroke volume, but with an elevated EDV and ESV, along with almost normal pressures as reported in the literature [45]. This results in a rightward shift without shrinking of the loop. By contrast, complete RV dysfunction reduces the LV filling likely due to systemic venous congestion, and the LV pV loops become smaller and move to the left. Looking at Fig. 4.9, the CVP computed for the univentricular circulation is higher than the physiological ranges of [42] as for the complete dysfunction (Fig. 4.9a). Nevertheless, the single ventricle of the Fontan circulation is still able to pump the adequate amount of blood, with the CI being within the physiological ranges of 2.5 - 4 L/min/m^2. On the contrary, the complete RV dysfunction affects LV filling resulting in hypoperfusion (Fig. 4.9b).

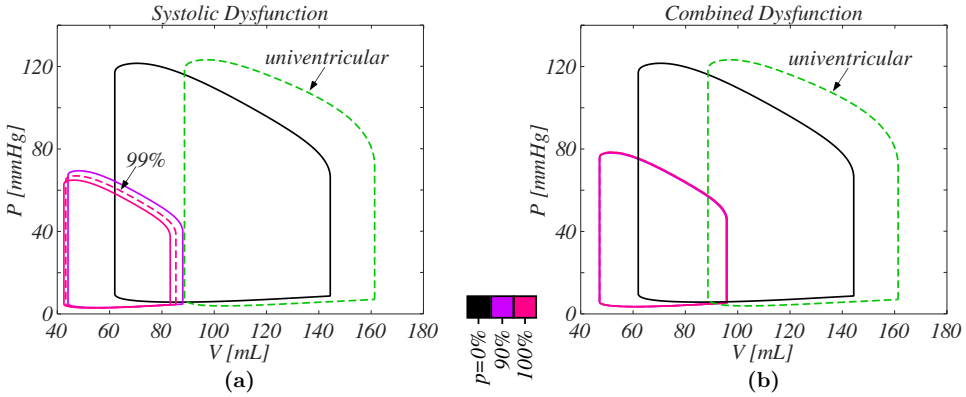

Figure 4.8: *Pressure-volume loops for the systemic ventricle, i.e., LV and the single ventricle for RV impairment and the Fontan circulation, respectively . a) systolic dysfunction, and b) combined systolic and diastolic dysfunction. Black solid line, healthy configuration; green dotted line, Fontan (univentricular) circulation; colored lines; 90% to 100% RV dysfunction, including the 99% impairment (magenta dotted line).*

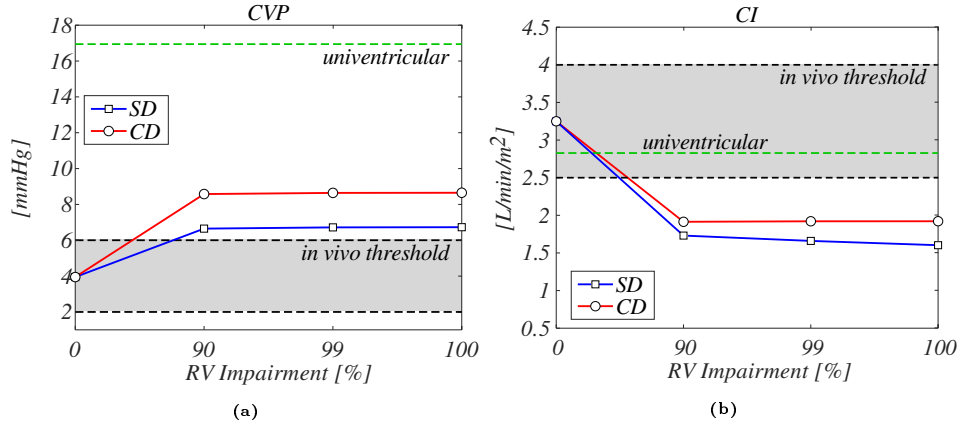

Figure 4.9: *Comparison at various rates of impairment between the different types of dysfunctions, in vivo reference data, and the univentricular circulation (green dotted line). □, systolic dysfunction, and ○, combined systolic and diastolic dysfunction. a) CVP, mean pressure in the central veins and in vivo data [42], and b) CI, cardiac index and in vivo data [42].*

4.4 Model Sensitivity Analysis

The sensitivity of the healthy biventricular model is computed as explained in Section 2.8. Particularly, 16 inputs are tested with sensitivities calculated after an increase of 25% [28], and 20 outputs are evaluated.

Table 4.4 reports the results. The inputs are ordered considering the

global influence, i.e., as the sum of $|S|$ for all the outputs analyzed, showing the most influential on the left. The outputs are ordered based on the overall sensitivity, computed as the median value of $|S|$ for all the inputs, with the most sensitive at the top. Fig. 4.10 shows the outputs listed on the horizontal axis and inputs listed on the vertical axis. Note that in the figure, the outputs are ordered with the most sensitive on the left, and the inputs are ordered with the most influential at the bottom. The most influential parameters are those related to heart chamber contractility. These parameters are known to affect pressures and flows, however, interestingly, the contractility of the LV is less influential. The most sensitive outputs are those related to the systemic arterial pressure and the heart volumes. The results of the sensitivity analysis are very similar to the ones found in Ch. 3 for the biventricular adult model. This behavior is expected since the two models share the same structure. As previously reported, also in this case, only few outputs are sensitive to the variation of inputs, and this is clearly visible from Fig. 4.10 that shows a cluster of larger data points in the left side. The least sensitive outputs signals are the right ventricular pressure and pulmonary venous flows, and this could be related to the reservoir functionality of the high-compliance pulmonary circulation. Again, in analogy to findings of Ch. 3.

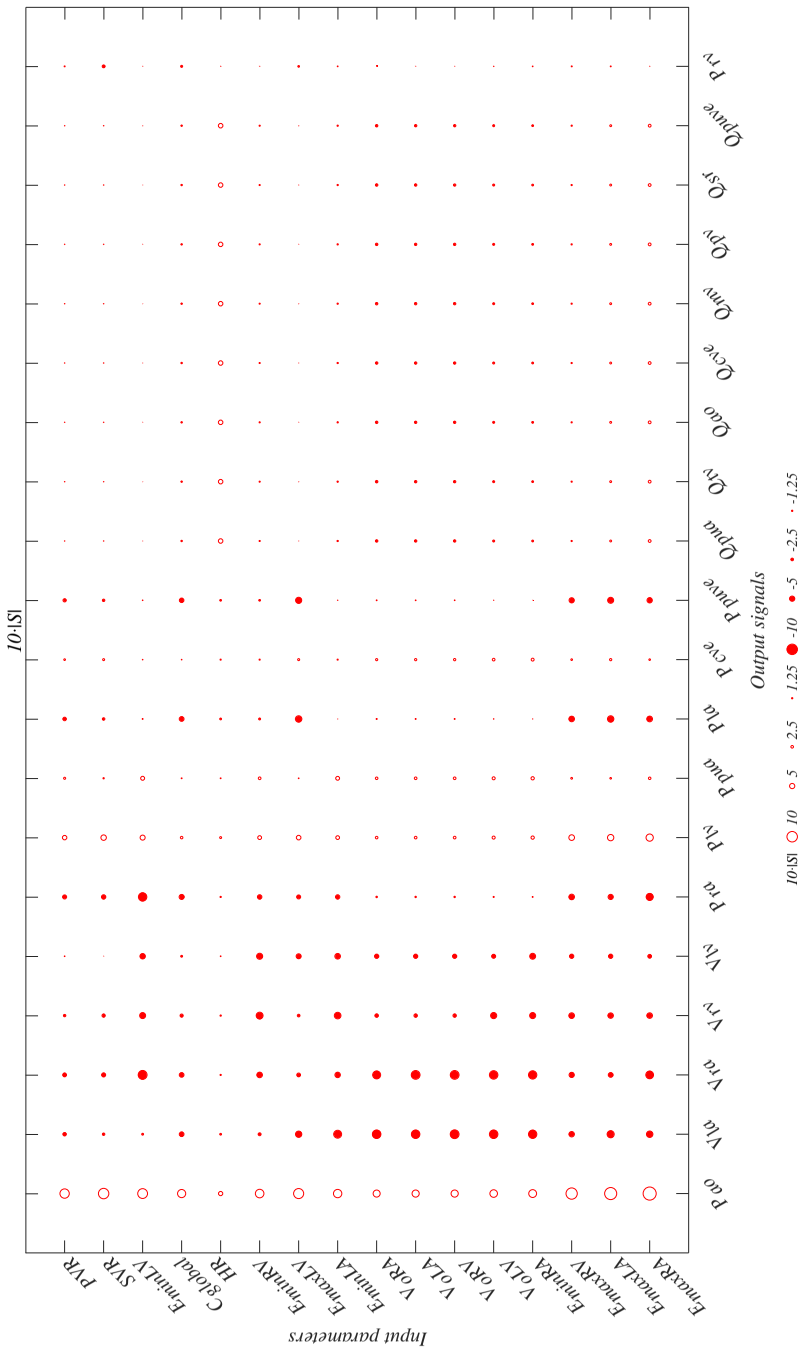

Figure 4.10: *Graphical representation of the sensitivity of the outputs to the 25% variation of the inputs. A larger symbol corresponds with higher sensitivity and filled/empty circles correspond to negative/positive S. Outputs are ordered according to the overall sensitivity (the most sensitive on the left) and inputs are ordered based on the global influence (the most influential at the bottom).*

Table 4.4: *Mean sensitivities (S) of output signals to the input parameters. The inputs are ordered based on the global influence (the most influential on the left), the outputs are ordered based on the overall sensitivity (the most sensitive at the top).*

	$\mathbf{E}_{max_{RA}}$	$\mathbf{E}_{max_{LA}}$	$\mathbf{E}_{max_{RV}}$	$\mathbf{E}_{min_{RA}}$	$\mathbf{V}_{p=0_{LV}}$	$\mathbf{V}_{p=0_{RV}}$	$\mathbf{V}_{p=0_{LA}}$	$\mathbf{V}_{p=0_{RA}}$	$\mathbf{E}_{min_{LA}}$	$\mathbf{E}_{max_{LV}}$	$\mathbf{E}_{min_{RV}}$	**HR**	**Cglobal**	$\mathbf{E}_{min_{LV}}$	**SVR**	**PVR**
Pao	1.251	1.154	1.077	0.750	0.724	0.685	0.681	0.672	0.798	0.963	0.817	0.408	0.778	0.939	0.995	0.892
Vla	-0.615	-0.679	-0.517	-0.796	-0.813	-0.838	-0.809	-0.815	-0.758	-0.600	-0.280	-0.170	-0.448	-0.180	-0.234	-0.327
Vra	-0.737	-0.458	-0.493	-0.795	-0.811	-0.835	-0.837	-0.762	-0.521	-0.360	-0.532	-0.113	-0.447	-0.850	-0.389	-0.366
Vrv	-0.535	-0.521	-0.536	-0.575	-0.588	-0.324	-0.326	-0.331	-0.632	-0.254	-0.656	-0.120	-0.297	-0.569	-0.308	-0.228
Vlv	-0.355	-0.410	-0.409	-0.564	-0.382	-0.404	-0.406	-0.411	-0.533	-0.475	-0.583	-0.068	-0.179	-0.512	0.016	-0.061
Pra	-0.674	-0.494	-0.532	-0.079	-0.101	-0.133	-0.136	-0.144	-0.415	-0.384	-0.428	-0.117	-0.479	-0.801	-0.417	-0.390
Plv	0.692	0.604	0.541	0.315	0.291	0.256	0.252	0.244	0.360	0.438	0.367	0.187	0.239	0.481	0.521	0.425
Ppua	0.240	0.156	0.169	0.313	0.289	0.254	0.251	0.242	0.368	0.067	0.256	0.079	0.080	0.378	-0.121	0.200
Pla	-0.545	-0.613	-0.532	-0.026	-0.048	-0.081	-0.084	-0.091	0.022	-0.618	-0.185	-0.174	-0.460	-0.079	-0.240	-0.336
Pcve	0.153	0.214	0.159	0.277	0.254	0.219	0.215	0.207	0.106	0.194	0.107	0.109	0.061	-0.053	0.190	0.161
Ppuve	-0.505	-0.574	-0.497	-0.009	-0.031	-0.064	-0.067	-0.075	0.040	-0.584	-0.163	-0.161	-0.433	-0.056	-0.234	-0.309
Qpua	0.266	0.180	0.116	-0.172	-0.192	-0.224	-0.227	-0.234	-0.121	0.016	-0.104	0.431	-0.135	0.011	0.045	-0.042
Qtv	0.265	0.180	0.116	-0.171	-0.192	-0.224	-0.227	-0.234	-0.122	0.016	-0.105	0.430	-0.135	0.009	0.043	-0.043
Qao	0.267	0.180	0.117	-0.171	-0.192	-0.223	-0.226	-0.234	-0.120	0.017	-0.104	0.431	-0.134	0.011	0.045	-0.042
Qcve	0.267	0.180	0.117	-0.171	-0.192	-0.223	-0.227	-0.234	-0.120	0.017	-0.103	0.431	-0.134	0.011	0.045	-0.042
Qmv	0.266	0.180	0.116	-0.170	-0.191	-0.223	-0.226	-0.233	-0.120	0.016	-0.103	0.430	-0.135	0.011	0.044	-0.043
Qpv	0.267	0.181	0.117	-0.171	-0.192	-0.223	-0.226	-0.234	-0.120	0.017	-0.103	0.431	-0.134	0.011	0.045	-0.042
Qsr	0.266	0.180	0.117	-0.171	-0.192	-0.224	-0.227	-0.234	-0.120	0.016	-0.104	0.431	-0.134	0.011	0.045	-0.042
Qpuve	0.267	0.181	0.118	-0.170	-0.191	-0.223	-0.226	-0.233	-0.119	0.017	-0.103	0.431	-0.133	0.012	0.045	-0.041
Prv	-0.024	-0.080	-0.092	0.065	0.042	0.009	0.006	-0.002	0.075	-0.159	0.011	-0.024	-0.195	-0.007	-0.268	-0.089

Pao, aortic (arterial vessel) pressure, Vla, LA volume, Vra, RA volume, Vrv, RV volume, Vlv, LV volume, Pra, RA pressure, Plv, LV pressure, Ppua, PuA pressure, Pla, LA pressure, Pcve, CVe pressure, Ppuve, PuVe pressure, Qpua, PuA flow, Qtv, tricuspid valve flow, Qao, aortic valve flow, Qcve, CVe flow, Qmv, mitral valve flow, Qpv, pulmonary valve flow, Qsr, systemic vascular bed flow, Qpuve, PuVe flow, and Prv, RV pressure.

4.5 Discussion

The importance of the right ventricle has often been underestimated, with a recent review even highlighting that "the perception of the right ventricle has fluctuated between an essential and a nonessential ventricle" [8]. A key reason why one might expect the RV to be non-essential is that patients with a Fontan circulation (i.e. who do not have a sub-pulmonary ventricle) survive into adulthood. However, to highlight the role of RV and the effects of its dysfunction on cardiac failure, *isolated* RV dysfunction is studied and compared with the Fontan circulation.
The normal (no dysfunction) condition is evaluated first, assessing the ability of the model to represent physiological pressures and flows as well as global hemodynamic variables in agreement with the literature data [30, 41, 37, 38, 39, 40]. In particular, the hemodynamic of the right side is well represented in all its characteristics, included the right heart flow waveforms [46].
Isolated systolic dysfunction (SD) impairs the effectiveness of the ventricle to eject blood mainly due to a reduction of the ventricular contractile force. The variation of systolic time with the rate of impairment, introduced for the first time in the present work, enhances the model capability to reproduce reasonable results when SD is considered, because it can represent the prolonged cardiac time intervals that are peculiar to the ventricular systolic dysfunction [22, 23]. According to the model, SD causes an increase in right ventricular end-diastolic pressure while reducing RV systolic pressures. These results are explained considering the impairment of contractility which causes blood accumulation in the RV as well as congestion in the RA and in the systemic veins with consequently reduction of ejected blood. In this condition, RA is forced to increase its pressure to overcome the pressure into the ventricle and open the tricuspid valve, while Ppua decreases [47]. On the other hand, Qtv E wave disappears due to the reduction of the pressure gradient, in part compensated by the increase of the A wave [48]. Importantly, when the contractile activity is absent, the model captures the expected nearly constant Prv and Qpv, with Fontan-like trend (Fig. 4.7). This trend is caused by the passive conduit behaviour of RV in which the blood flows from RA into PuA [49]. Indeed, RA function is maintained and therefore RA effectively 'takes over' as the main right-sided pump.
Isolated diastolic dysfunction (DD) is characterized by an increased wall stiffness, which resists filling of the chamber and hence causes higher filling pressures in diastole [50]. This pathology exhibits three grades of severity; the most severe here simulated is characterized by the increased ventricular stiffness and decreased tricuspid deceleration time. The model suggests that

the ventricle affected by this pathology almost preserves EF, exhibiting the features of the well recognized heart failure with preserved ejection fraction (HFpEF) that is however usually attributed to LV [51]. On the other hand, DD alters the pressures and the flows. It is peculiar in this sense the secondary late diastolic peak that arises in Qpv for severe impairments, as a consequence of the atrial contraction [52]. This occurs because the increased RV resistance to fill exceeds that of PuA, i.e., the pressure necessary to fill RV is higher than PuA pressure, with a consequent transtricuspid atrial systolic flow which does not fill RV but results in antegrade pulmonary arterial blood flow in which RV behaves as a passive conduit. However, if for SD RV behaves as a passive conduit because of the increased end-diastolic pressure due to the accumulated blood in the ventricle, in DD, the Qpv late peak reflects the RV diastolic dysfunction in which the ventricle demonstrates highly restricted filling [24, 50, 52]. The possibility of antegrade pulmonary arterial flow occurring in the presence of RV diastolic dysfunction is a very promising result. Indeed, the appearance of Qpv late peak in relation to diastolic dysfunction is still debated [52, 53]. However, since in this work, only ventricular parameters are changed to simulate RV dysfunction, all the secondary mechanisms that may arise are neglected. Thus, the appearance of a late peak in pulmonary flow seems intrinsically related to the increased stiffness of RV, supporting what previously supposed by clinicians [52, 53].
Finally, the combined systolic and diastolic dysfunction (CD) results from the non-linear superposition of the effects of the two previous dysfunctions with results deducible from the previous configurations, but producing an overall worse picture of hemodynamic performance. The comparison between the complete impairment and the Fontan circulation shows that the lack of contractile ventricular activity leads to almost constant pressure over the heartbeat (Fig. 4.7). However, the Fontan circulation is characterized by higher pressure likely due to the fact that the Fontan circulation maintains cardiac output, hence output and pressures of the single ventricle are much higher and venous pressure rises necessarily to support pulmonary flow.
The effects of RV dysfunction are also visible on the pV loops (Fig. 4.5). In the SD scenario, there is a reduction of the end-systolic pressure associated with an increment of the ventricular volume [54]. On the other hand, the computed EDPVR increase is found to be typical in the diastolic dysfunction [55, 35]. In the CD case, the right ventricle attempts to dilate for the lower contractility due to SD, but the increased passive stiffness due to DD opposes this volume dilation. For $p \geq 80\%$, the increased stiffness prevails and the RV ESV and EDV reduce, resulting also in a slight increment of ventricular performance (Fig. 4.6b-4.6d). Focusing on the LV pV loops, the

shift is always downward/leftward in all the investigated cases. LV reduces the work because it is entangled with a suffering RV, which progressively drops the SV. Therefore, the equal reduction of the left SV occurs, although LV maintains its full mechanical functionality. At the same time, the pressure in the left atrium decreases, as a consequence of the lower pressure in PuA (Fig. 4.4). Accordingly to the Frank-Starling law, the left SV appropriately reduces due to the leftward/downward shift of the end-diastolic and the end-systolic pV points along the unchanged left EDPVR and ESPVR curves (Fig. 4.5). Notice also that, the effect of RV dysfunction on LV is more severe in the CD than in the SD case. This result is not surprising because the loss of the passive action of the myocardium, expressed by its relaxation, worsens the ventricular working.
Considering CVP and CI (Fig. 4.6a-b), healthy ranges are 2-6 mmHg and 2.5-4 L/min/m^2, respectively [42, 56]. Larger values of CVP and smaller values of CI indicate a potential ventricular disease, results found in all the dysfunctions. This means that both the systolic and diastolic functionalities of the right ventricle are fundamental in order to guarantee the physiological hemodynamics. Notice also that adaptive processes such as vasodilation are not accounted for. Reduced flow in the absence of vasodilation might actually imply a reduced vasodilatatory reserve in reality. This means that, even if in real patient vasodilation leads to maintenance of the same blood flow, they might have less reserve and so have exercise intolerance for example. Moreover, the Fontan circulation seems to create worst pressure condition and better flow rate state (Fig. 4.9). This is confirmed by the ability of the Fontan circulation to sustain life, despite the well-known morbidities characterized by increased caval vein pressures. Thus, from these results, it seems that the complete right systolic dysfunction (with or without diastolic impairment) leads to life-threatening state in which the systemic ventricle behaves worst than in the single-ventricular circulation. Indeed, the inclusion of the not working pulmonary ventricle in the circulation determines hypoperfusion state.
The correct systolic functionality of the ventricle is also assessed clinically through EFs, namely EF_{RV}>44%[43] and EF_{LV}>52% [44]. EF_{RV} is lower than normal only from mild to moderate SD and CD, whereas abnormal values on EF_{LV} are identified for severe RV dysfunction. Moreover, initial decrease in EF_{RV} with SD is relatively flat, i.e., EF does not really change that much until severe degrees of SD. This might be clinically relevant since it may imply that EF may not be a good early marker for RV SD. Note also that in the Fontan circulation, despite the physiological stroke volume, the right shift of the single ventricle pV loop (Fig. 4.8) determines an EF value

smaller than the physiological one. Indeed, ESV and EDV are about 90 and 160 mL, respectively. The resulting stroke volume is (EDV-ESV) 70 mL, that divided by EDV gives an EF of about 44%. This may suggest that also for the Fontan circulation, the ejection fraction is not suitable to evaluate the hemodynamic condition.

The comparison between the model simulation with the *in vivo* clinical data reported in the study of Browning et al. [34] (Table 4.3) is illustrative for the potential application and to assess the model in a real scenario. The model's ability to reproduce the hemodynamic indexes is particularly promising. Indeed, the differences between simulated and observed outputs are acceptable, although all the alterations connected to the ventricular pathologies that may enhance the model predictions are not considered, e.g., the variations of the systemic vascular resistance. Thus, this result suggests that the ventricular parameters chosen to simulate RV dysfunction seem to govern the pathology. This is true also for the other types of dysfunction, with good agreement of the results with clinical evidence. This will need further validation, but if this is the case, the knowledge of most important parameters could help in identifying and treating the pathology. Since the model shows how flow and pressure change as a result of RV dysfunction, it may be useful in different clinical settings:
1) *Isolated right ventricular dysfunction: Uhl disease, right ventricular dysplasia, post-surgical right ventricular dysfunction.* This condition is rare, and the knowledge of heart chambers physiopathology as well as the clinical evolution assessment are hardly feasible. The present model may help to grade the correct ventricular dysfunction.
2) *Pulmonary arterial hypertension.* In this case, the pulmonary arterial pressure is augmented. The associated right heart hemodynamics can be due to the increased afterload or associated with a percentage of RV dysfunction. Distinguishing between these two cases is still a clinical challenge and a suitably implementation of the model assigning augmented pulmonary artery pressure conditions may help to identify the patients at higher risk to develop right HF.
3) *Cor pulmonare.* Left HF usually affects RV function due to the increase of left atrial pressure and the pulmonary arterial pressure. Similarly to setting 2), the RV dysfunction model, implemented with the LV impairment, may be appropriate to recognize the hemodynamics due to the left HF or associated to primitive right HF (bi-ventricular failure). This distinction is particularly important when a left ventricular assist device (VAD) is required. In the case of induced right HF, the right ventricular function recovers, partially

or completely, after the left VAD implantation. Conversely, when the right ventricular dysfunction occurs, usually a bi-VAD is the best clinical option. 4) *Single-ventricle or biventricular palliation.* Patients with functionally or anatomically borderline right ventricles may be clinically treated by a Fontan palliation or by a biventricular repair, i.e., one and one-half ventricle circulation. The clinical decision whether or not to perform the one and one-half circulation is still controversial [57] and the model may give interesting results in such a complex clinical decision process.

The present work provides an essential foundation for future work that could lead to the use of model-based clinical diagnostics. However, there are still a large number of steps and hurdles to be addressed. In this sense, future works will comprise the inclusion of heart valves dynamics, together with the sex and pediatric population analysis [58]. For example, Qao and Qmv (E/A ratio) are found to have non-physiological peaks [41]. This difference is likely due to the simplified model adopted to simulate the flow dissipation through the valves, and detailed valve modeling will help to overcome this poor left heart flow outputs. In particular, the inclusion of valve dynamics (e.g., the model proposed in Mynard et al.[32]) can likely overcome this issue. In addition, it has been demonstrated in the last years the growing importance of sex and gender research, and their role in the parameters that determine the hemodynamics [59, 60, 61]. Further aspects deserving attention to enhance the model description of the circulation are the physiological compensatory mechanisms, such as ventricular remodeling, and secondary diseases, as tricuspid valve insufficiency, which usually arise in advanced RV dysfunction [62]. Indeed, a big limitation to note is that adaptive processes, e.g., in presence of ventricular dysfunction other parts of the cardiovascular system will respond to maintain cardiac output (as in the Fontan), are not taken into account. This might include an increase in blood volume and heart rate, venous constriction to raise venous and pulmonary pressures by redistributing blood volume, and changes in LV function. These adaptations result from the activation of several neurohormonal compensatory mechanisms, e.g., the sympathetic system and the renin-angiotensin-aldosterone system, that are triggered by the fall in cardiac output and they are "aimed at improving the mechanical environment of the heart" [63]. All these are not included at this step, to avoid additional mechanisms in the evaluation of the pathological hemodynamics given by a primary RV dysfunction, but they cannot be neglected to implement a model capable of analyzing cardiovascular conditions more accurately.

4.6 Conclusion

In this chapter, the effect of RV on the overall hemodynamics is highlighted. The 0D circulation model seems to correctly simulate the pressures and flows in both the pulmonary and systemic circulations. Changes of RV functions lead to significant modifications of the overall hemodynamics, affecting also LV output due to a decreased preload. To the best of our knowledge, there is not such a previous engineering work aimed at understanding the hemodynamic implications of the development of RV impairment. In addition, the model matches clinical data of patients presenting RV diseases, representing a first step towards the set up and the assessment of a numerical tool able to support clinicians to improve the knowledge and the understating of the role played by RV on the blood circulation with potential future benefits in the diagnosis and treatment of RV pathologies.

Bibliography

[1] G. Comunale, M. Padalino, B. Castaldi, P. Peruzzo, and F. M. Susin, "The effect of active and passive dysfunction on the right ventricle performance," in *Proceedings of the 5th IAHR European Congress; New Challenges in Hydraulic Research and Engineering*, 2018.

[2] J. C. Sun and H. Joffe, *The Most Common Inpatient Problems in Internal Medicine E-Book: Ward Survival*. Elsevier Health Sciences, 2007.

[3] D. D. Bonnema, C. F. Baicu, and M. R. Zile, "Clinical approach to diastolic heart failure," in *Diastology*, pp. 11–25, Elsevier, 2008.

[4] J. Treece, H. Chemchirian, N. Hamilton, M. Jbara, V. Gangadharan, T. Paul, and S. J. Baumrucker, "A review of prognostic tools in heart failure," *American Journal of Hospice and Palliative Medicine®*, vol. 35, no. 3, pp. 514–522, 2018.

[5] F. Haddad, R. Doyle, D. J. Murphy, and S. A. Hunt, "Right ventricular function in cardiovascular disease, part ii: pathophysiology, clinical importance, and management of right ventricular failure," *Circulation*, vol. 117, no. 13, pp. 1717–1731, 2008.

[6] A. Kagan, "Dynamic responses of the right ventricle following extensive damage by cauterization," *Circulation*, vol. 5, no. 6, pp. 816–823, 1952.

[7] N. Silverton and G. Djaiani, "Right ventricular function and perioperative risk assessment: The time has come to stop being sinister," *Journal*

of Cardiothoracic and Vascular Anesthesia, vol. 33, no. 5, pp. 1287–1289, 2019.

[8] M. Amsallem, O. Mercier, Y. Kobayashi, K. Moneghetti, and F. Haddad, "Forgotten no more: a focused update on the right ventricle in cardiovascular disease," *JACC: Heart Failure*, vol. 6, no. 11, pp. 891–903, 2018.

[9] S. R. Mehta, J. W. Eikelboom, M. K. Natarajan, R. Diaz, C. Yi, R. J. Gibbons, and S. Yusuf, "Impact of right ventricular involvement on mortality and morbidity in patients with inferior myocardial infarction," *Journal of the American College of Cardiology*, vol. 37, no. 1, pp. 37–43, 2001.

[10] R. Padang, N. Chandrashekar, M. Indrabhinduwat, C. G. Scott, S. A. Luis, K. Chandrasekaran, H. I. Michelena, V. T. Nkomo, S. V. Pislaru, P. A. Pellikka, *et al.*, "Aetiology and outcomes of severe right ventricular dysfunction," *European heart journal*, vol. 41, no. 12, pp. 1273–1282, 2020.

[11] C. Selton-Suty and Y. Juillière, "Non-invasive investigations of the right heart: how and why?," *Archives of Cardiovascular Diseases*, vol. 102, no. 3, pp. 219–232, 2009.

[12] I. Kokalari, T. Karaja, and M. Guerrisi, "Review on lumped parameter method for modeling the blood flow in systemic arteries," 2013.

[13] T. Korakianitis and Y. Shi, "A concentrated parameter model for the human cardiovascular system including heart valve dynamics and atrioventricular interaction," *Medical engineering & physics*, vol. 28, no. 7, pp. 613–628, 2006.

[14] Y. Shi, P. Lawford, and R. Hose, "Review of zero-d and 1-d models of blood flow in the cardiovascular system," *Biomedical engineering online*, vol. 10, no. 1, p. 33, 2011.

[15] L. Formaggia and A. Veneziani, "Reduced and multiscale models for the human cardiovascular system," *Lecture notes VKI lecture series*, vol. 7, 2003.

[16] E. Maksuti, B. E. Westerhof, M. Ugander, D. W. Donker, M. Carlsson, and M. Broomé, "Cardiac remodeling in aortic and mitral valve disease: a simulation study with clinical validation," *Journal of Applied Physiology*, vol. 126, no. 5, pp. 1377–1389, 2019.

[17] L. Punnoose, D. Burkhoff, S. Rich, and E. M. Horn, "Right ventricular assist device in end-stage pulmonary arterial hypertension: insights from a computational model of the cardiovascular system," *Progress in cardiovascular diseases*, vol. 55, no. 2, pp. 234–243, 2012.

[18] S. Bozkurt, "Mathematical modeling of cardiac function to evaluate clinical cases in adults and children," *PloS one*, vol. 14, no. 10, p. e0224663, 2019.

[19] A. Ferreira, S. Chen, M. A. Simaan, J. R. Boston, and J. F. Antaki, "A nonlinear state-space model of a combined cardiovascular system and a rotary pump," in *Proceedings of the 44th IEEE Conference on Decision and Control*, pp. 897–902, IEEE, 2005.

[20] F. Seemann, P. Arvidsson, D. Nordlund, S. Kopic, M. Carlsson, H. Arheden, and E. Heiberg, "Noninvasive quantification of pressure-volume loops from brachial pressure and cardiovascular magnetic resonance," *Circulation: Cardiovascular Imaging*, vol. 12, no. 1, p. e008493, 2019.

[21] H. Fukuta and W. C. Little, "General principles, clinical definition, and epidemiology," in *Diastology*, pp. 63–72, Elsevier, 2008.

[22] C. Tei, L. H. Ling, D. O. Hodge, K. R. Bailey, J. K. Oh, R. J. Rodeheffer, J. A. Tajik, and J. B. Seward, "New index of combined systolic and diastolic myocardial performance: a simple and reproducible measure of cardiac function—a study in normals and dilated cardiomyopathy," *J cardiol*, vol. 26, pp. 357–366, 1995.

[23] O. Oketona, M. Balogun, A. Akintomide, O. Ajayi, R. Adebayo, T. Mene-Afejuku, O. Oketona, and O. Bamikole, "Right ventricular systolic function in hypertensive heart failure," *Vascular Health and Risk Management*, vol. 13, p. 353, 2017.

[24] P. M. Mottram and T. H. Marwick, "Assessment of diastolic function: what the general cardiologist needs to know," *Heart*, vol. 91, no. 5, pp. 681–695, 2005.

[25] S. F. Nagueh and W. A. Zoghbi, "Evaluation of right ventricular diastolic function," in *Diastology*, pp. 171–180, Elsevier, 2008.

[26] C. Luo, D. Ramachandran, D. L. Ware, T. S. Ma, and J. W. Clark, "Modeling left ventricular diastolic dysfunction: classification and key indicators," *Theoretical Biology and Medical Modelling*, vol. 8, no. 1, p. 14, 2011.

[27] G. Comunale, F. M. Susin, and J. P. Mynard, "A female-specific cardiovascular lumped-parameter model," in *2020 42nd Annual International Conference of the IEEE Engineering in Medicine Biology Society (EMBC)*, pp. 2654–2657, 42nd Annual International Conferences of the IEEE Engineering in Medicine and Biology Society in conjunction with the 43rd Annual Conference of the Canadian Medical and Biological Engineering Society, 2020.

[28] J. P. Mynard, *Computer modelling and wave intensity analysis of perinatal cardiovascular function and dysfunction*. PhD thesis, Department of Paediatrics, The University of Melbourne, Heart Research Group, Murdoch Childrens Research Institute, 2011.

[29] P. Kam and I. Power, *Principles of Physiology for the Anaesthetist*. CRC Press, 2015.

[30] W. Milnor, "Hemodynamic 2nd edn (baltimore, md: William and wilkins)," 1989.

[31] T. Tanaka, M. Arakawa, T. Suzuki, M. Gotoh, H. Miyamoto, and S. Hirakawa, "Compliance of human pulmonary "venous" system from pulmonary artery wedge pressure tracings: comparison with pulmonary arterial compliance," *Japanese Circulation Journal*, vol. 50, no. 2, pp. 127–139, 1986.

[32] J. Mynard, M. Davidson, D. Penny, and J. Smolich, "A simple, versatile valve model for use in lumped parameter and one-dimensional cardiovascular models," *International Journal for Numerical Methods in Biomedical Engineering*, vol. 28, no. 6-7, pp. 626–641, 2012.

[33] J. P. Mynard and J. J. Smolich, "One-dimensional haemodynamic modeling and wave dynamics in the entire adult circulation," *Annals of biomedical engineering*, vol. 43, no. 6, pp. 1443–1460, 2015.

[34] J. R. Browning, J. R. Hertzberg, J. D. Schroeder, and B. E. Fenster, "4d flow assessment of vorticity in right ventricular diastolic dysfunction," *Bioengineering*, vol. 4, no. 2, p. 30, 2017.

[35] S. Rain, M. L. Handoko, P. Trip, C. T.-J. Gan, N. Westerhof, G. J. Stienen, W. J. Paulus, C. A. Ottenheijm, J. T. Marcus, P. Dorfmüller, *et al.*, "Right ventricular diastolic impairment in patients with pulmonary arterial hypertension," *Circulation*, vol. 128, no. 18, pp. 2016–2025, 2013.

[36] K. Chatterjee and B. Massie, "Systolic and diastolic heart failure: differences and similarities," *Journal of cardiac failure*, vol. 13, no. 7, pp. 569–576, 2007.

[37] L. E. Hudsmith, S. E. Petersen, J. M. Francis, M. D. Robson, and S. Neubauer, "Normal human left and right ventricular and left atrial dimensions using steady state free precession magnetic resonance imaging," *Journal of cardiovascular magnetic resonance*, vol. 7, no. 5, pp. 775–782, 2005.

[38] B. Sievers, M. Addo, F. Breuckmann, J. Barkhausen, and R. Erbel, "Reference right atrial function determined by steady-state free precession cardiovascular magnetic resonance," *Journal of Cardiovascular Magnetic Resonance*, vol. 9, no. 5, pp. 807–814, 2007.

[39] A. M. Maceira, S. K. Prasad, M. Khan, and D. J. Pennell, "Reference right ventricular systolic and diastolic function normalized to age, gender and body surface area from steady-state free precession cardiovascular magnetic resonance," *European heart journal*, vol. 27, no. 23, pp. 2879–2888, 2006.

[40] P. Argiento, R. R. Vanderpool, M. Mulè, M. G. Russo, M. D'Alto, E. Bossone, N. C. Chesler, and R. Naeije, "Exercise stress echocardiography of the pulmonary circulation: limits of normal and sex differences," *Chest*, vol. 142, no. 5, pp. 1158–1165, 2012.

[41] M. Demir and E. Acartürk, "Clinical characteristics influence left and right ventricular diastolic function in healthy individuals," *Angiology*, vol. 52, no. 1, pp. 25–30, 2001.

[42] Edwards, "Normal hemodynamic parameters and laboratory values," *Edwards Corp.*, vol. 2, 2014.

[43] L. G. Rudski, W. W. Lai, J. Afilalo, L. Hua, M. D. Handschumacher, K. Chandrasekaran, S. D. Solomon, E. K. Louie, and N. B. Schiller, "Guidelines for the echocardiographic assessment of the right heart in adults: a report from the american society of echocardiography: endorsed by the european association of echocardiography, a registered branch of the european society of cardiology, and the canadian society of echocardiography," *Journal of the American Society of Echocardiography*, vol. 23, no. 7, pp. 685–713, 2010.

[44] S. A. Luis, J. Chan, and P. A. Pellikka, "Echocardiographic assessment of left ventricular systolic function: an overview of contemporary techniques, including speckle-tracking echocardiography," in *Mayo Clinic Proceedings*, vol. 94, pp. 125–138, Elsevier, 2019.

[45] H. Saiki, B. W. Eidem, T. Ohtani, M. A. Grogan, and M. M. Redfield, "Ventricular-arterial function and coupling in the adult fontan circulation," *Journal of the American Heart Association*, vol. 5, no. 9, p. e003887, 2016.

[46] N. Kachenoura, E. Bollache, A. Redheuil, S. Clément-Guinaudeau, L. Perdrix, B. Diebold, M. Ladouceur, and E. Mousseaux, "Right ventricular diastolic function evaluation in magnetic resonance imaging," in *2015 Computing in Cardiology Conference (CinC)*, pp. 89–92, IEEE, 2015.

[47] D. Fitchett, D. Sugrue, C. MacArthur, and C. Oakley, "Right ventricular dilated cardiomyopathy.," *Heart*, vol. 51, no. 1, pp. 25–29, 1984.

[48] S. F. Nagueh, O. A. Smiseth, C. P. Appleton, B. F. Byrd, H. Dokainish, T. Edvardsen, F. A. Flachskampf, T. C. Gillebert, A. L. Klein, P. Lancellotti, *et al.*, "Recommendations for the evaluation of left ventricular diastolic function by echocardiography: an update from the american society of echocardiography and the european association of cardiovascular imaging," *European Journal of Echocardiography*, vol. 17, no. 12, pp. 1321–1360, 2016.

[49] J.-N. Liao, T.-F. Chao, J.-Y. Kuo, K.-T. Sung, J.-P. Tsai, C.-I. Lo, Y.-H. Lai, C.-H. Su, C.-L. Hung, H.-I. Yeh, *et al.*, "Age, sex, and blood pressure-related influences on reference values of left atrial deformation and mechanics from a large-scale asian population," *Circulation: Cardiovascular Imaging*, vol. 10, no. 10, p. e006077, 2017.

[50] M. Federmann and O. Hess, "Differentiation between systolic and diastolic dysfunction," *European heart journal*, vol. 15, no. suppl_D, pp. 2–6, 1994.

[51] T. M. Gorter, M. Rienstra, and D. J. van Veldhuisen, "Right ventricular dysfunction in heart failure with reduced vs. preserved ejection fraction: non-identical twins?," *European Journal of Heart Failure*, vol. 19, no. 7, pp. 880–882, 2017.

[52] M. A. Gatzoulis, A. L. Clark, S. Cullen, C. G. Newman, and A. N. Redington, "Right ventricular diastolic function 15 to 35 years after repair

of tetralogy of fallot: restrictive physiology predicts superior exercise performance," *Circulation*, vol. 91, no. 6, pp. 1775–1781, 1995.

[53] S. Kutty, A. M. Valente, M. T. White, K. Hickey, D. A. Danford, A. J. Powell, and T. Geva, "Usefulness of pulmonary arterial end-diastolic forward flow late after tetralogy of fallot repair to predict a "restrictive" right ventricle," *The American journal of cardiology*, vol. 121, no. 11, pp. 1380–1386, 2018.

[54] X. Monnet, P. E. Marik, and J.-L. Teboul, "Prediction of fluid responsiveness: an update," *Annals of intensive care*, vol. 6, no. 1, p. 111, 2016.

[55] K.-P. Rommel, M. von Roeder, C. Oberueck, K. Latuscynski, C. Besler, S. Blazek, T. Stiermaier, K. Fengler, V. Adams, M. Sandri, *et al.*, "Load-independent systolic and diastolic right ventricular function in heart failure with preserved ejection fraction as assessed by resting and hand-grip exercise pressure–volume loops," *Circulation: Heart Failure*, vol. 11, no. 2, p. e004121, 2018.

[56] R. D. Miller, L. Eriksson, L. A. Fleisher, J. P. Wiener-Kronish, and W. L. Young, "Miller's anesthesia," in *Miller's anesthesia*, pp. 2827–2827, 2010.

[57] E. H. Stephens, M. Y. Qureshi, J. H. Anderson, E. Ashikhmina, and J. A. Dearani, "Bidirectional cavopulmonary shunt for right ventricular unloading," *The Annals of Thoracic Surgery*, 2020.

[58] J. Woods, P. Monteiro, and A. Rhodes, "Right ventricular dysfunction," *Current opinion in critical care*, vol. 13, no. 5, pp. 532–540, 2007.

[59] Y. Appelman, B. B. van Rijn, E. Monique, E. Boersma, and S. A. Peters, "Sex differences in cardiovascular risk factors and disease prevention," *Atherosclerosis*, vol. 241, no. 1, pp. 211–218, 2015.

[60] S. Purkiss and V. F. Huckell, "Cardiovascular physiology: similarities and differences between healthy women and men," *Journal of Obstetrics and Gynaecology Canada*, vol. 19, no. 8, pp. 853–859, 1997.

[61] L. Schiebinger and I. Klinge, "Gendered innovation in health and medicine," in *Sex-Specific Analysis of Cardiovascular Function*, pp. 643–654, Springer, 2018.

[62] M. C. Schwartz, A. C. Glatz, and M. J. Gillespie, "Valvular insufficiency and heart failure," in *Heart Failure in the Child and Young Adult*, pp. 297–306, Elsevier, 2018.

[63] G. Jackson, C. Gibbs, M. Davies, and G. Lip, "Abc of heart failure: Pathophysiology," *BMJ: British Medical Journal*, vol. 320, no. 7228, p. 167, 2000.

5 | III Application: Ventricular outflow obstruction

Contents

In this chapter, left and right ventricular outflow tract obstructions are analyzed. A simple and reliable numerical tool for the prediction of the pressure gradient and the cardiac output as a function of the obstruction size is developed, considering the case of a 2 year-old baby girl. Conditions from totally open up to almost completely closed tract are represented. Both the left and the right obstruction results in pressure gradient increasing and cardiac output decreasing as the narrowing of the tract worsens, as expected. The occlusion is found to impact mainly on the ventricular pressure and on cardiac output when it is placed in the left and right outflow tract, respectively, as clinically observed.

5.1 Introduction

Ventricular outflow tract (VOT) obstruction is a defect in which either the right or left ventricular outflow tract is partially or completely obstructed. There are several disorders that lead to VOT obstruction. In the pediatric population, on the right side, right VOT (RVOT) is mainly caused by defects in the pulmonary valve, the supravalvular region, or the pulmonary artery, e.g., pulmonary atresia, pulmonary valve stenosis, hypoplastic right heart syndrome, and Tetralogy of Fallot [1]. Analogously, left VOT (LVOT) is mainly due to defects in the aortic valve, or located at the subvalvular or supravalvular level, e.g., aortic valve stenosis, supravalvular aortic stenosis, coarctation of the aorta, and hypoplastic left heart syndrome [2]. Beyond these pathologies, RVOT or LVOT obstruction may also be caused by primary cardiac tumors in the proximity of the pulmonary or aortic valve. Primary cardiac tumors arise in the heart, and, usually, they are characterized by round or oval shape with a smooth or lobulated surface [3].
The indications for intervention have been recently reported by the American Heart Association, but, as Franchi et al. pointed out in [2], the guidelines refer to the peak-to-peak ventriculo-arterial gradient, a measurement derived by cardiac catheterization in sedated patients that is consistently lower than the measurement obtained by echocardiography. The latter is usually computed with the Bernoulli equation, i.e., $\Delta P = 4V^2$, with ΔP the pressure gradient and V the velocity [4], and it is the most common measurement that is used to assess disease severity in clinical practice. Moreover, the application of the Bernoulli equation in VOT is debatable as it assumes that pre-stenosis velocity can be neglected, i.e., less than 1 m/s, which may not be the case in LVOT, especially if cardiomyopathy or other issues (e.g., serial stenoses) are present [5, 6]. For these reasons, the simplified Bernoulli equation should overestimate ΔP, however, factors as poor alignment of the beam and low sampling may result in underestimation of the pressure gradient. Thus, the possibility to develop a mathematical model able to correlate the percentage of VOT obstruction to the pressure gradient and the cardiac output may help improve the evaluation of lesion severity and consequently clinical management.
Despite the clinical relevance of VOT (e.g., considering only the case of valvular aortic stenosis, which accounts for 3% to 6% of CHD with an incidence of 2.5-5 per 10000 live births [2]), the case of aortic valve stenosis in adults is, to the best of our knowledge, the only obstructive condition to which engineering research has devoted attention [7, 8, 9]. The physical and mathematical-numerical models that have been proposed over the years to

describe transvalvular hemodynamics are numerous, and with varying degrees of detail, e.g., from bulk flow parameters to local flow kinematic and dynamics, from rigid valve geometry to time dependent geometry, calcification modeling, and so on [8, 9, 10, 11, 12]. Modeling of obstructions other than aortic stenosis has been only sporadic, and in any case limited to the adult population.
The aim of this chapter is to derive a numerical model able to reproduce the hemodynamic changes that arise when the right or left VOT is obstructed, and to relate the percentage of obstruction to overall hemodynamic quantities. This work refers to a generic obstructive condition of the ventricular outflow tract, right or left. A lumped-parameter model of the complete circulation is coupled to a local model of hemodynamics through the narrowing so that, once the degree of obstruction is fixed in percentage terms with respect to the size of the outflow, the cardiac output, and the mean and peak pressure gradient through the obstruction are calculated. Particularly, the scenario investigated by the simulations refers to a 2-year-old female patient. The reason for the choice of the pediatric scenario is that obstructions in infants may be fatal much earlier than in adults due to the rapid rate of occlusion growth and the small dimension of the heart that makes ventricular obstructions more dangerous in infants than in adults [13].

5.2 Methods

5.2.1 Hemodynamic model

From the fluid dynamic point of view any cardiovascular obstruction, located in either vessels or heart chambers, can be seen as an obstacle to blood flow and, as such, as a source of disturbances that subtract mechanical energy to the bulk flow in the form of an irreversible pressure loss. When the bulk flow develops along one main direction, as in the case of vessels or, for the heart chambers, in the left or right ventricular outflow tract, the behavior of the obstructed blood flow can be effectively described by means of the classical equations of one-dimensional hydrodynamics [14]. Such an approach has been widely adopted to investigate cardiovascular flows in either physiological or pathological conditions. For example, a large amount of work has been done in the past twenty years to develop mathematical models able to reliably predict the pressure gradient across a stenotic aortic valve [7, 9].
Here, following that same approach, the blood flow through an obstruction located in either the right or the left ventricular outflow tract (such as a localized tumor mass, a subvalvular stenosis, or a supravalvular stenosis)

is assimilated to the one-dimensional flow in a circular pipe of diameter D and area A, partly occluded by the obstruction (Fig. 5.1a). The latter is geometrically described by the minimum cross-sectional area that the obstacle locally leaves free to the bulk flow, A_{free}. Due to the narrowing of the pipe, the flow is not able to maintain its proximal undisturbed character but rather behaves as depicted in Fig. 5.1b, i.e., it initially contracts up to the minimum area and then expands exhibiting distal vortices that cause blood pressure to decrease irreversibly due to viscous energy dissipation. The resulting pressure gradient across the obstruction, Δp_{obs}, which is the difference between the left (right) ventricle pressure Plv (Prv) and the pressure distal to the obstacle, p_{obs} can hence be calculated as (see Section 2.6 for details)

$$\Delta p_{obs} = K_{obs} \cdot Q^2 \tag{5.1}$$

where Q is the (instantaneous) flow rate through the obstruction (i.e., the flow rate ejected by the left or the right ventricle, depending on the obstruction location) and K_{obs} is a coefficient that depends on the shape and size of the obstacle. Following the approach reported in [7], the latter is here assumed as

$$K_{obs} = f_{shape} \frac{1}{2g} \left(\frac{1}{A_{free}} - \frac{1}{A} \right)^2 \tag{5.2}$$

with g the gravity acceleration and f_{shape} a factor $\geqslant 1$ that accounts for the obstruction morphology.

Eq. (5.1) and (5.2) represent the mathematical model of the flow in the narrowing, and allow the calculation of the pressure gradient across the obstruction Δp_{obs} given the narrowing ratio A_{free}/A and the ejected flow rate Q. However, it is worth stressing that the presence of the obstruction in the left (right) ventricular outflow tract may significantly impact on the cardiac output CO that the heart can eject, i.e., on the flow rate Q itself. For that reason, and in order to calculate not only Δp_{obs} but also Q and CO as a function of A_{free}/A, Eq. (5.1) and (5.2) are coupled to a previously developed lumped-parameter model (0D) of the complete cardiovascular circulation [15]. The 0D model reduces the cardiovascular system to the sum of multiple functional compartments (e.g., atria and ventricles, large arteries, microvasculature), and describes the hydrodynamic functionality of each compartment by suitably relating the local instantaneous pressure and blood flow rate/volume. Parameters peculiar to each compartment (e.g, heart chambers' elastance, large vessels' compliance, microvasculature's resistance) are adopted to characterize the compartment functionality and account for its effect on the complete circulation. As a result, the instanta-

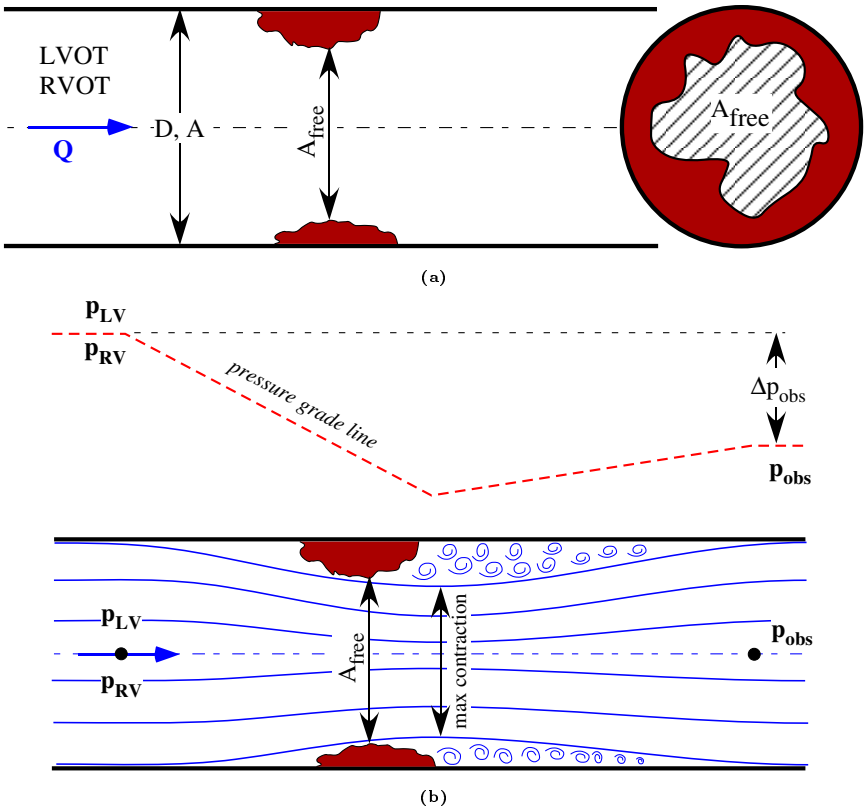

Figure 5.1: *(a) Scheme of the ventricular outflow tract simulated as a one-dimensional flow in a circular pipe of diameter D and area A. The obstruction reduces the cross-sectional area to the minimum Afree. (b) Streamlines of the flow and the pressure grade line (red dashed line) due to the presence of the obstruction. The obstruction causes a pressure drop which is only partially recovered in the downstream section, determining a pressure gradient Δp_{obs}. Eddies are present only on the downward section towards the artery. LVOT (RVOT), left (right) ventricular outflow tract, Q, the flow rate, Plv (Prv), pressure in the left (right) ventricle, and pobs, pressure distal to the obstruction.*

neous pressure and flow rate (or volume, in the case of cardiac chambers) are obtained in each compartment from the 0D model. A complete description of the model itself is given in Chapter 2. Here, it is just recalled that the model describes the flow across the heart valves by a relationship of the kind $\Delta p_v = R_v \cdot Q$, where Δp_v is the transvalvular pressure drop and R_v is the valve resistance parameter. For the aortic and pulmonary valve case, in particular, values for R_v are assumed such that normo-functioning valves are simulated, i.e., the pressure gradient across the valve results to be negligible and does not affect the pressure gradient due to the obstruction located in the ventricular outflow tract.

5.2.2 Simulations

Conditions pertaining to preserved cardiovascular functionality are reproduced despite the presence of the obstruction, i.e., no compensatory mechanism is accounted for even in the most severe obstruction condition. A child case of about 2 year-old with a heart rate HR = 111 bpm, body surface area BSA = 0.55 m^2, body mass BM = 12 Kg, and left (right) ventricular diameter D = 0.9 cm (D = 1.07 cm) is considered. Physiological values for that case are assigned to the functional parameters contained in the 0D model (see Subsection 5.2.4).
The 0D model alone is first implemented (i.e., no obstruction in either the left or the right ventricular outflow tract is considered) to calculate healthy hemodynamics and compare results with clinical data for model validation. Then, the 0D model coupled with Eq. (5.1) and (5.2) is repeatedly run to reproduce the cardiovascular circulation in presence of the obstruction. Both the cases of obstruction located in the left and in the right ventricular outflow tract are investigated. Simulations are performed for various degrees of obstruction severity by varying the narrowing ratio A_{free}/A in the range $0.05 - 1$, 1 being the case of ventricular outflow tract free from obstruction and 0.05 the case of ventricular outflow tract almost completely occluded. Lower A_{free}/A ratios are not considered because a further reduction of the flow area determines nonrealistic pathological conditions ($\sim$ null cardiac output). The shape factor f_{shape} contained in Eq. (5.2) is assumed equal to 1, i.e., an ideal round, annular, concentric morphology is assigned to the narrowing that obstructs the outflow tract (Fig. 5.2).

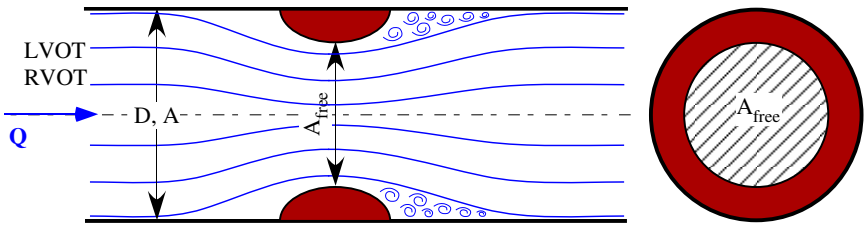

Figure 5.2: *Streamlines of the flow due to the presence of an ideal round obstruction, reported on the right.*

Results computed for each obstructed condition are also post-processed to obtain relevant hemodynamic parameters according to the following relationships

$$CO = \frac{1}{T}\int_T Q dt \tag{5.3}$$

T being the period of one heartbeat;

$$\Delta p_{obs,mean} = \frac{1}{T}\int_{T_e} \Delta p_{obs} dt \tag{5.4}$$

where $\Delta p_{obs,mean}$ is the mean pressure gradient across the obstacle, calculated in the ejection period T_e. The peak value of the gradient, $\Delta p_{obs,peak}$, is extracted as the maximum gradient calculated in one heartbeat.
Finally, a sensitivity analysis of model results to the shape factor f_{shape} is performed, which is varied in a realistic range estimated as explained in Subsection 5.2.3.

5.2.3 Sensitivity analysis of model results to the shape factor fshape

The simulations are conducted assuming $f_{shape} = 1$, i.e., considering that the blood flow approaching the obstruction contracts until it assumes A_{free} as a minimum transverse dimension. However, it is reasonable to think that the contraction may be, in reality, more pronounced in relation to the morphology of the obstruction, as the literature on 'orifice flows' has amply demonstrated (see, for example, [14]). In this case, the minimum transverse dimension of the flow through the obstruction is smaller than A_{free}, and can be expressed as $Cc \cdot A_{free}$ where Cc is the contraction coefficient ([14]). As a result, the f_{shape} factor assumes values greater than the unit. To estimate a realistic range of variability of f_{shape} it is convenient to rewrite the coefficient K_{obs} given by equation Eq. (5.2) as

$$K_{obs} = \frac{1}{2g}\left(\frac{1}{Cc \cdot A_{free}} - \frac{1}{A}\right)^2 \tag{5.5}$$

which immediately provides the relationship between the form factor and the size of the contraction

$$f_{shape} = \left(\frac{A - Cc \cdot A_{free}}{Cc \cdot A - Cc \cdot A_{free}}\right)^2. \tag{5.6}$$

In the literature there are numerous works that report the behavior of the contraction coefficient as the ratio between the orifice area and the area of the pipe, i.e., A_{free}/A. Here, it is referred to the report proposed by Ferrari [16], which proves to be in excellent agreement also with what illustrated in [17] for the case of flow through stenotic valve orifices. The trend of f_{shape} as a result of A_{free}/A, and assumed as range for the sensitivity analysis, is

shown in Fig. 5.3.

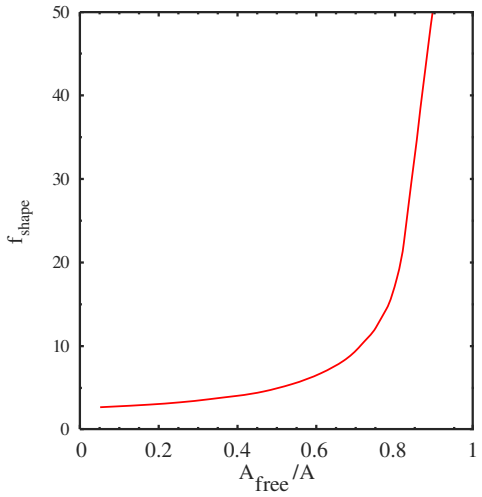

Figure 5.3: *The trend of f_{shape} as a result of A_{free}/A.*

5.2.4 Parameters' Values

To replicate the physiological hemodynamics, the 0D model is adequately calibrated as previously reported [15]. The total peripheral resistance (R_{tot}) for any compartment represented by Fig. 5.5b is calculated by considering a perfusion pressure of 65 mmHg [18], a cardiac output (CO) of 2.1 L/min [19], and the percentage of CO that supplies each organ [19, 20, 21]. Each resistance is computed considering $R_{art} = 5\% \cdot R_{tot}$, $R_{vb} = 92\% \cdot R_{tot}$, and $R_{ven} = 3\% \cdot R_{tot}$. Note, a fine tuning of the portal system resistance is performed to replicate the flow from the portal vein to the liver [15]. Given the resistance values, the corresponding arterial compliance (C_{art}) is computed harnessing the time constant of the systemic arterial system, $\tau = 0.81$ s, as $C_{art} = \tau / R_{vb}$ [20]; whereas the venous compliance is considered 30 times greater than C_{art} [19]. For the great vessels, resistance values in agreement with the allometric law of Baretta et al. [22] are imposed, adjusting the compliances to obtain the total compliance in the range of 2.0−2.5 mL/mmHg/kg [20]. For the pulmonary circulation, the compliance values are adjusted from [23], and the resistance values are derived as described above considering a pulmonary time constant of $\tau = 0.2$ s [20]. Inductance values are taken from [24] and adjusted considering the allometric law of Baretta et al. [22]. For the heart parameters, values from [20, 25] are imposed. Particularly, $V_{p=0}$ of Eq. (2.6) is adjusted to obtain the specific pediatric hemodynamics, whose values are then kept constant during the simulation of the left/right ventric-

ular outflow tract obstruction. Note that, the methodology here described to calibrate the pediatric model derives from the calibration of adult models. However, since the values result from pediatric-specific parameters (e.g., CO of 2.1 L/min) and adjustments by the allometric laws are performed, the methodology is reliable also for the pediatric population. Moreover, a sensitivity analysis is also performed.

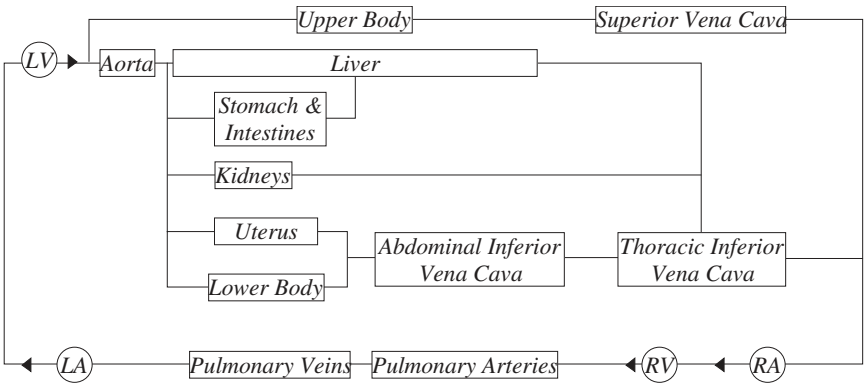

Figure 5.4: *Physiological circulation model. The model is composed by the aorta, Ao, the liver, the gastro-intestinal tract, the kidneys, the upper and lower body, the abdominal and thoracic inferior vena cava, IVCab and IVCth, respectively, the superior vena cava, SVC, the pulmonary arteries and veins, PuA and PuVe, respectively, and, the four heart chambers: left ventricle, LV, left atrium, LA, right ventricle, RV, right atrium LA, and ▶, heart valves.*

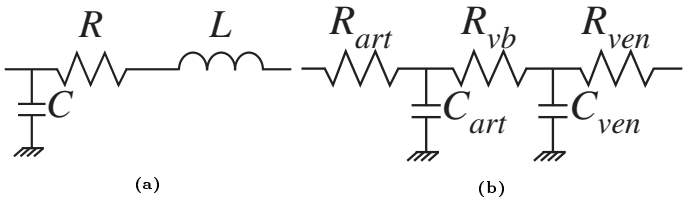

Figure 5.5: *Lumped scheme for (a) great vessels, and (b) organs of interest. R, resistance, C, capacitance, L, inductance, R_{art}, arterial-arteriolar resistance, R_{vb}, vascular bed resistance, R_{ven}, venous resistance, C_{art}, arterial-arteriolar compliance, and C_{ven}, venous compliance.*

5.3 Results

Table 5.1 shows the comparison between the output of the healthy baby 0D model and literature data for the pediatric population [26]. Physiological aortic pressure and flow rate calculated by the 0D model are reported in

Fig. 5.6, together with published *in vivo* measurements obtained in pediatric subjects.

Table 5.1: *Comparison of model hemodynamics with literature data specific for the pediatric case given as physiological ranges [26].*

Parameter	Unit	Model output	Reference
SVR	[mmHg·s/mL]	2.1	1.5-2.1
SBP	[mmHg]	97	90-110
DBP	[mmHg]	69	65-75
Prv	[mmHg]	21/5**	15-23/3-7
Ppua	[mmHg]	17/10**	15-23/10-16
Pla	[mmHg]	6.5*	5-10
Plv	[mmHg]	100/4**	90-110/7-9
Pra/CVP	[mmHg]	7.7*	2-6
CO	[L/min]	2.2	1.3-2.7

HR, heart rate, SVR, systemic vascular resistance, SBP, systolic blood pressure, DBP, diastolic blood pressure, Pra, right atrial pressure, Prv, right ventricular pressure, Ppua, pulmonary artery pressure, Pla, left atrial pressure, Plv, left ventricular pressure, CVP, central venous pressure, CO, cardiac output. $*$ mean value, $**$ systolic/diastolic values.

Fig. 5.7 compares the results obtained from the model for the physiologic case (panel (a)) and, as an example of obstruction in the LVOT, for the $A_{free}/A = 0.525$ case (panel (b)). Computed waveforms for obstructions located in the RVOT are not reported for sake of brevity.

The behavior of the mean and the peak pressure gradient across the obstruction as a function of the narrowing ratio A_{free}/A is shown in Fig. 5.8 (left panel: LVOT obstructions; right panel: RVOT obstructions). Possible threshold values for the mean (peak) pressure gradient as inferred from the literature are also drawn for comparison [27, 28, 29].

The reduction in the cardiac output calculated as the left (right) outflow tract obstruction worsens is plotted in Fig. 5.9.

5.4 Model Sensitivity Analysis

A model sensitivity analysis for the healthy case is shown in Fig. 5.10. A total of 21 input parameters are tested with sensitivities calculated after an increase of 25% [20]. 54 output signals are chosen for the analysis.
Table 5.2 reports the mean sensitivity with inputs and outputs ordered based on the global influence and overall sensitivity, respectively. In Fig. 5.10 the graphical representation of the sensitivity is reported (the outputs are ordered with the most sensitive on the left, and the inputs are ordered with the most influential at the bottom). The most influential parameters are those

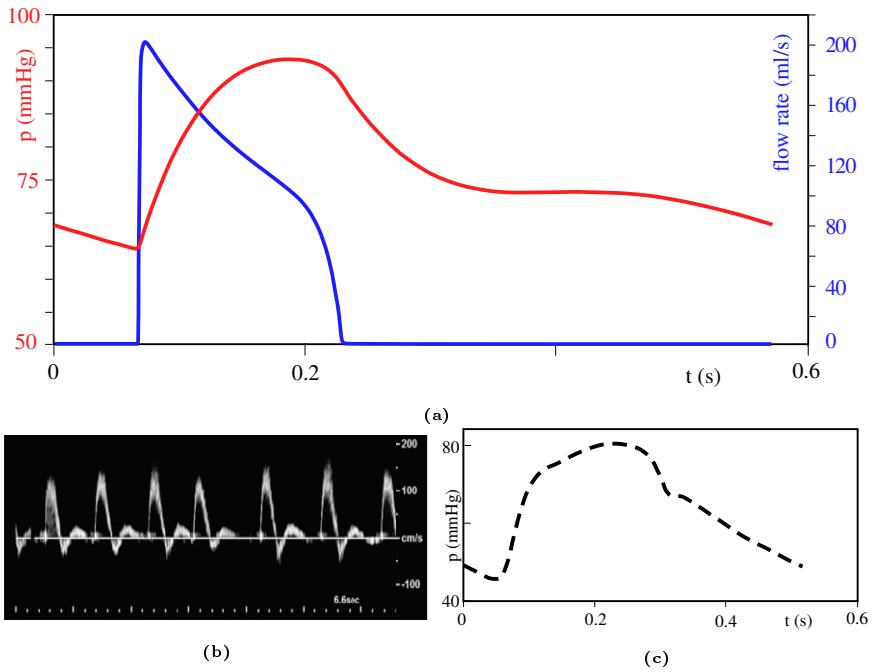

Figure 5.6: *(a) 0D model results for the physiologic case (aortic pressure, red curve; aortic flow rate, blue curve). (b) and (c) published in vivo data (aortic Doppler velocity waveform and aortic pressure). Note that, by assuming a constant valve area, the velocity waveform resembles the flow one except for the absolute values and the scale.*

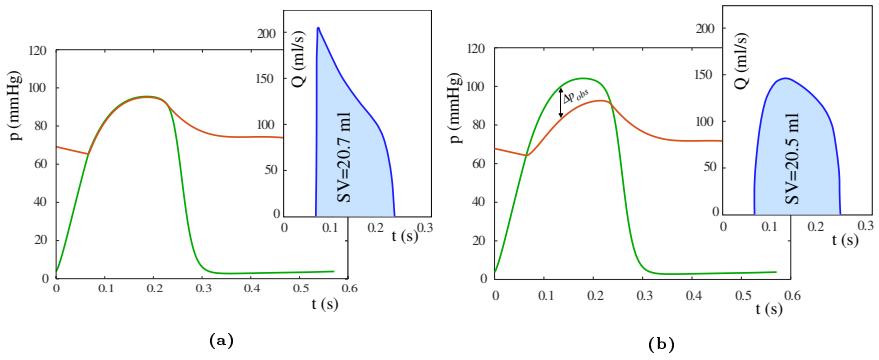

Figure 5.7: *Left ventricle pressure (green), aortic pressure (red) and aortic flow rate (blue) as calculated by the model for the physiologic case (panel (a)) and the case of obstruction located in the LVOT with* $A_{free}/A = 0.525$ *(panel (b)).*

related to the ventricular volume-related parameters ($V_{p=0}$) of Eq. (2.6) and PVR. The former is a mathematical construction that is kept constant during the simulations and thus it is not affecting the outcomes. Moreover, as reported in previous chapters, $V_{p=0}$ reflects chamber's dimension, thus, it

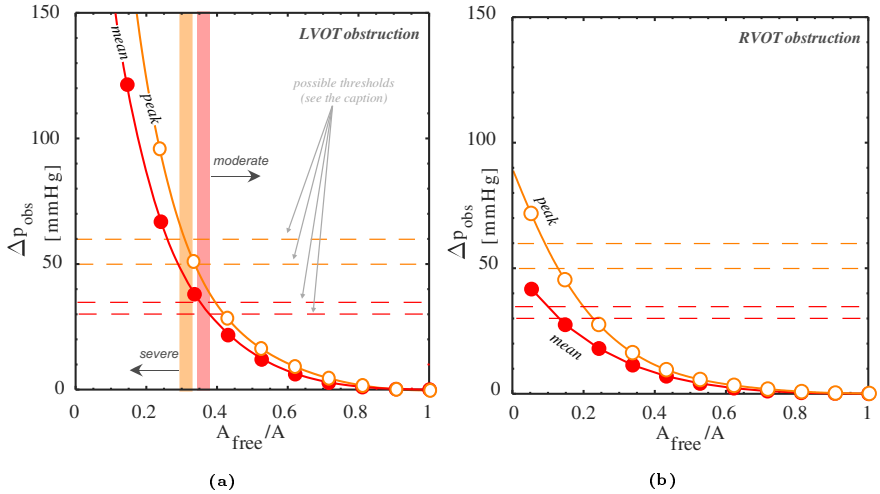

Figure 5.8: *Computed mean (red filled dotted line) and peak (orange open dotted line) pressure gradient for (a) LVOT and (b) RVOT obstruction. Dashed lines depict possible thresholds for moderate/severe obstruction, inferred from the literature as it follows: mean gradient 30 mmHg [28] and 35 mmHg [27], red lines; peak gradient 50 mmHg [29] and 60 mmHg [27], orange lines.*

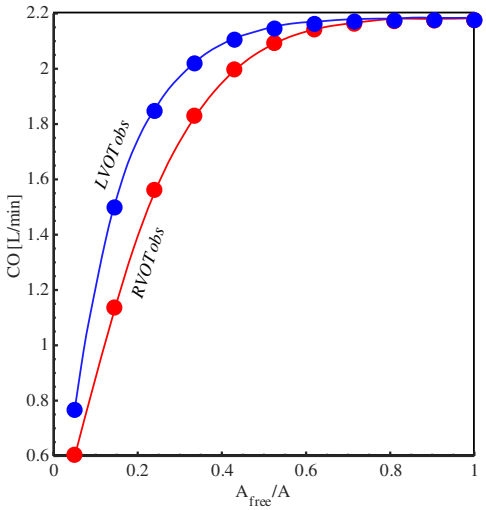

Figure 5.9: *Cardiac output (CO) reduction as the obstruction worsens for LVOT (blue) and RVOT (red).*

is realistic that higher/lower values affect the overall hemodynamics. The latter reproduces the pulmonary vascular resistance that is known to be particularly high and influential in infants due to the changing from the fetal to the adult circulation. Thus the model captures the high influence of PVR, suggesting also that particular attention has to be posed on the value to be

assigned to this parameter when simulating a specific case to assure the results' correspondence to real data. The atrial and right ventricular volumes are the most sensitive outputs. These dependencies may be ascribed (again) to PVR. In fact, since PVR is the afterload of the pulmonary circulation, its value affects not only the right heart but also LA due to the connection through the pulmonary veins. On the other hand, the left ventricle is not affected by PVR because it is completely separated from the pulmonary circulation (result found also in Ch. 3). Note, however, that Fig. 5.10 shows a cluster of larger data points on the left side meaning that only these few outputs are more sensitive to the variation of the inputs. The least sensitive outputs signals are the flows of the systemic organs considered, meaning that their overall amount of blood is not influenced by variations in the inputs.

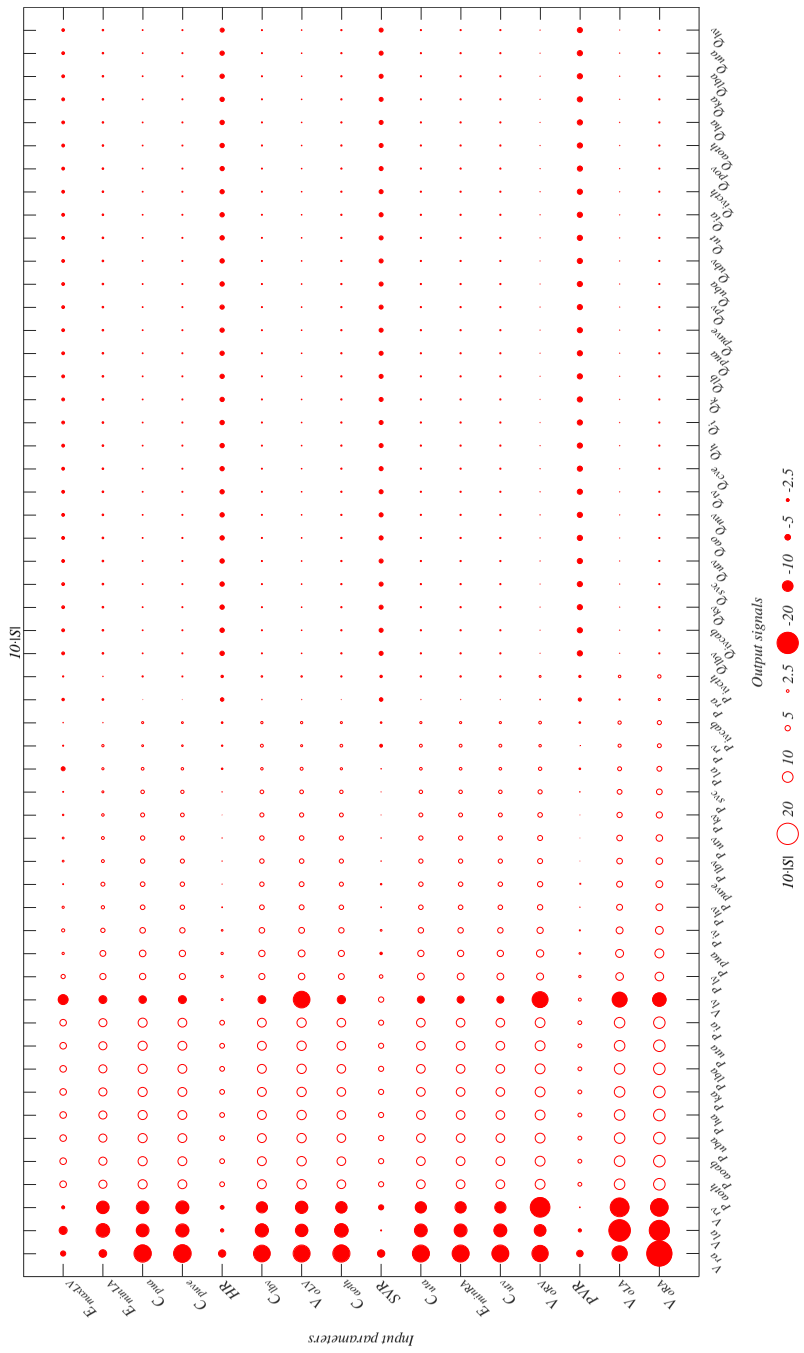

Figure 5.10: *Graphical representation of the sensitivity of the outputs to the 25% variation of the inputs for the 0D model. A larger symbol corresponds with higher sensitivity and filled/empty circles correspond to negative/positive S. Outputs are ordered according to the overall sensitivity (the most sensitive on the left) and inputs are ordered based on the global influence (the most influential at the bottom).*

Table 5.2: *Mean sensitivities (S) of output signals to the input parameters. The inputs are ordered based on the global influence (the most influential on the left), the outputs are ordered based on the overall sensitivity (the most sensitive at the top). Note that, due the limited space, only the first 16 most influential inputs are here reported.*

	VoRA	**VoLA**	**PVR**	**VoRV**	**Cutv**	**EminRA**	**Cuta**	**SVR**	**Caoth**	**VoLV**	**Clbv**	**HR**	**Cpuve**	**Cpua**	**EminLA**	**EmaxLV**
Vra	-2.367	-1.441	-0.611	-1.534	-1.593	-1.593	-1.593	-0.685	-1.606	-1.595	-1.571	-0.681	-1.657	-1.626	-0.714	-0.484
Vla	-1.891	-2.021	-0.302	-1.104	-1.209	-1.210	-1.209	-0.097	-1.273	-1.169	-1.237	-0.309	-1.234	-1.202	-1.281	-0.755
Vrv	-1.654	-1.763	-0.070	-1.845	-1.059	-1.059	-1.059	-0.483	-1.079	-1.158	-1.049	-0.350	-1.212	-1.186	-1.176	-0.286
Paoth	1.086	0.993	0.361	0.924	0.816	0.817	0.815	0.483	0.812	0.878	0.836	0.451	0.832	0.857	0.761	0.622
Paoab	1.085	0.993	0.361	0.923	0.816	0.816	0.815	0.482	0.811	0.877	0.835	0.450	0.831	0.856	0.760	0.621
Puba	1.084	0.991	0.360	0.922	0.814	0.815	0.813	0.481	0.810	0.876	0.834	0.449	0.830	0.855	0.759	0.620
Pha	1.083	0.990	0.359	0.921	0.814	0.814	0.812	0.480	0.809	0.875	0.833	0.448	0.829	0.854	0.758	0.619
Pka	1.083	0.990	0.359	0.921	0.813	0.814	0.812	0.480	0.808	0.875	0.833	0.448	0.829	0.853	0.758	0.619
Plba	1.083	0.990	0.359	0.921	0.813	0.814	0.812	0.480	0.808	0.875	0.833	0.448	0.829	0.854	0.758	0.619
Puta	1.083	0.990	0.359	0.921	0.813	0.814	0.812	0.480	0.808	0.875	0.833	0.448	0.829	0.853	0.758	0.619
Pia	1.079	0.987	0.357	0.918	0.811	0.811	0.809	0.477	0.806	0.872	0.830	0.445	0.826	0.850	0.754	0.616
Vlv	-1.272	-1.402	0.274	-1.499	-0.659	-0.661	-0.660	0.499	-0.773	-1.565	-0.735	0.181	-0.743	-0.708	-0.737	-0.936
Plv	0.809	0.721	0.216	0.656	0.636	0.635	0.636	0.336	0.549	0.612	0.574	0.225	0.569	0.592	0.583	0.402
Ppua	0.835	0.748	0.158	0.683	0.592	0.592	0.592	-0.233	0.572	0.639	0.596	0.214	0.596	0.618	0.547	0.214
Piv	0.733	0.649	0.107	0.587	0.510	0.510	0.510	0.166	0.504	0.545	0.526	0.159	0.503	0.525	0.405	0.296
Phv	0.640	0.558	0.038	0.497	0.428	0.428	0.428	0.081	0.422	0.457	0.443	0.078	0.415	0.436	0.309	0.207
Ppuve	0.642	0.558	0.001	0.496	0.418	0.418	0.418	-0.138	0.388	0.454	0.411	0.028	0.412	0.433	0.373	-0.086
Plbv	0.615	0.531	0.012	0.469	0.398	0.398	0.398	0.049	0.392	0.427	0.416	0.037	0.385	0.407	0.271	0.168
Putv	0.614	0.531	0.012	0.468	0.398	0.399	0.398	0.050	0.392	0.427	0.415	0.038	0.385	0.407	0.271	0.169
Pkv	0.580	0.497	-0.013	0.435	0.368	0.368	0.368	0.018	0.362	0.394	0.384	0.008	0.352	0.374	0.236	0.136

Continued on Next Page.

Table 5.2 – Continued

	VoRA	VoLA	PVR	VoRV	Cutv	EminRA	Cuta	SVR	Caoth	VoLV	Clbv	HR	Cpuve	Cpua	EminLA	EmaxLV
Psvc	0.535	0.453	-0.047	0.391	0.328	0.328	0.328	-0.024	0.321	0.350	0.344	-0.033	0.309	0.331	0.188	0.092
Pla	0.456	0.376	-0.149	0.316	0.250	0.250	0.250	-0.047	0.211	0.275	0.233	-0.151	0.235	0.255	0.206	-0.373
Prv	0.369	0.291	-0.010	0.232	0.267	0.267	0.267	-0.269	0.252	0.192	0.274	-0.136	0.153	0.172	0.215	-0.105
Pivcab	0.390	0.311	-0.154	0.252	0.201	0.201	0.201	-0.156	0.193	0.213	0.215	-0.158	0.173	0.193	0.039	-0.046
Pra	0.197	0.122	-0.297	0.065	0.029	0.029	0.029	-0.334	0.021	0.028	0.042	-0.328	-0.010	0.009	-0.163	-0.232
Pivcth	0.314	0.237	-0.210	0.179	0.134	0.134	0.134	-0.226	0.126	0.140	0.147	-0.224	0.101	0.121	-0.040	-0.118
Qlbv	0.107	0.032	-0.485	-0.025	-0.116	-0.116	-0.116	-0.380	-0.120	-0.062	-0.098	-0.411	-0.100	-0.079	-0.155	-0.270
Qivcab	0.109	0.033	-0.484	-0.023	-0.115	-0.115	-0.115	-0.380	-0.119	-0.061	-0.096	-0.410	-0.098	-0.078	-0.152	-0.269
Qkv	0.106	0.031	-0.483	-0.025	-0.115	-0.115	-0.115	-0.380	-0.119	-0.063	-0.098	-0.408	-0.100	-0.080	-0.153	-0.267
Qsvc	0.106	0.031	-0.484	-0.025	-0.115	-0.115	-0.115	-0.380	-0.119	-0.063	-0.098	-0.408	-0.100	-0.080	-0.152	-0.268
Qutv	0.106	0.030	-0.484	-0.026	-0.116	-0.115	-0.116	-0.380	-0.120	-0.063	-0.099	-0.409	-0.100	-0.080	-0.154	-0.268
Qao	0.100	0.026	-0.487	-0.028	-0.118	-0.118	-0.114	-0.380	-0.121	-0.067	-0.104	-0.404	-0.105	-0.082	-0.158	-0.270
Qmv	0.103	0.030	-0.484	-0.026	-0.115	-0.114	-0.114	-0.379	-0.117	-0.062	-0.099	-0.406	-0.100	-0.079	-0.151	-0.266
Qtv	0.103	0.030	-0.483	-0.026	-0.114	-0.114	-0.114	-0.378	-0.117	-0.062	-0.097	-0.402	-0.100	-0.079	-0.154	-0.264
Qcve	0.104	0.030	-0.482	-0.025	-0.113	-0.113	-0.113	-0.378	-0.117	-0.062	-0.097	-0.401	-0.099	-0.079	-0.149	-0.263
Qh	0.107	0.032	-0.483	-0.024	-0.114	-0.113	-0.115	-0.379	-0.118	-0.062	-0.098	-0.407	-0.099	-0.079	-0.152	-0.267
Qi	0.107	0.032	-0.483	-0.024	-0.114	-0.113	-0.115	-0.379	-0.118	-0.062	-0.098	-0.408	-0.099	-0.079	-0.153	-0.267
Qk	0.106	0.032	-0.483	-0.024	-0.113	-0.113	-0.114	-0.379	-0.117	-0.062	-0.098	-0.406	-0.099	-0.079	-0.152	-0.266
Qlb	0.106	0.032	-0.483	-0.024	-0.113	-0.113	-0.114	-0.379	-0.117	-0.062	-0.098	-0.406	-0.099	-0.079	-0.152	-0.266
Qpua	0.103	0.030	-0.482	-0.026	-0.114	-0.113	-0.114	-0.377	-0.118	-0.062	-0.098	-0.402	-0.099	-0.079	-0.151	-0.264
Qpuve	0.104	0.030	-0.482	-0.025	-0.114	-0.113	-0.115	-0.377	-0.117	-0.062	-0.097	-0.402	-0.099	-0.079	-0.151	-0.264
Qpv	0.104	0.029	-0.482	-0.026	-0.113	-0.114	-0.114	-0.378	-0.118	-0.063	-0.098	-0.401	-0.100	-0.079	-0.151	-0.265
Quba	0.105	0.031	-0.484	-0.025	-0.116	-0.113	-0.113	-0.380	-0.117	-0.062	-0.099	-0.407	-0.098	-0.078	-0.149	-0.267

Continued on Next Page.

Table 5.2 – Continued

	VoRA	VoLA	PVR	VoRV	Cutv	EminRA	Cuta	SVR	Caoth	VoLV	Clbv	HR	Cpuve	Cpua	EminLA	EmaxLV
Qubv	0.107	0.032	-0.483	-0.024	-0.113	-0.113	-0.114	-0.379	-0.117	-0.061	-0.097	-0.406	-0.098	-0.078	-0.152	-0.266
Qut	0.106	0.032	-0.483	-0.024	-0.113	-0.113	-0.115	-0.379	-0.117	-0.062	-0.098	-0.406	-0.099	-0.079	-0.152	-0.266
Qia	0.106	0.033	-0.485	-0.023	-0.115	-0.112	-0.112	-0.380	-0.117	-0.061	-0.098	-0.408	-0.098	-0.077	-0.148	-0.267
Qivcth	0.103	0.030	-0.481	-0.025	-0.113	-0.112	-0.113	-0.377	-0.116	-0.061	-0.097	-0.398	-0.098	-0.079	-0.148	-0.261
Qpov	0.103	0.030	-0.480	-0.025	-0.112	-0.112	-0.112	-0.376	-0.115	-0.061	-0.097	-0.397	-0.098	-0.078	-0.149	-0.260
Qaoth	0.107	0.034	-0.485	-0.022	-0.114	-0.111	-0.111	-0.380	-0.116	-0.060	-0.098	-0.406	-0.097	-0.076	-0.147	-0.265
Qha	0.108	0.034	-0.485	-0.022	-0.113	-0.110	-0.110	-0.380	-0.115	-0.059	-0.097	-0.406	-0.097	-0.076	-0.147	-0.265
Qka	0.107	0.034	-0.484	-0.022	-0.113	-0.110	-0.110	-0.380	-0.115	-0.059	-0.097	-0.405	-0.097	-0.076	-0.146	-0.265
Qlba	0.107	0.034	-0.484	-0.022	-0.113	-0.110	-0.110	-0.380	-0.115	-0.059	-0.097	-0.405	-0.097	-0.076	-0.146	-0.265
Quta	0.108	0.035	-0.484	-0.021	-0.113	-0.110	-0.109	-0.380	-0.114	-0.058	-0.097	-0.405	-0.096	-0.074	-0.146	-0.265
Qhv	0.096	0.027	-0.477	-0.026	-0.109	-0.109	-0.109	-0.373	-0.113	-0.061	-0.096	-0.382	-0.097	-0.078	-0.141	-0.250

Vrv, RV volume, Vra, RA volume, Vlv, LV volume, Vla, LA volume, Paoab, abdominal aortic pressure, Paoth, thoracic aortic pressure, Pha, hepatic arterial pressure, Pia, gastro-intestinal arterial pressure, Pka, renal arterial pressure, Plba, lower body arterial pressure, Puba, upper body arterial pressure, Puta, uterine arterial pressure, Qutv, uterine venous flow, Qh, hepatic flow, Qha, hepatic arterial flow, Qi, gastro-intestinal flow, Qia, gastro-intestinal arterial flow, Qk, renal flow, Qkv, renal venous flow, Qlb, lower body flow, Qsvc, superior vena cava flow, Qubv, upper body venous flow, Qut, uterine flow, Qao, aortic valve pressure, Qaoth, thoracic aortic flow, Qivcab, abdominal inferior vena cava flow, Qka, renal arterial flow, Qlba, lower body arterial flow, Qlbv, lower body venous flow, Qpov, portal vein flow, Quba, upper body arterial flow, Quta, uterine arterial flow, Qcve, caval vein flow, Qmv, mitral valve flow, Qpua, pulmonary arterial flow, Qpuve, pulmonary venous flow, Qpv, pulmonary valve flow, Qivcth, thoracic inferior vena cava flow, Qtv, tricuspid valve flow, Qhv, hepatic venous flow, Pra, RA pressure, Ppua, pulmonary arterial pressure, Piv, gastro-intestinal venous pressure, Plv, LV volume, Pivcth, thoracic inferior vena cava pressure, Phv, hepatic venous pressure, Ppuve, pulmonary venous pressure, Pivcab, abdominal inferior vena cava pressure, Plbv, lower body venous pressure, Putv, uterine venous pressure, Pla, LA pressure, Prv, RV pressure, Pkv, renal venous pressure, Psvc, superior vena cava pressure.

5.5 Discussion

Simulations performed under physiologic unobstructed conditions compare favorably with literature data, thus proving a good representation of the pediatric subjects. The values of global parameters are found to fall within the physiological ranges (Table 5.1) for both the left and right circulation; only the pressure in the caval veins/right atrium is slightly larger than expected, however the difference, smaller than 2 mmHg, falls within the measurement error. Moreover, pressure and flow rate waveform shape predicted by the model is in agreement with those given in the literature (Fig. 5.7a). Notice that the aortic backflow at end-systole is not predicted by the model, since the model simply assumes forward flow for positive and null flow for negative ventricular-aortic pressure difference, respectively. However, the attention is focused on the prediction of the severity of ventricle obstructions, i.e., in the ejection phase only.

As soon as the presence of the obstruction is included in the model, the effects of the obstruction itself appear in model's results. Fig. 5.7b shows that the left ventricular pressure increases while the aortic pressure is almost unchanged, thus resulting in a pressure gradient which is vice versa absent in the unobstructed condition (Fig. 5.7a). Similar findings are reported by [30], for the case of left ventricular outflow obstruction after transcatheter mitral valve replacement in adults. The presence of the obstruction also significantly affects the shape of the ejected flow rate waveform (Fig. 5.7). The steepness of the acceleration branch smooths, the branch peaks at a lower flow rate, the time of peak is delayed in the ejection period, which has a longer duration, and, as a result, the waveform moves from a rather triangular to a bell shape. It is worth noting that such a behavior is recognized to occur in presence of aortic stenosis [31, 32, 33, 34], which further confirm the robustness of the model in predicting obstructed flows characteristics. Notice also that similar results are found when RVOT obstructions are simulated.

As expected, both the mean and the peak pressure gradient, $\Delta p_{obs,mean}$ and $\Delta p_{obs,peak}$, increase as the obstruction becomes more severe (Fig. 5.8). Obstructions located in the LVOT or in the RVOT result in similar exponential behavior, but a larger rate of change of the gradient with A_{free}/A diminishing is found for left obstructions, i.e., LVOT obstructions impact the heart pressure state more heavily than RVOT ones, as it is recognized to occur for aortic vs pulmonary stenosis. This behavior might be related to the ability of RV to adapt to pulmonary valve stenosis, i.e., pressure overload conditions [35]. The degree of the impact, i.e., the obstruction severity, can be

estimated by comparing model predicted gradients to threshold values. For the case of obstructions due to tumors some reference values for the limit between moderate and severe obstruction can be inferred from the recent literature. Dyspnoeic children with left mean pressure gradient greater than 30 mmHg are reported by [28]; the case of a patient with moderate left obstruction, mean gradient 35 mmHg and peak gradient 60 mmHg is described in [27]; finally, Padalino et al. [29] define as significant a left or right obstruction with peak gradient larger than 50 mmHg. By applying the above thresholds to the results (Fig. 5.8), moderate/severe obstruction is found to fall around $A_{free}/A = 0.3 - 0.37$ and $A_{free}/A = 0.1 - 0.15$ for LVOT and RVOT obstruction, respectively. The predicted right critical narrowing ratio might seem so small to be unrealistic. However, such a result is coherent with the statement reported in [35] that "*In moderate-to-severe pulmonary valve stenosis, patients remain asymptomatic until adulthood*". The relationships obtained between the gradient and the level of the obstruction (Fig. 5.8) also provide indications on how much the obstruction should be resected to acceptably lower the pressure gradient, e.g., for the LVOT obstruction case resection leading to A_{free}/A around 0.45 is required to diminish the mean pressure gradient below 20 mmHg, which is typically considered a more than acceptable condition. Hence, the proposed model could potentially help in planning surgical treatments.
RVOT obstructions turn out to affect the cardiac output more than what LVOT ones do (Fig. 5.9). In particular, CO=2.0 L/min (i.e., almost normal) and CO=0.9 L/min (i.e., significantly depressed) is found when the critical pressure gradient (mean gradient about $30 - 35$ mmHg) is attained in the left and in the right outflow tract, respectively. The model hence captures the recognized lower efficiency of the right ventricle to suitably respond to increased afterload [36, 37], suggesting that critical conditions should be defined in terms of cardiac output rather than of pressure gradient when it is the right outflow tract to be obstructed.

5.5.1 Limitations and future developments

The main limitation of the investigation proposed here is that the actual shape of the obstruction is approximated with an ideal round, annular and concentric narrowing, i.e., the actual value of the loss coefficient K_{obs} might be underestimated by Eq. (5.2). However, a sensitivity analysis of model results to the factor f_{shape} is performed to have a first but reliable idea of the importance of obstacle's shape effects. Calculations show that accounting for a larger contraction of the proximal flow due to the real shape of the

obstruction, i.e., a larger K_{obs} for the given A_{free}/A, leads to modest variations of model's predictions for the left case: the critical obstruction (mean and peak pressure gradient equal to about 35 and 50 mmHg, respectively) shifts to $A_{free}/A = 0.48$, with cardiac output still around 2.0 L/min. For the right case, the effects of f_{shape} are found to be so small to be undiscernible. Other limitations are related to the fact that the model does not account for complex geometry seen in many pediatric patients, in particular on those with CHD, and also adaptive and remodeling processes are here neglected. These may have a significant impact on the pressure gradient and the maintenance of cardiac output, and these aspects would need to be studied in more detail in future work. However, the model presented here, despite its simplicity, captures the changes in shape, in pressure gradient, and in cardiac output, suggesting that the main hemodynamic effects are here reproduced. Moreover, the model may be thought of as a first step, reproducing the hemodynamics of children with only a primary cardiac tumor, i.e., without the presence of complex structures.
Despite our promising results, acquisition and analysis of *in vivo* morpho-hemodynamic data of the obstructed outflow tract, together with obstruction classification based on clinical examination of patients, is recommended to further corroborate the model here presented. Future work will hence focus on the creation of a database listing imaging, echo, catheter and other data, and the comparison of *in vivo* data to model's prediction to optimize the estimation of f_{shape} and K_{obs} for a given size, shape, and type of obstruction.

5.6 Conclusion

A lumped-parameter model of the whole circulation able to reproduce the hemodynamic changes that arise when the right or the left ventricular outflow tract is obstructed is developed. Although employing a very simple model and assuming an ideal shape to represent the obstruction, the model reliably predicted the changes in shape, in pressure gradient, and in cardiac output. Thus, the potential of the model in identifying the obstruction size that produces a given pressure gradient and/or a given cardiac output could make the model, with further development and validation, a useful tool for both the prediction of critical conditions and the planning of surgery aimed at restoring normal/acceptable hemodynamics.

Bibliography

[1] T. M. Bashore, "Adult congenital heart disease: right ventricular outflow tract lesions," *Circulation*, vol. 115, no. 14, pp. 1933–1947, 2007.

[2] E. Franchi, M. Cantinotti, N. Assanta, C. Viacava, L. Arcieri, and G. Santoro, "State of the art and prospective for percutaneous treatment for left ventricular outflow tract obstruction," *Progress in Pediatric Cardiology*, vol. 51, pp. 55–61, 2018.

[3] B. Ramlawi and M. J. Reardon, "Cardiac tumors: Treatment," in *Clinical Cardio-Oncology*, pp. 91–119, Elsevier, 2016.

[4] H. Baumgartner, J. Hung, J. Bermejo, J. B. Chambers, A. Evangelista, B. P. Griffin, B. Iung, C. M. Otto, P. A. Pellikka, and M. Quiñones, "Echocardiographic assessment of valve stenosis: Eae/ase recommendations for clinical practice," *Journal of the American Society of Echocardiography*, vol. 22, no. 1, pp. 1–23, 2009.

[5] D. C. Scantlebury, J. B. Geske, and R. A. Nishimura, "Limitations of doppler echocardiography in the evaluation of serial stenoses," *Circulation: Cardiovascular Imaging*, vol. 6, no. 5, pp. 850–852, 2013.

[6] I. Almeida, F. Caetano, J. Trigo, P. Mota, and A. L. Marques, "High left ventricular outflow tract gradient: Aortic stenosis, obstructive hypertrophic cardiomyopathy or both?," *Revista Portuguesa de Cardiologia (English Edition)*, vol. 34, no. 5, pp. 357–e1, 2015.

[7] F. M. Susin, "Complete unsteady one-dimensional model of the net aortic pressure drop," *The Open Biomedical Engineering Journal*, vol. 13, no. 1, 2019.

[8] Z. Keshavarz-Motamed, P. K. Motamed, and N. Maftoon, "Non-invasive determination of transcatheter pressure gradient in stenotic aortic valves: An analytical model," *Medical engineering & physics*, vol. 37, no. 3, pp. 321–327, 2015.

[9] D. Garcia, P. Pibarot, and L.-G. Durand, "Analytical modeling of the instantaneous pressure gradient across the aortic valve," *Journal of biomechanics*, vol. 38, no. 6, pp. 1303–1311, 2005.

[10] J. Bermejo, J. C. Antoranz, I. G. Burwash, J. Alvarez, M. Moreno, M. A. García-Fernández, and C. M. Otto, "In-vivo analysis of the instantaneous transvalvular pressure difference-flow relationship in aortic

valve stenosis: implications of unsteady fluid-dynamics for the clinical assessment of disease severity.," *The Journal of heart valve disease*, vol. 11, no. 4, p. 557, 2002.

[11] G. B. Fiore, M. Grigioni, C. Daniele, G. D'Avenio, V. Barbaro, and R. Fumero, "Hydraulic functional characterisation of aortic mechanical heart valve prostheses through lumped-parameter modelling," *Journal of biomechanics*, vol. 35, no. 10, pp. 1427–1432, 2002.

[12] Y. Aboelkassem, D. Savic, and S. G. Campbell, "Mathematical modeling of aortic valve dynamics during systole," *Journal of theoretical biology*, vol. 365, pp. 280–288, 2015.

[13] M. A. Padalino, C. Basso, G. S. Moreolo, G. Thiene, and G. Stellin, "Left atrial myxoma in a child: case report and review of the literature," *Cardiovascular Pathology*, vol. 12, no. 4, pp. 233–236, 2003.

[14] F. M. White, *Fluid mechanics*. Mcgraw-Hill series in mechanical engineering, 2011.

[15] G. Comunale, F. M. Susin, and J. P. Mynard, "A female-specific cardiovascular lumped-parameter model," in *2020 42nd Annual International Conference of the IEEE Engineering in Medicine Biology Society (EMBC)*, pp. 2654–2657, 42nd Annual International Conferences of the IEEE Engineering in Medicine and Biology Society in conjunction with the 43rd Annual Conference of the Canadian Medical and Biological Engineering Society, 2020.

[16] A. Ferrari, "Fluid dynamics of acoustic and hydrodynamic cavitation in hydraulic power systems," *Proceedings of the Royal Society A: Mathematical, Physical and Engineering Sciences*, vol. 473, no. 2199, p. 20160345, 2017.

[17] D. Garcia, P. Pibarot, C. Landry, A. Allard, B. Chayer, J. G. Dumesnil, and L.-G. Durand, "Estimation of aortic valve effective orifice area by doppler echocardiography: effects of valve inflow shape and flow rate," *Journal of the American Society of Echocardiography*, vol. 17, no. 7, pp. 756–765, 2004.

[18] G. N. Cattermole, P. M. Leung, P. S. Mak, S. S. Chan, C. A. Graham, and T. H. Rainer, "The normal ranges of cardiovascular parameters in children measured using the ultrasonic cardiac output monitor," *Critical care medicine*, vol. 38, no. 9, pp. 1875–1881, 2010.

[19] P. Kam and I. Power, *Principles of Physiology for the Anaesthetist*. CRC Press, 2015.

[20] J. P. Mynard, *Computer modelling and wave intensity analysis of perinatal cardiovascular function and dysfunction*. PhD thesis, Department of Paediatrics, The University of Melbourne, Heart Research Group, Murdoch Childrens Research Institute, 2011.

[21] T. Heldt, *Computational models of cardiovascular response to orthostatic stress*. PhD thesis, Massachusetts Institute of Technology, 2004.

[22] A. Baretta, C. Corsini, W. Yang, I. E. Vignon-Clementel, A. L. Marsden, J. A. Feinstein, T.-Y. Hsia, G. Dubini, F. Migliavacca, G. Pennati, *et al.*, "Virtual surgeries in patients with congenital heart disease: a multi-scale modelling test case," *Philosophical Transactions of the Royal Society A: Mathematical, Physical and Engineering Sciences*, vol. 369, no. 1954, pp. 4316–4330, 2011.

[23] T. Tanaka, M. Arakawa, T. Suzuki, M. Gotoh, H. Miyamoto, and S. Hirakawa, "Compliance of human pulmonary "venous" system from pulmonary artery wedge pressure tracings: comparison with pulmonary arterial compliance," *Japanese Circulation Journal*, vol. 50, no. 2, pp. 127–139, 1986.

[24] F. Liang, H. Senzaki, C. Kurishima, K. Sughimoto, R. Inuzuka, and H. Liu, "Hemodynamic performance of the fontan circulation compared with a normal biventricular circulation: a computational model study," *American Journal of Physiology-Heart and Circulatory Physiology*, vol. 307, no. 7, pp. H1056–H1072, 2014.

[25] J. P. Mynard and J. J. Smolich, "One-dimensional haemodynamic modeling and wave dynamics in the entire adult circulation," *Annals of biomedical engineering*, vol. 43, no. 6, pp. 1443–1460, 2015.

[26] B. Boville and L. C. Young, "Quick guide to pediatric cardiopulmonary care," 2015.

[27] M. R. Krishna, S. P. Marathe, A. Maghsoudi, G. McCowage, M. C. Sherwood, and Y. Orr, "Emergency ross procedure for pediatric aortic valve myxofibrosarcoma," *The Annals of thoracic surgery*, vol. 107, no. 3, pp. e183–e185, 2019.

[28] E. M. D. Walter, M. F. Javier, F. Sander, B. Hartmann, A. Ekkernkamp, and R. Hetzer, "Primary cardiac tumors in infants and children: surgical strategy and long-term outcome," *The Annals of thoracic surgery*, vol. 102, no. 6, pp. 2062–2069, 2016.

[29] M. A. Padalino, V. L. Vida, G. Boccuzzo, M. Tonello, G. E. Sarris, H. Berggren, J. V. Comas, D. Di Carlo, R. M. Di Donato, T. Ebels, *et al.*, "Surgery for primary cardiac tumors in children: early and late results in a multicenter european congenital heart surgeons association study," *Circulation*, vol. 126, no. 1, pp. 22–30, 2012.

[30] A. De Vecchi, D. Marlevi, D. A. Nordsletten, I. Ntalas, J. Leipsic, V. Bapat, R. Rajani, and S. A. Niederer, "Left ventricular outflow obstruction predicts increase in systolic pressure gradients and blood residence time after transcatheter mitral valve replacement," *Scientific reports*, vol. 8, no. 1, pp. 1–11, 2018.

[31] Z. Keshavarz-Motamed, "A diagnostic, monitoring, and predictive tool for patients with complex valvular, vascular and ventricular diseases," *Scientific Reports*, vol. 10, no. 1, pp. 1–19, 2020.

[32] Z. Keshavarz-Motamed, J. Garcia, P. Pibarot, E. Larose, and L. Kadem, "Modeling the impact of concomitant aortic stenosis and coarctation of the aorta on left ventricular workload," *Journal of biomechanics*, vol. 44, no. 16, pp. 2817–2825, 2011.

[33] R. Rajani, J. Hancock, and J. B. Chambers, "The art of assessing aortic stenosis," *Heart*, vol. 98, no. Suppl 4, pp. iv14–iv22, 2012.

[34] W. A. Zoghbi, J. B. Chambers, J. G. Dumesnil, E. Foster, J. S. Gottdiener, P. A. Grayburn, B. K. Khandheria, R. A. Levine, G. R. Marx, F. A. Miller, *et al.*, "Recommendations for evaluation of prosthetic valves with echocardiography and doppler ultrasound: a report from the american society of echocardiography's guidelines and standards committee and the task force on prosthetic valves, developed in conjunction with the american college of cardiology cardiovascular imaging committee, cardiac imaging committee of the american heart association, the european association of echocardiography, a registered branch of the european society of cardiology, the japanese society of echocardiography and the canadian society of echocardiography, endorsed by the american college of cardiology foundation, american heart association, european

association of echocardiography, a registered branch of the european society of cardiology, the japanese society of echocardiography, and canadian society of echocardiography," *Journal of the American Society of Echocardiography*, vol. 22, no. 9, pp. 975–1014, 2009.

[35] M. Foschi, M. Di Mauro, F. Tancredi, C. Capparuccia, R. Petroni, L. Leonzio, S. Romano, S. Gallina, M. Penco, M. Cibelli, *et al.*, "The dark side of the moon: the right ventricle," *Journal of Cardiovascular Development and Disease*, vol. 4, no. 4, p. 18, 2017.

[36] F. Haddad, R. Doyle, D. J. Murphy, and S. A. Hunt, "Right ventricular function in cardiovascular disease, part ii: pathophysiology, clinical importance, and management of right ventricular failure," *Circulation*, vol. 117, no. 13, pp. 1717–1731, 2008.

[37] C. E. Ventetuolo and J. R. Klinger, "Management of acute right ventricular failure in the intensive care unit," *Annals of the American Thoracic Society*, vol. 11, no. 5, pp. 811–822, 2014.

6 IV Application: Woman-specific model

Contents

This chapter focuses on the development of sex-specific cardiovascular models. Particularly, the purpose is to build woman-specific models and to point out the sex-specific differences.

First the derivation of a woman-specific model is shown, second, differences with man-specific models are highlighted. The first part has been presented at the 42nd Annual International Conferences of the IEEE Engineering in Medicine and Biology Society in conjunction with the 43rd Annual Conference of the Canadian Medical and Biological Engineering Society [1]. The second part has been presented at the XXXVI National Conference on Hydraulics and Hydraulic Constructions [2].

6.1 Introduction

Cardiovascular diseases (CVDs) are the leading cause of death worldwide. They have been considered as a peculiar male disease for decades but, recently, evidence has shown that these diseases widely affect also women. New cardiovascular risk factors exclusive to women have been highlighted, and it has been shown that CVDs affect more women than men [3]. Sex-specific research is helping to increase the awareness of sex differences but, despite the American Heart Association (AHA) developed a women-specific clinical recommendation for CVD prevention already in 1999, the management is still the same for both sexes in the clinical practice [3]. Indeed, up to now medical research has focused on the male case. This resulted in a standardization of clinical presentations, and in treatments not adequate for both men and women. For example, the clinical manifestation of the acute myocardial infarction is often "atypical" (referred to what is considered typical but which is, to say the truth, typical of male population) in women, resulting in a delayed diagnosis and treatment and worst outcomes [4]. Moreover, sex research helped in highlighting that also hemodynamic quantities differ widely due to sex, age, and weight [5, 6, 7]. However, if on one hand, sex is increasingly being considered in clinical research and practice, on the other hand, the same attention is still lacking in modeling studies of the cardiovascular system. Indeed, the 70 Kg male case is usually the standard representation for the whole population. To help overcoming this sex-gap, sex-specific blood circulation models are here developed. Particularly, first, a woman-specific model of the blood circulation of an average young (18-40 y.o.) woman with BSA of 1.6 m^2 is developed. The lumped-parameters model, which includes the uterus, is calibrated with female-specific parameters and validated with sex-specific literature data. Second, a sex-independent model (i.e., reproductive organs are not specifically modeled) is considered and also the standard case of an average man is simulated. The aim is to compare the two models and to emphasize the hemodynamic differences between men and women, highlighting the need to develop sex-specific models.

6.2 A female-specific cardiovascular lumped-parameters model

The development of a woman-specific model is presented in this section.

6.2.1 Methods

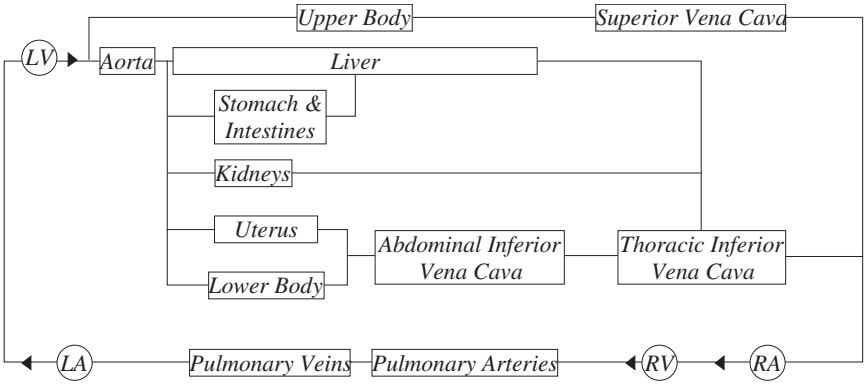

Figure 6.1: *Woman-specific model composed by: left ventricle, LV, aorta, Ao, liver, gastro-intestinal tract, kidneys, uterus, upper and lower body, great veins (superior vena cava, SVC, thoracic and abdominal inferior vena cava, IVCab and IVCth, respectively), right ventricle, RV, right atrium RA, pulmonary arteries and veins, PuA and PuVe, and, left atrium, LA.*

The lumped-parameter methodology is utilized to represent the whole cardiovascular system. Particularly, the methodology described in Chapter 2 is used to build the circulation model.

To simulate the female cardiovascular system, a sex-specific model is created by 1) taking into account the organs that are peculiar to the female case, and 2) calibrating the model by means of female-specific data. Particularly, the female model is constructed taking into account *i)* the four heart chambers, *ii)* the systemic circulation comprising the aorta, Ao, the liver, h, the gastro-intestinal tract, i, the kidneys, k, the uterus, ut, and the upper, ub, and lower body, lb, and, *iii)* the pulmonary circulation (Fig. 6.1). This configuration allows hemodynamic analysis of the major organs of interest, especially the uterus. The great vessels (main arteries and veins) are reproduced considering a compliance, a resistance and an inductance effect (Fig. 6.2a), whereas, the organs of interest are represented rearranging and combining the lumped-parameters and neglecting the inertial effect. Particularly, the arterial-arteriolar and the venous sections are reproduced by a compliance and a resistance, whereas the vascular bed is represented by a resistance (6.2b) (Eq. (2.3)). This choice of lumped-parameters allows to reproduce the elastic properties of the arteries and veins, and the dissipation effects that characterize the small vessels of the vascular bed. The heart is modeled by the time-elastance theory as described in Section 2.3. Finally, the heart valves are represented considering their opening and closing dynamics (Subsection 2.4.2).

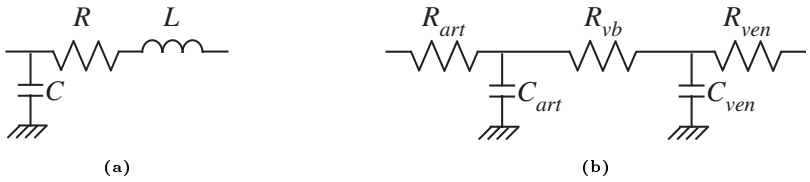

Figure 6.2: *Lumped-parameters model for (a) the great vessels and (b) the organs of interest considered in the woman-specific model.*

The calibration is conducted as described in Section 2.7. Particularly, a young woman (18-40 years old) of 58 Kg and BSA of 1.6 m^2 is considered. The total peripheral resistance (R_{tot}) for any compartment represented by Fig. 6.2b - liver, gastro-intestinal tract, kidneys, uterus, upper and lower body - is calculated by considering a perfusion pressure of 76 mmHg, a cardiac output (CO) of 4.9 L/min, and the percentage of CO that supplies each organ (Table 6.1) [8], [9], [10]. Each resistance in Fig. 6.2b is then computed by applying the rules reported in Subsection 2.7.1. Notice that a fine-tuning of the portal system resistance is performed to represent the unique physiological portal system in which blood flows from a capillary bed, i.e., the gastrointestinal bed, into another capillary bed, i.e., the hepatic bed, through veins, i.e., the portal veins. Given the resistance values, the corresponding arterial compliance (C_{art}) is computed harnessing the time constant of the systemic arterial system, $\tau = 0.81$ s, as $C_{art} = \tau / R_{vb}$ [8]; whereas the venous compliance is considered 30 times greater than C_{art} [10]. For the great vessels of the systemic circulation (Fig. 6.2a), values from [9] are imposed, adjusting the aortic compliance to obtain a total compliance in the range of 2.0-2.5 mL/mmHg/kg [8].

Table 6.1: *Blood distribution (%CO).*

Compartment	**%CO**
Hepatic artery	7%
Gastro-intestinal tract	26%
Kidneys	21%
Uterus	0.44%
Upper body	22%
Lower body	23.56%

For the pulmonary circulation, the compliance values are computed from [11], considering a woman of 58 Kg and deriving the resistance values as described above for a pulmonary time constant of $\tau = 0.5$ s [12].
Inductance values are taken from [13]. For the heart parameters, values from

[8, 14] are imposed. Particularly, E_{max} and $V_{p=0}$ are adjusted to obtain female pressures and flows. Values are reported in Table 6.2.
Heart valves parameters are calculated considering the valvular annular dimensions from [15].
To run the model, a heart rate of 75 bpm [16] and appropriate initial values are imposed to obtain pressures and flows in the female range.

Table 6.2: *Heart parameters values.*

	LV	**RV**	**LA**	**RA**
$E_{max}[mmHg/mL]$	2.464	0.396	0.1274	0.081
$E_{min}[mmHg/mL]$	0.07	0.035	0.09	0.045
$V_{p=0}[mL]$	2	0	14	5
$\tau_1[s]$	$0.269T$	$0.269T$	$0.110T$	$0.110T$
$\tau_2[s]$	$0.452T$	$0.452T$	$0.180T$	$0.180T$
$m_1[-]$	1.32	1.32	1.99	1.99
$m_2[-]$	27.4	27.4	13.1	13.1
$t_{onset}[s]$	0	0	$0.85T$	$0.85T$

T is heartbeat period.

6.2.2 Results

The ability of the model to simulate the female-specific hemodynamics is first analyzed considering the global hemodynamic variables. Table 6.3 reports the outputs of the model compared with woman-specific *in vivo* data.
The comparison is then made between calculated and literature waveforms. In this regard it is noted that, to the best of my knowledge, no female-specific waveforms are available in the medical literature. For this reason, reference is made to sex-independent waveforms normally used in clinical practice.

Total resistances

The systemic vascular resistance (SVR) and the pulmonary vascular resistance (PVR) are in agreement with the values in [16].

Volumes and flows

The end-diastolic (EDV) and end-systolic (ESV) volumes are within the ranges given in [18] for both the right and left ventricles. Good agreement is found for the stroke volume (SV) which leads to a CO within the range given in [18]. The same holds for the ejection fraction (EF) of LV and RV.

Table 6.3: *Comparison of model hemodynamics with female-specific in vivo reference data.*

Parameter	Units	Model	Reference
Total resistance			
SVR	mmHg·s/mL	1.02	0.9945 (±0.0165)[16]
PVR	mmHg·s/mL	0.1	0.096 (±0.042)[17]
Volume			
EDV_{LV}	mL	107	96 (52-141)[18]
ESV_{LV}	mL	41	32 (13-51)[18]
EDV_{RV}	mL	110	106 (58-154)[18]
ESV_{RV}	mL	44	40 (12-68)[18]
Cardiac flows			
SV_{LV}	mL	65	65 (33-97)[18]
SV_{RV}	mL	65	66 (35-98)[18]
EF_{LV}	%	61	67 (56-78)[18]
EF_{RV}	%	59	63 (47-80)[18]
CO	L/min	4.9	4.3 (2.65-5.98)[18]
E/A ratio			
Mitral	-	1.9	1.4 (0.6-2.6)[19]
Tricuspid	-	1.4	1.5 (0.8-2.3)[19]
Flow			
Q_{ut}	mL/s	0.38	0.35 (±0.15)[20]
Pressure			
SBP	mmHg	107	108 (±2)[16]
DBP	mmHg	68	67 (±1)[16]
PuA (systolic)	mmHg	18.2	21.8 (±1.5)[17]
PuA (mean)	mmHg	14.1	15.1 (±2.9)[17]
PuA (diastolic)	mmHg	12	(8-12)[21]
LAP (mean)	mmHg	6.7	8.1 (±1.4)[17]
CVP	mmHg	3.3	(2-6)[21]

Reference data given as a mean, with range or standard deviation in parentheses.
See text for abbreviation.

The upper and lower body mean flows are 19.9 and 20.8 mL/s, respectively. The total hepatic mean flow is 21.9 mL/s, with 5.5 mL/s coming from the hepatic artery and 16.4 mL/s from the portal system, and the mean renal flow is 18.5 mL/s. For these values, a female-specific reference is not found, but they agree with sex-independent literature as [10]. Finally, the mean uterine arterial flow (Qut) well agrees with the study of Hale et al. [20].

Pressures

The systolic (SBP) and diastolic (DBP) blood pressures are within the ranges given in [16]. Good agreement is found also for the pulmonary artery pressure (PuA) with the mean and diastolic values within the ranges given in [17] and [21], respectively, whereas the systolic value is slightly smaller compared to that in [17].

The mean left atrial pressure (LAP) and the central venous pressure (CVP) are within the ranges given in [17] and [21], respectively. Finally, the mean pressures in the hepatic artery, vein and portal system are 81 mmHg, 4.2 mmHg, and 7 mmHg, respectively. Again, for these quantities, female-specific published data are not found, but they agree with population-specific ranges given in [8].

Physiological trends are also found when considering the waveforms. Fig. 6.3 represents the pressures, flows, and volumes, and these well resemble the typical physiological hemodynamics. The left ventricle is characterized by higher pressure and lower volume compared to the RV with the same SV of about 65 mL and a pressure ratio of about 6:1. Fig. 6.3c displays the pressure-volume loop for the left and right ventricle. The valves' model represents the physiological backward flow of the semilunar valves and the typical double peaks shape of the atrioventricular valves. Particularly, the aortic valve flow has a peak value of 525 mL/s, and the pulmonary valve has 513 mL/s. The E/A ratios are 1.9 and 1.4 for the mitral and tricuspid valves, respectively.

6.3 Blood circulation: is it a matter of sex?

After the realization of a woman-specific model, the role of male and female parameters and of the uterus are analyzed in the following section.

6.3.1 Methods

The woman-specific (W) model presented in the Subsection 6.2.1 (Fig. 6.1) is here compared with a sex-independent (SI) model (Fig. 6.4). The two models differ because the latter does not specifically represent reproductive organs. Rather the male (female) reproductive system is included in the 'lower body' district. The sex-independent model is derived as the woman-specific model, following the methodology described in Chapter 2. Particularly, to analyze differences due to sex and understand the role of the parameters, each model is run adopting both male- and female-specific parameters. This means that

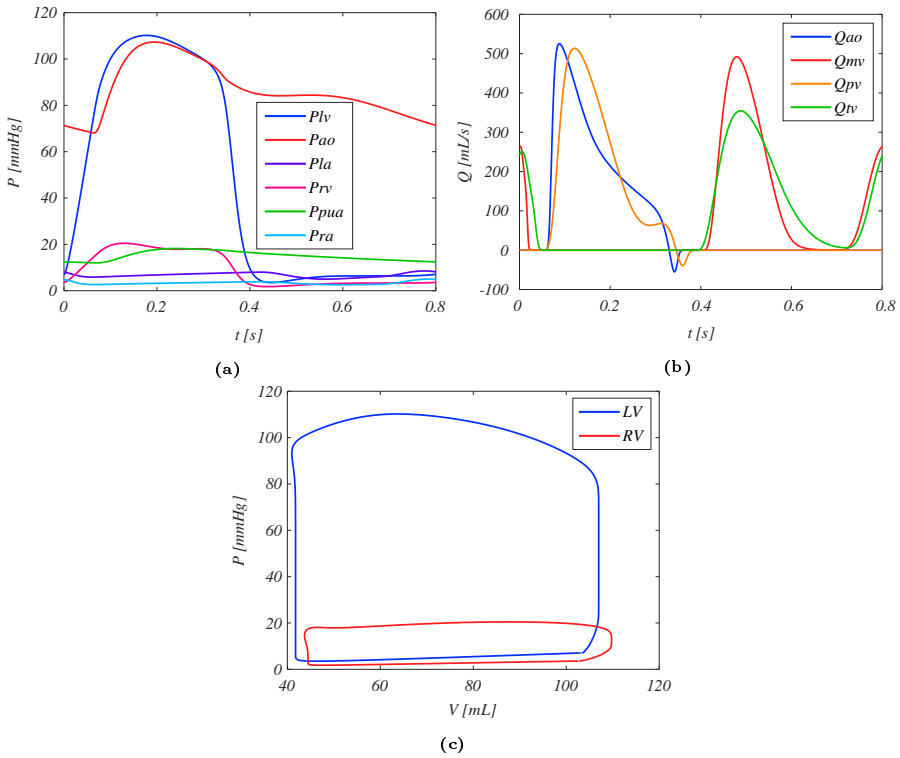

Figure 6.3: *Simulation results of the female blood circulation model. (a) Presures in various districts of the circulation, (b) flows across the heart valves, and (c) pressure-volume loops of the ventricles. LV, left ventricle, Ao, aorta, LA, left atrium, RV, right ventricle, PuA, pulmonary artery, RA, right atrium, MV, mitral valve, PV, pulmonary valve, TV, tricuspid valve.*

the woman-specific model (Fig. 6.1), is calibrated considering the case of an average young woman of 58 Kg and BSA of 1.6 m^2, but also considering the case of an average man of 70 Kg and BSA of 1.81 m^2. The same is done for the sex-independent model (Fig. 6.4). Clearly, considering the woman-specific model with male parameters is not physiological, however, the application of both male and female parameters to both the models allow to understand if the differences are due to the different model structures or if the calibration parameters are important in the results. Thus, four scenarios are simulated and analyzed: *i)* the sex-independent model with male parameters (SIM); *ii)* the sex-independent model with female parameters (SIF); *iii)* the woman-specific model with female parameters (WF), and, *iv)* the woman-specific model with male parameters (WM).

In agreement with literature data, differences between male and female parameters emerge as reported in the following. For the female case, higher heart rate and systemic vascular resistance, and lower compliances, cardiac

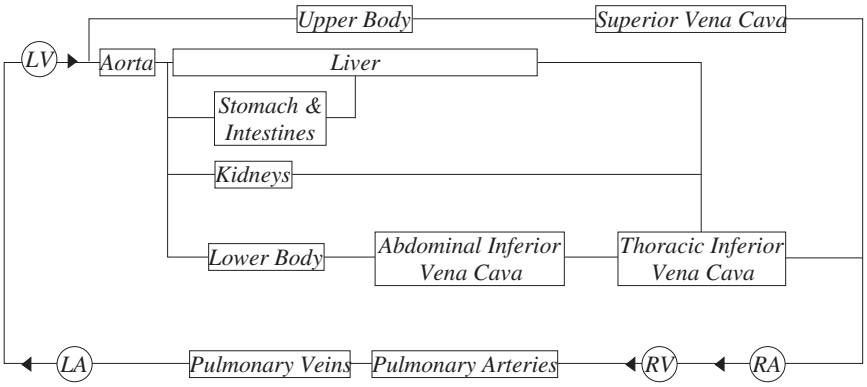

Figure 6.4: *Sex-independent model composed by: left ventricle, LV, aorta, Ao, liver, gastro-intestinal tract, kidneys, uterus, upper and lower body, great veins (superior vena cava, SVC, thoracic and abdominal inferior vena cava, IVCab and IVCth, respectively), right ventricle, RV, right atrium RA, pulmonary arteries and veins, PuA and PuVe, and, left atrium, LA.*

mechanics parameters and geometrical valve dimensions are imposed [11, 15, 22]. Table 6.4 reports the differences in the lumped-parameters. Note that these inputs are derived considering the rules described in Section 2.7: female paramters as previously described (Subsection 6.2.1), male parameters by imposing a perfusion pressure of 80 mmHg, CO of 6 L/min, HR of 70 bpm, and by using the blood distribution of Table 6.1, and adding the uterus percentage to the lower body compartment. For the heart parameters, Table 6.2 and 6.5 show the values for the female and male case, respectively.

Table 6.4: *Input parameters for M, male and F, female cases. R, resistances and C, (arterial and venous) compliances for the simulated compartments. Ao, aorta, L, liver, G.I., gastro-intestinal tract, K, kidneys, UB, upper body, LB, lower body, SVC, superior vena cava, and Pu, pulmonary circulation.*

	R [mmHg·s/mL]	**C [mmHg/mL]**
	M/F	**M/F**
Ao	0.021/0.021	1.10/0.70
L.	12.32/14.54	50.00/41.76
G.I.	4.30/4.80	7.274/6.419
K.	3.80/4.50	7.183/6.065
UB.	3.49/4.17	0.245/0.205
LB	3.30/4.00	27.267/26.140
SVC	0.108/0.129	7.337/6.143
Pu	0.0845/0.102	28.40/23.56

Table 6.5: *Male heart parameters values.*

	LV	**RV**	**LA**	**RA**
$E_{max}[mmHg/mL]$	2.8	0.45	0.13	0.09
$E_{min}[mmHg/mL]$	0.07	0.035	0.09	0.045
$V_{p=0}[mL]$	10	40	3	7
$\tau_1[s]$	$0.269T$	$0.269T$	$0.110T$	$0.110T$
$\tau_2[s]$	$0.452T$	$0.452T$	$0.180T$	$0.180T$
$m_1[-]$	1.32	1.32	1.99	1.99
$m_2[-]$	27.4	27.4	13.1	13.1
$t_{onset}[s]$	0	0	$0.85T$	$0.85T$

T is heartbeat period.

6.3.2 Results

First, the hemodynamics computed with the sex-independent model is evaluated considering the male parameters. Table 6.6 compares the outputs with *in vivo* male-specific reference data. The computed global hemodynamic signals agree with the male ranges with values very closed to the mean values or within the male ranges. This validates the sex-independent model, at least for the male population.

Since both the woman-specific model and the sex-independent model are validated, the analysis of the effect of the parameters and of the role of the uterus are conducted.

Table 6.7 reports the global hemodynamic variables for the four considered scenarios and compares the male and female hemodynamics given by the two models. The following can be observed:
1) For a given set of parameters (i.e., male- or female-specific): *i)*the sex-independent model and the woman-specific model return exactly the same overall hemodynamics except for the uterus district, since the sex-independent model does not reproduce it at all. *ii)* The above evidence is expected, given that it is well known that in physiological conditions the uterine district drains only a minimal part of the CO, and therefore produces a minimal effect on the overall hemodynamics of the entire circulation. Therefore, the presence/absence of the uterus is not the element on which to focus the attention in the construction of a model attentive to sex differences, at least in the physiological condition.
2) For a given model (i.e., sex-independent or woman-specific): the importance of the choice of the set of parameters is immediately evident. It should be noted, in particular, that the prediction of the flow in the uterine

Table 6.6: *Comparison of the hemodynamic parameters of the sex-independent model with male parameters with in vivo male-specific data.*

Parameter(Unit)	Model	Reference
CO [L/min]	6.9	6.5 (3.6-9.4)[23]
SV_{LV} [mL]	98	112 (±19)[24]
SV_{RV} [mL]	98	113 (±19)[24]
EF_{LV} [%]	65	69 (±6)[24]
EF_{RV} [%]	53	59 (±6)[24]
EDV_{LV} [mL]	150	160 (±29)[24]
EDV_{RV} [mL]	184	190 (±33)[24]
ESV_{LV} [mL]	51	50 (±16)[24]
ESV_{RV} [mL]	85	78 (±20)[24]
SBP [mmHg]	130	130 (±4)[25]
DBP [mmHg]	85	77 (±5)[25]
sPuA [mmHg]	22.1	22.5 (±1.0)[17]

Reference data given as a mean, with range or standard deviation in parentheses.
See text for abbreviation.

district is overestimated by about 40% when adopting male-specific rather than female-specific parameters.

Focusing now on the sex-independent model implemented with either male or female parameters, the outputs of the systemic and pulmonary circulation deserve attention, as shown in Fig. 6.5 and 6.6, respectively. Particularly, waveforms and mean values (dotted lines) of both the absolute and normalized values are reported (normalization is made with respect to both the body surface area (BSA) and the body mass (BM)). Results highlight that: *i)* the central role played by the sex of the population (i.e., by the set of parameters) is evident both in terms of waveforms and average values on the entire circulation. *ii)* All the different hemodynamic variables represented (pressures, flows, and volumes) show significantly different behavior in the male and female population with a general tendency, when the absolute quantities are considered, to have higher values in men. *iii)* The normalization of the results with respect to BSA or BM generally induces a reduction in sex-specific differences, without however never canceling them and on the contrary, for some of the variables, maintaining them significant. Normalization with BM seems to somehow bring the results closer. *iv)* Evidence that sex differences persist despite normalization suggests the possibility that there are sex differences in the mechanisms underlying the

Table 6.7: *Comparison of the hemodynamic parameters in the four scenarios: SIM, SIF, WF, WM. CO, cardiac output; SV, stroke volume; EF, ejection fraction; EDV, end-diastolic volume; ESV, end-systolic volume; SBP, systolic blood pressure, DBP, diastolic blood pressure, sPuA, systolic pulmonary pressure; dPuA, diastolic pulmonary pressure; LAP, left atrial pressure; CVP, central venous pressure; Ppov, portal venous pressure and Qut, uterine flow.*

Parameter(Unit)	**SIM/WM**	**SIF/WF**
CO [L/min]	6.9/6.9	4.9/4.9
SV_{LV} [mL]	97.9/97.9	63.8/63.8
SV_{RV} [mL]	97.9/97.8	63.8/63.8
EF_{LV} [%]	65/65	60/60
EF_{RV} [%]	53/53	59/59
EDV_{LV} [mL]	150.3/150.3	106.2/106.3
EDV_{RV} [mL]	183.7/183.6	108.3/108.2
ESV_{LV} [mL]	51.0/51.1	41.4/41.5
ESV_{RV} [mL]	84.9/84.9	43.5/43.5
SBP [mmHg]	129.5/129.7	108.0/108.1
DBP [mmHg]	85.2/85.4	69.2/69.3
sPuA [mmHg]	22.1/22.1	18.1/18.1
dPuA [mmHg]	14.4/14.4	12.0/12.0
LAP [mmHg]	8.5/8.5	6.7/6.7
CVP [mmHg]	4.1/4.1	3.3/3.3
Ppov [mmHg]	8.5/8.5	6.9/6.9
Qut [mL/s]	-/0.54	-/0.38

hemodynamic response, which are reflected in differences in characteristic cardiovascular function parameters. *v)* The above applies to systemic and pulmonary circulation, in the same way.

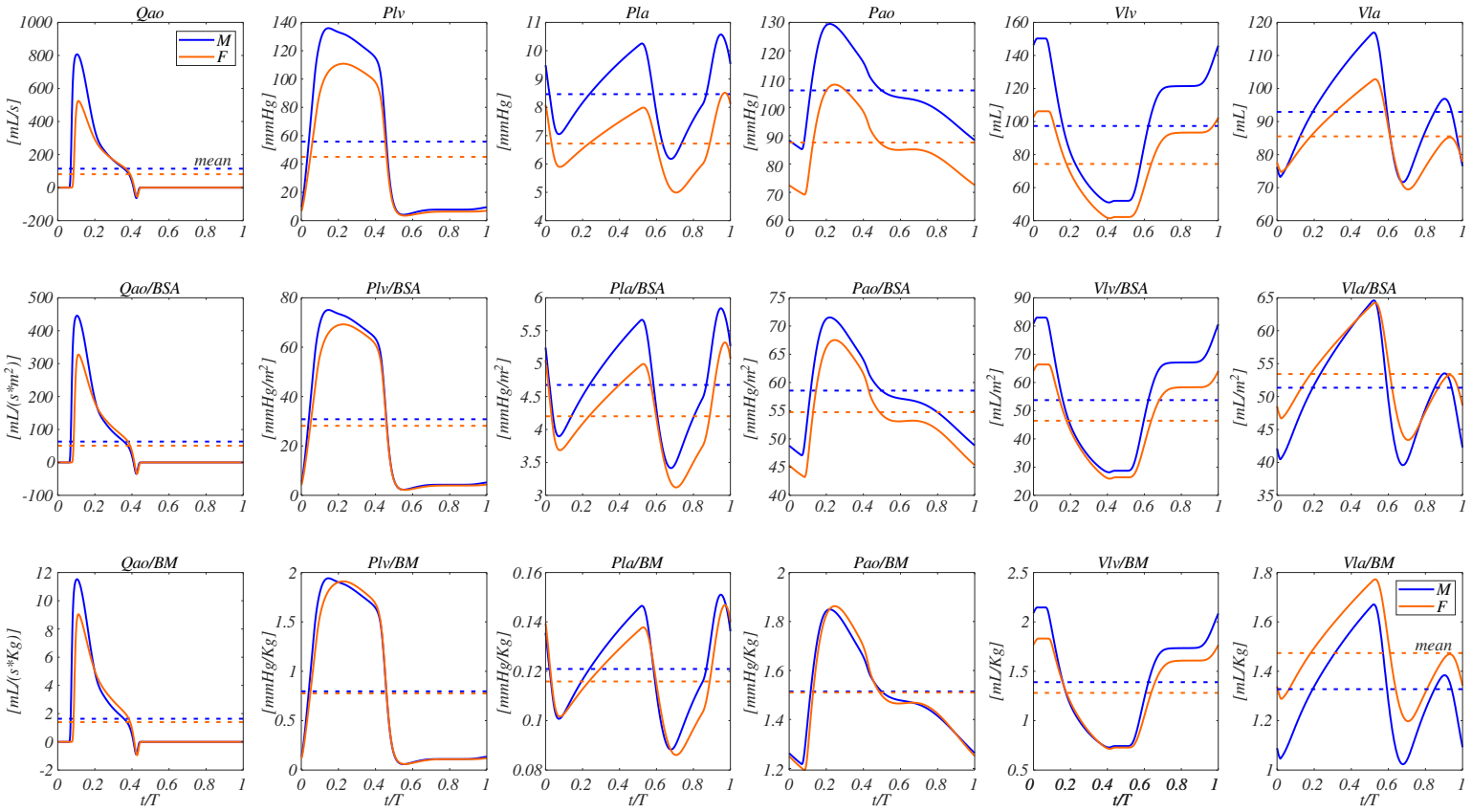

Figure 6.5: *Outputs of the sex-independent model for male (blue) and female (orange) parameters, considering the systemic circulation. There are reported both waveforms and mean values, the latter with dotted lines. First row, absolute values, second row, output normalized to the body surface area (BSA), and third row, outputs normalized to the body mass (BM). Qao, aortic valve flow, Plv, LV pressure, Pla, LA pressure, Pao, aortic pressure, Vlv, LV volume, and Vla, LA volume.*

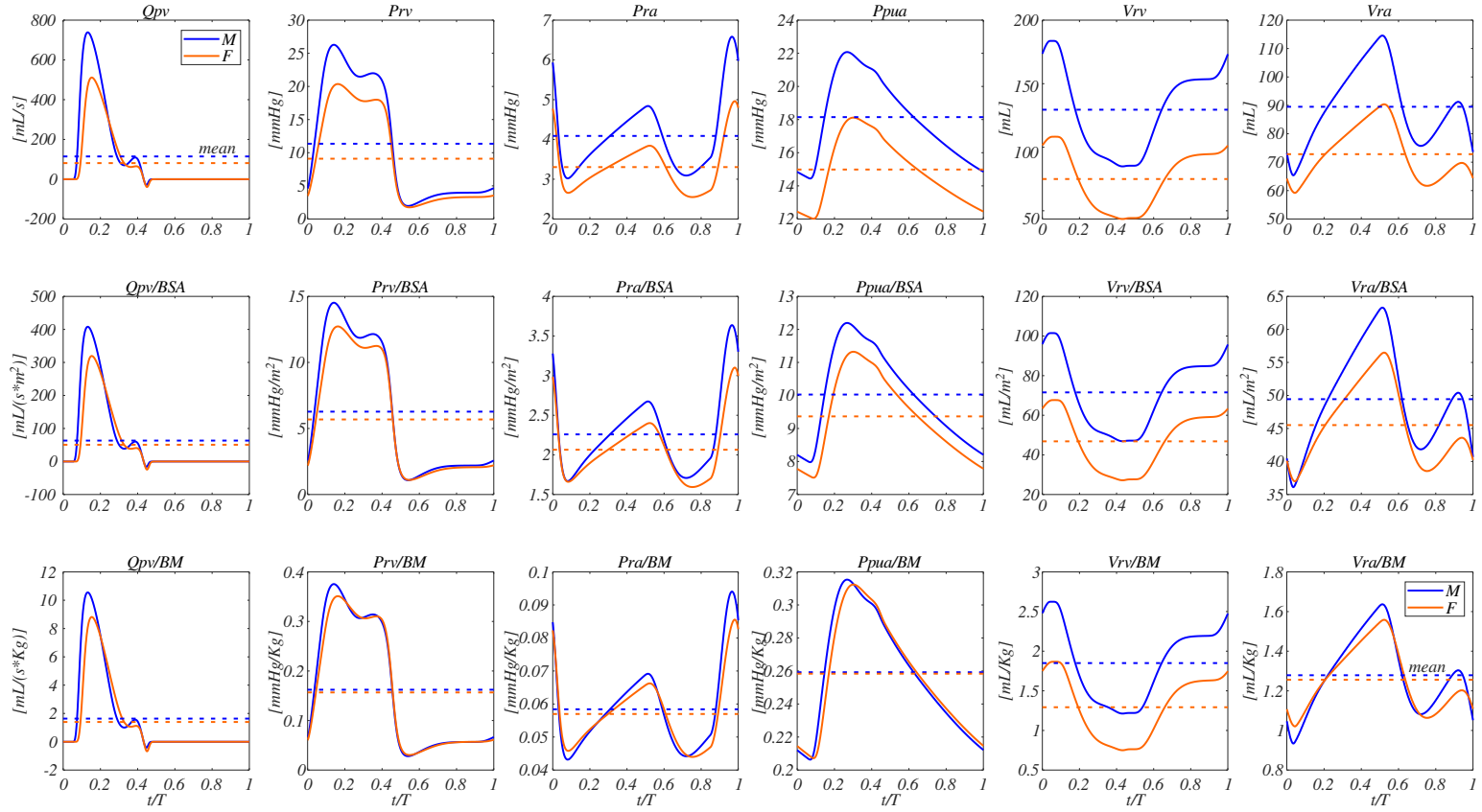

Figure 6.6: *Outputs of the sex-independent model for male (blue) and female (orange) parameters, considering the pulmonary circulation. There are reported both waveforms and mean values, the latter with dotted lines. First row, absolute values, second row, output normalized to the body surface area (BSA), and third row, outputs normalized to the body mass (BM). Qpv, pulmonary valve flow, Prv, RV pressure, Pra, RA pressure, Ppua, pulmonary arterial pressure, Vrv, RV volume, and Vra, RA volume.*

Finally, pressure-volume loops of the sex-independent model implemented with male and female parameters are reported in Fig. 6.7, for both the left and right ventricle. These are compared with sex-specific literature evidences [22]. Even after volume normalization to BSA differences between the male and female configurations remain, and the female case results in smaller and left-shifted loops. Differences in pV loops also determine differences in stroke work (SW). Table 6.8 shows the SW computed for the left and right ventricle by SIM and SIF. The SW for SIF is almost half the SW in SIM for both LV and RV, and, the right ventricle in both the scenarios (SIM, SIF) works almost 20% less than the left one. Notice that all the above observation are in accordance with evidences obtained from real cases (Fig. 6.7b).

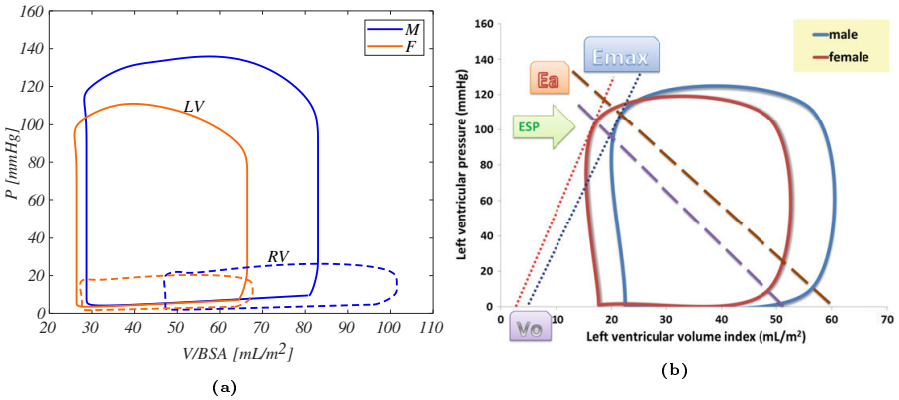

Figure 6.7: *(a) Pressure-volume loops normalized to BSA for SIM (blue) and SIF (orange) obtained from the model: LV, continuous line, RV, dashed line, and (b) pressure-volume loop in sex-specific literature [22].*

Table 6.8: *Stroke work (SW) for left (LV) and right (RV) ventricles in SIM and SIF (SW in Joule).*

	$\mathbf{SW}_{LV}$ **[J]**	$\mathbf{SW}_{RV}$ **[J]**
SIM	2.40	0.49
SIF	1.38	0.23

6.4 Model Sensitivity Analysis

The sensitivity of the models is computed as explained in Section 2.8. 21 and 19 inputs are varied, and 54 and 49 outputs are evaluated for the woman-specific and sex-independent models, respectively.

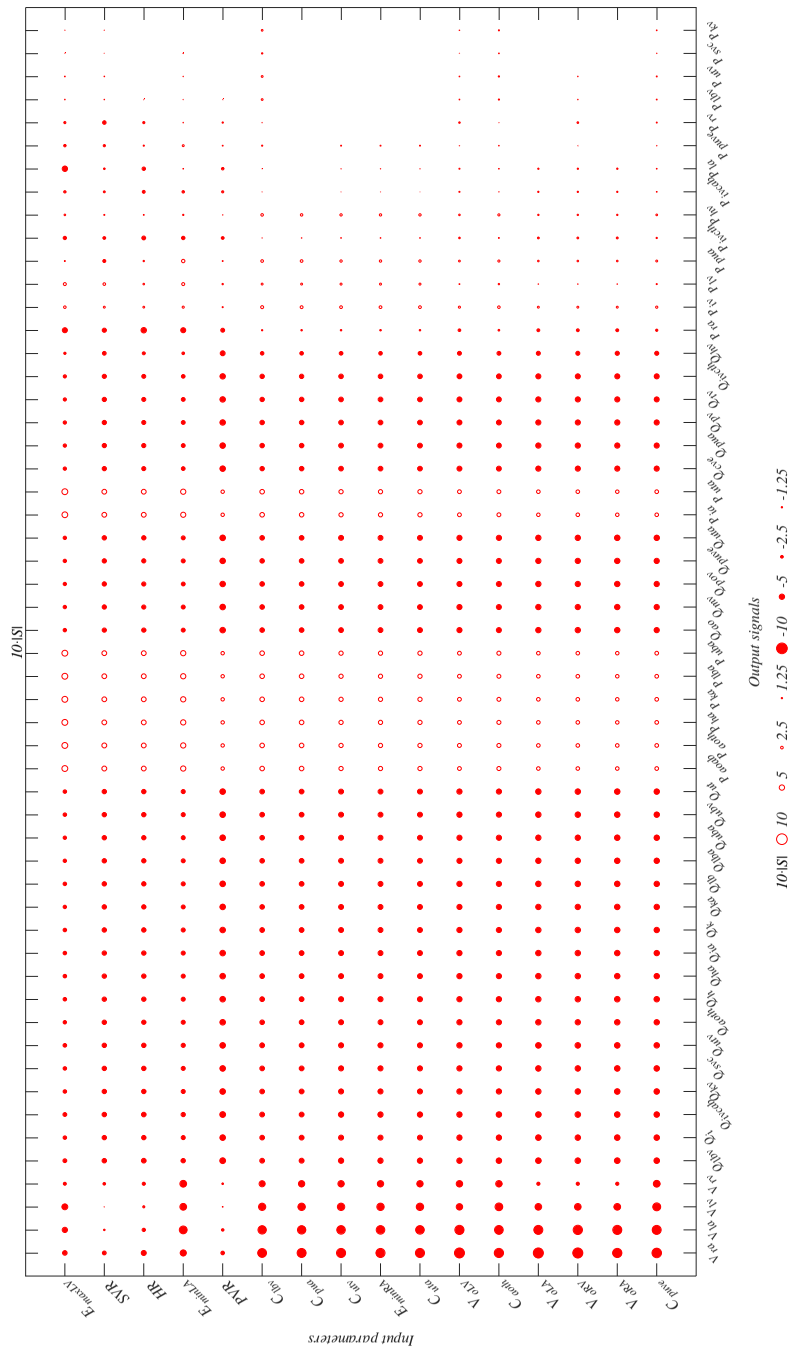

Figure 6.8: *Graphical representation of the sensitivity of the outputs to the 25% variation of the inputs for the woman-specific model. A larger symbol corresponds with higher sensitivity and filled/empty circles correspond to negative/positive S. Outputs are ordered according to the overall sensitivity (the most sensitive on the left) and inputs are ordered based on the global influence (the most influential at the bottom).*

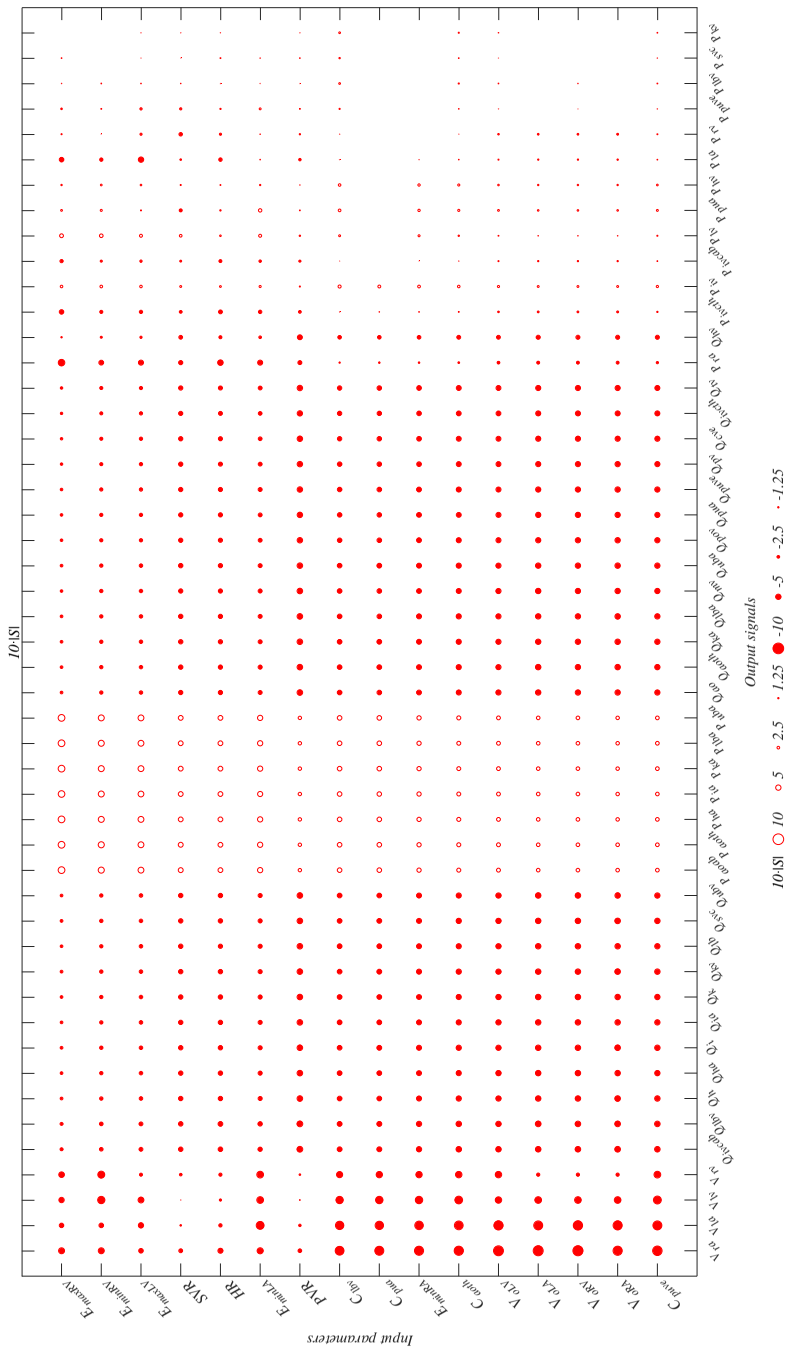

Figure 6.9: *Graphical representation of the sensitivity of the outputs to the 25% variation of the inputs for the sex-independent model. A larger symbol corresponds with higher sensitivity and filled/empty circles correspond to negative/positive S. Outputs are ordered according to the overall sensitivity (the most sensitive on the left) and inputs are ordered based on the global influence (the most influential at the bottom).*

Table 6.9: *Mean sensitivities (S) of output signals to the input parameters for the woman-specific model. The inputs are ordered based on the global influence (the most influential on the left), the outputs are ordered based on the overall sensitivity (the most sensitive at the top). Note that, due the limited space, only the first 16 most influential inputs are here reported.*

	Cpuve	$\mathbf{V}_{p=0_{RA}}$	$\mathbf{V}_{p=0_{RV}}$	$\mathbf{V}_{p=0_{LA}}$	**Caoth**	$\mathbf{V}_{p=0_{LV}}$	**Cuta**	$\mathbf{E}_{min_{RA}}$	**Cutv**	**Cpua**	**Clbv**	**PVR**	$\mathbf{E}_{min_{LA}}$	**HR**	**SVR**	$\mathbf{E}_{max_{LV}}$
Vra	-0.890	-0.860	-0.940	-0.940	-0.860	-0.930	-0.850	-0.850	-0.850	-0.840	-0.820	-0.340	-0.570	-0.470	-0.360	-0.430
Vla	-0.840	-0.850	-0.870	-0.840	-0.820	-0.860	-0.800	-0.800	-0.800	-0.780	-0.780	-0.230	-0.730	-0.310	-0.140	-0.490
Vlv	-0.740	-0.620	-0.620	-0.620	-0.720	-0.600	-0.690	-0.690	-0.690	-0.690	-0.680	-0.070	-0.630	-0.200	0.030	-0.550
Vrv	-0.630	-0.300	-0.300	-0.300	-0.600	-0.600	-0.590	-0.590	-0.590	-0.590	-0.570	-0.150	-0.630	-0.290	-0.240	-0.280
Qlbv	-0.520	-0.530	-0.520	-0.520	-0.510	-0.500	-0.490	-0.490	-0.490	-0.460	-0.450	-0.540	-0.410	-0.440	-0.420	-0.360
Qi	-0.510	-0.520	-0.510	-0.520	-0.490	-0.490	-0.470	-0.470	-0.470	-0.450	-0.440	-0.520	-0.380	-0.410	-0.410	-0.330
Qivcab	-0.510	-0.520	-0.520	-0.520	-0.510	-0.500	-0.490	-0.490	-0.490	-0.450	-0.450	-0.540	-0.400	-0.430	-0.420	-0.360
Qkv	-0.510	-0.520	-0.510	-0.510	-0.490	-0.490	-0.470	-0.470	-0.470	-0.450	-0.440	-0.520	-0.380	-0.410	-0.410	-0.330
Qsvc	-0.510	-0.520	-0.510	-0.510	-0.490	-0.490	-0.470	-0.470	-0.470	-0.450	-0.440	-0.520	-0.380	-0.410	-0.410	-0.330
Qutv	-0.510	-0.520	-0.520	-0.520	-0.490	-0.500	-0.470	-0.470	-0.470	-0.450	-0.450	-0.520	-0.390	-0.410	-0.410	-0.340
Qaoth	-0.500	-0.510	-0.500	-0.510	-0.480	-0.490	-0.460	-0.460	-0.460	-0.440	-0.430	-0.520	-0.380	-0.400	-0.410	-0.320
Qh	-0.510	-0.520	-0.510	-0.510	-0.490	-0.490	-0.470	-0.470	-0.470	-0.440	-0.440	-0.520	-0.380	-0.410	-0.410	-0.330
Qha	-0.500	-0.510	-0.510	-0.510	-0.480	-0.490	-0.460	-0.460	-0.460	-0.440	-0.440	-0.520	-0.380	-0.410	-0.410	-0.330
Qia	-0.500	-0.510	-0.510	-0.510	-0.480	-0.490	-0.460	-0.460	-0.460	-0.440	-0.440	-0.520	-0.380	-0.410	-0.410	-0.330
Qk	-0.500	-0.510	-0.510	-0.510	-0.480	-0.490	-0.460	-0.460	-0.460	-0.440	-0.440	-0.520	-0.380	-0.410	-0.410	-0.330
Qka	-0.500	-0.510	-0.500	-0.500	-0.480	-0.480	-0.460	-0.460	-0.460	-0.440	-0.430	-0.520	-0.370	-0.400	-0.410	-0.320
Qlb	-0.500	-0.510	-0.510	-0.510	-0.480	-0.490	-0.460	-0.460	-0.460	-0.440	-0.440	-0.520	-0.380	-0.400	-0.410	-0.330
Qlba	-0.500	-0.510	-0.500	-0.500	-0.480	-0.480	-0.460	-0.460	-0.460	-0.440	-0.430	-0.520	-0.370	-0.400	-0.410	-0.320
Quba	-0.500	-0.510	-0.500	-0.500	-0.480	-0.480	-0.460	-0.460	-0.460	-0.440	-0.430	-0.520	-0.370	-0.400	-0.410	-0.320
Qubv	-0.500	-0.510	-0.510	-0.510	-0.480	-0.490	-0.460	-0.460	-0.460	-0.440	-0.440	-0.520	-0.380	-0.410	-0.410	-0.330

Continued on Next Page.

Table 6.9 – Continued

	Cpuve	$V_{p=0_{RA}}$	$V_{p=0_{RV}}$	$V_{p=0_{LA}}$	Caoth	$V_{p=0_{LV}}$	Cuta	$E_{min_{RA}}$	Cutv	Cpua	Clbv	PVR	$E_{min_{LA}}$	HR	SVR	$E_{max_{LV}}$
Qut	-0.500	-0.510	-0.510	-0.510	-0.480	-0.490	-0.460	-0.460	-0.460	-0.440	-0.440	-0.520	-0.380	-0.410	-0.410	-0.330
Paoab	0.350	0.340	0.340	0.340	0.380	0.360	0.400	0.400	0.400	0.430	0.430	0.320	0.490	0.450	0.460	0.550
Paoth	0.350	0.340	0.340	0.340	0.380	0.370	0.400	0.400	0.400	0.430	0.430	0.320	0.490	0.450	0.460	0.550
Pha	0.350	0.330	0.340	0.340	0.380	0.360	0.400	0.400	0.400	0.430	0.430	0.320	0.490	0.450	0.450	0.550
Pka	0.350	0.330	0.340	0.340	0.370	0.360	0.400	0.400	0.400	0.430	0.430	0.320	0.490	0.450	0.450	0.550
Plba	0.350	0.330	0.340	0.340	0.370	0.360	0.400	0.400	0.400	0.430	0.430	0.320	0.490	0.450	0.450	0.550
Puba	0.350	0.330	0.340	0.340	0.380	0.360	0.400	0.400	0.400	0.430	0.430	0.320	0.490	0.450	0.450	0.550
Qao	-0.490	-0.500	-0.500	-0.500	-0.470	-0.480	-0.460	-0.450	-0.450	-0.430	-0.430	-0.520	-0.370	-0.400	-0.400	-0.320
Qmv	-0.490	-0.500	-0.490	-0.500	-0.470	-0.480	-0.450	-0.450	-0.450	-0.430	-0.430	-0.520	-0.370	-0.390	-0.400	-0.320
Qpov	-0.490	-0.500	-0.490	-0.500	-0.470	-0.470	-0.450	-0.450	-0.450	-0.430	-0.430	-0.510	-0.360	-0.390	-0.400	-0.310
Qpuve	-0.490	-0.500	-0.490	-0.490	-0.470	-0.470	-0.450	-0.450	-0.450	-0.430	-0.420	-0.510	-0.370	-0.390	-0.400	-0.320
Quta	-0.500	-0.510	-0.500	-0.500	-0.480	-0.480	-0.460	-0.460	-0.460	-0.430	-0.430	-0.520	-0.370	-0.400	-0.410	-0.320
Pia	0.340	0.330	0.340	0.330	0.370	0.360	0.400	0.400	0.400	0.420	0.430	0.320	0.480	0.450	0.450	0.540
Puta	0.350	0.330	0.340	0.340	0.370	0.360	0.400	0.400	0.400	0.420	0.430	0.320	0.490	0.450	0.450	0.550
Qcve	-0.480	-0.480	-0.480	-0.480	-0.460	-0.460	-0.440	-0.440	-0.440	-0.420	-0.410	-0.510	-0.350	-0.380	-0.400	-0.310
Qpua	-0.480	-0.490	-0.490	-0.490	-0.460	-0.470	-0.450	-0.450	-0.450	-0.420	-0.420	-0.510	-0.360	-0.390	-0.400	-0.310
Qpv	-0.480	-0.490	-0.480	-0.480	-0.460	-0.460	-0.440	-0.440	-0.440	-0.420	-0.420	-0.510	-0.360	-0.380	-0.400	-0.310
Qtv	-0.470	-0.480	-0.480	-0.480	-0.460	-0.460	-0.440	-0.440	-0.440	-0.420	-0.410	-0.510	-0.360	-0.380	-0.400	-0.300
Qivcth	-0.470	-0.470	-0.470	-0.470	-0.450	-0.450	-0.430	-0.430	-0.430	-0.410	-0.410	-0.500	-0.340	-0.370	-0.390	-0.300
Qhv	-0.380	-0.390	-0.380	-0.380	-0.360	-0.370	-0.340	-0.340	-0.340	-0.330	-0.330	-0.460	-0.250	-0.280	-0.350	-0.210
Pra	-0.210	-0.270	-0.270	-0.270	-0.160	-0.250	-0.140	-0.140	-0.140	-0.140	-0.120	-0.370	-0.470	-0.510	-0.390	-0.470
Piv	0.210	0.180	0.180	0.180	0.240	0.200	0.260	0.260	0.260	0.270	0.280	0.100	0.200	0.170	0.180	0.240
Plv	0.100	0.050	0.050	0.050	0.130	0.080	0.190	0.190	0.190	0.180	0.180	0.130	0.280	0.150	0.250	0.280

Continued on Next Page.

Table 6.9 – Continued

	Cpuve	$\mathbf{V}_{p=0_{RA}}$	$\mathbf{V}_{p=0_{RV}}$	$\mathbf{V}_{p=0_{LA}}$	**Caoth**	$\mathbf{V}_{p=0_{LV}}$	**Cuta**	$\mathbf{E}_{min_{RA}}$	**Cutv**	**Cpua**	**Clbv**	**PVR**	$\mathbf{E}_{min_{LA}}$	**HR**	**SVR**	$\mathbf{E}_{max_{LV}}$
Ppua	0.180	0.150	0.150	0.150	0.200	0.170	0.220	0.220	0.220	0.250	0.250	0.080	0.320	0.130	-0.280	0.090
Pivcth	-0.120	-0.180	-0.170	-0.170	-0.080	-0.150	-0.060	-0.060	-0.060	-0.050	-0.030	-0.260	-0.320	-0.360	-0.260	-0.310
Phv	0.160	0.130	0.130	0.130	0.200	0.150	0.220	0.220	0.220	0.230	0.240	0.040	0.120	0.080	0.100	0.150
Pivcab	-0.070	-0.120	-0.120	-0.120	-0.030	-0.100	-0.010	-0.010	-0.010	0.000	0.020	-0.200	-0.230	-0.270	-0.180	-0.220
Pla	-0.070	-0.130	-0.120	-0.120	-0.060	-0.100	-0.030	-0.030	-0.030	-0.010	-0.010	-0.230	0.060	-0.320	-0.150	-0.500
Ppuve	0.040	0.000	0.010	0.000	0.060	0.030	0.090	0.090	0.090	0.110	0.110	-0.080	0.180	-0.110	-0.210	-0.220
Prv	-0.090	-0.170	-0.160	-0.160	-0.020	-0.140	0.000	0.000	0.000	-0.020	0.030	-0.120	0.050	-0.200	-0.330	-0.200
Plbv	0.080	0.040	0.050	0.050	0.110	0.070	0.130	0.130	0.130	0.150	0.170	-0.010	0.030	-0.010	0.050	0.060
Putv	0.090	0.050	0.050	0.050	0.120	0.070	0.140	0.140	0.140	0.160	0.170	0.000	0.040	0.000	0.060	0.070
Psvc	0.040	-0.010	0.000	0.000	0.070	0.020	0.100	0.100	0.100	0.110	0.130	-0.060	-0.040	-0.080	-0.010	-0.020
Pkv	0.070	0.030	0.030	0.030	0.100	0.050	0.120	0.130	0.130	0.140	0.160	-0.030	0.000	-0.030	0.030	0.030

Vra, RA volume, Vla, LA volume, Vlv, LV volume, Vrv, RV volume, Qlbv, lower body venous flow, Qi, gastro-intestinal flow, Qivcab, abdominal inferior vena cava flow, Qkv, renal venous flow, Qsvc, superior vena cava flow, Qutv, uterine venous flow, Qaoth, thoracic aortic flow, Qh, hepatic flow, Qha, hepatic arterial flow, Qia, gastro-intestinal arterial flow, Qk, renal flow, Qka, renal arterial flow, Qlb, lower body flow, Qlba, lower body arterial flow, Quba, upper body arterial flow, Qubv, upper body venous flow, Qut, uterine flow, Paoab, abdominal aortic pressure, Paoth, thoracic aortic pressure, Pha, hepatic arterial pressure, Pka, renal arterial pressure, Plba, lower body arterial pressure, Puba, upper body arterial pressure, Qao, aortic valve pressure, Qmv, mitral valve flow, Qpov, portal vein flow, Qpuve, pulmonary venous flow, Quta, uterine arterial flow, Pia, gastro-intestinal arterial pressure, Puta, uterine arterial pressure, Qcve, caval vein flow, Qpua, pulmonary arterial flow, Qpv, pulmonary valve flow, Qtv, tricuspid valve flow, Qivcth, thoracic inferior vena cava flow, Qhv, hepatic venous flow, Pra, RA pressure, Piv, gastro-intestinal venous pressure, Plv, LV volume, Ppua, pulmonary arterial pressure, Pivcth, thoracic inferior vena cava pressure, Phv, hepatic venous pressure, Pivcab, abdominal inferior vena cava pressure, Pla, LA pressure, Ppuve, pulmonary venous pressure, Prv, RV pressure, Plbv, lower body venous pressure, Putv, uterine venous pressure, Psvc, superior vena cava pressure, Pkv, renal venous pressure.

Table 6.10: *Mean sensitivities (S) of output signals to the input parameters for the sex-independent model. The inputs are ordered based on the global influence (the most influential on the left), the outputs are ordered based on the overall sensitivity (the most sensitive at the top). Note that, due the limited space, only the first 16 most influential inputs are here reported.*

	Cpuve	$\mathbf{V}_{p=0_{RA}}$	$\mathbf{V}_{p=0_{RV}}$	$\mathbf{V}_{p=0_{LA}}$	$\mathbf{V}_{p=0_{LV}}$	**Caoth**	$\mathbf{E}_{min_{RA}}$	**Cpua**	**Clbv**	**PVR**	$\mathbf{E}_{min_{LA}}$	**HR**	**SVR**	$\mathbf{E}_{max_{LV}}$	$\mathbf{E}_{min_{RV}}$	$\mathbf{E}_{max_{RV}}$
Vra	-0.890	-0.860	-0.940	-0.940	-0.930	-0.860	-0.850	-0.840	-0.820	-0.340	-0.570	-0.470	-0.360	-0.430	-0.560	-0.560
Vla	-0.840	-0.850	-0.870	-0.840	-0.860	-0.820	-0.800	-0.780	-0.780	-0.230	-0.730	-0.310	-0.140	-0.490	-0.430	-0.420
Vlv	-0.740	-0.620	-0.620	-0.620	-0.600	-0.720	-0.690	-0.690	-0.680	-0.070	-0.630	-0.200	0.030	-0.550	-0.680	-0.500
Vrv	-0.630	-0.300	-0.300	-0.300	-0.600	-0.600	-0.590	-0.590	-0.570	-0.150	-0.630	-0.290	-0.240	-0.280	-0.650	-0.520
Qivcab	-0.520	-0.530	-0.520	-0.520	-0.500	-0.510	-0.490	-0.460	-0.450	-0.540	-0.400	-0.430	-0.420	-0.360	-0.340	-0.280
Qlbv	-0.520	-0.530	-0.520	-0.530	-0.500	-0.510	-0.490	-0.460	-0.450	-0.540	-0.410	-0.440	-0.420	-0.360	-0.340	-0.280
Qh	-0.510	-0.520	-0.510	-0.510	-0.490	-0.490	-0.470	-0.440	-0.440	-0.520	-0.380	-0.410	-0.410	-0.330	-0.320	-0.260
Qha	-0.500	-0.510	-0.510	-0.510	-0.490	-0.480	-0.460	-0.440	-0.440	-0.520	-0.380	-0.410	-0.410	-0.330	-0.310	-0.250
Qi	-0.510	-0.520	-0.510	-0.510	-0.490	-0.490	-0.470	-0.450	-0.440	-0.520	-0.380	-0.410	-0.410	-0.330	-0.320	-0.260
Qia	-0.500	-0.510	-0.510	-0.510	-0.490	-0.480	-0.460	-0.440	-0.440	-0.520	-0.380	-0.410	-0.410	-0.330	-0.310	-0.250
Qk	-0.500	-0.510	-0.510	-0.510	-0.490	-0.480	-0.460	-0.440	-0.440	-0.520	-0.380	-0.410	-0.410	-0.330	-0.310	-0.250
Qkv	-0.510	-0.520	-0.510	-0.510	-0.490	-0.490	-0.470	-0.450	-0.440	-0.520	-0.380	-0.410	-0.410	-0.330	-0.320	-0.260
Qlb	-0.500	-0.510	-0.510	-0.510	-0.490	-0.480	-0.460	-0.440	-0.440	-0.520	-0.380	-0.400	-0.410	-0.330	-0.310	-0.250
Qsvc	-0.510	-0.520	-0.510	-0.510	-0.490	-0.490	-0.470	-0.450	-0.440	-0.520	-0.380	-0.410	-0.410	-0.330	-0.320	-0.260
Qubv	-0.500	-0.510	-0.510	-0.510	-0.490	-0.480	-0.460	-0.440	-0.440	-0.520	-0.380	-0.410	-0.410	-0.330	-0.310	-0.250
Paoab	0.350	0.340	0.340	0.340	0.370	0.380	0.400	0.430	0.430	0.320	0.490	0.450	0.460	0.550	0.570	0.630
Paoth	0.350	0.340	0.340	0.340	0.370	0.380	0.400	0.430	0.430	0.320	0.490	0.450	0.460	0.550	0.570	0.630
Pha	0.350	0.330	0.340	0.340	0.360	0.380	0.400	0.430	0.430	0.320	0.490	0.450	0.450	0.550	0.560	0.630
Pia	0.340	0.330	0.340	0.340	0.360	0.370	0.400	0.420	0.430	0.320	0.480	0.450	0.450	0.540	0.560	0.620
Pka	0.350	0.330	0.340	0.340	0.360	0.370	0.400	0.430	0.430	0.320	0.490	0.450	0.450	0.550	0.560	0.630

Continued on Next Page.

Table 6.10 – Continued

	Cpuve	$V_{p=0_{RA}}$	$V_{p=0_{RV}}$	$V_{p=0_{LA}}$	$V_{p=0_{LV}}$	Caoth	$E_{min_{RA}}$	Cpua	Clbv	PVR	$E_{min_{LA}}$	HR	SVR	$E_{max_{LV}}$	$E_{min_{RV}}$	$E_{max_{RV}}$
Plba	0.350	0.330	0.340	0.340	0.360	0.370	0.400	0.430	0.430	0.320	0.490	0.450	0.450	0.550	0.560	0.630
Puba	0.350	0.330	0.340	0.340	0.360	0.380	0.400	0.430	0.430	0.320	0.490	0.450	0.450	0.550	0.560	0.630
Qao	-0.490	-0.500	-0.500	-0.500	-0.480	-0.470	-0.450	-0.430	-0.430	-0.520	-0.370	-0.400	-0.400	-0.320	-0.310	-0.250
Qaoth	-0.500	-0.510	-0.500	-0.510	-0.480	-0.480	-0.460	-0.440	-0.430	-0.520	-0.380	-0.400	-0.410	-0.320	-0.310	-0.250
Qka	-0.500	-0.510	-0.500	-0.500	-0.480	-0.480	-0.460	-0.440	-0.430	-0.520	-0.370	-0.400	-0.410	-0.320	-0.310	-0.250
Qlba	-0.500	-0.510	-0.500	-0.500	-0.480	-0.480	-0.460	-0.430	-0.430	-0.520	-0.370	-0.400	-0.410	-0.320	-0.310	-0.250
Qmv	-0.490	-0.500	-0.490	-0.500	-0.480	-0.470	-0.450	-0.430	-0.430	-0.520	-0.370	-0.390	-0.400	-0.320	-0.310	-0.240
Quba	-0.500	-0.510	-0.500	-0.500	-0.480	-0.480	-0.460	-0.440	-0.430	-0.520	-0.370	-0.400	-0.410	-0.320	-0.310	-0.250
Qpov	-0.490	-0.500	-0.490	-0.490	-0.470	-0.470	-0.450	-0.430	-0.420	-0.510	-0.360	-0.390	-0.400	-0.310	-0.300	-0.240
Qpua	-0.480	-0.490	-0.490	-0.490	-0.470	-0.460	-0.450	-0.420	-0.420	-0.510	-0.360	-0.390	-0.400	-0.310	-0.300	-0.240
Qpuve	-0.490	-0.500	-0.490	-0.490	-0.470	-0.470	-0.450	-0.430	-0.420	-0.510	-0.370	-0.390	-0.400	-0.310	-0.300	-0.240
Qpv	-0.480	-0.490	-0.480	-0.480	-0.460	-0.460	-0.440	-0.420	-0.420	-0.510	-0.360	-0.380	-0.400	-0.310	-0.290	-0.230
Qcve	-0.480	-0.480	-0.480	-0.480	-0.460	-0.460	-0.440	-0.420	-0.410	-0.510	-0.350	-0.380	-0.400	-0.310	-0.290	-0.230
Qivcth	-0.470	-0.470	-0.470	-0.470	-0.450	-0.450	-0.430	-0.410	-0.410	-0.500	-0.340	-0.370	-0.390	-0.300	-0.280	-0.220
Qtv	-0.470	-0.480	-0.480	-0.480	-0.460	-0.460	-0.440	-0.420	-0.410	-0.510	-0.360	-0.380	-0.400	-0.300	-0.290	-0.230
Pra	-0.210	-0.270	-0.270	-0.270	-0.250	-0.160	-0.140	-0.140	-0.120	-0.370	-0.470	-0.510	-0.390	-0.470	-0.450	-0.610
Qhv	-0.380	-0.380	-0.380	-0.380	-0.360	-0.360	-0.340	-0.330	-0.330	-0.460	-0.250	-0.280	-0.350	-0.210	-0.190	-0.130
Pivcth	-0.120	-0.180	-0.170	-0.170	-0.150	-0.080	-0.060	-0.050	-0.030	-0.260	-0.320	-0.360	-0.260	-0.310	-0.290	-0.420
Piv	0.210	0.180	0.180	0.180	0.200	0.240	0.260	0.270	0.290	0.100	0.200	0.170	0.180	0.240	0.250	0.240
Pivcab	-0.070	-0.120	-0.120	-0.120	-0.100	-0.030	-0.010	0.000	0.020	-0.200	-0.230	-0.270	-0.180	-0.220	-0.200	-0.300
Plv	0.100	0.050	0.050	0.050	0.080	0.130	0.190	0.180	0.180	0.130	0.280	0.150	0.250	0.280	0.340	0.360
Ppua	0.180	0.150	0.150	0.150	0.170	0.200	0.220	0.250	0.250	0.080	0.320	0.130	-0.280	0.090	0.190	0.170
Phv	0.160	0.130	0.130	0.130	0.150	0.200	0.220	0.230	0.240	0.040	0.120	0.080	0.100	0.150	0.160	0.130

Continued on Next Page.

Table 6.10 – Continued

	Cpuve	$\mathbf{V}_{p=0_{RA}}$	$\mathbf{V}_{p=0_{RV}}$	$\mathbf{V}_{p=0_{LA}}$	$\mathbf{V}_{p=0_{LV}}$	**Caoth**	$\mathbf{E}_{min_{RA}}$	**Cpua**	**Clbv**	**PVR**	$\mathbf{E}_{min_{LA}}$	**HR**	**SVR**	$\mathbf{E}_{max_{LV}}$	$\mathbf{E}_{min_{RV}}$	$\mathbf{E}_{max_{RV}}$
Pla	-0.070	-0.130	-0.120	-0.120	-0.100	-0.060	-0.030	-0.010	-0.010	-0.230	0.060	-0.320	-0.150	-0.500	-0.310	-0.430
Prv	-0.090	-0.170	-0.160	-0.160	-0.140	-0.020	0.000	-0.020	0.030	-0.120	0.050	-0.200	-0.330	-0.200	-0.010	-0.100
Ppuve	0.040	0.000	0.010	0.000	0.030	0.060	0.090	0.110	0.110	-0.080	0.180	-0.110	-0.210	-0.220	-0.080	-0.150
Plbv	0.080	0.040	0.050	0.050	0.070	0.110	0.130	0.150	0.170	-0.010	0.030	-0.010	0.050	0.060	0.070	0.040
Psvc	0.040	-0.010	0.000	0.000	0.020	0.070	0.100	0.110	0.130	-0.060	-0.040	-0.080	-0.010	-0.020	0.000	-0.060
Pkv	0.070	0.030	0.030	0.030	0.050	0.100	0.120	0.140	0.160	-0.030	0.000	-0.030	0.030	0.030	0.050	0.000

Vra, RA volume, Vla, LA volume, Vlv, LV volume, Vrv, RV volume, Qivcab, abdominal inferior vena cava flow, Qlbv, lower body venous flow, Qh, hepatic flow, Qha, hepatic arterial flow, Qi, gastro-intestinal flow, Qia, gastro-intestinal arterial flow, Qk, renal flow, Qkv, renal venous flow, Qlb, lower body flow, Qsvc, superior vena cava flow, Qubv, upper body venous flow, Paoab, abdominal aortic pressure, Paoth, thoracic aortic pressure, Pha, hepatic arterial pressure, Pia, gastro-intestinal arterial pressure, Pka, renal arterial pressure, Plba, lower body arterial pressure, Puba, upper body arterial pressure, Qao, aortic valve pressure, Qaoth, thoracic aortic flow, Qka, renal arterial flow, Qlba, lower body arterial flow, Qmv, mitral valve flow, Quba, upper body arterial flow, Qpov, portal vein flow, Qpua, pulmonary arterial flow, Qpuve, pulmonary venous flow, Qpv, pulmonary valve flow, Qcve, caval vein flow, Qivcth, thoracic inferior vena cava flow, Qtv, tricuspid valve flow, Pra, RA pressure, Qhv, hepatic venous flow, Pivcth, thoracic inferior vena cava pressure, Piv, gastro-intestinal venous pressure, Pivcab, abdominal inferior vena cava pressure, Plv, LV volume, Ppua, pulmonary arterial pressure, Phv, hepatic venous pressure, Pla, LA pressure, Prv, RV pressure, Ppuve, pulmonary venous pressure, Plbv, lower body venous pressure, Psvc, superior vena cava pressure, Pkv, renal venous pressure.

Tables 6.9 and 6.10 show the results of the sensitivity analysis for the woman-specific and sex-independent models, respectively. The inputs are ordered considering the global influence, i.e., as the sum of $|S|$ for all the outputs analyzed, showing the most influential on the left. The outputs are ordered based on the overall sensitivity, computed as the median value of $|S|$ for all the inputs, with the most sensitive at the top. Note that, due to the lack of space, only the first 16 most influential inputs are reported. Fig. 6.8 and 6.9 report the graphical representation of the sensitivity analysis for the W and SI models, respectively. This time, the outputs are listed on the horizontal axis and the inputs are listed on the vertical axis. Note that in the figures, the outputs are ordered with the most sensitive on the left, and the inputs are ordered with the most influential at the bottom.

For the woman-specific circulation, the most influential parameters are the venous pulmonary and aortic compliances and the ventricular volume-related parameters ($V_{p=0}$). The latter, as reported in other chapters, once identified the value that matches simulated and real hemodynamics, i.e., adequate chamber's dimension, is kept constant during the simulations and thus does not affect the outcomes. On the other hand, the compliances represent the pulsatile component of the afterload. Thus, it is reasonable, and already known from the physiology, that variations in the afterload affect the overall hemodynamics also in terms of its mean values. The sensitivity analysis results prove that the model captures the effects of the compliances on the hemodynamics and, at the same time, show that it is crucial to assign to compliances the values pertinent to the real case to be simulated. The most sensitive outputs are the heart chambers volumes. A variation in the pulsatile component of the afterload determines changes in the heart volumes that in turn affect the cardiac force in agreement with the Frank-Starling law, further affecting the overall hemodynamics. Fig. 6.8 shows a cluster of larger data points in the left side for those parameters that are more sensitive. The least sensitive output signals are the right ventricular and systemic venous pressures and this could be related to the reservoir functionality of the high-compliance venous circulation.

For the sex-independent model, results analogous to the woman-specific model are found. The most influential parameters are again the venous pulmonary and aortic compliances and the ventricular volume-related parameters ($V_{p=0}$). Similarly, the most sensitive outputs are the heart chambers volumes. As previously, Fig. 6.9 shows a cluster of larger data points in the left side for those parameters that are more sensitive. The least sensitive outputs signals are, again, the right ventricular and systemic venous pressures.

Thus, the two models present very similar sensitivity, and this is expected since they only differ in the presence/absence of the uterus compartment.

6.5 Discussion

The importance of sex-specific research has been emphasized in the recent years, particularly in the cardiovascular field. Indeed, as Schiebinger reported in [6], *"cardiology offers one of the best developed examples of gendered innovations: sex and gender analyses have shown, for example, that cardiovascular disease, long defined as primarily a male disease, is the number one killer of adult women"*. Moreover, with the development of sex analysis it is possible to better understand sex-specific symptoms and diseases, improving the efficacy of treatments. However, while it is true that attention is increasingly devoted to sex-related aspects by the medical research, the same can not be said for what the modeling research is concerned, at least in the field of cardiovascular fluid dynamics modeling. Sex-analysis is hence here simulated by both developing a female-specific and a sex-independent model (i.e., with/without the uterus explicitly represented in the model) and investigating the effect of sex-specific input parameter's values on the global hemodynamics.

Results obtained by implementing the sex-independent model with either male- or female-specific input parameter's values are found to satisfactorily agree with the sex-specific clinical literature [18, 22, 24], thus proving the capability of the model to capture physiological hemodynamics for both the sexes. Importantly, male and female hemodynamics result to differ in terms of waveforms and mean values, even after normalization to BSA or BM. Such an occurrence suggests that female and male circulations are not just a scale version of each other. Rather, it suggests the possibility that the biomechanical mechanisms that drive the cardiovascular response somehow differ in men and women as medical research has recently started to point out [22]. For example, pressure-volume loops depicted in Fig. 6.7 show that in the female case the loops are smaller and left-shifted, and enclose a smaller stroke work. In this case, it can be speculated that the smaller cardiac work in women represent a sort of footprint of a work 'reserve' made available by the female heart to fulfill the augmented cardiac output request during pregnancy. This hypothesis needs (and seems to deserve) further investigation. Moreover, the normalization to BSA or BM highlights the maintenance of sex differences for RV volume while reducing them for LV, result found in the clinical practice [24] and reproduced also by the model.

The role of the uterus is assessed by analyzing the woman-specific model *vs* the sex-independent model implemented with female parameters. The comparison points out that, when the healthy physiological circulation is considered, the uterus has a minor impact on the overall hemodynamics. This result is expected because in the specific case of healthy condition, the uterus is perfused by a very small amount of blood ($\sim$0.4%CO). However, it is worth noting that when the uterine flow is the variable of interest or an altered condition, e.g., pregnancy, wants to be studied, the woman-specific model has to be used. In this case, the choice of values to be adopted for the functional parameters is pivotal in order to avoid overestimation of Qut as large as 40%. Such a consideration is far from being trivial when observing that cardiovascular parameter's values adopted in literature numerical models are often extracted from medical researches that do not specify the sex of the reference patients' group.

Note that, currently, clinical data of pressure and volume are known for the female population in insufficient quantity. Indeed, for some pressure and flow quantities, female values to compare with the outcomes of the female-specific simulation are not available (e.g., hepatic pressure). This suggests that sex-specific research needs further development, focusing also on the female-specific hemodynamics of organs such as kidneys, liver, and uterus. The understanding of physiological quantities of the female population is fundamental to detect abnormal functions. Indeed, since it has been shown that morphological parameters (especially those for RV) are sex-dependent even after normalization to BSA [18], only the knowledge of physiological male or female values gives the possibility to highlight altered or pathological conditions. Moreover, the availability of sex-specific quantities (i.e., pressures and flows) will allow an easier validation of numerical models. Thus, further research that provides insights into the pressures and flows in all organs considering both male and female subjects will be imperative.

6.6 Conclusion

A woman-specific model and a sex-independent model are developed and validated considering sex-specific *in vivo* clinical data. Both the models result to suitably represent the hemodynamics of both an average woman of 58 kg and BSA of 1.6 m^2 and an average man of 70 kg and BSA of 1.81 m^2 in healthy conditions. Results show that cardiovascular circulation is a matter of sex-related parameters rather than sex-related organs. Indeed, if the focus

is not the uterine flow, it is not relevant to include the sex-specific reproductive organ, e.g., uterus in the female case, in the model, but it is pivotal to feed the model with sex-specific parameters. This is further confirmed by the fact that differences between male and female cases remain even after normalization to BSA and BM. On the other hand, the woman-specific model is useful whenever alterations from the physiological conditions need to be studied in a woman, considering the uterine hemodynamics. Typically when pregnancy or diseased conditions of the reproductive apparatus are of interest. However, a severe lack of extensive data on female-specific pressures and flows in various organs is still present. Thus, a further development of sex research, both in the clinical and numerical fields, is necessary to guarantee an adequate understanding of sex-specific hemodynamics.

Bibliography

[1] G. Comunale, F. M. Susin, and J. P. Mynard, "A female-specific cardiovascular lumped-parameter model," in *Proceedings of the 42nd Annual International Conferences of the IEEE Engineering in Medicine and Biology Society in conjunction with the 43rd Annual Conference of the Canadian Medical and Biological Engineering Society*, 42nd Annual International Conferences of the IEEE Engineering in Medicine and Biology Society in conjunction with the 43rd Annual Conference of the Canadian Medical and Biological Engineering Society, 2020.

[2] G. Comunale, J. P. Mynard, and F. M. Susin, "Blood circulation: is it a matter of sex?," in *Atti del XXXVII Convegno Nazionale di Idraulica e Costruzioni Idrauliche*, 2020.

[3] Y. Appelman, B. B. van Rijn, E. Monique, E. Boersma, and S. A. Peters, "Sex differences in cardiovascular risk factors and disease prevention," *Atherosclerosis*, vol. 241, no. 1, pp. 211–218, 2015.

[4] L. S. Mehta, T. M. Beckie, H. A. DeVon, C. L. Grines, H. M. Krumholz, M. N. Johnson, K. J. Lindley, V. Vaccarino, T. Y. Wang, K. E. Watson, *et al.*, "Acute myocardial infarction in women: a scientific statement from the american heart association," *Circulation*, vol. 133, no. 9, pp. 916–947, 2016.

[5] S. Purkiss and V. F. Huckell, "Cardiovascular physiology: similarities and differences between healthy women and men," *Journal of Obstetrics and Gynaecology Canada*, vol. 19, no. 8, pp. 853–859, 1997.

[6] L. Schiebinger, "Gendered innovations in biomedicine and public health research," in *Sex and Gender Aspects in Clinical Medicine*, pp. 5–8, Springer, 2012.

[7] J. McSweeney, M. Cody, P. O'Sullivan, K. Elberson, D. Moser, and B. Barvin, "Women's early warning symptoms of acute myocardial infarction," *ACC Current Journal Review*, vol. 3, no. 13, p. 9, 2004.

[8] J. P. Mynard, *Computer modelling and wave intensity analysis of perinatal cardiovascular function and dysfunction*. PhD thesis, Department of Paediatrics, The University of Melbourne, Heart Research Group, Murdoch Childrens Research Institute, 2011.

[9] T. Heldt, *Computational models of cardiovascular response to orthostatic stress*. PhD thesis, Massachusetts Institute of Technology, 2004.

[10] P. Kam and I. Power, *Principles of Physiology for the Anaesthetist*. CRC Press, 2015.

[11] T. Tanaka, M. Arakawa, T. Suzuki, M. Gotoh, H. Miyamoto, and S. Hirakawa, "Compliance of human pulmonary "venous" system from pulmonary artery wedge pressure tracings: comparison with pulmonary arterial compliance," *Japanese Circulation Journal*, vol. 50, no. 2, pp. 127–139, 1986.

[12] A. Bellofiore, Z. Wang, and N. C. Chesler, "What does the time constant of the pulmonary circulation tell us about the progression of right ventricular dysfunction in pulmonary arterial hypertension?," *Pulmonary Circulation*, vol. 5, no. 2, pp. 291–295, 2015.

[13] F. Liang, H. Senzaki, C. Kurishima, K. Sughimoto, R. Inuzuka, and H. Liu, "Hemodynamic performance of the fontan circulation compared with a normal biventricular circulation: a computational model study," *American Journal of Physiology-Heart and Circulatory Physiology*, vol. 307, no. 7, pp. H1056–H1072, 2014.

[14] J. P. Mynard and J. J. Smolich, "One-dimensional haemodynamic modeling and wave dynamics in the entire adult circulation," *Annals of biomedical engineering*, vol. 43, no. 6, pp. 1443–1460, 2015.

[15] M. D. Pettersen, W. Du, M. E. Skeens, and R. A. Humes, "Regression equations for calculation of z scores of cardiac structures in a large cohort of healthy infants, children, and adolescents: an echocardiographic

study," *Journal of the American Society of Echocardiography*, vol. 21, no. 8, pp. 922–934, 2008.

[16] S. C. Robson, S. Hunter, R. J. Boys, and W. Dunlop, "Serial study of factors influencing changes in cardiac output during human pregnancy," *American Journal of Physiology-Heart and Circulatory Physiology*, vol. 256, no. 4, pp. H1060–H1065, 1989.

[17] P. Argiento, R. R. Vanderpool, M. Mulè, M. G. Russo, M. D'Alto, E. Bossone, N. C. Chesler, and R. Naeije, "Exercise stress echocardiography of the pulmonary circulation: limits of normal and sex differences," *Chest*, vol. 142, no. 5, pp. 1158–1165, 2012.

[18] C. H. Lorenz, E. S. Walker, V. L. Morgan, S. S. Klein, and T. P. Graham, "Normal human right and left ventricular mass, systolic function, and gender differences by cine magnetic resonance imaging," *Journal of Cardiovascular Magnetic Resonance*, vol. 1, no. 1, pp. 7–21, 1999.

[19] M. Demir and E. Acartürk, "Clinical characteristics influence left and right ventricular diastolic function in healthy individuals," *Angiology*, vol. 52, no. 1, pp. 25–30, 2001.

[20] S. A. Hale, A. Schonberg, G. J. Badger, and I. M. Bernstein, "Relationship between prepregnancy and early pregnancy uterine blood flow and resistance index," *Reproductive Sciences*, vol. 16, no. 11, pp. 1091–1096, 2009.

[21] E. J. Bridges, S. Womble, M. Wallace, and J. McCartney, "Hemodynamic monitoring in high-risk obstetrics patients, i expected hemodynamic changes in pregnancy," *Critical Care Nurse*, vol. 23, no. 4, pp. 53–62, 2003.

[22] P. L. Kerkhof and V. M. Miller, *Sex-specific analysis of cardiovascular function*, vol. 1065. Springer, 2018.

[23] W. Milnor, "Hemodynamic 2nd edn (baltimore, md: William and wilkins)," 1989.

[24] L. E. Hudsmith, S. E. Petersen, J. M. Francis, M. D. Robson, and S. Neubauer, "Normal human left and right ventricular and left atrial dimensions using steady state free precession magnetic resonance imaging," *Journal of cardiovascular magnetic resonance*, vol. 7, no. 5, pp. 775–782, 2005.

[25] A. M. Maceira, S. K. Prasad, M. Khan, and D. J. Pennell, "Reference right ventricular systolic and diastolic function normalized to age, gender and body surface area from steady-state free precession cardiovascular magnetic resonance," *European heart journal*, vol. 27, no. 23, pp. 2879–2888, 2006.

7 V Application: Pregnancy model and Cardiac remodeling

Contents

Pregnancy is a unique and dynamic process characterized by significant changes in the maternal cardiovascular system to satisfy the increased maternal and fetal metabolic demands. Profound structural and hemodynamic adaptations occur during healthy pregnancy that allow the mother to maintain healthy hemodynamics and provide the uteroplacental blood circulation required for a physiological fetal development. The analysis of both hemodynamic and cardiac structural changes is fundamental to fully understand and highlight the complicated process of pregnancy and on the clinical side, to check the mother status. However, no previous modeling studies have

investigated the maternal cardiac structural changes that occur during gestation. The study presented in this chapter is undertaken with two aims. First, the hypothesis that myofiber stress and wall shear stress homeostasis principles can be used to predict cardiac remodeling that occurs during pregnancy is formulated. Second, to verify the aforementioned hypothesis, two lumped-parameter models are developed. One is a *novel* model of the whole maternal circulation that is able to replicate both the hemodynamic and cardiac structural changes during pregnancy, i.e., with the controlled remodeling algorithm. The other, which reproduces only the hemodynamic variations, i.e., with the not controlled remodeling algorithm. The results of the two models are compared and analyzed with reference clinical data. While both models reproduce the hemodynamic variations that arise in pregnancy, it is shown, importantly, that the structural changes that occur with pregnancy could be predicted by assuming and imposing invariant homeostatic 'target' values of myocardial wall stress and chamber wall shear stress.

7.1 Introduction

Pregnancy is a unique and dynamic process characterized by significant changes in the maternal cardiovascular system that are required to satisfy the increased maternal and fetal metabolic demands. Significant structural and hemodynamic adaptations occur during healthy pregnancy that allow the mother to maintain healthy hemodynamics and guarantee an adequate uteroplacental blood supply to support fetal development. Starting from early pregnancy, increased heart rate (HR) and stroke volume (SV), which lead to an increased cardiac output (CO) are amongst the key hemodynamic changes. They are also accompanied by a decrease in total vascular resistance (TVR) and pulmonary vascular resistance (PVR), whereas total systemic vascular compliance (Ctsv) increases. As a result, blood volume increase, while maintaining an almost unaltered blood pressure [1, 2, 3]. The induced blood volume overload typical of pregnancy, leads to changes in the cardiac structure. Increased atrial and ventricular end-diastolic volume (EDV), wall thickness, and mass, which constitute physiological remodeling [1, 2, 3, 4, 5, 6, 7] hence, take place.
When maternal adaptations are insufficient, both maternal and fetal morbidities can arise, for example, maternal hypertension can result from an inadequate TVR reduction [8]. Moreover, cardiac remodeling is found to be eccentric, as in athletes, when physiological pregnancies occur, whereas concentric hypertrophy, as typical of some cardiovascular diseases, e.g., valve

diseases, is often found in pathological pregnancies, e.g., preeclamptic women [1, 8]. Thus, the analysis of both hemodynamic and geometrical changes is fundamental to developing a full understanding of both normal and high-risk pregnancies.

Despite the fundamental role of the maternal cardiovascular system in pregnancy, prior modeling studies have focused almost exclusively on the fetal side or on the interaction between mother and fetus [9, 10, 11, 12, 13], and as far as we are aware, there are only two works that study the whole maternal blood circulation during pregnancy [14, 15]. Corsini et al. were the first to describe a lumped-parameter model of the maternal circulation, achieving reasonable agreement between model outputs and *in vivo* data [15]. More recently, Carson et al. described a one-dimensional model suitable for estimating volumetric blood flow to the uterus via the utero-ovarian communicating arteries and for capturing wave propagation phenomena in the utero-ovarian circulation [14]. However, although these focused on the mother, they only replicated the hemodynamic changes but did not consider the structural remodeling that occurs during gestation. In the present work, cardiac remodeling is represented by assuming that, following the work by Maksuti et al. in the setting of valve disease [16], myofiber stress (σ_f) and chamber wall shear stress (σ_{wss}) homeostasis principles drive the cardiac remodeling typical of pregnancy. Particularly, two lumped-parameter models of the whole maternal circulation are implemented to demonstrate that the hemodynamic and geometrical changes are governed by σ_f and σ_{wss} homeostasis. To investigate our hypothesis, two models are designed with and without the maintenance of the homeostatic values of myofiber and wall shear stresses, i.e., with the controlled (CRA) and not controlled remodeling algorithm (NCRA). The results of the two models are compared with clinical data.

7.2 Methods

The woman-specific lumped-parameter model presented in Ch. 6 (Section 6.2) is here utilized.

To study and analyze the hemodynamic and structural changes during pregnancy, first, the circulation of the non-pregnant case (NPC) is considered, then, the variations typical of each trimester are applied, considering: *i)* the first (T1), *ii)* the second (T2), *iii)* the third (T3) trimesters, and *iv)* the end of pregnancy (Term).

7.2.1 Hemodynamic model

The model builds on work presented in Subsection 6.2.1 that describes a model parameterized specifically for simulating hemodynamics in a representative woman.

7.2.2 Geometrical model

To compute the cardiac geometrical parameters, a geometry to each heart chamber is assigned. Particularly, the simplified geometry proposed in [16] is assumed, where the left and right atria (LA, RA) are considered spheres, the left ventricle (LV) is a half ellipsoid, and the right ventricle (RV) is represented as a quarter ellipsoid (Fig. 7.1). Each chamber is described by wall thickness (h) and inner radius (r), and the ventricular longitudinal dimension is defined as $3r$. Chambers' volumes are hence computed as

$$\begin{cases} V_{lumen_a} = \frac{4\pi r^3}{3} \\ V_{myo_a} = \frac{4\pi(r+h)^3}{3} - \frac{4\pi r^3}{3} \end{cases} \tag{7.1}$$

where V_{lumen_a} represents the atrial blood (fluid) volume and V_{myo_a} is the atrial myocardial volume, i.e., the wall volume. Accordingly, the left (V_{lv}, $V_{myo_{lv}}$) and right (V_{rv}, $V_{myo_{rv}}$) fluid and wall ventricular volumes are computed as

$$\begin{cases} V_{lv} = 2\pi r^3 \\ V_{myo_{lv}} = \frac{1}{2}\frac{4\pi(3r+h)(r+h)^2}{3} - 2\pi r^3 \end{cases} \tag{7.2}$$

$$\begin{cases} V_{rv} = \pi r^3 \\ V_{myo_{rv}} = \frac{\pi(3r+h)(r+h)^2}{3} - \pi r^3 \end{cases} \tag{7.3}$$

Interaction among chambers, e.g., volume variations due to atrial/ventricular septum movement, is neglected.

7.2.3 Pregnancy

Pregnancy is simulated by applying the following alterations that reflect adaptive processes in the cardiovascular system during gestation.

Blood distribution. It is known that vascular resistances decrease during pregnancy [1, 20]. Hence, the distribution of CO to various organs changes according to trimester [15, 21, 22, 23]. Blood distribution to each organ is imposed according to literature data (Table 7.1). Note that this deter-

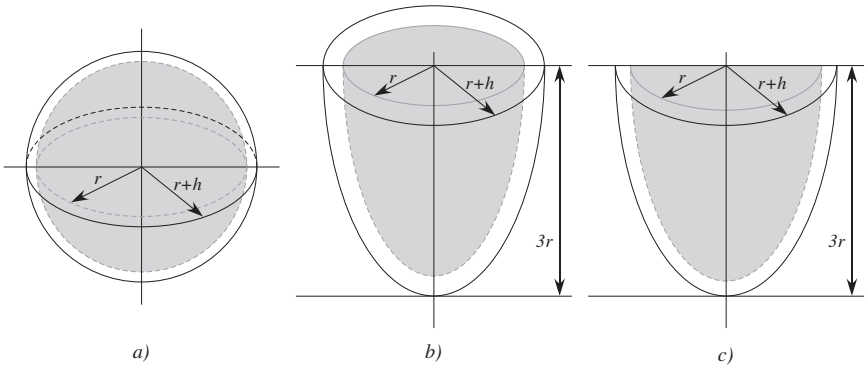

Figure 7.1: *Geometrical model of a) atria, b) left ventricle, and c) right ventricle. Each chamber has a constant thickness of h, and an inner radius of r. The ventricular longitudinal dimension is 3r.*

mines a change in the values of the lumped-parameters that describe each compartment (see Subsection 7.2.5).

Table 7.1: *Blood flow distribution during gestation. Percentages are given with respect to CO.*

%CO	NPC	T1	T2	T3	Term
Qliver	7%	6%	5%	4%	4%
Qsi	26%	32%	35%	36%	35%
Qub	22%	19%	16%	14%	12%
Qk	21%	24%	23%	21%	18%
Qut	0.44%	4%	6%	11%	15%
Qlb	23.56%	15%	15%	14%	16%

NPC, non-pregnant case, T1, first trimester, T2, second trimester, T3, third trimester and Term, end of pregnancy. Qliver, hepatic flow, Qsi, flow to the stomach and intestines, Qub, upper body flow, Qk, renal flow, Qut, uterine flow, Qlb, lower body flow. Data from [15, 21, 22, 23]

Total vascular resistance and systemic global compliance. TVR and systemic compliances are reduced and increased, respectively, according to data reported by Melchiorre et al. [1] (Table 7.2).

Heart rate. Heart rate increases as pregnancy proceeds and changes reported in the literature [24] are imposed as a model input (see Table 7.4).

Heart valves. Valves' area increases during pregnancy [26, 27, 28]. Moreover, Pettersen et al. [25] measured the variations of heart valve dimensions depending on the body surface area (BSA), finding that valve dimensions increase as BSA increases (see Fig. 7.2). Thus, during the different phases of gestation, the increase in BSA (Table 7.4) determines an increase in valve dimensions, in agreement with the values of Pettersen et al. [25].

Table 7.2: *Percentage changes in total vascular resistance and total systemic vascular compliance during gestation. Variations are given with respect to NPC and in according to Melchiorre et al. [1].*

Parameter	T1	T2	T3	Term
TVR	-5%	-4%	-15%	-8%
Ctsv	30%	30%	30%	30%

NPC, non-pregnant case, T1, first trimester, T2, second trimester, T3, third trimester and Term, end of pregnancy. TVR, total vascular resistance and Ctsv, total systemic vascular compliance.

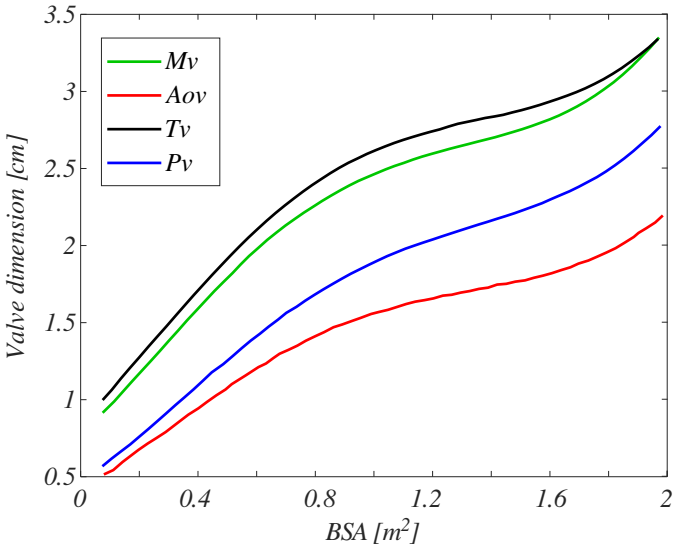

Figure 7.2: *Mean heart valves' dimensions versus body surface area (BSA). Values in agreement with Pettersen et al. [25]. Mv, mitral valve, Aov, aortic valve, Pv, pulmonary valve, and Tv, tricuspid valve.*

7.2.4 Cardiac remodeling

Cardiac remodeling is the genetic, molecular, cellular, and interstitial changes arising in the heart due to hemodynamic overload that leads to adaptation in mass, size, geometry, and function to restore the optimal hemodynamics [29]. Thus, the volume overload condition typical of pregnancy triggers this mechanism with the purpose to assure physiological conditions while increasing CO.

Maksuti et al. in [16] proposed an algorithm to study cardiac remodeling in cardiovascular disease. They supposed that the preservation of myofiber stress and wall shear stress accurately predicts the cardiac remodeling seen in patients with valve diseases. The former has a crucial role in determining a variation in wall thickness; whereas the latter causes chamber dilation in

response to increasing flow. Here, these key principles are maintained, and, moreover, the algorithm is adjusted to account for the fact that remodeling during pregnancy is mainly directed towards supporting an increased CO. Therefore, the rules in which myofiber stress and wall shear stress are kept constant (equal to NPC values) are adopted and a rule that determines a change in blood volume to meet the required CO is added. The latter can be seen as an increase in the total blood volume within the body, which implies a variation in myofiber length and affects the cardiac force, according to the Frank-Starling law. Thus, to satisfy the required hemodynamics during pregnancy, blood volume increases and so does the size of the chambers.

The above three rules are implemented as described in the following. Note that, the solution of the hemodynamic model, i.e., the woman-specific model, is utilized to define the three remodeling rules.

i) Increase in blood volume: it is realized by changing the initial values of the model's variables so that the difference between the computed ($CO_{computed}$) and the desired cardiac output (CO_{target}) meets a given tolerance. In fact, in lumped-parameter models the amount of blood in the circuit is determined by the initial conditions. The target value for each trimester is taken from [24] (Table 7.4) and a tolerance of 2% is imposed. In particular, first, the error (err_{CO}) is computed as

$$err_{CO} = \frac{CO_{target} - CO_{computed}}{CO_{target}} \tag{7.4}$$

then, if $err_{CO} > 2\%$, variations are applied to the initial values of the model's variables by computing and imposing the percentage change (p_{CO}) in the following way

$$\begin{aligned} p_{CO}(\%) &= fact_{CO} \cdot err_{CO} \cdot CO_{target} \cdot 100 \\ Y^{'}(t=0)_{iter=i+1} &= Y(t=T)_{iter=i} \cdot (1 + p_{CO}/100) \end{aligned} \tag{7.5}$$

where $fact_{CO} = 0.01$ and is factor to reduce the variations imposed to the initial values to guarantee stability, i.e., avoiding big fluctuations in the system, and $Y^{'}(t=0)_{iter=i+1}$ is the new initial value computed from the last value of the previous heartbeat simulated, i.e., the solution of the hemodynamic model ($Y(t=T)_{iter=i}$). The use of $Y(t=T)_{iter=i}$ allows to work in the range of stability of the system, reducing the iterations required to converge. Note also that p_{CO} can be positive or negative depending on $CO_{computed}$ and hence allowing both higher and smaller initial values.

ii) Maintenance of physiological myofiber stress: in agreement with the work of Maksuti et al. [16], this rule is realized by changing the myocardial wall volume, and assuming that the myocardium is distributed among the four heart chambers in proportion to their stiffness and contractility [16]. The target value (during pregnancy) for each heart chamber is the NPC value reported in Table 7.3 and, as previously, a tolerance of 2% is imposed. Thus, first, the error (err_{σ_f}) between the computed ($\sigma_{f_{computed}}$) and the desired myofiber stress ($\sigma_{f_{target}}$) is computed as

$$err_{\sigma_f} = \frac{\sigma_{f_{computed}} - \sigma_{f_{target}}}{\sigma_{f_{target}}}. \tag{7.6}$$

Then, if $err_{\sigma_f} > 2\%$ the following changes are applied

$$\begin{aligned} v_{wall_{iter=i+1}} &= fact_{\sigma_f} \cdot err_{\sigma_f} \cdot \sigma_{f_{target}} + v_{wall_{iter=i}} \\ E_{max_{iter=i+1}} &= \frac{v_{wall_{iter=i+1}}}{v_{wall_{iter=i}}} \cdot E_{max_{iter=i}} \\ E_{min_{iter=i+1}} &= \frac{v_{wall_{iter=i+1}}}{v_{wall_{iter=i}}} \cdot E_{min_{iter=i}} \end{aligned} \tag{7.7}$$

where $fact_{\sigma_f} = 0.005$ and has the same role of $fact_{CO}$, $v_{wall_{iter=i+1}}$ is the new value of wall chamber computed from the previous iteration value ($v_{wall_{iter=i}}$), and $E_{max_{iter=i+1}}$ and $E_{min_{iter=i+1}}$ are the new maximum and minimum heart elastance (i.e., maximum force and stiffness, respectively) computed from the previous iteration values ($E_{max_{iter=i}}$ and $E_{min_{iter=i}}$), respectively. Note also that v_{wall}, E_{max}, and E_{min} are heart chamber-dependent. Moreover, σ_f is computed differently from [16]. Maksuti et al. used $\sigma_f = p \cdot \frac{3}{\ln\left(1+\frac{v_{wall}}{v_{lumen}}\right)}$ [16], whereas the formula used in clinical practice is here applied, which allows to compare the results with the clinical data: $\sigma_f = 1.35 \cdot P_{es} \cdot \frac{2r}{4 \cdot PW_s \cdot \left(1+\frac{PW_s}{2r}\right)}$, where P_{es}, PW_s, and r are the pressure, thickness and radius of each chamber at end-systole respectively [8, 24].

iii) Maintenance of physiological wall shear stress: analogous to the previous rule and as previous reported, also this rule is in agreement with the work of Maksuti et al. [16]. In particular, the maintenance of σ_{wss} is obtained by varying the unstressed volume ($V_{p=0}$) of Eq. (2.6). The target value (during pregnancy) for each heart chamber is, again, the NPC value reported in Table 7.3 and, as previously, a tolerance of 2% is imposed. Thus, in analogy to the previous two rules, first, the error ($err_{\sigma_{wss}}$) between the

computed ($\sigma_{wss_{computed}}$) and the desired wall shear stress ($\sigma_{wss_{target}}$) is computed as

$$err_{\sigma_{wss}} = \frac{\sigma_{wss_{computed}} - \sigma_{wss_{target}}}{\sigma_{wss_{target}}}. \tag{7.8}$$

Then, if $err_{\sigma_{wss}} > 2\%$, $V_{p=0}$ is adjusted as

$$V_{p=0_{iter=i+1}} = fact_{\sigma_{wss}} \cdot err_{\sigma_{wss}} \cdot \sigma_{wss_{target}} + V_{p=0_{iter=i}} \tag{7.9}$$

where $fact_{\sigma_{wss}} = 1000$ and has the same role of $fact_{CO}$ and $fact_{\sigma_f}$. Also $V_{p=0}$ is heart chamber-dependent. Moreover, σ_{wss} is computed assuming a laminar flow of Poiseuille's type through a cylindrical pipe as

$$\begin{cases} \sigma_{wss} = \frac{4\mu q_{chamber}}{\pi r^3} \\ q_{chamber} = \frac{|q_{inlet}|+|q_{outlet}|}{2} \end{cases} \tag{7.10}$$

where μ is the dynamic viscosity, and q_{inlet} and q_{outlet} are the inlet and outlet valve blood flow, respectively. Note that, if flow conditions are turbulent, the σ_{wss} expression (Eq. (7.10)) should be different, but this is beyond the purpose of this work.

Table 7.3: *Myofiber and wall shear stresses computed by the models for each heart chamber in the NPC configuration.*

Parameter	**LV**	**RV**	**LA**	**RA**
σ_f [g/cm^2]	70	82	114	62
σ_{wss} [mmHg]	0.0025	0.0012	0.0023	0.0033

Finally, the two lumped-parameter models are hence built as follow:

- The *Controlled remodeling algorithm* (CRA) results from the set of the three conditions described above. CRA is hence implemented in the woman-specific model to describe the pregnancy in terms of both the hemodynamic variations and the cardiac remodeling conditioned by homeostatic values of stresses.
- The *Not controlled remodeling algorithm* (NCRA) considers only the hemodynamic changes of the pregnancy whereas the cardiac remodeling is unconditional, i.e., NCRA solves only rule *i)*.

In particular, for each lumped model, the following steps are executed:

1 The woman-specific model (hemodynamic model) is run;

2 from the hemodynamic solution, err_{CO}, and err_{σ_f} and $err_{\sigma_{wss}}$ (only for CRA), are computed;

3 if errors are higher than the tolerances, go to step **4**, otherwise go to step **6**;

4 update of the parameters (v_{wall}, E_{max}, E_{min}, and $V_{p=0}$ only for CRA, and $Y^{'}(t=0)_{iter=i+1}$);

5 the procedure is repeated from step **1**;

6 exit the procedure.

Note that in the following, values of σ_f and σ_{wss} will refer only to the left ventricle due to the absence of references for the other chambers. In fact, only for LV *in vivo* data are available [8, 16, 24, 30].

7.2.5 Parameters' Values

To properly calibrate the model, the methodology proposed in [17] (Section 2.7) is used, which requires a target CO, perfusion pressure (PerfP), i.e., the mean pressure that perfuses the systemic organs, along with prescribed RC time constants for the systemic and pulmonary circulations, flow distribution among organs, and assumed ratio of arterial to venous compliance. In agreement with published clinical data, values of resistances and compliances change at every trimester (Table 7.2). Lumped-parameters (R, C, L) are defined as described in Ch. 6, Subsection 6.2.1. Note that the distribution among the three resistances of each organ (i.e., arterial, venous, and micro-vascular sections) is the same for all the different phases of gestation, and equal to the NPC one (Subsection 6.2.1), as well as the pulmonary and systemic RC time constants are assumed to not change during pregnancy. As reported in previous chapters, also in the NPC configuration, adjustment of the unstressed volume ($V_{p=0}$) of Eq. (2.6) is necessary in order to meet the desired female-specific hemodynamics. The obtained values are then kept constant during the different phases of gestation.

7.2.6 Clinical validation

To validate the models, several clinically-relevant variables are computed and the mathematical description, when needed, is here reported.

- Chamber mass (M), computed as $M = \rho \cdot V_{myo}$, with ρ the myocardial density (1.04 g/mL) and V_{myo} the myocardial volume;
- Systolic (SBP), diastolic (DBP), and mean (MAP) blood pressures;

- Stroke volume (SV) and cardiac output;
- Total vascular resistance (TVR), computed as $TVR = 80 \cdot MAP/CO$ [24];
- Cardiac work (CW), defined as $CW = CO \cdot MAP$;
- Relative wall thickness (RWT), that is the ratio between the LV thickness and diameter at end diastole, h_{ED} and LVEDD, respectively [8, 24];
- Left atrial diameter (LAD), computed as the mean diameter over one heartbeat.

7.2.7 Simulations

To properly analyze the different stages of pregnancy, the female-specific circulation of an 'average' non-pregnant woman is first considered, calibrating the model to meet the NPC hemodynamics. Particularly, a woman of 56 kg and BSA of 1.27 m^2, having a HR of 71 bpm, a cardiac output of 4.9 L/min, and a perfusion pressure of 76 mmHg [24] is simulated. A total myocardial volume of 109 mL derived from [16] and scaled for BSA is also assumed. The three trimesters of pregnancy are then considered (Table 7.4) with the two models, i.e., the controlled (CRA) and not controlled remodeling algorithm (NCRA).
To identify the effect of σ_f and σ_{wss} on hemodynamics, the remodeling algorithm is also run with alternative σ_f target values that are within physiological ranges (55-85 g/cm^2) [8, 24, 30], and due to lack of clinical data, the same percentage change is applied to σ_{wss}.
A sensitivity analysis is also performed (see Section 7.4) to verify the influence of parameters on the model.

Table 7.4: *Input parameters used to simulate the hemodynamics of pregnancy [24].*

Parameters	**T1**	**T2**	**T3**	**Term**
Weight [Kg]	62	65	70	75
BSA [m^2]	1.39	1.51	1.62	1.72
HR [bpm]	75	76	82	79
CO [L/min]	5.7	5.9	6.4	6.8
Perfusion pressure [mmHg]	70	72	76	76

BSA, body surface area, HR, heart rate, and CO, cardiac output.

7.3 Results

The ability of the NPC model to represent female-specific hemodynamics is first evaluated. Table 7.5 shows the global hemodynamic variables. There is a very good agreement between the characteristic female-specific *in vivo* variables and the model outputs, with hemodynamic and chamber indices within the physiological ranges and close to the mean/median value of the reference. Physiological trends are also found when considering the waveforms. Fig. 7.3 represents the pressures, flows, and volumes, and these well resemble the characteristic physiological hemodynamics. The left ventricle is characterized by higher pressure and lower volume compared to the RV with the same SV of about 70 mL and a pressure ratio of about 5:1. Moreover, the valve model replicates the small amount of backward flow through the semilunar valves and the typical double peaks shape of the atrioventricular valve flow [35, 36, 37, 38, 39].

Table 7.6 shows the global hemodynamic variables during pregnancy, distinguishing the outputs between NCRA and CRA. The two models return almost the same overall hemodynamics in terms of pressures and CO; however, as the pregnancy proceeds, the differences of chambers volumes and performances, and geometrical indices between the reference values and the NCRA outputs increase. Fig. 7.4 shows the percentage variations from NPC for the mean atrial diameter (LAD), the end-diastolic LV diameter (LVEDD), the relative wall thickness (RWT), and the LV mass (LVM). As pregnancy progresses, the diameters increase slightly or are approximately constant for NCRA (maximum increment of about 6%), but increase for CRA. Looking at RWT, both the models return smaller values compared to the reference that increase slightly as pregnancy progresses. RWT slightly decreases for NCRA, whereas it is approximately constant or increases very slightly for CRA. Finally, LV mass computed with CRA agrees very well with [24] with an NPC value of 88 g that increases during pregnancy until a final value of 123 g, equal to a 40% increment. On the other hand, NCRA naturally returns a constant value of 88 g due to the absence of the remodeling algorithm.

Fig. 7.5 reports the percentage variations of the geometrical indices for each heart chamber. As expected, NCRA returns a constant myocardial volume during pregnancy (first row). CRA instead captures the increase in V_{myo} with a percentage increment at Term of about 40%, 60%, 100%, and 120% for LV, RV, LA, and RA, respectively. For the mean chamber's radius, both the models return an increasing trend but CRA results in higher values with ventricles and atria that increase their radius of about 10% and 12%,

Table 7.5: *Outputs of the non-pregnant case (NPC) simulations.*

Parameters	**NPC**	**Reference**
TVR [dynes·s/cm^5]	1329	1278 (1133-1496)[24]
SBP [mmHg]	110	110 (100-115)[24]
DBP [mmHg]	68	70 (60-80)[24]
MAP [mmHg]	82	83 (71-90)[24]
CO [L/min]	4.9	4.9 (4.3-5.8)[24]
LVEDV [mL]	105	96± 23 (52-141)[40]
LVESV [mL]	34	32± 9 (13-51)[40]
RVEDV [mL]	110	106± 24 (58-154)[40]
RVESV [mL]	40	40± 14 (12-68)[40]
SV [mL]	69	70 (66-79)[24]
EF [%]	66	65 (55–69)[24]
CW [mmHg·L/min]	404	407 (333-478)[24]
σ_f [g/cm^2]	70	71 (60-86)[24]
LVM [g]	88	88 (71-110)[24]
RWT [-]	0.29	0.32 (0.27-0.36)[24]
LAD [cm]	4.6	3.1 (2.8-3.3)[24]
LVEDD [cm]	5.0	4.4 (4.2-4.7)[24]

The values are compared with female-specific *in vivo* data reported as median (interquartile range) or mean ± SD with 95% confidence intervals (1.96 SD) in parentheses. TVR, total vascular resistance, SBP, systolic blood pressure, DBP, diastolic blood pressure, MAP, mean arterial pressure, CO, cardiac output, LVEDV, left ventricular end-diastolic volume, LVESV, left ventricular end-systolic volume, RVEDV, right ventricular end-diastolic volume, RVESV, right ventricular end-systolic volume, SV, stroke volume, EF, ejection fraction, CW, cardiac work ($CW = CO \cdot MAP$), σ_f, the myofiber stress, LVM, left ventricular mass, RWT, relative wall thickness, LAD, left atrial diameter, and LVEDD, left ventricular end-diastolic diameter.

respectively. For the mean chamber's thickness, NCRA returns a decrease in chamber dimensions due to the constant V_{myo} and increased radii, whereas CRA exhibits an increase in all the heart chamber thicknesses during pregnancy. Interestingly, RV increases its thickness of about 30% at Term *vs* the 14% of LV, and the atria enlarges their thickness of about 60%.

While the above results assumed a constant homeostatic value of σ_f and σ_{wss} during pregnancy equal to the NPC value, Table 7.7 reports the outputs of the model when the target values are equal to the upper and lower limits of previously reported values [8, 24, 30] (e.g., 55-85 g/cm^2), each value kept constant during pregnancy. Due to the lack of specific clinical data, σ_{wss} is

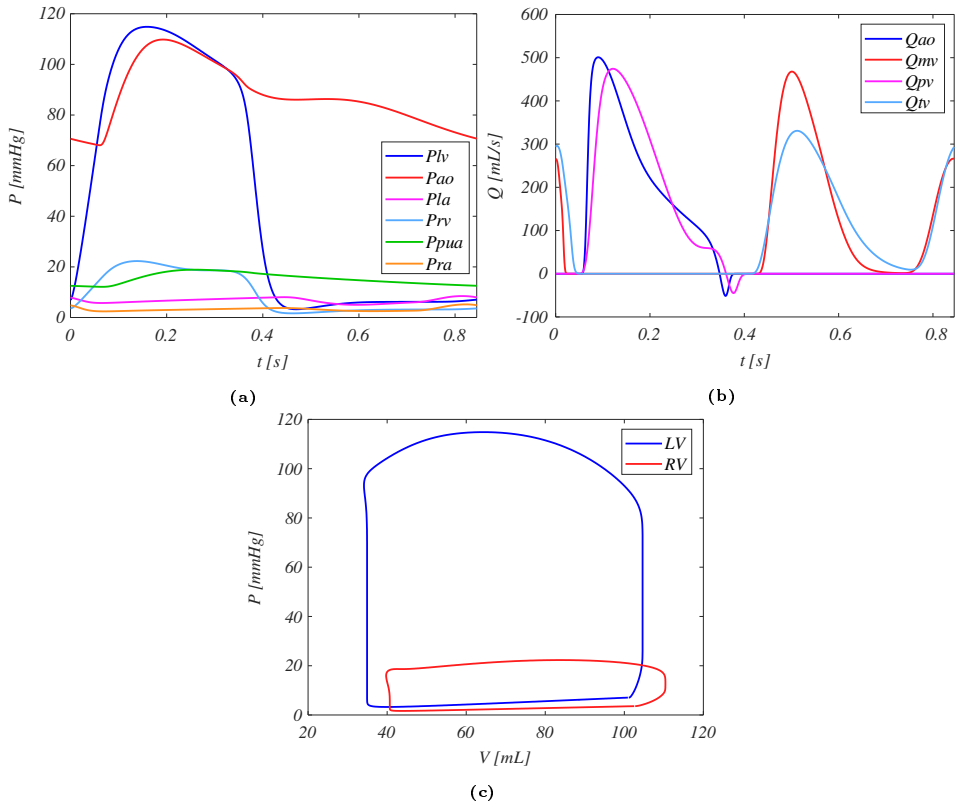

Figure 7.3: *Hemodynamic outputs of the NPC model. (a) Pressures, (b) flows, and (c) pressure-volume loops. LV, left ventricle, RV, right ventricle, LA, left atrium, and RA, right atrium. Plv, LV pressure, Pao, aortic pressure, Pla, LA pressure, Prv, RV pressure, Ppua, pulmonary arterial pressure, Pra, RA pressure, Qao, aortic valve flow, Qmv, mitral valve flow, Qpv, pulmonary valve flow, Qtv, tricuspid valve flow.*

assumed to vary with the same percentage as σ_f. From the table, it is clear that σ_{wss} causes bigger variations compared to σ_f. However, most values are within the reported *in vivo* ranges. Fig. 7.6 shows the myocardial volume, the radius, and the thickness for the four heart chambers as the pregnancy proceeds and considering the variations of σ_f and σ_{wss}. All the variables vary from the baseline (in green) due σ_f or σ_{wss} variation. Interestingly, there is an inverse relationship between σ_f or σ_{wss} and V_{myo}, r, and h. Indeed, higher and lower values of σ_f or σ_{wss} determine a decrease and increase respectively in V_{myo}, r, and h.

Table 7.6: *Comparison of pregnancy simulations with the controlled (CRA) and not controlled remodeling algorithm (NCRA) against in vivo data [24].*

Parameters	T1			T2			T3			Term		
	Model		Reference	Model		Reference	Model		Reference	Model		Reference
	NCRA	CRA		NCRA	CRA		NCRA	CRA		NCRA	CRA	
TVR [dynes·s/cm^5]	1094	1099	1059 (936-1234)	1134	1142	1093 (863-1248)	1011	1022	977 (828-1177)	1038	1056	1000 (832-1138)
SBP [mmHg]	99	103	100 (90-106)	100	111	100 (98-110)	98	109	100 (98-110)	97	120	110 (100-120)
DBP [mmHg]	63	66	63 (60-70)	64	71	68 (60-72)	62	68	70 (60-72)	61	74	70 (60-75)
MAP [mmHg]	75	78	77 (70-83)	76	84	79 (73-83)	74	82	83 (73-87)	73	90	83 (74-90)
CO [L/min]	5.5	5.7	5.7 (5.1-6.5)	5.4	5.9	5.9 (5.0-7.3)	5.9	6.4	6.4 (5.4-7.8)	5.6	6.8	6.8 (6.0-7.7)
LVEDV [mL]	104	118	-	103	121	-	102	127	-	101	137	-
LVESV [mL]	30	41	-	31	43	-	29	48	-	29	50	-
SV [mL]	73	76	76 (66-87)	71	78	78 (67-93)	72	78	80 (69-97)	71	86	83 (76-95)
EF [%]	70	65	61 (56–66)	69	64	63 (55–67)	70	61	60 (54-65)	71	63	60 (55-64)
CW [mmHg·L/min]	416	446	445 (383-513)	411	497	469 (391-576)	436	523	524 (437-607)	413	610	564 (475-649)
σ_f [g/cm^2]	55	72	70 (56-84)	57	72	67 (51-87)	53	72	69 (60-78)	50	72	80 (64-92)
LVM [g]	88	92	103 (83-127)	88	104	106 (92-127)	88	110	110 (88-130)	88	123	123 (104-143)
RWT [-]	0.29	0.27	0.33 (0.30-0.37)	0.28	0.3	0.33 (0.29-0.37)	0.28	0.3	0.36 (0.31-0.43)	0.26	0.3	0.37 (0.31-0.38)
LAD [cm]	4.6	4.8	3.2 (2.9-3.4)	4.7	4.9	3.3 (3.0-3.6)	4.7	5	3.5 (3.3-3.8)	4.9	5.1	3.5 (3.2-3.7)
LVEDD [cm]	5.1	5.3	4.5 (4.3-4.8)	5.1	5.3	4.6 (4.4-4.8)	5.1	5.4	4.6 (4.4-5.0)	5.3	5.6	4.8 (4.4-4.9)

The clinical data are reported as median (interquartile range). See Table 7.5 for abbreviation.

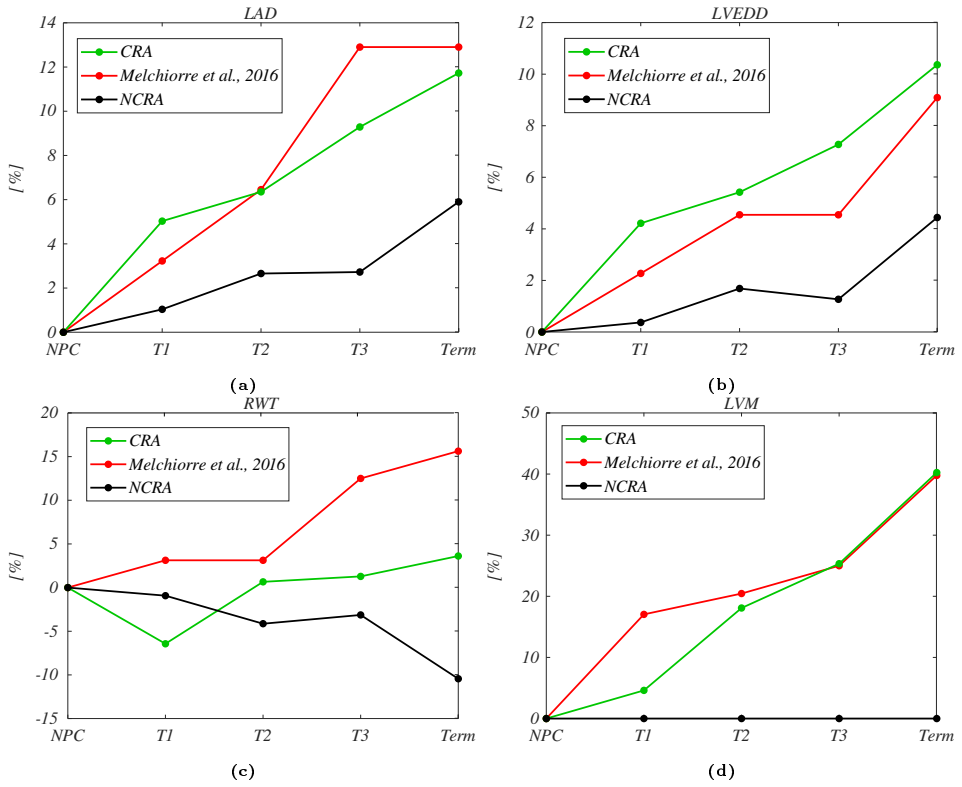

Figure 7.4: *Percentage changes in the outputs of the simulations at the different trimesters of pregnancy from the non-pregnant case (NPC) value. The results are compared with in vivo data. a) Mean left atrial diameter, b) left ventricular end diastolic diameter, c) relative wall thickness, and d) left ventricular mass. In green, the controlled remodeling algorithm (CRA) simulation, in black, the results of the not controlled remodeling algorithm (NCRA), and in red, the in vivo data.*

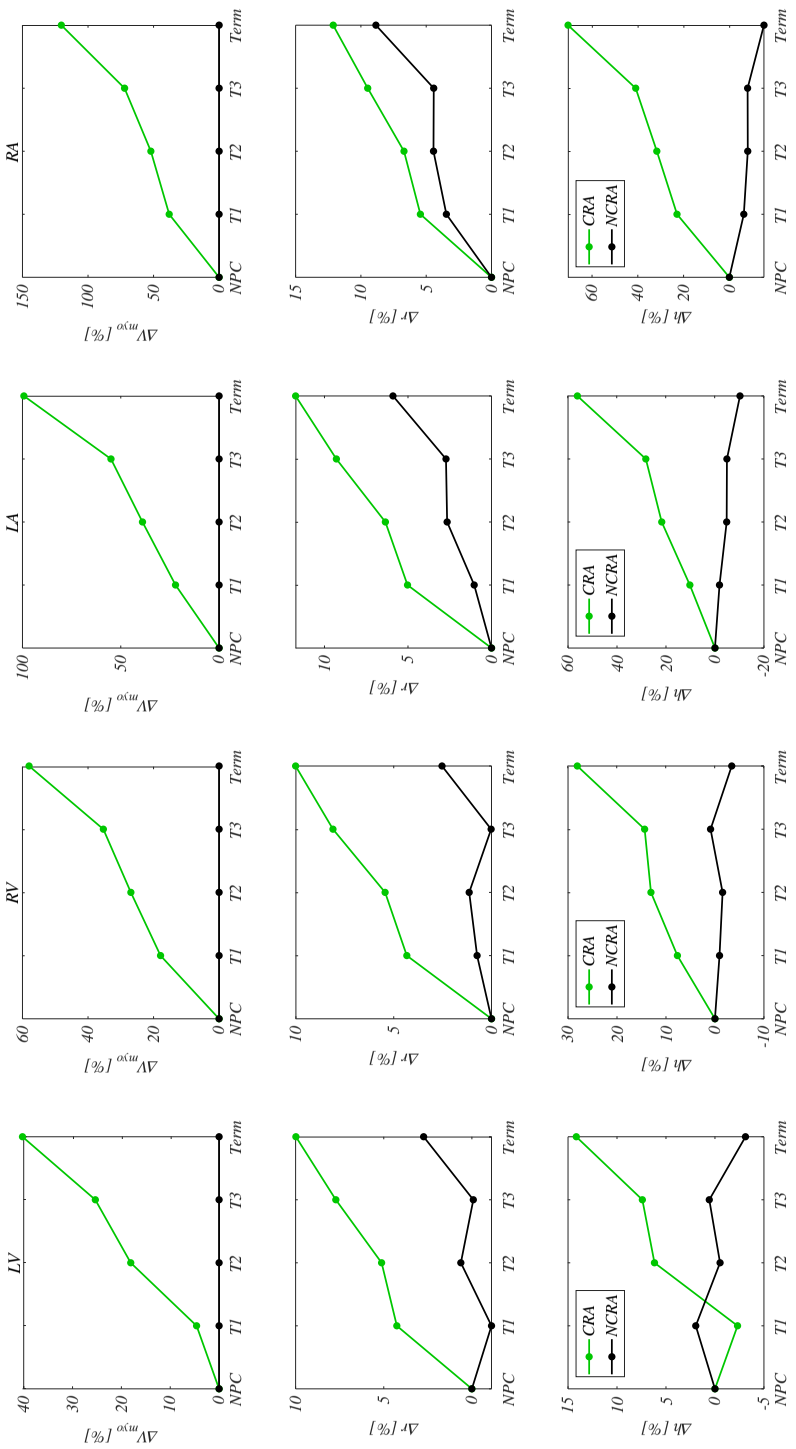

Figure 7.5: *The percentage of changes in the outputs of the simulations for the four heart chambers at the different trimesters of pregnancy. In the first row, the myocardial volume, in the second row, the mean chamber's radius, and in the third row, the mean chamber's thickness. In green, the controlled remodeling algorithm (CRA) simulation, in black, the results of the not controlled remodeling algorithm (NCRA).*

Table 7.7: *Percentage variations of the controlled remodeling algorithm (CRA) model by changing separately the myofiber stress (σ_f) and wall shear stress (σ_{wss}). σ_f changes within physiological ranges, whereas, due to the lack of clinical data, σ_{wss} is changed by applying the same percentage change as σ_f. The outputs are reported as percentage variation and ranges due σ_f or σ_{wss} change in parenthesis (if the parameter changes).*

Parameters	**T1**		**T2**	
	σ_f	σ_{wss}	σ_f	σ_{wss}
TVR [dynes·s/cm^5]	2% (1092-1113)	3% (1088-1121)	2% (1134-1160)	3% (1132-1169)
SBP [mmHg]	4% (102-106)	6% (101-107)	5% (109-114)	5% (109-115)
DBP [mmHg]	0%	2% (66-67)	0%	1% (71-72)
MAP [mmHg]	1% (78-79)	3% (78-80)	2% (84-86)	2% (84-86)
CO [L/min]	0%	0%	0%	0%
LVEDV [mL]	0%	26% (107-138)	0%	26% (110-142)
LVESV [mL]	0%	76% (30-61)	2% (32-63)	72% (32-63)
SV [mL]	0%	0%	0%	0%
EF [%]	0%	25% (55-71)	0%	23% (55-70)
CW [mmHg·L/min]	2% (443-452)	3% (443-452)	3% (492-505)	3% (493-508)
LAD [cm]	0%	13% (4.6-5.2)	0%	14% (4.6-5.3)
LVEDD [cm]	0%	9% (5.1-5.6)	2% (5.3-5.4)	9% (5.1-5.6)
LVM [g]	43% (80-120)	65% (73-133)	48% (86-136)	66% (82-151)
RWT [-]	37% (0.24-0.34)	26% (0.25-0.32)	37% (0.26-0.37)	27% (0.26-0.37)

Continued on Next Page.

Table 7.7: Continued

Parameters	T3		Term	
	σ_f	σ_{wss}	σ_f	σ_{wss}
TVR [dynes·s/cm^5]	3% (1014-1040)	4% (1010-1048)	4% (1046-1086)	5% (1042-1097)
SBP [mmHg]	5% (107-112)	6% (107-113)	6% (118-125)	8% (118-127)
DBP [mmHg]	1% (68-69)	1% (68-69)	3% (74-76)	4% (74-77)
MAP [mmHg]	2% (81-83)	4% (81-84)	3% (89-92)	4% (89-93)
CO [L/min]	0%	0%	0%	0%
LVEDV [mL]	1% (127-128)	28% (115-150)	1% (137-138)	27% (124-161)
LVESV [mL]	0%	73% (37-74)	0%	74% (37-74)
SV [mL]	0%	0%	0%	0%
EF [%]	0%	26% (52-68)	0%	25% (53-69)
CW [mmHg·L/min]	2% (519-532)	4% (516-536)	4% (604-628)	5% (602-634)
LAD [cm]	0%	14% (4.7-5.4)	0%	16% (4.8-5.6)
LVEDD [cm]	0%	9% (5.2-5.7)	2% (5.5-5.6)	9% (5.4-5.9)
LVM [g]	47% (92-144)	64% (86-156)	49% (103-163)	70% (94-180)
RWT [-]	37% (0.26-0.37)	27% (0.27-0.35)	40% (0.26-0.38)	30% (0.27-0.36)

See Table 7.5 for abbreviation.

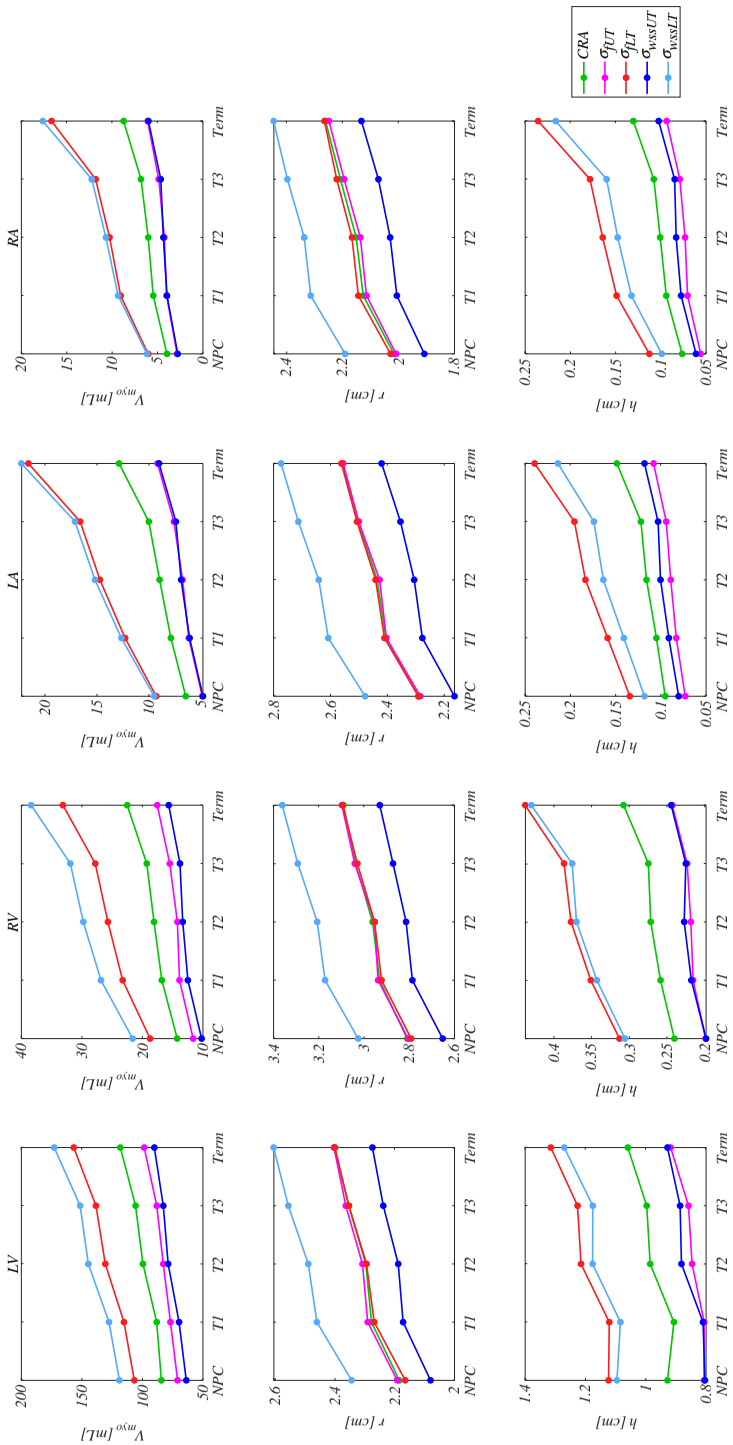

Figure 7.6: *Outputs of the controlled remodeling algorithm (CRA) model by changing separately σ_f and σ_{wss}. σ_f changes within physiological ranges, whereas, due to the lack of clinical data, σ_{wss} is changed by applying the same percentage change as σ_f. The results are reported for the four heart chambers for the different trimesters of pregnancy. In the first row, the myocardial volume, in the second row, the mean chamber's radius, and in the third row, the mean chamber's thickness. In green, the CRA simulation, in magenta, $\sigma_{f_{UT}}$ (upper threshold), in red, $\sigma_{f_{LT}}$ (lower threshold), in blue,$\sigma_{wss_{UT}}$ (upper threshold), and in light blue, $\sigma_{wss_{LT}}$ (lower threshold).*

7.4 Model Sensitivity Analysis

A model sensitivity analysis is shown in Fig. 7.7. A total of 15 input parameters were tested with sensitivities calculated after an increase of 25% [31]. 54 output signals are chosen for the analysis.
Table 7.8 reports the mean sensitivity with inputs and outputs ordered based on the global influence and overall sensitivity, respectively. In Fig. 7.7 is reported the graphical representation of the sensitivity (the outputs are ordered with the most sensitive on the left, and the inputs are ordered with the most influential at the bottom). The most influential parameters are those related to the chamber's contractility and the ventricular volume-related parameters ($V_{p=0}$) of Eq. (2.6). The former are known from the physiology to influence the pressures and flows. Thus, an high sensitivity is expected, suggesting also that attention is required to calibrate these parameters. $V_{p=0}$ reflects the chamber's dimension, this is known to affect the outputs. However, once identified the value, $V_{p=0}$ is not varied during the simulations hence is not influencing the results. The atrial and right ventricular volumes are the most sensitive outputs, followed by the pressure in the aorta and in the arterial side of the modeled organs. These variables are intrinsically related to the most influential input parameters, relation derived from the physiology. Thus, deep attention is required to calibrate the input values to obtain reliable results. However, the figure shows a cluster of larger data points on the left side meaning that only these few outputs are more sensitive to the variation of the inputs. The least sensitive outputs signals are the pulmonary and systemic venous pressures, and this could be related to the reservoir functionality of the high-compliance pulmonary and venous circulations. Note also that differences are visible in the sensitivity analysis compared to Ch. 6, despite the same model structure is considered. This is mainly due to the fact that in this chapter, for the sensitivity analysis, the compliances are considered all together within the parameter 'Ctsv', whereas in Ch. 6 the single effect of each compartment compliance is analyzed.

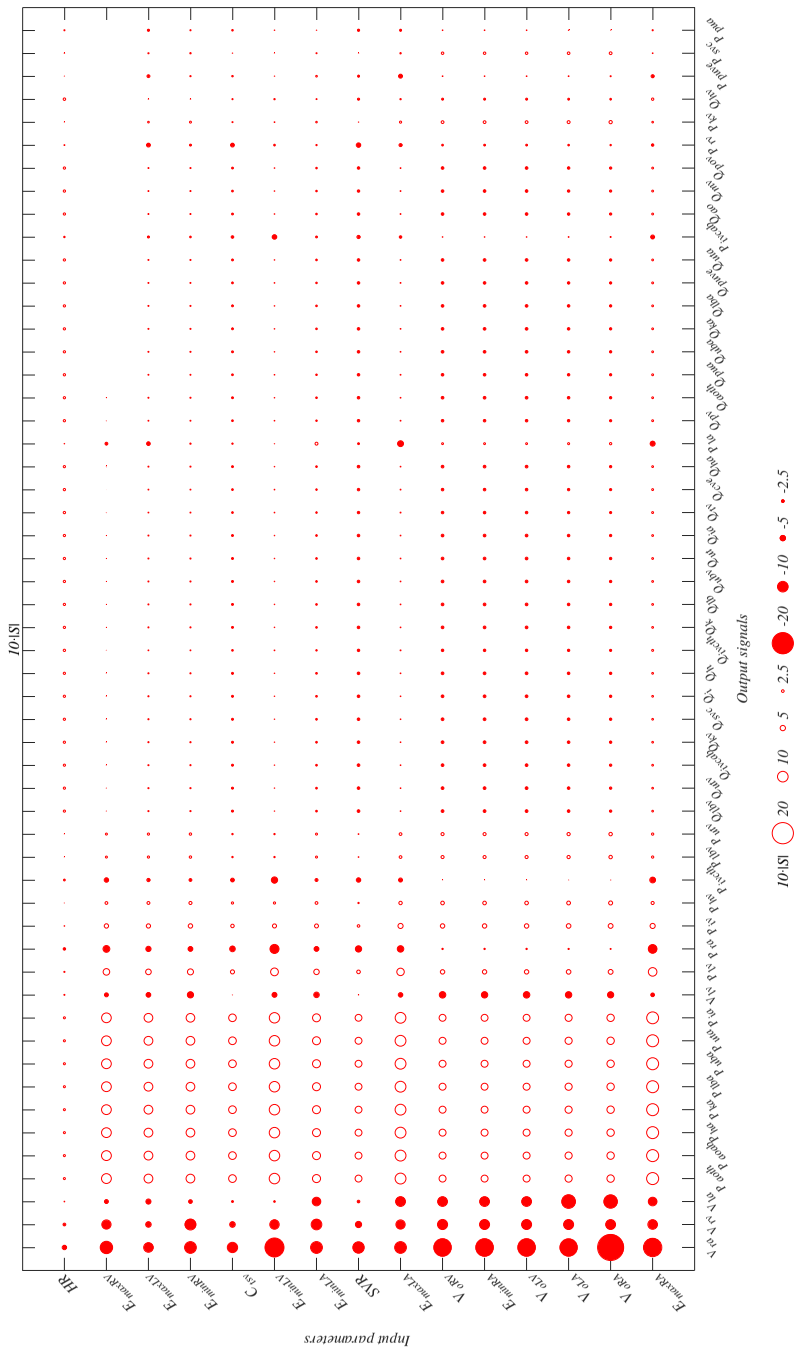

Figure 7.7: *Graphical representation of the sensitivity of the outputs to the 25% variation of the inputs for the woman-specific model. A larger symbol corresponds with higher sensitivity and filled/empty circles correspond to negative/positive S. Outputs are ordered according to the overall sensitivity (the most sensitive on the left) and inputs are ordered based on the global influence (the most influential at the bottom).*

Table 7.8: *Mean sensitivities (S) of output signals to the input parameters. The inputs are ordered based on the global influence (the most influential on the left), the outputs are ordered based on the overall sensitivity (the most sensitive at the top).*

	$\mathbf{E}_{max_{RA}}$	$\mathbf{V}_{p=0_{RA}}$	$\mathbf{V}_{p=0_{LA}}$	$\mathbf{V}_{p=0_{LV}}$	$\mathbf{E}_{min_{RA}}$	$\mathbf{V}_{p=0_{RV}}$	$\mathbf{E}_{max_{LA}}$	**SVR**	$\mathbf{E}_{min_{LA}}$	$\mathbf{E}_{min_{LV}}$	**Ctsv**	$\mathbf{E}_{min_{RV}}$	$\mathbf{E}_{max_{LV}}$	$\mathbf{E}_{max_{RV}}$	**HR**
Vra	-1.730	-2.460	-1.640	-1.660	-1.660	-1.660	-1.100	-1.070	-1.110	-1.790	-0.970	-1.110	-0.900	-1.160	-0.420
Vrv	-0.910	-0.930	-0.940	-0.940	-0.940	-0.950	-0.870	-0.580	-1.000	-0.890	-0.530	-1.030	-0.520	-0.870	-0.260
Vla	-0.810	-1.270	-1.290	-0.920	-0.920	-0.920	-0.920	-0.250	-0.810	-0.150	-0.170	-0.350	-0.480	-0.370	-0.070
Paoab	1.130	0.700	0.670	0.660	0.650	0.660	1.020	0.650	0.760	0.990	0.730	0.820	0.830	0.920	0.190
Paoth	1.130	0.700	0.670	0.660	0.650	0.660	1.020	0.650	0.760	0.990	0.730	0.820	0.830	0.930	0.190
Pha	1.130	0.700	0.670	0.650	0.650	0.650	1.020	0.650	0.750	0.990	0.720	0.820	0.830	0.920	0.190
Pia	1.120	0.690	0.670	0.650	0.650	0.650	1.010	0.640	0.750	0.980	0.720	0.820	0.820	0.910	0.190
Pka	1.130	0.700	0.670	0.650	0.650	0.650	1.020	0.650	0.750	0.990	0.720	0.820	0.830	0.920	0.190
Plba	1.130	0.700	0.670	0.650	0.650	0.650	1.020	0.650	0.750	0.990	0.720	0.820	0.830	0.920	0.190
Puba	1.130	0.700	0.670	0.650	0.650	0.650	1.020	0.650	0.760	0.990	0.720	0.820	0.830	0.920	0.190
Puta	1.130	0.700	0.670	0.650	0.650	0.650	1.020	0.650	0.750	0.990	0.720	0.820	0.830	0.920	0.190
Vlv	-0.340	-0.580	-0.600	-0.610	-0.600	-0.610	-0.420	-0.030	-0.520	-0.460	0.020	-0.580	-0.440	-0.370	-0.090
Plv	0.810	0.450	0.430	0.410	0.410	0.410	0.700	0.340	0.520	0.730	0.380	0.570	0.530	0.620	0.110
Pra	-0.820	-0.090	-0.110	-0.120	-0.120	-0.120	-0.610	-0.590	-0.450	-0.850	-0.530	-0.450	-0.490	-0.640	-0.230
Piv	0.480	0.450	0.430	0.420	0.420	0.420	0.480	0.240	0.370	0.390	0.330	0.410	0.400	0.410	0.060
Phv	0.290	0.380	0.360	0.340	0.340	0.340	0.320	0.120	0.260	0.210	0.210	0.290	0.270	0.260	0.020
Pivcth	-0.540	0.020	0.000	-0.010	-0.010	-0.010	-0.380	-0.410	-0.280	-0.590	-0.350	-0.270	-0.310	-0.420	-0.170
Plbv	0.220	0.330	0.300	0.290	0.290	0.290	0.260	0.070	0.190	0.120	0.130	0.230	0.210	0.190	-0.010
Putv	0.220	0.330	0.300	0.290	0.290	0.290	0.260	0.070	0.190	0.120	0.130	0.230	0.210	0.190	-0.010
Qivcab	0.160	-0.220	-0.240	-0.250	-0.250	-0.250	0.070	-0.250	-0.160	0.040	-0.190	-0.100	-0.100	-0.020	0.210
Qkv	0.160	-0.220	-0.240	-0.260	-0.260	-0.260	0.060	-0.240	-0.160	0.040	-0.190	-0.110	-0.100	-0.020	0.210

Continued on Next Page.

Table 7.8 – Continued

	$\mathbf{E}_{max_{RA}}$	$\mathbf{V}_{p=0_{RA}}$	$\mathbf{V}_{p=0_{LA}}$	$\mathbf{V}_{p=0_{LV}}$	$\mathbf{E}_{min_{RA}}$	$\mathbf{V}_{p=0_{RV}}$	$\mathbf{E}_{max_{LA}}$	**SVR**	$\mathbf{E}_{min_{LA}}$	$\mathbf{E}_{min_{LV}}$	**Ctsv**	$\mathbf{E}_{min_{RV}}$	$\mathbf{E}_{max_{LV}}$	$\mathbf{E}_{max_{RV}}$	**HR**
Qlbv	0.160	-0.220	-0.240	-0.260	-0.260	-0.260	0.060	-0.250	-0.160	0.040	-0.190	-0.110	-0.100	-0.020	0.200
Qsvc	0.160	-0.220	-0.240	-0.260	-0.260	-0.260	0.060	-0.240	-0.160	0.040	-0.190	-0.110	-0.100	-0.020	0.210
Qutv	0.160	-0.220	-0.240	-0.260	-0.260	-0.260	0.060	-0.240	-0.160	0.040	-0.190	-0.110	-0.100	-0.020	0.210
Pla	-0.470	0.210	0.190	0.180	0.180	0.180	-0.550	-0.180	0.280	0.030	-0.120	-0.120	-0.340	-0.270	-0.050
Qaoth	0.170	-0.220	-0.240	-0.250	-0.250	-0.250	0.070	-0.240	-0.150	0.050	-0.180	-0.100	-0.090	-0.010	0.210
Qcve	0.180	-0.200	-0.220	-0.240	-0.240	-0.240	0.080	-0.230	-0.140	0.060	-0.160	-0.090	-0.080	0.000	0.220
Qh	0.160	-0.220	-0.240	-0.250	-0.260	-0.250	0.070	-0.240	-0.160	0.050	-0.180	-0.100	-0.100	-0.010	0.210
Qha	0.170	-0.220	-0.240	-0.250	-0.250	-0.250	0.070	-0.240	-0.160	0.050	-0.180	-0.100	-0.090	-0.010	0.210
Qi	0.160	-0.220	-0.240	-0.260	-0.260	-0.250	0.070	-0.240	-0.160	0.040	-0.180	-0.100	-0.100	-0.010	0.210
Qia	0.170	-0.220	-0.240	-0.250	-0.250	-0.250	0.070	-0.240	-0.160	0.050	-0.180	-0.100	-0.090	-0.010	0.210
Qivcth	0.180	-0.200	-0.220	-0.230	-0.230	-0.230	0.090	-0.230	-0.130	0.070	-0.160	-0.080	-0.080	0.010	0.220
Qk	0.170	-0.220	-0.240	-0.250	-0.250	-0.250	0.070	-0.240	-0.160	0.050	-0.180	-0.100	-0.090	-0.010	0.210
Qka	0.170	-0.210	-0.230	-0.250	-0.250	-0.250	0.070	-0.240	-0.150	0.050	-0.180	-0.100	-0.090	-0.010	0.210
Qlb	0.170	-0.220	-0.240	-0.250	-0.250	-0.250	0.070	-0.240	-0.160	0.050	-0.180	-0.100	-0.090	-0.010	0.210
Qlba	0.170	-0.210	-0.230	-0.250	-0.250	-0.250	0.070	-0.240	-0.150	0.050	-0.180	-0.100	-0.090	-0.010	0.210
Qpua	0.180	-0.210	-0.230	-0.240	-0.240	-0.240	0.080	-0.230	-0.140	0.060	-0.170	-0.090	-0.080	0.000	0.210
Qpuve	0.180	-0.210	-0.230	-0.240	-0.240	-0.240	0.080	-0.230	-0.150	0.060	-0.170	-0.090	-0.090	0.000	0.210
Qpv	0.180	-0.210	-0.220	-0.240	-0.240	-0.240	0.080	-0.230	-0.140	0.060	-0.160	-0.090	-0.080	0.000	0.220
Qtv	0.180	-0.200	-0.220	-0.240	-0.240	-0.230	0.090	-0.230	-0.140	0.070	-0.160	-0.090	-0.080	0.010	0.220
Quba	0.170	-0.220	-0.230	-0.250	-0.250	-0.250	0.070	-0.240	-0.150	0.050	-0.180	-0.100	-0.090	-0.010	0.210
Qubv	0.170	-0.220	-0.240	-0.250	-0.250	-0.250	0.070	-0.240	-0.160	0.050	-0.180	-0.100	-0.090	-0.010	0.210
Qut	0.170	-0.220	-0.240	-0.250	-0.250	-0.250	0.070	-0.240	-0.160	0.050	-0.180	-0.100	-0.090	-0.010	0.210
Quta	0.170	-0.210	-0.230	-0.250	-0.250	-0.250	0.070	-0.240	-0.150	0.050	-0.180	-0.100	-0.090	-0.010	0.210

Continued on Next Page.

Table 7.8 – Continued

	$\mathbf{E}_{max_{RA}}$	$\mathbf{V}_{p=0_{RA}}$	$\mathbf{V}_{p=0_{LA}}$	$\mathbf{V}_{p=0_{LV}}$	$\mathbf{E}_{min_{RA}}$	$\mathbf{V}_{p=0_{RV}}$	$\mathbf{E}_{max_{LA}}$	**SVR**	$\mathbf{E}_{min_{LA}}$	$\mathbf{E}_{min_{LV}}$	**Ctsv**	$\mathbf{E}_{min_{RV}}$	$\mathbf{E}_{max_{LV}}$	$\mathbf{E}_{max_{RV}}$	**HR**
Pivcab	-0.370	0.090	0.070	0.060	0.060	0.060	-0.230	-0.300	-0.170	-0.430	-0.240	-0.160	-0.190	-0.280	-0.130
Prv	-0.220	-0.130	-0.150	-0.170	-0.170	-0.170	-0.290	-0.420	-0.110	-0.160	-0.360	-0.180	-0.370	-0.260	-0.080
Qao	0.170	-0.210	-0.230	-0.250	-0.250	-0.250	0.080	-0.240	-0.150	0.060	-0.170	-0.090	-0.090	-0.010	0.210
Qmv	0.170	-0.210	-0.230	-0.240	-0.240	-0.240	0.080	-0.230	-0.150	0.050	-0.170	-0.100	-0.080	0.000	0.220
Qpov	0.170	-0.210	-0.230	-0.250	-0.250	-0.240	0.080	-0.240	-0.150	0.060	-0.170	-0.090	-0.090	0.000	0.210
Pkv	0.150	0.300	0.280	0.260	0.260	0.260	0.200	0.030	0.150	0.060	0.090	0.180	0.160	0.140	-0.020
Qhv	0.220	-0.160	-0.180	-0.190	-0.190	-0.190	0.120	-0.200	-0.080	0.120	-0.100	-0.040	-0.030	0.050	0.240
Ppuve	-0.290	0.100	0.080	0.060	0.060	0.060	-0.370	-0.190	0.160	0.040	-0.140	-0.110	-0.270	-0.190	0.020
Psvc	0.070	0.270	0.240	0.230	0.230	0.230	0.130	-0.020	0.100	-0.020	0.040	0.130	0.110	0.070	-0.040
Ppua	-0.100	-0.020	-0.040	-0.060	-0.060	-0.060	-0.190	-0.210	0.040	0.050	-0.150	-0.100	-0.200	-0.120	0.100

Vra, RA volume, Vrv, RV volume, Vla, LA volume, Paoth, thoracic aortic pressure, Paoab, abdominal aortic pressure, Pha, hepatic arterial pressure, Pka, renal arterial pressure, Plba, lower body arterial pressure, Puba, upper body arterial pressure, Puta, uterine arterial pressure, Pia, gastro-intestinal arterial pressure, Vlv, LV volume, Plv, LV volume, Pra, RA pressure, Piv, gastro-intestinal venous pressure, Phv, hepatic venous pressure, Pivcth, thoracic inferior vena cava pressure, Plbv, lower body venous pressure, Putv, uterine venous pressure, Qlbv, lower body venous flow, Qutv, uterine venous flow, Qivcab, abdominal inferior vena cava flow, Qkv, renal venous flow, Qsvc, superior vena cava flow, Qi, gastro-intestinal flow, Qh, hepatic flow, Qivcth, thoracic inferior vena cava flow, Qk, renal flow, Qlb, lower body flow, Qubv, upper body venous flow, Qut, uterine flow, Qia, gastro-intestinal arterial flow, Qtv, tricuspid valve flow, Qcve, caval vein flow, Qha, hepatic arterial flow, Pla, LA pressure, Qpv, pulmonary valve flow, Qaoth, thoracic aortic flow, Qpua, pulmonary arterial flow, Quba, upper body arterial flow, Qka, renal arterial flow, Qlba, lower body arterial flow, Qpuve, pulmonary venous flow, Quta, uterine arterial flow, Pivcab, abdominal inferior vena cava pressure, Qao, aortic valve pressure, Qmv, mitral valve flow, Qpov, portal vein flow, Prv, RV pressure, Pkv, renal venous pressure, Qhv, hepatic venous flow, Ppuve, pulmonary venous pressure, Psvc, superior vena cava pressure, Ppua, pulmonary arterial pressure.

7.5 Discussion

Pregnancy is a volume overload condition characterized by hormonal changes [41], that determine a cardiac stress condition [4]. However, it is a physiological state characterized by physiological eccentric hypertrophy [4, 5]. Indeed, pregnancy is a prolonged but reversible condition produced by increased cardiac workload [5]. The resulting cardiac remodeling develops as a homeostatic control to maintain the mechanical/hemodynamic loads within physiological ranges [42]. Indeed, during pregnancy, the hemodynamic perturbation is compensated by the homeostatic system that manifests in adaptation of the cardiac geometry [42]. Particularly, in this study it is hypothesized that during pregnancy, the key drivers of cardiac remodeling are the homeostatic values of myofiber (σ_f) and wall shear (σ_{wss}) stresses. In support of this hypothesis, the lumped-parameter model incorporating these cardiac remodeling processes is able to predict the main cardiac structural changes that appear during pregnancy. This is achieved by starting with our previous work in which a woman-specific model has been developed [17], enforcing reasonable cardiovascular target variables required by the changing physiological demands during pregnancy and applying an updated version of the cardiac remodeling algorithm of Maksuti et al. [16]. From the NPC model, the physiological changes typical of pregnancy are considered by comparing the application of only the hemodynamic changes (NCRA), and the combination of hemodynamic and geometrical changes (CRA). Cardiac output, heart rate, total vascular compliance and total vascular resistance changes are prescribed in both the models. On the other hand, homeostatic values of σ_f and σ_{wss} are imposed only for CRA.

CO and SV are reported to increase by at least 30% and by about 20-30% [1], respectively. Given that CO is a target value and HR is prescribed, both NCRA and CRA reflected these basic hemodynamic changes, with achieved SV and CO of 37% and 22% for NCRA and 39% and 25% for CRA. Considering the blood pressures, both the models returned slightly higher values compared to reference data [24], however, the values are still within the physiological ranges. The observed differences are likely due to the imposed TVR values, which are slightly higher compared to the reported values.

The imposition of a target CO leads to an increase in LAD and LVEDD for both the models, however, only changes seen with CRA agreed with the reported increases of about 15% and 10%, respectively [1, 24]. Indeed, CRA results in LAD and LVEDD increase of about 12% and 10%, respectively; whereas, with NCRA, only 6% and 5% increments are found. Note that the differences of the LAD and LVEDD absolute values between the refer-

ence data [24] and the NPC output are likely due to the simplified geometry assumed. Indeed, in the geometrical model, the atria and ventricles are simulated as perfect spheres or part of an ellipsoid. This is not true in reality with the heart chambers characterized by a much more complex geometry.
Literature reports an LV thickness increment of 15-25% because of the increased preload and afterload, and as an adaptation to minimize the wall stress [1, 8]. This result is met only with CRA (increase of about 14%) whereas NCRA resulted in an LV thickness reduction (of about 3%), which is not representative of normal physiological remodeling with pregnancy [4, 5, 43, 44]. Moreover, as expected, only CRA determined an LVM increase of about 40% that agrees well with the *in vivo* augmentation of about 50% [1, 3, 24, 26]. Moreover, LVM in T1 (CRA) increases by only 5% compared to the NPC value, and this agrees with the lack of alteration found in [20]. Also RVM is found to increase of about 40% in the third trimester [26], in agreement with our CRA findings at T3. Concerning RWT, the models return an almost constant value, in agreement with the features of eccentric hypertrophy [4, 42]. The reference values, on the other hand, exhibit a bigger increase towards the end of pregnancy, with Melchiorre et al. [24] reporting emergence of cardiac maladaptation (i.e. increased wall stress) near term in apparently healthy women, a finding not reproduced by our model due to the imposed assumption of a constant wall stress. Moreover, the diagram of (RWT, LVM/BSA) shows that, in all the trimesters for both the models, there is a normal geometry [45], in agreement with the simulation of physiological healthy pregnancy.
Remodeling based on constant homeostatic values of σ_f and σ_{wss} seems to closely replicate the cardiac changes that occur during pregnancy. Variations of the prescribed values within previously reported values [8, 24, 30], e.g., σ_f =55 g/cm^2 and σ_f =85 g/cm^2, do alter the absolute values of the heart structure, but within physiological ranges. Particularly, a bigger σ_f (or σ_{wss}) value leads to smaller V_{myo}, r, and h, and vice versa, consistent with expectations. Indeed, this behavior is expected for two reasons: *i)* there is a direct proportional relation between myofiber stress and pressure, and wall shear stress and flow; and *ii)* cardiac remodeling, i.e., increase in V_{myo}, r, and h to restore homeostatic value of stresses, is triggered for hemodynamic conditions that determine stress values higher than the targets. Thus, when higher stress values are considered as homeostatic targets, higher pressure and flow values can arise before triggering the remodeling and consequently maintaining lower V_{myo}, r, and h. The opposite happens if lower stress values are considered.
To the best of our knowledge, this is the first attempt to simulate both the

hemodynamic and geometrical changes that occur in the maternal circulation. It is demonstrated that, although NCRA is able to replicate pregnant hemodynamics, it cannot capture cardiac remodeling. On the other hand, CRA is able to predict the altered gestational hemodynamics and the physiological remodeling typical of pregnancy, and, for this reason, CRA may be useful for studying remodeling during both healthy and abnormal pregnancies. Moreover, the sensitivity of the model is restricted to the volumes, and, for all the outputs, the variations due to a 25% input change is contained, confirming the reliability of the simulations.

7.5.1 Clinical implications and future development

The CRA model is a tool able to reproduce the physiological changes that occur during pregnancy. Particularly, it allows to analyze the pressures, flows, and heart structure as pregnancy proceeds. This can be a useful tool to better understand the cardiovascular system during pregnancy, gaining a greater understanding of the adaptive processes that occur during pregnancy, which may be useful for understanding physiology and cardiac function/remodeling in high risk pregnancies. Moreover, a further development will consider altered pregnancy condition, for example the gestational hypertension. The possibility to obtain a full description of the cardiovascular system in this pathological condition will help in understanding the hemodynamic and geometrical changes typical of this pathology, perhaps providing insights for designing effective therapies.

7.5.2 Limitations

The developed model is based on a simplified heart geometry, which may limit future applications in settings such as complex congenital heart disease. The NPC absolute values of LAD and LVEDD are higher than the reference values, although it is shown that the percentage changes during pregnancy agreed very closely with the literature. In addition, σ_f and σ_{wss} are assumed to constitute fixed homeostatic 'target' values for the remodeling process. Although these two simple assumptions result in an excellent prediction of changes in cardiac geometry, compared with literature data, in reality it is likely that cardiac remodeling is affected by other factors. For example, genetic factors are known to play a key role in some forms of pathological remodeling, as well as hormones [46, 47].

7.6 Conclusion

A lumped-parameter model of the whole circulation able to reproduce the hemodynamic changes that arise during pregnancy, and incorporated a controlled remodeling algorithm based wall stress and chamber wall shear stress homeostasis principles is developed. Although employing two very simple assumptions, CRA predicts changes in cardiac mass and geometry that are very similar to those reported in normal human pregnancies. These techniques provide insight into the biomechanical basis of cardiac remodeling during pregnancy and may be useful in future to investigate cardiovascular problems that arise in some pregnancies.

Bibliography

[1] K. Melchiorre, R. Sharma, and B. Thilaganathan, "Cardiac structure and function in normal pregnancy," *Current Opinion in Obstetrics and Gynecology*, vol. 24, no. 6, pp. 413–421, 2012.

[2] J. G. Ouzounian and U. Elkayam, "Physiologic changes during normal pregnancy and delivery," *Cardiology clinics*, vol. 30, no. 3, pp. 317–329, 2012.

[3] M. Sanghavi and J. D. Rutherford, "Cardiovascular physiology of pregnancy," *Circulation*, vol. 130, no. 12, pp. 1003–1008, 2014.

[4] E. Chung and L. A. Leinwand, "Pregnancy as a cardiac stress model," *Cardiovascular research*, vol. 101, no. 4, pp. 561–570, 2014.

[5] G. W. Dorn, "The fuzzy logic of physiological cardiac hypertrophy," *Hypertension*, vol. 49, no. 5, pp. 962–970, 2007.

[6] P. L. Kerkhof and V. M. Miller, *Sex-specific analysis of cardiovascular function*, vol. 1065. Springer, 2018.

[7] M. Suresh, R. L. Preston, R. Fernando, and M. C LaToya Mason, *Shnider and Levinson's anesthesia for obstetrics*. Lippincott Williams & Wilkins, 2012.

[8] L. A. Simmons, A. G. Gillin, and R. W. Jeremy, "Structural and functional changes in left ventricle during normotensive and preeclamptic pregnancy," *American Journal of Physiology-Heart and Circulatory Physiology*, vol. 283, no. 4, pp. H1627–H1633, 2002.

[9] I. L. Chernyavsky, O. E. Jensen, and L. Leach, "A mathematical model of intervillous blood flow in the human placentone," *Placenta*, vol. 31, no. 1, pp. 44–52, 2010.

[10] P. Garcia-Canadilla, P. A. Rudenick, F. Crispi, M. Cruz-Lemini, G. Palau, O. Camara, E. Gratacos, and B. H. Bijens, "A computational model of the fetal circulation to quantify blood redistribution in intrauterine growth restriction," *PLoS computational biology*, vol. 10, no. 6, 2014.

[11] G. Pennati, M. Bellotti, and R. Fumero, "Mathematical modelling of the human foetal cardiovascular system based on doppler ultrasound data," *Medical engineering & physics*, vol. 19, no. 4, pp. 327–335, 1997.

[12] A. B. Queyam, S. K. Pahuja, and D. Singh, "Simulation and analysis of umbilical blood flow using markov-based mathematical model," *International Journal of Intelligent Systems and Applications*, vol. 9, no. 3, p. 41, 2017.

[13] R. G. Shah, T. Girardi, G. Merz, P. Necaise, and C. M. Salafia, "Hemodynamic analysis of blood flow in umbilical artery using computational modeling," *Placenta*, vol. 57, pp. 9–12, 2017.

[14] J. Carson, M. Lewis, D. Rassi, and R. Van Loon, "A data-driven model to study utero-ovarian blood flow physiology during pregnancy," *Biomechanics and modeling in mechanobiology*, vol. 18, no. 4, pp. 1155–1176, 2019.

[15] C. Corsini, E. Cervi, F. Migliavacca, S. Schievano, T.-Y. Hsia, and G. Pennati, "Mathematical modelling of the maternal cardiovascular system in the three stages of pregnancy," *Medical Engineering & Physics*, vol. 47, pp. 55–63, 2017.

[16] E. Maksuti, B. E. Westerhof, M. Ugander, D. W. Donker, M. Carlsson, and M. Broomé, "Cardiac remodeling in aortic and mitral valve disease: a simulation study with clinical validation," *Journal of Applied Physiology*, vol. 126, no. 5, pp. 1377–1389, 2019.

[17] G. Comunale, F. M. Susin, and J. P. Mynard, "A female-specific cardiovascular lumped-parameter model," in *Proceedings of the 42nd Annual International Conferences of the IEEE Engineering in Medicine and Biology Society in conjunction with the 43rd Annual Conference of the Canadian Medical and Biological Engineering Society*, 42nd Annual

International Conferences of the IEEE Engineering in Medicine and Biology Society in conjunction with the 43rd Annual Conference of the Canadian Medical and Biological Engineering Society, 2020.

[18] H. Suga, K. Sagawa, and A. A. Shoukas, "Load independence of the instantaneous pressure-volume ratio of the canine left ventricle and effects of epinephrine and heart rate on the ratio," *Circulation research*, vol. 32, no. 3, pp. 314–322, 1973.

[19] J. Mynard, M. Davidson, D. Penny, and J. Smolich, "A simple, versatile valve model for use in lumped parameter and one-dimensional cardiovascular models," *International Journal for Numerical Methods in Biomedical Engineering*, vol. 28, no. 6-7, pp. 626–641, 2012.

[20] S. De Haas, C. Ghossein-Doha, L. Geerts, S. van Kuijk, J. van Drongelen, and M. Spaanderman, "Cardiac remodeling in normotensive pregnancy and in pregnancy complicated by hypertension: systematic review and meta-analysis," *Ultrasound in Obstetrics & Gynecology*, vol. 50, no. 6, pp. 683–696, 2017.

[21] K. Abduljalil, P. Furness, T. N. Johnson, A. Rostami-Hodjegan, and H. Soltani, "Anatomical, physiological and metabolic changes with gestational age during normal pregnancy," *Clinical pharmacokinetics*, vol. 51, no. 6, pp. 365–396, 2012.

[22] K. Flo, T. Wilsgaard, Å. Vårtun, and G. Acharya, "A longitudinal study of the relationship between maternal cardiac output measured by impedance cardiography and uterine artery blood flow in the second half of pregnancy," *BJOG: An International Journal of Obstetrics & Gynaecology*, vol. 117, no. 7, pp. 837–844, 2010.

[23] S. A. Hale, A. Schonberg, G. J. Badger, and I. M. Bernstein, "Relationship between prepregnancy and early pregnancy uterine blood flow and resistance index," *Reproductive Sciences*, vol. 16, no. 11, pp. 1091–1096, 2009.

[24] K. Melchiorre, R. Sharma, A. Khalil, and B. Thilaganathan, "Maternal cardiovascular function in normal pregnancy: evidence of maladaptation to chronic volume overload," *Hypertension*, vol. 67, no. 4, pp. 754–762, 2016.

[25] M. D. Pettersen, W. Du, M. E. Skeens, and R. A. Humes, "Regression equations for calculation of z scores of cardiac structures in a large cohort of healthy infants, children, and adolescents: an echocardiographic

study," *Journal of the American Society of Echocardiography*, vol. 21, no. 8, pp. 922–934, 2008.

[26] R. A. Ducas, J. E. Elliott, S. F. Melnyk, S. Premecz, K. Cleverley, P. Wtorek, G. S. Mackenzie, M. E. Helewa, D. S. Jassal, *et al.*, "Cardiovascular magnetic resonance in pregnancy: insights from the cardiac hemodynamic imaging and remodeling in pregnancy (chirp) study," *Journal of Cardiovascular Magnetic Resonance*, vol. 16, no. 1, p. 1, 2014.

[27] C. Pessel and C. Bonanno, "Valve disease in pregnancy," in *Seminars in perinatology*, vol. 38, pp. 273–284, Elsevier, 2014.

[28] S. C. Robson, S. Hunter, R. J. Boys, and W. Dunlop, "Serial study of factors influencing changes in cardiac output during human pregnancy," *American Journal of Physiology-Heart and Circulatory Physiology*, vol. 256, no. 4, pp. H1060–H1065, 1989.

[29] P. A. Cavalcante, M. S. Perilhão, A. A. da Silva, A. J. Serra, A. F. Júnior, and D. S. Bocalini, "Cardiac remodeling and physical exercise: a brief review about concepts and adaptations," *International Journal of Sports Science*, vol. 6, no. 2, pp. 52–61, 2016.

[30] K. Melchiorre, G. R. Sutherland, A. Baltabaeva, M. Liberati, and B. Thilaganathan, "Maternal cardiac dysfunction and remodeling in women with preeclampsia at term," *Hypertension*, vol. 57, no. 1, pp. 85–93, 2011.

[31] J. P. Mynard, *Computer modelling and wave intensity analysis of perinatal cardiovascular function and dysfunction*. PhD thesis, Department of Paediatrics, The University of Melbourne, Heart Research Group, Murdoch Childrens Research Institute, 2011.

[32] A. Bellofiore, Z. Wang, and N. C. Chesler, "What does the time constant of the pulmonary circulation tell us about the progression of right ventricular dysfunction in pulmonary arterial hypertension?," *Pulmonary Circulation*, vol. 5, no. 2, pp. 291–295, 2015.

[33] P. Kam and I. Power, *Principles of Physiology for the Anaesthetist*. CRC Press, 2015.

[34] J. P. Mynard and J. J. Smolich, "One-dimensional haemodynamic modeling and wave dynamics in the entire adult circulation," *Annals of biomedical engineering*, vol. 43, no. 6, pp. 1443–1460, 2015.

[35] T. Boonyasirinant, P. Rajiah, R. M. Setser, M. L. Lieber, H. M. Lever, M. Y. Desai, and S. D. Flamm, "Aortic stiffness is increased in hypertrophic cardiomyopathy with myocardial fibrosis: novel insights in vascular function from magnetic resonance imaging," *Journal of the American College of Cardiology*, vol. 54, no. 3, pp. 255–262, 2009.

[36] M. Broomé, E. Maksuti, A. Bjällmark, B. Frenckner, and B. Janerot-Sjöberg, "Closed-loop real-time simulation model of hemodynamics and oxygen transport in the cardiovascular system," *Biomedical engineering online*, vol. 12, no. 1, pp. 1–20, 2013.

[37] J. M. Gardin, C. S. Burn, W. J. Childs, and W. L. Henry, "Evaluation of blood flow velocity in the ascending aorta and main pulmonary artery of normal subjects by doppler echocardiography," *American heart journal*, vol. 107, no. 2, pp. 310–319, 1984.

[38] C. Ginghina, C. C. Beladan, M. Iancu, A. Calin, and B. A. Popescu, "Respiratory maneuvers in echocardiography: a review of clinical applications," *Cardiovascular ultrasound*, vol. 7, no. 1, p. 42, 2009.

[39] W. F. Graettinger, E. R. Greene, and W. F. Voyles, "Doppler predictions of pulmonary artery pressure, flow, and resistance in adults," *American heart journal*, vol. 113, no. 6, pp. 1426–1436, 1987.

[40] C. H. Lorenz, E. S. Walker, V. L. Morgan, S. S. Klein, and T. P. Graham, "Normal human right and left ventricular mass, systolic function, and gender differences by cine magnetic resonance imaging," *Journal of Cardiovascular Magnetic Resonance*, vol. 1, no. 1, pp. 7–21, 1999.

[41] J. Li, S. Umar, M. Amjedi, A. Iorga, S. Sharma, R. D. Nadadur, V. Regitz-Zagrosek, and M. Eghbali, "New frontiers in heart hypertrophy during pregnancy," *American journal of cardiovascular disease*, vol. 2, no. 3, p. 192, 2012.

[42] T. Arts, J. Lumens, W. Kroon, and T. Delhaas, "Control of whole heart geometry by intramyocardial mechano-feedback: a model study," *PLoS Comput Biol*, vol. 8, no. 2, p. e1002369, 2012.

[43] N. Kametas, F. McAuliffe, J. Hancock, J. Chambers, and K. Nicolaides, "Maternal left ventricular mass and diastolic function during pregnancy," *Ultrasound in Obstetrics and Gynecology: The Official Journal of the International Society of Ultrasound in Obstetrics and Gynecology*, vol. 18, no. 5, pp. 460–466, 2001.

[44] M. Nii, M. Ishida, K. Dohi, H. Tanaka, E. Kondo, M. Ito, H. Sakuma, and T. Ikeda, "Myocardial tissue characterization and strain analysis in healthy pregnant women using cardiovascular magnetic resonance native t1 mapping and feature tracking technique," *Journal of Cardiovascular Magnetic Resonance*, vol. 20, no. 1, p. 52, 2018.

[45] R. M. Lang, L. P. Badano, V. Mor-Avi, J. Afilalo, A. Armstrong, L. Ernande, F. A. Flachskampf, E. Foster, S. A. Goldstein, T. Kuznetsova, *et al.*, "Recommendations for cardiac chamber quantification by echocardiography in adults: an update from the american society of echocardiography and the european association of cardiovascular imaging," *European Heart Journal-Cardiovascular Imaging*, vol. 16, no. 3, pp. 233–271, 2015.

[46] F. Ahmad, J. Seidman, and C. E. Seidman, "The genetic basis for cardiac remodeling," *Annu. Rev. Genomics Hum. Genet.*, vol. 6, pp. 185–216, 2005.

[47] J. A. Hill and E. N. Olson, "Cardiac plasticity," *New England Journal of Medicine*, vol. 358, no. 13, pp. 1370–1380, 2008.

8 Discussion and Conclusion

Contents

This chapter provides a summary of the work presented in this thesis, a synthesis with available literature, the limitations and novelty of the studies presented, and the clinical implications. The directions for future work are also discussed. Note that all the work presented in this thesis has been developed in collaboration with Pediatric Cardiologists and Heart Surgeons of the University Hospital of Padova (Italy). Of interest, the topics here considered are often clinical needs that haven't been addressed yet in the clinical/engineering research field.

8.1 Discussion

In this thesis, the lumped-parameter (0D) methodology was used to study several hemodynamic conditions because it allows fast simulations and adequately captures the major features of cardiac function and vascular pressure and flow dynamics throughout the whole cardiovascular system. The application of these models has a long history, as described in Chapter 2. Indeed, the first recorded use of lumped models dates back to 1899 with the work of Otto Frank [1]. Since that study, many advancements have been made to simulate the whole circulation, including the extension from single compartment models to multi-compartment models as well as multi-dimensional models [2]. These models have been used for several purposes. For example, Heldt studied the cardiovascular response to othostatic stress [3], Olufsen et al. used a 0D model to describe the hemodynamic variations during postural

changes [4], and Kim et al. coupled the heart cellular mechanics with the arterial hemodynamics [5]. 0D models have also been utilized to study the fetal hemodynamics [6, 7, 8]. Moreover, these models have been used also when considering pathological conditions. For example, Corsini et al. used the 0D methodology to derive a patient-specific model of the univentricular circulation [9], Kung et al. studied the exercise capacity of Fontan patients [10], and Di Molfetta et al. analyzed the effect of ventricular assist devices on the Fontan circulation [11]. These are only few examples of the expanse of literature that apply the lumped-parameter modeling. Indeed, these models have been widely used because they allow to represent the entire circulation, maintaining low the computational cost and highlighting the relations between each element of the system.

Although lumped-parameter modeling has been widely used, each model has a specific use or goal. Particularly, 0D models can be used when designing new medical devices or to better understand a complex system [12, 13, 14, 15, 16, 17, 18, 19, 20]. Models are helpful tools for these purposes because by simplifying a very complex system, they allow to understand the intrinsic functionalities of each component of the system. Moreover, beyond the cultural role of extending knowledge about the cardiovascular system, the knowledge gained from these models may eventually lead to social and economic benefits to society. Indeed, as Kokalari et al. pointed out in [21], a deeper understanding of the cardiovascular system allows more effective and less expensive medical treatments, models may reduce the experiments on animals, and numerical tools may be used as a testing and training platform for students. It is in this context that the work presented in this thesis has been developed. Indeed, the common thread of every chapter is the development of knowledge of a particular physiological or pathological condition, analyzing the hemodynamic cascade that links each functional element of the circulation. Moreover, a better understanding of complex pathological conditions is likely to contribute to goals of improving diagnosis, management, and outcomes.

Lumped-parameter modeling is very useful whenever the whole circulation is to be studied. Indeed, it allows to understand the effect of a localized or distributed condition over the entire circulation, i.e., the global hemodynamics. Moreover, this methodology is characterized by high flexibility that allows the researcher to create the model depending on the need: more or less detailed models can be constructed. For example, the model described in Chapter 3 may be considered a simplified version of the model presented

in Chapter 7. This because the purpose of Chapter 3 was to understand the global differences between the biventricular and univentricular circulations, without the need to focus on a particular organ. On the other hand, in Chapter 7 the focus is to understand the overall hemodynamic changes during gestation, whilst also considering the localized hemodynamics of particular organs, such as the uterus. Thus, once understood the lumped methodology, it is possible to analyze a wide range of conditions constructing the model depending on the needs. Of course, this methodology has also limitations. Indeed, lumped-parameter modeling does not represent wave propagation (although transmission line models are technically 0D, these ignore non-linearities), or 0D models cannot be applied for applications that are heavily dependent on complex flow patterns (such as assessing localized wall shear stress patterns).

To build a proper model it is fundamental to include also a proper description of the heart. In this thesis, the heart is represented by the well-known time-varying elastance model, which represents myocardial contraction and relaxation as an increase and decrease in chamber elastance (i.e. the inverse of compliance) respectively [22, 23, 24].
Finally, the inclusion of the heart valves is essential to represent hemodynamic interactions within the heart and between the heart and blood vessels. In the literature, both the ideal diode (instantaneous valve opening/closing) [11, 20, 25] and more detailed models that include valve dynamics [26, 27, 28] have been considered. The choice of valve model likely has a limited impact when considering global hemodynamics (such as mean pressures and flows), but becomes more important when the aim is to reproduce central waveforms more accurately. Indeed, both the models allow to represent physiological hemodynamics, and, as it is demonstrated also in this thesis, also a more simple model is able to simulate the intrinsic features of the hemodynamics considered (e.g., Chapter 3).

Even though lumped-parameter modeling is widely used, the development of a model able to accurately represent the whole cardiovascular system is not trivial, especially when many compartments are considered. Indeed, each model is a set of mathematical equations of variables, e.g., pressures and flows, interweave with several parameters, e.g, valves' dimensions, compliances, resistances, heart functionalities and so on. These parameters are usually difficult or impossible to be directly measured [21]. For this reason, the methodology introduced in Section 2.7 is a powerful tool. Indeed, from very few parameters, derived from literature or clinical measurements, it is

possible to construct a 0D model with every level of complexity in terms of number of compartments. Moreover, the few rules derived from physiology, is an efficient approach that could be applied to when building new models. Importantly, the methodology was applied in all the chapters, and it is shown that the approach led to close agreement with data available in the literature.

8.1.1 Novelty and relevance

In this thesis, several topics were considered. First, the focus was posed on the Fontan circulation. In Chapter 3, the Fontan circulation was compared to the biventricular one, considering both the pediatric and adult patients. The results highlight the limitations of the Fontan circulation. Indeed, for the first time, it was shown with an engineering approach that it is the suction function of the single ventricle that constitutes an intrinsic limit of this circulation. This conclusion supports the hypothesis advanced by Gewellig and Brown [29] that ventricular suction is one of the pivotal limiting factors in the Fontan circulation. Right ventricular dysfunction was considered in Chapter 4. This study arose from the desire to better elucidate the importance of the pulmonary ventricle and its functionality. For the first time, a numerical model able to represent the right ventricular dysfunction was developed. This pathology has long been underestimated compared to the left ventricular dysfunction, and for this reason, there is less data available and understanding of the impact of right ventricular dysfunction. Moreover, a deeper understanding of the manifestation and features of RV dysfunction is a need arising among clinicians [30]. Thus, the work presented in Chapter 4 shows the hemodynamic features of RV dysfunction. Particularly, the results support the debated hypothesis advanced by Gatzoulis et al. [31] that the appearance of a late peak in pulmonary flow, in association with the RV conduit behavior, is intrinsically related to an increased ventricular stiffness. In Chapter 5 ventricular obstruction in pediatric patients was considered. This model has the potentiality to be applied to several pathological conditions, i.e., cardiac tumors, subvalvular stenosis, supravalvular stenosis, and so on. The choice to consider pediatric patients, particularly babies of 2-3 years of age, is particularly relevant because these types of pathologies can be fatal much sooner in this age group than in adults, and ventricular outflow tract obstruction in the neonate and infant is still a significant challenge [32]. A numerical tool able to identify the obstruction size that produces a given pressure gradient and/or a given cardiac output may become in the future a very useful tool for clinicians, supporting the decision making in

prediction of critical conditions and in surgery planning aimed at restoring normal hemodynamics. Finally, Chapters 6 and 7 are developed to help address the paucity of modeling work aimed at understanding sex-specific physiology and disease, the importance of which is increasingly being recognized in clinical and experimental research [33, 34, 35, 36]. For the first time, a woman-specific model was developed, considering female parameters and validating it with *only* female-specific *in vivo* data. From this model, a sex-independent model was developed, without any particular reproductive organ. The comparison between the male and female models showed that hemodynamic differences exist and are maintained even after normalization to the body surface area or the body mass. Thus, results highlight the importance of considering sex-specific parameters also when numerical models are built. The woman specific model allows also to analyze the different phases of gestation. Particularly, a lumped-parameter model of the whole maternal circulation, able to reproduce the hemodynamic changes that arise during pregnancy and incorporating a cardiac remodeling algorithm based on myofiber and wall shear stresses homeostasis principles, was developed for the first time. Although employing two very simple assumptions, changes in cardiac mass and geometry were correctly predicted. These techniques provide insight into the biomechanical basis of cardiac remodeling during pregnancy and may be useful in future to investigate cardiovascular problems that arise in some pregnancies, although the mechanistic (i.e. mechanbiological) basis of these findings requires further study.

8.1.2 Limitations and future works

This thesis has demonstrated the broad utility of lumped-parameter models for investigating cardiovascular dynamics. However, contrary to higher-order models, this methodology does not allow to obtain spatial information. Indeed, the pressure and flow waveforms are obtained considering a uniform distribution over each compartment. Despite that, to overcome this limitation to some degree, the use of multi-compartment models provided sufficient information about the spatial distribution of hemodynamic quantities in different territories of the circulation. Moreover, since these models allow to represent the whole blood circulation, they clearly involve a number of simplifications. Thus, it is important to have in mind that they allow to better understand the hemodynamics of interest but they are not an exact replica of the physiological system.

The elastance theory employed in this thesis derives from experimental

measurements and it has been widely validated [18, 20, 23, 24, 37, 38, 39, 40]. Also the numerical results reported here confirm the possibility to reasonable represents the hemodynamics of interest. Despite the wide use of the double-Hill function, the relation between τ and m and the duration of the different phases of the heartbeat and the resulting contraction/relaxation are clear, however, the quantitative links between these parameters and the cardiac mechanics are still unclear. Future work will be addressed to try to overcome this issue. Moreover, as done by others [18, 20, 37, 38, 39], the chamber interactions have been neglected in this thesis, however, the influence of chamber interactions should be addressed in future work.

Another fundamental aspect is the validation of 0D models. Indeed, in order to be reliable, these models must be properly validated. In this thesis, this step was done with only *in vivo* clinical data obtained from literature. Indeed, it is very difficult to obtain direct measurements from humans. However, future works will aim at building research programs to further validate the models presented. In accordance with that, further considerations should address also the inclusion of regulatory mechanisms, both in the early- and long-term regulation, to better simulate real patients. For example, the inclusion of neurohormonal compensatory mechanisms in the presence of ventricular dysfunction [41] will enhance the description of the hemodynamics understanding also how these regulatory mechanisms help in restoring physiological hemodynamics but may further deteriorate the ventricular functions when they are sustained for long periods [41]. Thus, the inclusion of compensatory mechanisms will allow to obtain a full description of the hemodynamics of interest. Beyond that, more realistic models of the Fontan circulation will be considered, including for example the liver. This will allow to understand the role of this organ that is known to be fundamental in the long-term outcomes [42, 43, 44]. In addition, an important topic of future research relates to the cardiovascular adaptations to pregnancy for women with a Fontan circulation, given that many girls with a Fontan circulation are now surviving to a child-bearing age, but little is known about how this unique circulation adapts to the physiological challenge of gestation, as well as the limitations and dangers this poses to both the woman and fetus [45, 46, 47].

Finally, the sensitivity analyses conducted in this thesis did not consider the effects of combined parameters on the outputs, i.e., global sensitivity analysis, but focuses on the influence of a single parameter at a time, i.e., local sensitivity analysis. However, as already pointed out in Chapter 2,

the models here developed do not have strong non-linearities, and thus, the absence of strong interactions between parameters can be assumed. The relevant parameters to be analyzed are hence derived from physical and physiological model relations [28].

8.2 Conclusion

In this thesis, lumped-parameter modeling was utilized to study several important physiopathological conditions. The methodology allows to consider the whole blood circulation highlighting the effect of each functional element of the cardiovascular system. The common thread behind every physiopathological condition considered is a desire to extend the knowledge of those conditions that historically have been neglected. The use of models is very promising because it allows to study any system of interest at very low cost, understanding *non-invasively* the function of the whole cardiovascular system. Particularly, lumped-parameter models enable the global representation of pressures, flows, and volumes of the systemic and pulmonary networks. With further development and validation, models such as these may become powerful tools in supporting clinicians in their decision process, supporting the development of knowledge, the identification of symptoms, the treatments of complicated pathologies, and in the future, they could be used to extract more specific and/or useful information from non-invasive measurements.

Bibliography

[1] K. Sagawa, R. K. Lie, and J. Schaefer, "Translation of otto frank's paper "die grundform des arteriellen pulses" zeitschrift für biologie 37: 483–526 (1899)," *Journal of molecular and cellular cardiology*, vol. 22, no. 3, pp. 253–254, 1990.

[2] Y. Shi, P. Lawford, and R. Hose, "Review of zero-d and 1-d models of blood flow in the cardiovascular system," *Biomedical engineering online*, vol. 10, no. 1, p. 33, 2011.

[3] T. Heldt, *Computational models of cardiovascular response to orthostatic stress*. PhD thesis, Massachusetts Institute of Technology, 2004.

[4] M. S. Olufsen, J. T. Ottesen, H. T. Tran, L. M. Ellwein, L. A. Lipsitz, and V. Novak, "Blood pressure and blood flow variation during postural

change from sitting to standing: model development and validation," *Journal of applied physiology*, vol. 99, no. 4, pp. 1523–1537, 2005.

[5] Y.-T. Kim, J. S. Lee, C.-H. Youn, J.-S. Choi, and E. B. Shim, "An integrative model of the cardiovascular system coupling heart cellular mechanics with arterial network hemodynamics," *Journal of Korean Medical Science*, vol. 28, no. 8, pp. 1161–1168, 2013.

[6] M. B. Yigit, W. J. Kowalski, D. J. Hutchon, and K. Pekkan, "Transition from fetal to neonatal circulation: modeling the effect of umbilical cord clamping," *Journal of biomechanics*, vol. 48, no. 9, pp. 1662–1670, 2015.

[7] J. P. van den Wijngaard, B. E. Westerhof, D. J. Faber, M. M. Ramsay, N. Westerhof, and M. J. Van Gemert, "Abnormal arterial flows by a distributed model of the fetal circulation," *American Journal of Physiology-Regulatory, Integrative and Comparative Physiology*, vol. 291, no. 5, pp. R1222–R1233, 2006.

[8] P. Garcia-Canadilla, P. A. Rudenick, F. Crispi, M. Cruz-Lemini, G. Palau, O. Camara, E. Gratacos, and B. H. Bijens, "A computational model of the fetal circulation to quantify blood redistribution in intrauterine growth restriction," *PLoS computational biology*, vol. 10, no. 6, 2014.

[9] C. Corsini, C. Baker, E. Kung, S. Schievano, G. Arbia, A. Baretta, G. Biglino, F. Migliavacca, G. Dubini, G. Pennati, *et al.*, "An integrated approach to patient-specific predictive modeling for single ventricle heart palliation," *Computer methods in biomechanics and biomedical engineering*, vol. 17, no. 14, pp. 1572–1589, 2014.

[10] E. Kung, G. Pennati, F. Migliavacca, T.-Y. Hsia, R. Figliola, A. Marsden, and A. Giardini, "A simulation protocol for exercise physiology in fontan patients using a closed loop lumped-parameter model," *Journal of biomechanical engineering*, vol. 136, no. 8, 2014.

[11] A. Di Molfetta, G. Ferrari, S. Filippelli, L. Fresiello, R. Iacobelli, M. G. Gagliardi, and A. Amodeo, "Use of ventricular assist device in univentricular physiology: the role of lumped parameter models," *Artificial Organs*, vol. 40, no. 5, pp. 444–453, 2016.

[12] L. Asner, M. Hadjicharalambous, R. Chabiniok, D. Peresutti, E. Sammut, J. Wong, G. Carr-White, P. Chowienczyk, J. Lee, A. King, *et al.*, "Estimation of passive and active properties in the human heart using

3d tagged mri," *Biomechanics and modeling in mechanobiology*, vol. 15, no. 5, pp. 1121–1139, 2016.

[13] A. Baretta, C. Corsini, A. L. Marsden, I. E. Vignon-Clementel, T.-Y. Hsia, G. Dubini, F. Migliavacca, G. Pennati, and T. M. O. C. H. Alliance, "Respiratory effects on hemodynamics in patient-specific cfd models of the fontan circulation under exercise conditions," *European Journal of Mechanics-B/Fluids*, vol. 35, pp. 61–69, 2012.

[14] S. Safaei, C. P. Bradley, V. Suresh, K. Mithraratne, A. Muller, H. Ho, D. Ladd, L. R. Hellevik, S. W. Omholt, J. G. Chase, *et al.*, "Roadmap for cardiovascular circulation model," *The Journal of physiology*, vol. 594, no. 23, pp. 6909–6928, 2016.

[15] F. Migliavacca, G. Pennati, G. Dubini, R. Fumero, R. Pietrabissa, G. Urcelay, E. L. Bove, T.-Y. Hsia, and M. R. de Leval, "Modeling of the norwood circulation: effects of shunt size, vascular resistances, and heart rate," *American Journal of Physiology-Heart and Circulatory Physiology*, vol. 280, no. 5, pp. H2076–H2086, 2001.

[16] W. P. Santamore and D. Burkhoff, "Hemodynamic consequences of ventricular interaction as assessed by model analysis," *American Journal of Physiology-Heart and Circulatory Physiology*, vol. 260, no. 1, pp. H146–H157, 1991.

[17] M. Vollkron, H. Schima, L. Huber, and G. Wieselthaler, "Interaction of the cardiovascular system with an implanted rotary assist device: simulation study with a refined computer model," *Artificial organs*, vol. 26, no. 4, pp. 349–359, 2002.

[18] L. Punnoose, D. Burkhoff, S. Rich, and E. M. Horn, "Right ventricular assist device in end-stage pulmonary arterial hypertension: insights from a computational model of the cardiovascular system," *Progress in cardiovascular diseases*, vol. 55, no. 2, pp. 234–243, 2012.

[19] E. Lanzarone, R. Vismara, and G. B. Fiore, "A new pulsatile volumetric device with biomorphic valves for the in vitro study of the cardiovascular system," *Artificial organs*, vol. 33, no. 12, pp. 1048–1062, 2009.

[20] S. Bozkurt, "Mathematical modeling of cardiac function to evaluate clinical cases in adults and children," *PloS one*, vol. 14, no. 10, p. e0224663, 2019.

[21] I. Kokalari, T. Karaja, and M. Guerrisi, "Review on lumped parameter method for modeling the blood flow in systemic arteries," 2013.

[22] H. Suga, K. Sagawa, and A. A. Shoukas, "Load independence of the instantaneous pressure-volume ratio of the canine left ventricle and effects of epinephrine and heart rate on the ratio," *Circulation research*, vol. 32, no. 3, pp. 314–322, 1973.

[23] H. Senzaki, C.-H. Chen, and D. A. Kass, "Single-beat estimation of end-systolic pressure-volume relation in humans: a new method with the potential for noninvasive application," *Circulation*, vol. 94, no. 10, pp. 2497–2506, 1996.

[24] J. P. Mynard, *Computer modelling and wave intensity analysis of perinatal cardiovascular function and dysfunction*. PhD thesis, Department of Paediatrics, The University of Melbourne, Heart Research Group, Murdoch Childrens Research Institute, 2011.

[25] C. Luo, D. Ramachandran, D. L. Ware, T. S. Ma, and J. W. Clark, "Modeling left ventricular diastolic dysfunction: classification and key indicators," *Theoretical Biology and Medical Modelling*, vol. 8, no. 1, p. 14, 2011.

[26] J. Mynard, M. Davidson, D. Penny, and J. Smolich, "A simple, versatile valve model for use in lumped parameter and one-dimensional cardiovascular models," *International Journal for Numerical Methods in Biomedical Engineering*, vol. 28, no. 6-7, pp. 626–641, 2012.

[27] F. Liang, H. Senzaki, C. Kurishima, K. Sughimoto, R. Inuzuka, and H. Liu, "Hemodynamic performance of the fontan circulation compared with a normal biventricular circulation: a computational model study," *American Journal of Physiology-Heart and Circulatory Physiology*, vol. 307, no. 7, pp. H1056–H1072, 2014.

[28] M. Broomé, E. Maksuti, A. Bjällmark, B. Frenckner, and B. Janerot-Sjöberg, "Closed-loop real-time simulation model of hemodynamics and oxygen transport in the cardiovascular system," *Biomedical engineering online*, vol. 12, no. 1, pp. 1–20, 2013.

[29] M. Gewillig and S. C. Brown, "The fontan circulation after 45 years: update in physiology," *Heart*, vol. 102, no. 14, pp. 1081–1086, 2016.

[30] R. Padang, N. Chandrashekar, M. Indrabhinduwat, C. G. Scott, S. A. Luis, K. Chandrasekaran, H. I. Michelena, V. T. Nkomo, S. V. Pislaru,

P. A. Pellikka, *et al.*, "Aetiology and outcomes of severe right ventricular dysfunction," *European heart journal*, vol. 41, no. 12, pp. 1273–1282, 2020.

[31] M. A. Gatzoulis, A. L. Clark, S. Cullen, C. G. Newman, and A. N. Redington, "Right ventricular diastolic function 15 to 35 years after repair of tetralogy of fallot: restrictive physiology predicts superior exercise performance," *Circulation*, vol. 91, no. 6, pp. 1775–1781, 1995.

[32] B. Alsoufi, T. Karamlou, B. W. McCrindle, and C. A. Caldarone, "Management options in neonates and infants with critical left ventricular outflow tract obstruction," *European journal of cardio-thoracic surgery*, vol. 31, no. 6, pp. 1013–1021, 2007.

[33] L. Schiebinger, "Gendered innovations in biomedicine and public health research," in *Sex and Gender Aspects in Clinical Medicine*, pp. 5–8, Springer, 2012.

[34] V. M. Miller, "Why are sex and gender important to basic physiology and translational and individualized medicine?," *American Journal of Physiology-Heart and Circulatory Physiology*, 2014.

[35] M. della Salute, "Il genere come determinante della salute. lo sviluppo della medicina di genere per garantire equità e appropriatezza della cura," *Quaderni del Ministero della Salute*, vol. 26, 2016.

[36] M. Sanghavi and J. D. Rutherford, "Cardiovascular physiology of pregnancy," *Circulation*, vol. 130, no. 12, pp. 1003–1008, 2014.

[37] E. Maksuti, B. E. Westerhof, M. Ugander, D. W. Donker, M. Carlsson, and M. Broomé, "Cardiac remodeling in aortic and mitral valve disease: a simulation study with clinical validation," *Journal of Applied Physiology*, vol. 126, no. 5, pp. 1377–1389, 2019.

[38] A. Ferreira, S. Chen, M. A. Simaan, J. R. Boston, and J. F. Antaki, "A nonlinear state-space model of a combined cardiovascular system and a rotary pump," in *Proceedings of the 44th IEEE Conference on Decision and Control*, pp. 897–902, IEEE, 2005.

[39] F. Seemann, P. Arvidsson, D. Nordlund, S. Kopic, M. Carlsson, H. Arheden, and E. Heiberg, "Noninvasive quantification of pressure-volume loops from brachial pressure and cardiovascular magnetic resonance," *Circulation: Cardiovascular Imaging*, vol. 12, no. 1, p. e008493, 2019.

[40] J. T. Ottesen and M. Danielsen, "Modeling ventricular contraction with heart rate changes," *Journal of theoretical biology*, vol. 222, no. 3, pp. 337–346, 2003.

[41] G. Jackson, C. Gibbs, M. Davies, and G. Lip, "Abc of heart failure: Pathophysiology," *BMJ: British Medical Journal*, vol. 320, no. 7228, p. 167, 2000.

[42] A. Agarwal, C. Cunnington, A. Sabanayagam, L. Zier, C. E. McCulloch, I. S. Harris, E. Foster, D. Atkinson, A. Bryan, P. Jenkins, *et al.*, "Cardiopulmonary exercise testing in the evaluation of liver disease in adults who have had the fontan operation," *Archives of cardiovascular diseases*, vol. 111, no. 4, pp. 276–284, 2018.

[43] M. Gewillig and D. J. Goldberg, "Failure of the fontan circulation," *Heart failure clinics*, vol. 10, no. 1, pp. 105–116, 2014.

[44] C. de Lange, "Imaging of complications following fontan circulation in children—diagnosis and surveillance," *Pediatric Radiology*, 2020.

[45] R. Hatton, J. M. Colman, M. Sermer, S. C. Siu, and C. K. Silversides, "Congenital heart disease: Pregnancy and contraception," in *Evidence-Based Cardiology Consult*, pp. 481–496, Springer, 2014.

[46] D. Zentner, D. S. Celermajer, T. Gentles, Y. d'Udekem, J. Ayer, G. M. Blue, C. Bridgman, L. Burchill, M. Cheung, R. Cordina, *et al.*, "Management of people with a fontan circulation: a cardiac society of australia and new zealand position statement," *Heart, Lung and Circulation*, vol. 29, no. 1, pp. 5–39, 2020.

[47] E. Moroney, E. Posma, A. Dennis, Y. d'Udekem, R. Cordina, and D. Zentner, "Pregnancy in a woman with a fontan circulation: A review," *Obstetric medicine*, vol. 11, no. 1, pp. 6–11, 2018.

A | MATLAB Code: Example of lumped parameter model

In this Appendix is reported, as an example, the code used to solve a lumped parameter model.

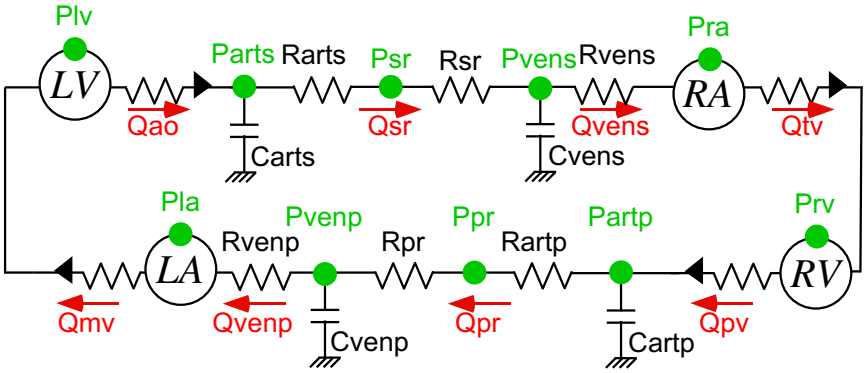

Figure A.1: *Circulation model composed of: left ventricle (LV), systemic arteries, vascular bed, and veins, right ventricle (RV), right atrium (RA), pulmonary arteries, vascular bed, and veins, left atrium (LA), and heart valves (▶).Subscripts: ao, aortic valve, arts, systemic arteries, sr, systemic small vessels, vens, systemic veins, tv, tricuspid valve, pv, pulmonary valve, artp, pulmonary arteries, pr, pulmonary small vessels, venp, pulmonary veins, mv, mitral valve.*

Given the model reported in Fig. A.1, the following equations are required to compute the hemodynamics:

```
1       Pla = Ela*(Vla-in.VoLA); % [mmHg]
2       Pra = Era*(Vra-in.VoRA); % [mmHg]
3       Plv = Elv*(Vlv-in.VoLV); % [mmHg]
4       Prv = Erv*(Vrv-in.VoRV); % [mmHg]
5
6       % ------------- Qpv -------------
7       Qpv = (Prv≥Partp)*(Prv-Partp)/(in.Rpv); % [ml/s]
8       % ------------- Qao -------------
9       Qao = (Plv≥Parts)*(Plv-Parts)/(in.Raov); % [ml/s]
```

```
10      % ------------- Qtv -------------
11      Qtv = (Pra≥Prv)*(Pra-Prv)/in.Rtv; % [ml/s]
12      % ------------- Qmv -------------
13      Qmv = (Pla≥Plv)*(Pla-Plv)/in.Rmv; % [ml/s]
14
15      Qsr = (Parts-Pvens)/(in.Rsr+in.Rarts); % [ml/s]
16      Qvens = (Pvens-Pra)/in.Rvens; % [ml/s]
17      Qpr = (Partp-Pvenp)/(in.Rpr+in.Rartp); % [ml/s]
18      Qvenp = (Pvenp-Pla)/in.Rvenp; % [ml/s]
19
20      % Vlv
21      dy(1) = Qmv-Qao; % [ml]
22      % Vrv
23      dy(2) = Qtv-Qpv; % [ml]
24      % Vla
25      dy(3) = Qvenp-Qmv; % [ml]
26      % Vra
27      dy(4) = Qvens-Qtv; % [ml]
28      % Parts
29      dy(5) = (Qao-Qsr)/in.Carts; % [mmHg]
30      % Pvens
31      dy(6) = (Qsr-Qvens)/in.Cvens; % [mmHg]
32      % Partp
33      dy(7) = (Qpv-Qpr)/in.Cartp; % [mmHg]
34      % Pvenp
35      dy(8) = (Qpr-Qvenp)/in.Cvenp; % [mmHg]
```

Who should be interested in the MATLAB Code developed at the present thesis, please contact me at giulia.comunale@dicea.unipd.it.

Acknowledgments

Throughout these three years of my Ph.D. I have received a great deal of support and assistance, and for this, I would like to thank all of you.

First, I would like to thank my supervisor, Professor Francesca M. Susin, whose expertise was invaluable in formulating the research questions and methodology. Your insightful feedback pushed me to sharpen my thinking and brought my work to a higher level. Thank you for your guidance and support during this time, not only in the Ph.D. research. A special thank you is for showing me *how to take the sourest lemon of life and turned it into something resembling lemonade*[1].

I would like to deeply acknowledge Doctor Jonathan P. Mynard, co-supervisor of my work. Thank you for your time and effort in helping me. Thank you for the possibility to come overseas, improve my personal skills, be inspired by a different culture, and gain research experience. The time at the Murdoch Children's Research Institute has been one of the best opportunities during these three years of Ph.D.

I would also like to thank Doctor Paolo Peruzzo and all the clinicians of the University Hospital of Padova. Thank you Paolo for your time, help, and for being always available when I needed it. Thank Professor Giovanni Di Salvo, Doctor Biagio Castaldi, and Professor Massimo Padalino for formulating always interesting clinical questions, and for helping me in gaining clinical knowledge and perspective. Thank you for your time, expertise, and motivation. Your work is very inspiring and the collaboration with you and the possibility to personally contribute to solving at least in part clinical problems have been the motivations behind all the efforts of these three years.

Thank you to my Italian and Australian colleagues to share good and bad times and making these three years funnier.

I would like to thank my parents and my sister, my grandparents, and all my (biological and acquired) family. Your support and sympathetic ear have been very helpful. You are always there for me.

In addition, I could not have completed this thesis without the support

[1] *This is us.*

of my friends, my *BFFs*, who provided stimulating discussions as well as happy distractions to rest my mind outside of my research. Thank you for making me laugh and feel part of a big family. It wouldn't have been the same without you.

Thank you, Julie and Raffaella, my Australian family and among the best person of my life. You made me feel at home and loved, you made my Australian time easier, funnier, and more adventured. Thank you!

Last but not least, thank you, Matteo. You are my special sunshine. Thank you for your love and support, and for always believing in me. You are one of the best and smartest people I know, you motivate me in being better every day. A special and loving thank to you.